Spectroscopic Imaging and Simulations of Coherent Solar Radio Emission Sources in a Turbulent Corona

Daniel L. Clarkson
BSc (Hons)

Submitted in fulfilment of the requirements for the
Degree of Doctor of Philosophy

School of Physics & Astronomy
College of Science and Engineering
University of Glasgow

April 2023

This thesis is my own composition except where indicated in the text.
No part of this thesis has been submitted elsewhere for any other degree or qualification.

30 April 2023

There is as yet insufficient data for a meaningful answer.

—Isaac Asimov, *The Last Question*

Abstract

Solar activity sporadically erupts due to the release of magnetic energy that manifest as impulsive bursts of electromagnetic emission. Solar radio bursts provide a valuable diagnostic of the low corona where the energy release originates and of the environment through which the exciter of radio emission propagates. However, the corona is a turbulent environment such that the escaping radiation is significantly modulated, concealing the intrinsic exciter characteristics and spatial location. In this thesis, radio burst fine structures that can be embedded within or separate from broadband bursts are investigated. In particular, solar radio spikes are analysed using the LOw Frequency ARray (LOFAR), for the first time providing much needed time and frequency resolved imaging of individual spikes over sub-second scales at decametre frequencies. The characteristics of spikes are statistically compared across decades in frequency, demonstrating the prevalence of radio-wave scattering up to ~ 1 GHz that governs the observed decay time, rather than collisional damping. Consequently, the findings suggest that the duration of energy release of which spikes may be a direct signature, could be shorter than implied from observations, particularly at decametre frequencies. Analysis of the characteristics of decametre spikes and striae from the same event presents similarity in morphology, spatial location, and polarisation, indicating that the spikes are likely generated via plasma emission. The escaping spike and striae radiation presents superluminal centroid motion directed non-radially which implies the presence of an extended coronal loop with strong anisotropic turbulence. Imaging observations suggest that the magnetic structure is perturbed via the passage of a CME shock front, with the loop structure slowly restoring towards the prior configuration over time, exciting frequent magnetic reconnection that manifests as radio spike emission. As a result, the site of electron beam acceleration, the characteristics of the beam, and the prevailing turbulent conditions together determine the emitting location. However, the scattering component obscures it, making interpretation of the source in radio images challenging. A quantitative analysis of the spatial and spectral evolution of solar radio burst fine structures as the radiation escapes through a dipolar magnetic structure with anisotropic turbulence is presented via radio-wave scattering simulations. The observed spatial location and motion of the spikes and striae is replicated, as well as the suppressed fine structure drift rate in dynamic spectra. The combination of high resolution observations with state-of-the-art simulations show that sub-second solar radio burst fine structures must be decoupled from anisotropic scattering effects in order to assess the intrinsic emitter. As such, the apparent source location, magnetic field structure, and turbulent conditions must be considered simultaneously.

Contents

List of Tables

List of Figures

List of Publications

Publications

1 **Clarkson, D. L.**, Kontar, E. P., Gordovskyy, M., Chrysaphi, N., and Vilmer, N., "First Frequency-time-resolved Imaging Spectroscopy Observations of Solar Radio Spikes", *The Astrophysical Journal Letters*, vol. 917, no. 2, 2021. doi:10.3847/2041-8213/ac1a7d.

2 Gordovskyy, M., Kontar, E. P., **Clarkson, D. L.**, Chrysaphi, N., and Browning, P. K., "Sizes and Shapes of Sources in Solar Metric Radio Bursts", *The Astrophysical Journal*, vol. 925, no. 2, 2022. doi:10.3847/1538-4357/ac3bb7.

3 Chen, X., Kontar, E. P., **Clarkson, D. L.**, and Chrysaphi, N., "The frequency ratio and time delay of solar radio emissions with fundamental and harmonic components", *Monthly Notices of the Royal Astronomical Society*, vol. 520, no. 2, 2023. doi:10.1093/mnras/stad325.

4 **Clarkson, D. L.**, Kontar, E. P., Vilmer, N., Gordovskyy, M., Chen, X., and Chrysaphi, N., "Solar Radio Spikes and Type IIIb Striae Manifestations of Sub-second Electron Acceleration Triggered by a Coronal Mass Ejection", *The Astrophysical Journal*, vol. 946, no. 1, 2023. doi:10.3847/1538-4357/acbd3f.

5 Kontar, E. P., Emslie, G., **Clarkson, D. L.**, Chen, X., Chrysaphi, N., Azzollini, F., Jeffrey, N. L. S., and Gordovskyy, M. "An Anisotropic Density Turbulence Model from the Sun to 1 au Derived From Radio Observations", *Submitted to The Astrophysical Journal*, 2023.

Preface

Chapter 1 provides an introduction to the relevant background material required in this thesis. It describes the solar atmosphere in regards to its structure and activity in the form of active regions, flares, coronal mass ejections and jets. The coronal magnetic field and density models are presented, and the connection between solar activity and space weather is discussed. The main mechanisms for the generation of radio emission considered in this thesis are presented, with a description of various types of broadband solar radio bursts. Th effects of scattering on the propagation radio-waves is discussed, and the implication of ionospheric refraction. The chapter concludes with an overview of the instrumentation used in the thesis.

Chapter 2 presents an overview of solar radio burst fine structures: striae, drift pairs, and spikes. The origin of such fine structures is presented, as well as recent observations and their typical characteristics. The chapter focuses on solar radio spikes, which form the bulk of interest for this thesis. In addition, the connection between spikes and communication disruption at Earth is presented.

Chapter 3 presents the first time and frequency resolved imaging observations of sub-second solar radio spikes at decametre frequencies using LOFAR. The chapter begins with an overview of the event that produced the spikes. The methods of measuring the spike parameters are discussed, and their typical characteristics presented. The results show that spikes and striae arise from the same region of the corona and share similar properties, suggesting that these decametre spikes are produced via plasma emission. The individual spike evolution in the time and fixed frequencies suggests that the radiation escapes through strong anisotropic turbulence, broadening the time profiles and inducing superluminal, non-radial motion across the sky-plane. The dominance of scattering suggests that the energy release time is likely shorter than assumed from observations.

In chapter 4, a statistical approach is adopted, analysing over 1000 spikes and 250 striae from the same event. Observations of a bi-directional Type IIIb burst provides insight into the acceleration region height. The striae centroid trajectories that drift over time due to scattering are inconsistent with the trajectory of the centroids along the burst spine (the peak of each striae at different frequencies). This suggests that the emitter was propagating in a different direction than the scattered radio-waves, and thus likely originated from an acceleration region that is lower in the loop structure than where the source is observed, in a region where the magnetic field direction matches the exciter motion. Moreover, the observed spike and striae heights are shown to lose their frequency dependence with height at the time of the coronal mass ejection (CME) eruption. The heights then begin to increase over time for subsequent burst observations at a given frequency, suggesting that the loop structure was perturbed by the CME shock to lie along the line-of-sight, which then slowly restored back towards the prior configuration. The fixed frequency motion of spikes and striae that are close in time and frequency are shown to almost completely overlap, suggesting the sources emit radio-waves from the same region of space. The spike centroid velocities induced from scattering have a wide spread suggesting that the anisotropy, turbulence level, and emission angle within the loop may vary from burst to burst. The statistical observed spike areas are compared with the few observations in the literature at decimetre frequencies, presenting a trend consistent with scattering predictions up to ~ 1 GHz. Assuming plasma emission, the fractional spike bandwidth is replicated via the Langmuir wave dispersion relation, which agrees with observational data across decades in frequency, with the spread in bandwidth accounted for by different magnetic field strengths.

Chapter 5 presents the results of radio-wave propagation simulations with a dipolar magnetic field structure, in order to replicate the results in the previous chapters. The simulations use a recently developed 3D radio-wave propagation code with an anisotropic density fluctuation spectrum. The previously used radial magnetic field is replaced with a dipole, with the dipole and source locations varied across the solar disk. The evolution of an injected radio source is presented in the context of the observed centroid motion for spikes and striae in chapters 3 and 4. The centroid trajectory and location is replicated for an injected source at $\theta = 50°$ from the observers line of sight, with strong anisotropy of $\alpha = 0.2$. The simulations suggest that the intrinsic emitter location was 0.13 $R_\odot$ away from the observed location in the sky-plane. For regions of strong anisotropy $\alpha = 0.1$, it is shown that the source may split into two components. Furthermore, the effect of radio-wave scattering on the suppression of the fine structure drift rate is shown.

Acknowledgements

I would first like to express my sincere gratitude to my supervisor, Professor Eduard P. Kontar, for his expert guidance over the past few years. Your unwavering support on this journey has been invaluable in shaping both the project and myself. I extend this gratitude to Dr. Nicole Vilmer, for her incredibly valuable insight over the years.

Thank you to the Defense Science and Technology Laboratory (Dstl) for their funding that made it possible for me to embark to this journey.

I would like to thank my friends and family for shaping me into who and where I am today. Thank you Jon for reminding me why I chose to do this, and keeping me sane here in Glasgow. Thank you to my parents and grandparents for their support and encouragement in life, no matter what I chose to do. And of course, thank you to all in Room 604 who made the start of this journey so welcoming.

Most importantly, I owe everything to my wonderful partner in life Paula. Without you, none of this would have been possible. You kept me grounded in what was undoubtedly a difficult time. Tú significas todo para mí, para siempre. Finally, I must thank the best companion anyone could hope for, our dog Biscuit, and his persistent reminders that I need to take a break and go for a walk.

1

Introduction

1.1 The Solar Atmosphere

The Sun is a main sequence star in the middle of its life cycle. In this sense it's relatively stable, providing the energy and conditions required for humanity to observe it for thousands of years. The fusion of hydrogen nuclei into helium at the solar core releases energy that diffuses outwards through the radiative zone of the solar interior, before reaching the convective zone at a region called the tachocline. Through convective fluid flows, energy is transported towards the solar 'surface' called the photosphere with a radius of $1\ \mathrm{R}_\odot \simeq 6.96 \times 10^{10}$ cm, where the optical depth (a measure of the transparency of a medium) is such that photons can escape. Assuming a black body spectrum, the Sun peaks in optical wavelengths, and so the photosphere is defined as the layer where the optical depth at 5000 Å (green) (1 Å = 0.1 nm) is equal to approximately one. The bright circular disk that we observed from Earth may appear to have rather uniform brightness, but the reality is quite different. The photosphere is comprised of convection cells of hot plasma called granules with an effective temperature of around 5785 K (Priest, 2014). The granulated appearance forms from hot rising and cooler falling plasma, with a typical size around 1 Mm (1000 km) (Priest, 2014). In the region above the photosphere is the ~ 2 Mm thick chromosphere. The temperature rises to $\sim 2.5 \times 10^4$ K, marking the boundary of the ~ 200 km thick transition region, where the temperature rapidly increases to approximately 1 MK, and the density decreases by about two orders of magnitude (McLean & Labrum, 1985).

Beyond the chromosphere lies the corona, a hot (1–2 MK), tenuous, and inhomogeneous plasma. The bright photospheric light obscures the corona at optical wavelengths such that the corona is best observed throughout solar eclipses, or by using a coronagraph to block the glare from the photospheric light. The heating of the corona remains an outstanding problem in solar physics (e.g. Klimchuk, 2006), in part due to the difficulty of identifying a heating source compatible with the myriad of processes occurring on different spatial scales, and the complex dynamics of the chromospheric and coronal magnetic field. Despite this, the continual evolution and interaction of coronal magnetic structures combined with X-ray observations of small scale energy release termed nanoflares (Parker, 1988) with energies of $\sim 10^{24}$ erg (Lin et al., 1984; Parker, 1988) is a promising theory. The extreme temperature results in the ionisation of hydrogen such that there is an equal density of protons n_i and electrons n_e. The central focus of this thesis is on low frequency coronal radio emission. Specifically, the regime in which the energy of photons is much lower than the thermal energy of the emitting particles, i.e. $hf \ll k_B T$ where h is the Planck constant, k_B is the Boltzmann constant, and f (also denoted as ν) is the frequency. Under this condition, the Rayleigh-Jeans approximation is applicable, giving a brightness temperature of

$$T_B = \frac{c^2 I_\nu}{2 f^2 k_B}, \tag{1.1}$$

where I_ν is the measured specific intensity which is an intrinsic property of the source that describes the power per unit frequency, per unit solid angle, crossing a unit surface area, essentially describing the variation in brightness across an extended source. Therefore, the total intensity is given by

$$I_{\text{tot}} = \int_0^\infty I_\nu \, \mathrm{d}\nu. \tag{1.2}$$

For coronal sources that subtend a solid angle Ω, the observed flux is given as a flux density S_ν in solar flux units where $1\,\mathrm{sfu} = 10^{-22}\,\mathrm{W\,m^{-2}\,Hz^{-1}}$—i.e. the specific intensity integrated over Ω as

$$S_\nu = \int_{\text{source}} I_\nu \, \mathrm{d}\Omega. \tag{1.3}$$

Since $\int \mathrm{d}\Omega \propto 1/r^2$, S_ν depends on the distance between the source and observer as $S_\nu \propto r^{-2}$. The relation between brightness temperature and flux density is given by

$$S_\nu = \frac{2 k_B T_B \nu^2}{c^2} \Omega. \tag{1.4}$$

In the rest of this thesis, the flux density is given as the symbol I.

1.1.1 Coronal Structure

Observations in extreme ultraviolet (EUV) wavelengths reveal a diverse range of structures in the solar corona, including coronal holes and interconnecting loops. Coronal holes are typically found near the solar poles, particularly during solar minimum, and are associated with open magnetic field lines that allow plasma to escape and contribute to the fast solar wind. The relative depletion of hot plasma from these regions leads to a dimmer appearance compared to magnetically closed regions near the equator. These coronal loops are observable due to emitting plasma flowing along closed magnetic field lines with their foot-points located at sites of opposite magnetic polarity. If these footpoints extend over a large distance, they may form loop arcades (Aschwanden, 2005). Bright streamers are often observed atop the coronal loops, and they can increase the density by a factor of 3–10 (Priest, 2014). They are large, long-lived structures that are oriented radially outwards from the Sun for several solar radii (Aschwanden, 2005). At X-ray wavelengths, coronal observations are best conducted by spacecraft due to X-ray absorption by the Earth's atmosphere. They reveal small, bright points around 20 Mm in diameter (Priest, 2014), mostly situated above pairs of opposite magnetic polarity (e.g. Harvey, 1996). These bright points are associated with regions of the solar surface that are particularly active in terms of energy release. Indeed, X-ray activity in flaring regions can be complex, and is discussed further in section 1.1.2.2.

The corona expands out into interplanetary space in the form of the solar wind: a continuous stream of charged particles—mainly protons, electrons, α particles, and heavy ions. This wind has been studied extensively through in-situ observations by spacecraft such as Helios and Wind (Ogilvie et al., 1995), as well as the recently launched Solar Orbiter (Müller et al., 2020) and Parker Solar Probe (Fox et al., 2016). Furthermore, the Voyager 1 & 2 spacecraft have reached the boundary of the solar system and provided invaluable data on the solar wind beyond our local environment. The solar wind is characterised by two main components: the slow solar wind, with a typical velocity on the order of 500 km s^{-1}, and the fast solar wind, with a velocity around 800 km s^{-1} (McLean & Labrum, 1985). In addition, the slow solar wind has a increased density and decreased temperature of protons, along with an increased electron temperature. Moreover, the first ionisation potential (the measure of energy required to remove the valence electron) is increased in the slow solar wind, along with higher heavy ion ionisation states (Abbo et al., 2016)—i.e. a larger number of heavy ions are ionised. The constant release of plasma streaming out from the Sun makes for a turbulent coronal environment, particularly above eruptive regions.

1.1.2 The Active Sun

The Sun is a dynamic and active star that displays a wide range of phenomena on a regular basis. These phenomena include magnetic activity, eruptions, and energetic releases that can have significant effects on space weather and Earth-based technology.

1.1.2.1 Active Regions

Regions where the magnetic field protrudes through the surface form active regions around the equatorial belt within $\pm 30°$. These regions can develop over periods of a few days, reach maximum activity after around 10–15 days and can persist for weeks (Priest, 2014). At the centre of an active region are sunspots where the magnetic flux is concentrated, suppressing convection, and causing the region to appear darker and cooler than the surrounding plasma. Sunspots are an indication of increased solar activity, and their presence can vary over time due to the 11 year solar cycle. This cycle is defined by cyclic changes in the Sun's magnetic field that produce fluctuations in solar activity, known as solar minimum and maximum. During solar minimum, very few visible on the solar disk.

Active regions exhibit a bipolar magnetic structure, with the magnetic flux flowing between two islands of opposite polarity. Plasma flow is confined along the field lines owing to the plasma beta parameter (equation 1.5 discussed in section 1.1.3) having a value < 1, and forms loops and arches that extend high into the corona. Regions where the magnetic field is mainly horizontal and overlying a neutral line where the magnetic polarity inverses are filled with gas cooler than the hot corona, with a temperature around 2×10^4 K (McLean & Labrum, 1985), leading to the appearance of dark absorption features called filaments. When viewed from the limb, these features are known as prominences and can appear as emission structures. In association with flaring regions, they tend to have a length on the order of 10 Mm with densities $\geq 10^{11}$ cm^{-3} with stronger magnetic field. On the other hand, quiescent prominences are long-lived structures that can persist for months on scales of 1000 Mm (Priest, 2014). Above active regions, the corona has enhanced density and temperature, likely controlled by the stronger magnetic field that may contain denser material than the surrounding quiet regions (McLean & Labrum, 1985).

1.1.2.2 Solar Flares

A solar flare is a sudden, transient brightening near active regions caused by the rapid release of up to 10^{32} erg of magnetic energy (e.g. Emslie et al., 2005). These events can manifest across the entire electromagnetic (EM) spectrum from gamma rays to radio waves (Fletcher et al., 2011), and typically last from minutes to tens of minutes. Flaring events can be divided into different phases that may not all be present in a given flare. As described in Priest (2014), the pre-flare phase involves a gradual brightening over tens of minutes in soft X-ray (SXR) emission, produced from the thermal distribution of the plasma. The impulsive phase typically lasts a few minutes and releases emission in hard X-rays (HXR) produced via bremsstrahlung and gyrosynchrotron emission from non-thermal electrons. The main flare phase features a declining intensity that lasts up to an hour.

The release of magnetic energy associated with and without a solar flare can manifest as particle acceleration that in turn may produce phenomena such as radio emission (section 1.3.1), coronal mass ejections that drive shock waves (sections 1.1.2.3 and 1.3.2), and energetic particles that can propagate out to 1 AU and beyond (section 1.1.5). A key signature of a solar flare is the presence of non-thermal accelerated electrons with a power-law distribution (e.g. Krucker et al., 2007) with energies between approximately 10 keV to hundreds of keV that can produce the HXR emission via bremsstrahlung radiation (Brown & Smith, 1980; Vilmer, 1987) in the dense lower atmosphere. This non-thermal component can be an order of magnitude larger than a thermal component (Emslie et al., 2012) which manifests as SXRs below 10 keV and may be directly heated coronal material, or ablated chromospheric material (Benz, 2017). The temporal coincidence of the thermal and non-thermal emission components in some flares is thought to be caused via the energy released in the lower atmosphere heating the chromospheric plasma, known as the Neupert effect (Neupert, 1968).

The release of magnetic energy during solar flares is suggested to be related to magnetic reconnection. This was initially proposed by both Parker (1957) and Sweet (1958) for a long current sheet across a boundary of oppositely directed magnetic fields, yet the reconnection rate was found to be too slow for a solar flare (Priest & Forbes, 2002; Aschwanden, 2005). Petschek (1964) suggested a smaller current sheet, allowing for a faster reconnection rate of about three orders of magnitude, owing to a shorter propagation time across the current sheet (Aschwanden, 2005). Observations of the chaotically distributed, short duration solar radio spikes in dynamic spectra (section 2.3), often considered a signature of the energy release itself, has led to suggestions of fragmented energy release in flares across numerous small sites, termed 'microflares', with each releasing energy on the order of 10^{26} erg over millisecond timescales (Benz, 1985).

The classification of solar flares is based on their peak X-ray flux measured in the wavelength range of 1–8 Å by the Geostationary Operational Environmental Satellite (GOES) (section 1.5.5). The flares are categorised into five categories: A, B, C, M, and X, with sub-ranges from 1 to 9 within each category. The X-class flares are the most powerful, and even though thousands of flares are detected each year, such flares are relatively rare with only 1–10 events per year (Aschwanden & Freeland, 2012).

1.1.2.3 Coronal Mass Ejections

Coronal mass ejections (CMEs) are large-scale structures composed of magnetic flux and confined plasma that are explosively released from the Sun with typical ejection speeds of hundreds of kilometres per second (Schwenn, 2006). Not all CMEs have a flare association (Gosling, 1993; Andrews, 2003), although those that are correlated to a flare have been associated with the onset of HXR energy release (Temmer et al., 2008). A CME can drive large-scale shock front throughout the heliosphere with clearly defined flanks. The leading edge of the shock is a region of compressed plasma with increased density, with a density depletion in the wake of the CME. Interplanetary CMEs can propagate vast distances throughout the heliosphere and be detected in the vicinity of Earth's orbit (Vilmer et al., 2003). The morphology of CMEs can vary, with angular widths ranging from a few degrees to more than 120° (Schwenn, 2006). One contribution to the observed CME width is the projection effect, where a CME located near the solar disk centre can surround the occulting coronagraph, termed halo CMEs, (e.g. Howard et al., 1982). Another variety is termed a streamer-puff CME (Bemporad et al., 2005), which consists of narrow ejections near the solar limb originating from compact flare sources near the base of coronal streamers. The ejections cause the streamer to expand due to the propagating shock (e.g. Chrysaphi et al., 2020). The shock fronts can also excite radio emission known as Type II solar radio bursts (section 1.3.2), providing an alternative diagnostic of their propagation through space.

1.1.2.4 Jets

Coronal jets are collimated plasma flow structures that can originate near active regions, but are also observed in the quiet Sun. They are short lived, typically lasting only a few to tens of minutes, and are thought to be produced via magnetic reconnection in the chromosphere (Shibata et al., 2007). Observations have shown that the propagating plasma has velocities in the range of a few hundreds of kilometres per second (Mulay et al., 2016), and they have been observed in EUV, X-ray, and Hα (Kundu et al., 1995; Chen et al., 2013; Chandra et al., 2015; Mulay et al., 2016). Jets have been associated with Type III radio bursts (section 1.3.3), implying the existence of open magnetic field lines (Kundu et al., 1995; Chen et al., 2013) that the heated plasma flows along. Occasionally, jets can split into two components known as bifurcation, caused by the uncoupling of the erupting filament (Shen et al., 2012). This bifurcation has been associated with individual peaks of X-ray flux as well as the driver of multiple CMEs (Chrysaphi et al., 2020).

1.1.3 Coronal Magnetic Field

The solar magnetic field is suggested to be generated via the solar dynamo (Parker, 1955a). Electric currents generated in the Sun from ionised gases in turn create a magnetic field. The rotation of conducting fluid produces a dipolar magnetic field, currently suggested to occur in a region at the bottom of the convective zone called the tachocline (e.g. Browning et al., 2006; Ghizaru et al., 2010). The field rises due to buoyancy and emerges at the photosphere where the differential rotation of the solar atmosphere interacts with the toroidal magnetic field causing it to become wrapped around the Sun (Parker, 1955b). The protruding magnetic flux tubes produce bipolar sunspot pairs that are tilted with respect to lines of latitude due to the Coriolis effect. The large-scale poloidal magnetic field is suggested to be regenerated through the Babcock-Leighton effect (Babcock, 1961; Leighton, 1969)—when these emerged flux tubes decay, some of the flux migrates to the poles, contributing to the generation of a new poloidal field.

As the plasma density decreases into the corona, the magnetic field fans out owing to the magnetic field pressure $\rho_B = B^2/2\mu_0$ (where B is the field strength, and μ_0 is the permeability of free space) exceeding that of the gas pressure $\rho = n_e k_B T_e$, (where n_e is the plasma density, k_B is the Boltzmann constant, and T_e is the plasma temperature). Whether the magnetic field or the plasma pressure dominates a region is quantified by the plasma beta parameter

$$\beta = \frac{\rho}{\rho_B} = \frac{n_e k_B T_e}{B^2/2\mu}. \tag{1.5}$$

When $\beta < 1$, the magnetic pressure dominates and plasma is confined to the local magnetic field. In the corona, β is low, typically between 10^{-1} and 10^{-4} (McLean & Labrum, 1985). The global structure of the solar magnetic field comprises two major zones: the open-field regions towards the poles which are the source of the fast solar wind, and the closed-field regions towards the equator which are the source of the slow solar wind. The large scale closed magnetic structures are transcended by open fields known as coronal helmet streamers. It was numerically shown by Pneuman & Kopp (1971) that since the field decreases rapidly with height, the pressure and inertial forces of the solar wind will eventually dominate, and cause the field to form a current sheet at the boundary of the open and closed flux and above the cusp. The field then extends outwards into interplanetary space, forming the Parker spiral structure due to the solar rotation (Parker, 1958).

The magnetic field is not directly observable, yet its magnitude can be inferred via the Zeeman effect. This effect causes a spectral line to split into multiple components in the presence of a magnetic field (such as the Fe I line), and is exploited by remote spacecraft observations (e.g. SDO/HMI, see section 1.5.3.2), as well as ground based observatories (the GONG network) to produce magnetograms. One method of estimating the coronal magnetic field structure is to use magnetograms as a lower boundary and a source surface is used as the upper boundary at, for example, 2.5 $R_\odot$ where the field lines are considered radial on the spatial scales considered. These extrapolations are known as Potential-Field Source-Surface (PFSS) models (e.g. Schatten et al., 1969). However, such models have limitations and should be used with caution; for example, they can only capture the quiescent state without any transient phenomena. More sophisticated methods include non-linear force-free field (NLFFF) model, the magnetohydrostatic model, and the magnetohydrodynamics model (see Wiegelmann et al., 2017, for a review). An additional method to estimate the magnetic field strength is to consider the polarisation of the radio emission, as detailed by Alissandrakis & Gary (2021), but in comparison to Zeeman splitting, this method is measured at particular locations rather than across the entire photosphere, typically near active regions.

Empirical models have also been developed to estimate the magnetic field strength at different heights in the corona. For example, Dulk & McLean (1978) combine in-situ measurements above 0.5 AU from different techniques such as the Zeeman effect, photospheric magnetogram extrapolations, and radio bursts. They provide an average magnetic field strength above active regions that follows the relation

$$B(r) = 0.5\left(r/R_\odot - 1\right)^{-1.5} \text{[G]}, \tag{1.6}$$

between 1.02 and 10 $R_\odot$, as shown in Figure 1.1. However, it should be emphasised that the model is consistent to the data within a factor of three. Moreover, the radio data used to derive the model is related to the magnetic field via the Alfvén speed $v_A = B/\sqrt{4\pi n_e m_i}$ where m_i is the ion mass, and describes the speed of a propagating plasma wave of ion fluctuations (an Alfvén wave) as well as magnetic field oscillations, which requires a density model. Gary (2001) present another model for the magnetic field above an umbra, which extends to a height of $\sim$ 14 $R_\odot$. Their model has the form

$$B(r) = \frac{2500\,\mathrm{G}}{(1+r/0.0007\,\mathrm{R}_\odot)^3} + \frac{50\,\mathrm{G}}{(1+r/0.1\,\mathrm{R}_\odot)^3} + \frac{1\,\mathrm{G}}{(1+r/1\,\mathrm{R}_\odot)^3} \tag{1.7}$$

also shown in Figure 1.1. Each quantity is chosen such that the model agrees with observations and extrapolations in different coronal regions. The two models presented here are considered throughout this thesis.

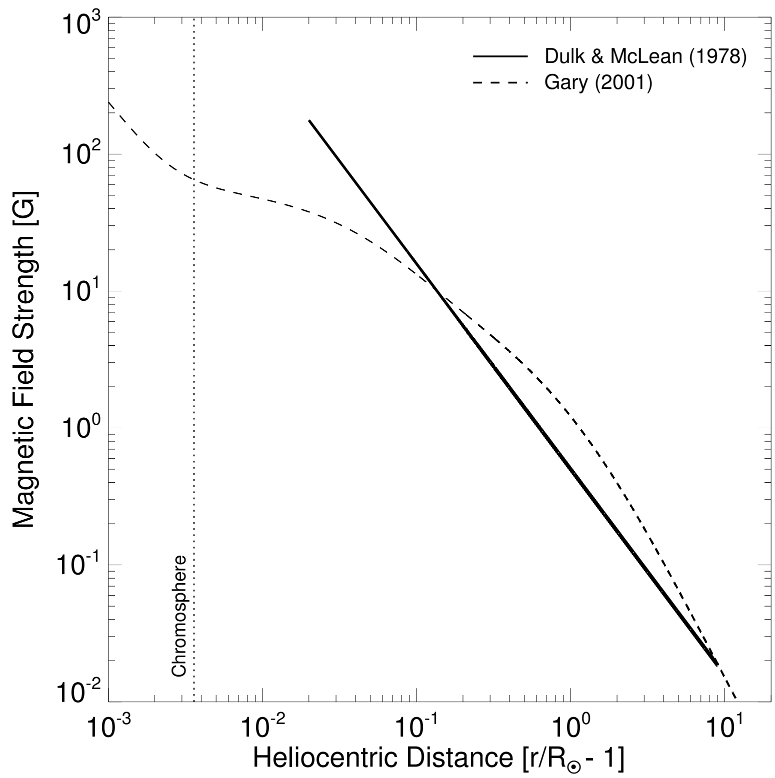

Figure 1.1: Magnetic field models from Dulk & McLean (1978) and Gary (2001). The vertical dotted line represents the boundary between the corona and chromosphere at 2500 km above the solar surface as denoted in Gary (2001).

1.1.4 Plasma Density

At the base of the corona, the transition region from the chromosphere ($\sim 0.003\ \mathrm{R}_\odot$) marks a sharp drop in electron number density n_e whilst the temperature increases by about two orders of magnitude (Fontenla et al., 1990). The density in the low corona varies between the quiet Sun and within over-dense structures. For example, Aschwanden (2005) show a compilation of measurements in the low corona—at a height of $0.2\ \mathrm{R}_\odot$, the quiet Sun has densities in the range of $\sim (0.3-1)\times 10^8\ \mathrm{cm}^{-3}$, coronal holes range from $\sim (0.5-2)\times 10^7\ \mathrm{cm}^{-3}$, streamers from $\sim (0.7-1)\times 10^8\ \mathrm{cm}^{-3}$, and active regions as high as $(0.1-1)\times 10^9\ \mathrm{cm}^{-3}$. Moreover, the density also varies with latitude, having increased density near the solar equator, and decreased density towards the poles—for example, at solar minimum, van de Hulst (1950) show a density minima near a latitude of 70° at a height of $0.15\ \mathrm{R}_\odot$. The coronal density is measured from a variety of techniques as described by Aschwanden (2005). White-light images during a solar eclipse can be used under the assumption that the polarised brightness and spectral line emission in different coronal regions is proportional to the integrated line-of-sight electron density. The continuum emission of the K-corona concerns Thompson scattering and dominates close to the Sun, and the F-corona from diffraction of light from dust particles producing Fraunhofer absorption lines, dominating far from the Sun. Such measurements were conducted by van de Hulst (1950) during a solar eclipse. The frequency of radio bursts as they propagate through the corona can directly indicate the electron density assuming that they emit at the plasma frequency or its harmonic. EUV and X-ray observations of the emission measure can also be used to estimate the electron density as this quantity is proportional to the integral of the squared density along the line-of-sight. Further into interplanetary space, the electron density can be estimated via radio source scintillation (e.g. Erickson, 1964).

The large scale variation of the coronal electron number density varies as a function of radius r, decreasing with increasing distance from the Sun. At smaller scales, the density is not uniform, fluctuating on scales $\lesssim 1\%$, discussed further in section 1.4.1. As noted above, attempts at modelling the coronal density produce different results depending on whether the density is estimated for the quiet Sun, or above an active region, as well as at the solar equator or towards. Figure 1.2 shows various average density models at different distances between 1–215 $\mathrm{R}_\odot$, where $215\ \mathrm{R}_\odot \simeq 1$ AU. Each model is defined in Table 1.1.

In the region of Earth's orbit, the various density models tend to agree with relatively small spread between them, but deviations occur below $\sim 1.5\ \mathrm{R}_\odot$. One widely used empirical model for distances $\leq 2\ \mathrm{R}_\odot$ is that by Newkirk (1961) based on observations during solar maximum, and is often adjusted by a constant to match a given event. Another frequently used model is that by Leblanc et al. (1998) based on observations of Type III radio bursts (section 1.3.3). In Figure 1.2, the red curve represents a density model based on Parker's solar wind solution (Parker, 1958) as described by Mann et al. (1999). This radially symmetric,

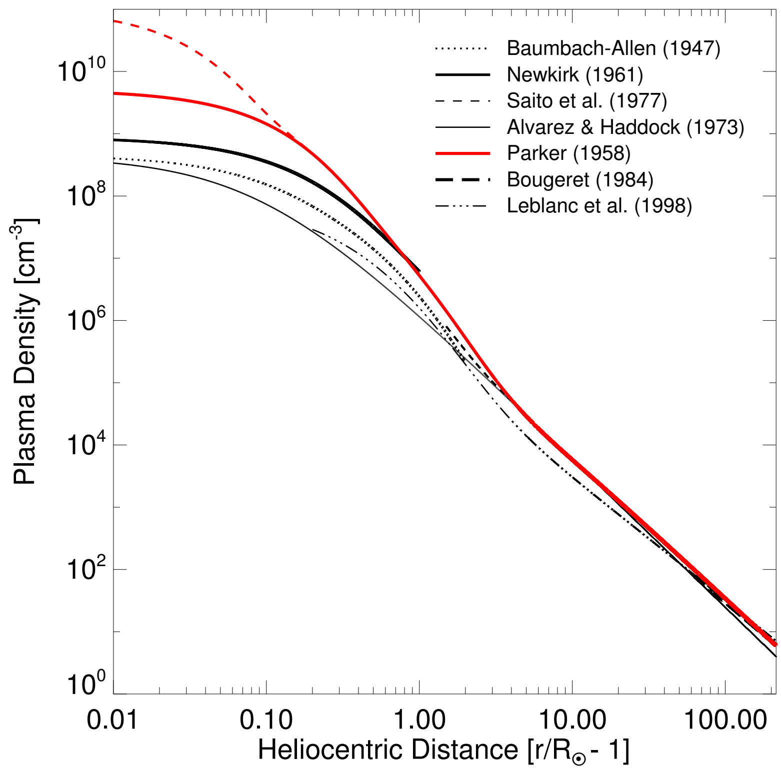

Figure 1.2: Coronal density models from Allen (1947); Parker (1958); Newkirk (1961); Saito et al. (1977); Bougeret et al. (1984); Leblanc et al. (1998). The red curve represents a power-law fit to the numerical solution to the Parker model as presented in (Kontar et al., 2019). The red dashed curve includes a term to account for the sharp increased in chromospheric density n_c, as described in the text.

isothermal model is given by the equations

$$\frac{v(r)^2}{v_c^2} - \ln\left(\frac{v(r)^2}{v_c^2}\right) = 4\ln\left(\frac{r}{r_c}\right) + 4\left(\frac{r_c}{r}\right) - 3, \tag{1.8}$$

$$r^2 n_e(r) v(r) = C, \tag{1.9}$$

where $v_c = \left(k_B T_e/\tilde{\mu} m_p\right)^{1/2}$ is a critical velocity, with mean atomic weight in the corona $\tilde{\mu} = 0.6$ (Priest, 2014), and proton mass m_p, and $r_c = GM_s/2v_c^2$ is a critical radius where the corona becomes supersonic, where G and M_s are the gravitational constant and solar mass, respectively. The density model is obtained by substituting the solution of $v(r)$ into equation 1.9. Equation 1.8 is solved numerically as in Kontar (2001a). The normalisation constant is fixed from average in-situ satellite density measurements at 1 AU (Mann et al., 1999) at $n_e = 6.59$ cm^{-3}, resulting in a mean solar wind speed of 425 km s^{-1}. Substituting into equation 1.9 gives $C = 6.3 \times 10^{34}$ s^{-1}. The solution is fit with a power-law model to

	Definition n_e [cm^{-3}]	Valid Height [R$_\odot$]
Baumbach-Allen (1947)	$\frac{1.55\times10^8}{r^6}+\frac{2.99\times10^8}{r^{16}}$	1–3
Newkirk (1961)	$4.2\times10^4\cdot10^{4.32\,\mathrm{R}_\odot/r}$	1–2
Saito et al. (1977)	$\frac{1.36\times10^6}{r^{2.14}}+\frac{1.68\times10^8}{r^{6.13}}$	2.5–5.5
Alvarez & Haddock (1973)	$1.41\times10^6(r-0.91)^{-2.38}$	1–215
Parker (1958)†	$C/r^2v(r)$	1–215
Bougeret (1984)	$6.14r^{-2.10}$	64.5–215
Leblanc et al. (1998)	$\frac{3.3\times10^5}{r^2}+\frac{4.1\times10^6}{r^4}+\frac{8\times10^7}{r^6}$	1.2–215

Table 1.1: Density model parameters as shown in Figure 1.2. †The normalisation constant C is described in the text.

provide a simple analytical approximation

$$n_e(r) = \frac{4.8\times10^9}{r^{14}} + \frac{3\times10^8}{r^6} + \frac{1.39\times10^6}{r^{2.3}}, \tag{1.10}$$

where r is given in solar radii and n_e has units of cm^{-3}, as used in Kontar et al. (2019); Kuznetsov et al. (2020); Chen et al. (2020); Musset et al. (2021); Chen et al. (2023a).

The sharp density increase near the transition region into the chromosphere can be several orders of magnitude to as high as 10^{11} cm^{-3} in flaring loops (Aschwanden, 2005). The dashed red curve in Figure 1.2 accounts for this by including an additional term to equation 1.10 given by

$$n_c(r) = n_0 \exp\left(-\frac{r-1}{h_0}\right) + n_1 \exp\left(-\frac{r-1}{h_1}\right), \tag{1.11}$$

where $n_0 = 1.17\times10^{17}$ cm^{-3} gives the density at the solar surface with a scale height of $h_0 = 144$ km (Kontar et al., 2008), and $n_1 = 10^{-11}$ cm^{-3} and $h_1 = 0.02$ km (e.g. Battaglia & Kontar, 2012).

Coronal loops have been observed in hydrostatic equilibrium (Aschwanden, 2005) with stationary density, pressure, and temperature profiles. In such a scenario, the density is considered using an exponential model (e.g. Aschwanden et al., 1999) of the form

$$n_e(l) = A_n \exp\left(-\frac{r(l)}{r_n}\right) \tag{1.12}$$

where $r(l)$ is the distance along the loop, A_n sets the foot-point density, and r_n is the density scale height. Such models have been used in conjunction with observations of radio emission from electron beam propagation along coronal loops (e.g. Reid & Kontar, 2017). The density models of equations 1.10, 1.11 and 1.12 are considered in this thesis.

1.1.5 Space Weather

The processes described in section 1.1.2 can have a significant impact on the Earth and near-Earth environment, collectively known as 'space weather'. Space weather is caused by a variety of factors, including solar energetic particles (SEPs), CMEs, ionising radiation from flares, and excess radio noise (see section 2.3.3, for example). Such phenomena can manifest as geomagnetic storms and ionospheric disturbances, leading to technological hazards to the power grid and communication infrastructure (Gary & Keller, 2004).

Some of the most severe effects of space weather are associated with powerful flares and interplanetary CMEs that cross the sun-lit Earth at 1 AU. These events cause an excess of charged particles (Reames, 1999) that follow Earth's magnetic field to the auroral regions and can incite ionospheric currents. These time varying ionospheric currents induce magnetic variations that generate geomagnetic induced currents (GIC) that flow in conducting paths such as the ground, bodies of water, and electrical systems (Boteler, 1994; Pulkkinen et al., 2017). Such events can cause significant financial damages—for example, an outage of the electricity grid occurred in Quebec, 1989 (Bolduc, 2002) due to an X15-class solar flare and CME (Allen et al., 1989; Feynman & Hundhausen, 1994).

In addition to the transport of energetic particles, solar radio bursts (discussed in section 1.3) can cause interference from excess noise (section 2.3.3). Wireless cell sites operating in the low GHz range are particularly vulnerable. At an ambient Earth temperature of $T_{\oplus} = 273$ K, a bandwidth of $\Delta f = 1$ Hz leads to a receiver noise power of $P = k_B T_{\oplus} \Delta f = 3.8 \times 10^{-21}$ W, or measured in decibels relative to 1 mW, $P_{\mathrm{dBm}} = 10 \log_{10}(k_B T \Delta f / 1\ \mathrm{mW}) = -174$ dBm. Considering the effective area $A_e = g\lambda^2/4\pi$ of a single polarisation antenna, the received power is $P = 0.5 \Delta f A_e I$ where g is the antenna gain, and λ is the wavelength (note the factor half comes from the antenna being sensitive to one polarisation only, whereas noise is assumed to be unpolarised). For a cellular receiver operating at 900 MHz, the flux density I required to match the noise floor is $\sim 9 \times 10^{-20}$ W m^{-2} Hz^{-1} = 900 sfu. Therefore, solar radio bursts with an equivalent flux density of $\sim 10^3$ sfu can impact the receivers (Bala et al., 2002) (a similar assessment for GPS receivers is shown in section 2.3.3). According to Bala et al. (2002), the frequency of radio bursts per day follows a power-law distribution with respect to flux. Specifically, a burst with flux density $> 10^3$ sfu could occur every 10–20 days, although this rate can vary depending on the level of solar activity during a given solar cycle. At solar minimum for instance, Nita et al. (2002) found that the time between events with peak flux $> 10^3$ sfu is 18.5 days, whereas at solar maximum, this time drops to just 3.5 days.

Global Navigation of Satellite Systems (GNSS) offer real-time geolocation to a receiver at any point on Earth that has an unobstructed line of sight to at least four of the satellites. The Global Positioning System (GPS), which transmits at frequencies of 1575.42 MHz (L1) and 1227.70 MHz (L2), is one such system. However, changes to the ionospheric density caused by SEPs, as well as X-ray and strong EUV flux from solar flares (Thome & Wagner, 1971), can lead to propagation delays. Furthermore, excess noise from radio bursts with peak flux $> 2\times10^4$ sfu could affect the signal-to-noise ratio (SNR) of a GPS signal (Klobuchar et al., 1999). The aforementioned statistical study by Nita et al. (2002) notes that a radio burst with a peak flux above this level between $1-1.7$ GHz could occur every 244 days at solar minimum, and every 86 days at solar maximum. Such disruption of GPS signals coincident with radio bursts has been recorded. For example, Chen et al. (2005) reported severe signal delays of receivers in the sun-lit hemisphere that were correlated with an X17.2-class flare with a radio burst flux between $4\times10^3-1.2\times10^4$ sfu at 1.415 GHz. Another X17.2-class flare with a peak flux of 8.7×10^3 sfu caused a reduction in SNR at the time of the burst (Cerruti et al., 2006). An even more intense radio burst occurred in December 2006 during solar minimum, peaking at 10^6 sfu at 1.4 GHz, affecting many GPS receivers in the sun-lit hemisphere (Cerruti et al., 2008). Aside from the disruption of Global Navigation Satellite Systems (GNSS), radar signals may also be impacted. For instance, Marqué et al. (2018) show association of an M-class flare and radio emission peaking at $\sim 10^5$ sfu with anomalous air traffic disturbances (further discussion of this event can be found in section 2.3.3). High-frequency (HF) radio signals (3–30 MHz) which are used for long distance radio communication are particularly sensitive to space weather. HF signals utilise the F region of the ionosphere (at a height between $\sim 200-500$ km) to reflect signals to greater distances. At the bottom of the ionosphere is the so-called D region that can become ionised by X-ray emission of solar flares, leading to the attenuation of HF signals, called a 'HF fadeout'.

The understanding and characterisation of solar eruptive events that lead to energetic particles and radio bursts is of clear importance to the safety of critical systems at Earth. Understanding of the complete picture of this complex phenomena will improve efforts for the prediction and mitigation of such events.

1.2 Coherent Solar Radio Emission

Solar radio emission can be categorised as either coherent or incoherent. Incoherent emission can be produced by electrons undergoing Coulomb collisions with ions resulting in free-free emission which is predominant in the quiet Sun. In the presence of a magnetic field, the electrons gyrate around the field line producing gyroresonance and gyrosynchrotron emission which is present in regions of high magnetic fields in the lower corona (Dulk, 1985). Coherent emission occurs when energy from non-thermal electrons is converted into wave modes of the plasma such as electron-cyclotron waves (electromagnetic waves), and electron oscillations that are longitudinal waves known as Langmuir waves. The former has a characteristic frequency (in CGS units) of

$$\omega_{\mathrm{ce}} = \frac{eB}{m_e c}, \tag{1.13}$$

where e is the electron charge, m_e is the electron mass, and c the speed of light. The latter oscillate at the plasma frequency given by

$$\omega_{\mathrm{pe}} = \left(\frac{4\pi n_e e^2}{m_e}\right)^{1/2}. \tag{1.14}$$

Equations 1.13 and 1.14 denote angular frequencies, and conversion to temporal frequency is achieved through $f = \omega/2\pi$. The plasma frequency can be expressed as

$$f_{\mathrm{pe}}\,[\mathrm{MHz}] \simeq 8.93\times10^{-3}\sqrt{n_e\,[\mathrm{cm}^{-3}]}, \tag{1.15}$$

accounting for the constants. The above frequencies are much higher than any collisional frequency in the corona. As such, particle collisions can be neglected, and the plasma is considered to be 'collisionless'. The low rate of collisions is quantified by a large Coulomb logarithm, typically $\ln\Lambda \approx 20-23$ in the corona (e.g. Aschwanden, 2005; Holman et al., 2011). Coherent emission is typically distinguished by its high brightness temperature (Melrose, 2009). In this thesis, the focus is on distances of $r \simeq 1.4-2\ \mathrm{R}_\odot$ from the photosphere, corresponding to radio frequencies between 20–80 MHz where coherent emission dominates.

1.2.1 Plasma Emission

Plasma emission is produced at the plasma frequency f_{pe} and its second harmonic $2f_{\mathrm{pe}}$. This two-stage process is illustrated in Figure 1.3, and begins with the acceleration of electron beam populations which generate Langmuir waves. These waves then interact coherently with different wave modes (see section 1.2.1.4), resulting in the production of transverse EM waves (Ginzburg & Zheleznyakov, 1958; Melrose, 2017). In the presence of a magnetic field, magneto-ionic theory states that the magnetic field will split a transverse wave mode into two modes: the ordinary mode (o-mode), and the extraordinary mode (x-mode). O-mode waves are ordinary in the sense that their dispersion relation is the same as that in an unmagnetised plasma, and the electric field oscillates in the plane parallel to the magnetic field (Chen, 2016). Plasma emission is produced in the o-mode (Aschwanden, 2005).

1.2.1.1 Electron Beams

As discussed in section 1.1.2.2, solar flares routinely accelerate populations of electrons that propagate along magnetic field lines either away from or towards the Sun. In the collision-

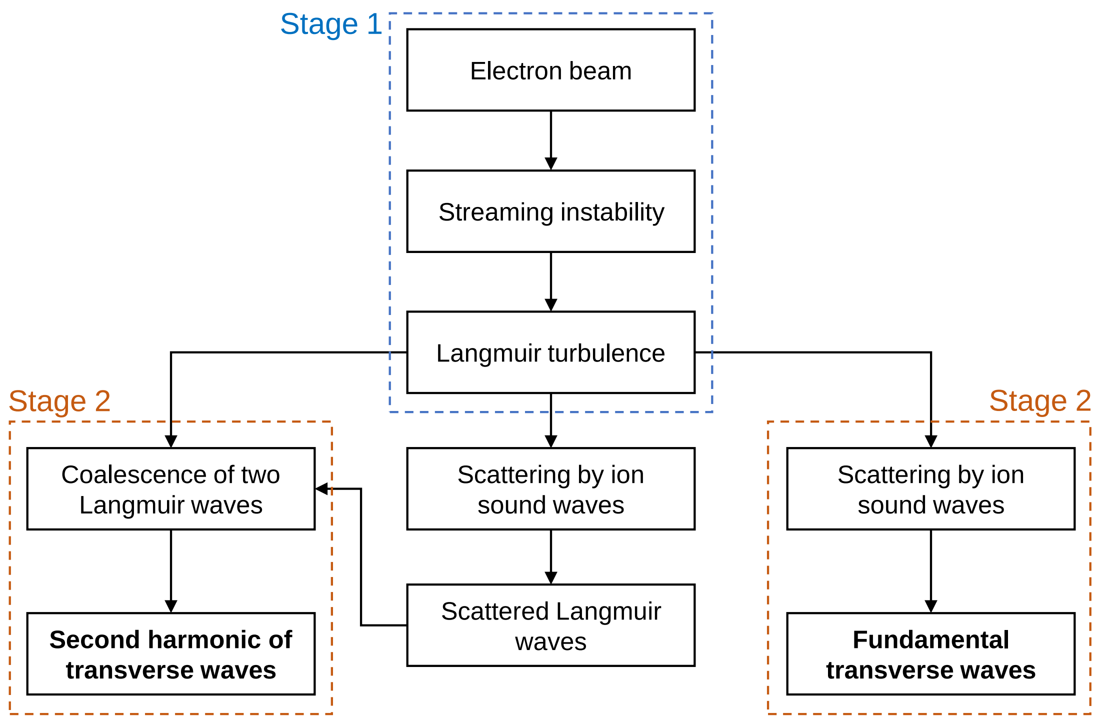

Figure 1.3: The plasma emission process, adapted from Melrose (2017).

less coronal plasma, the electron beams propagate adiabatically, allowing velocity dispersion where higher energy electrons with velocity v_b outpace the lower energy electrons in an assumed Maxwellian background population (Aschwanden, 2005) with thermal velocity $v_{\mathrm{Te}} = \sqrt{k_B T_e / m_e}$. This creates an unstable beam in the region where the electron velocity distribution function $f(v)$ has a positive gradient $\partial f / \partial v > 0$, known as the bump-in-tail instability (Aschwanden, 2005). Figure 1.4 illustrates this process where at a time t_1, the fastest electrons form a 'bump' in $f(v)$. At later times t_2 and t_3, the electrons lose energy to Langmuir wave growth. This resonant interaction occurs due to the Čerenkov effect where the speed of the electron exceeds the phase speed of the wave with the condition $\omega_L = k_L v$ where ω_L and k_L are the Langmuir wave angular frequency and wavenumber, described in section 1.2.1.3. The energy loss occurs via Landau damping where the thermal background electrons absorb the Langmuir waves. Beam electrons that lose energy then diffuse in velocity space causing the bump to move to lower velocities and a plateau to form where $\partial f / \partial v = 0$, a process called quasilinear relaxation (Grognard, 1985). The characteristic time of this process is given by the quasilinear time

$$\tau_{\mathrm{ql}} = \frac{n_e}{\omega_{\mathrm{pe}} n_b} \tag{1.16}$$

where n_b is the electron beam density. For example, at a beam density of $n_b = 500\ \mathrm{cm}^{-3}$ and a height of 1.4 $\mathrm{R}_\odot$ where the plasma density is approximately $n_e \sim 8.4 \times 10^7\ \mathrm{cm}^{-3}$ according to equation 1.10, $\tau_{ql} \simeq 0.036$ s. For lower beam densities, τ_{ql} increases, causing the distance between the acceleration location and site of quasilinear relaxation to become significant, and the onset of radio emission to be at greater heights (Kontar, 2001b).

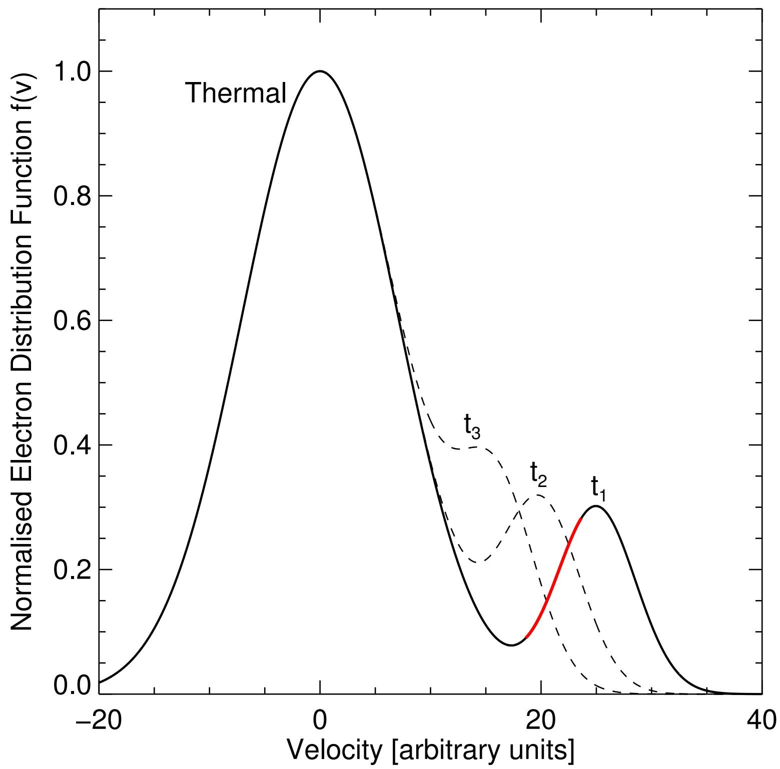

Figure 1.4: Velocity space evolution of an electron beam distribution function in the tail of a thermal distribution. Time progresses from t_1 to t_3.

1.2.1.2 Beam-plasma Structure

One dilemma associated with the fast growth rate of the instability is the rapid loss of energy from the electron beam due to the production of Langmuir waves over a short distance (Sturrock, 1964). However, observations revealed that electron beams propagate over large distances, reaching up to 1 AU and beyond (Lin et al., 1981). A solution, initially by Zheleznyakov & Zaitsev (1970a), is that the higher energy electrons in the beam lose their energy to the formation of Langmuir waves in the region where $\partial f/\partial v > 0$, while the lower energy electrons at the back of the beam absorb the energy from the Langmuir waves. In this way, energy is transferred throughout the beam (McLean & Labrum, 1985). The electrons that gain energy will then propagate faster, forming instabilities and allowing the process to cycle, maintaining propagation of this beam-plasma structure over vast distances at an average velocity of the beam electrons (Mel'nik et al., 1999; Mel'nik & Kontar, 2000). It is shown in Kontar (2001a) for example, that the decreasing density of the coronal plasma acts as a dissipative medium, such that as the beam-plasma structure propagates, part of the energy is lost from the structure in the form of Langmuir waves as they move out of resonance with the beam[1]. In addition, the expanding magnetic flux tubes act to rarefy the electron beam to the extent that its density becomes too low to generate Langmuir waves (**?**). Such effects will quench instability that causes the growth of Langmuir waves and ultimately cause radio emission to cease.

1.2.1.3 Langmuir Waves

Langmuir waves are a type of plasma wave that arise due to the displacement of an electron population with respect to ions in the plasma. These waves exhibit rapid, longitudinal oscillations of electrons, which are restored via the Coulomb force. The dispersion relation for Langmuir waves ω_L in an unmagnetised plasma is

$$\omega_{\mathrm{L}}^2(k) = \omega_{\mathrm{pe}}^2 + 3k^2 v_{\mathrm{Te}}^2, \tag{1.17}$$

where $k = \omega_{\mathrm{pe}}/v$ is the wavenumber, ω_{pe} is the plasma frequency (equation 1.14), and v_{Te} is electron thermal velocity. Expressing equation 1.17 as

$$k_{\mathrm{L}} = \left(\frac{m_e(\omega_{\mathrm{L}}^2 - \omega_{\mathrm{pe}}^2)}{3k_B T_e} \right)^{1/2} \tag{1.18}$$

shows that a cut-off occurs when $\omega_{\mathrm{L}} = \omega_{\mathrm{pe}}$. Consequently, Langmuir waves are produced near the local plasma frequency.

In a weakly magnetised plasma where $\omega_{\mathrm{ce}} \ll \omega_{\mathrm{pe}}$, Langmuir waves and upper hybrid waves (also called z-mode waves, where $\omega_{\mathrm{uh}} \approx \omega_{\mathrm{pe}}^2 + \omega_{\mathrm{ce}}^2 \sin^2\psi$) form a single, modified mode (McLean & Labrum, 1985) with a dispersion relation given by

$$\omega_{\mathrm{L}}^2(k,\theta) = \omega_{\mathrm{pe}}^2 + 3k^2 v_{\mathrm{Te}}^2 + \omega_{\mathrm{ce}}^2 \sin^2\psi, \tag{1.19}$$

where ψ is the angle between the plasma wave direction and magnetic field which can vary up to $\sim 30°$ (e.g. Malaspina & Ergun, 2008; Kellogg et al., 2009). Expanding equation 1.19 using a binomial expansion for fractional powers of the form $(1+x)^n = 1 + nx + \ldots$, we have

$$\omega_{\mathrm{L}}(k,\theta) = \omega_{\mathrm{pe}}^2 + \frac{3k^2 v_{\mathrm{Te}}^2}{2\omega_{\mathrm{pe}}} + \frac{\omega_{\mathrm{ce}}^2}{2\omega_{\mathrm{pe}}} \sin^2\psi. \tag{1.20}$$

[1] Such losses are noted not to occur in a homogeneous plasma. In this case, all the plasma waves generated at the front of the beam are absorbed by the back of the structure.

1.2.1.4 Wave-wave Interactions

The Langmuir waves generated by a fast electron beam via the bump-in-tail instability interact with other wave modes leading to the conversion of energy into escaping EM radiation. In Figure 1.3, stage 2 shows three possible wave-wave interactions that may lead to transverse waves. As outlined by Melrose (2017), three wave modes are considered, with frequencies ω_L, ω_S, and ω_T. The latter two refer to ion-sound waves with dispersion relation

$$\omega_\mathrm{S}(k) = kv_s, \tag{1.21}$$

where $v_s \approx v_\mathrm{Te}/43$ is the ion sound speed[2], and transverse EM waves with dispersion relation

$$\omega_\mathrm{T}^2(k) = \omega_\mathrm{pe}^2 + k^2c^2. \tag{1.22}$$

Coalescence or decay of the waves occurs with the conditions

$$\begin{aligned} \omega_1 + \omega_2 &= \omega_3 \\ \boldsymbol{k}_1 + \boldsymbol{k}_2 &= \boldsymbol{k}_3, \end{aligned} \tag{1.23}$$

where ω_{1-3} and $\boldsymbol{k}_{1-3}$ denote the angular frequency and wavenumber of each wave. The possible interactions that may lead to EM emission are

$$L + S \rightarrow L' \tag{1.24a}$$
$$L + S \rightarrow T \tag{1.24b}$$
$$T + S \rightarrow L \tag{1.24c}$$
$$T + S \rightarrow T \tag{1.24d}$$
$$L + L' \rightarrow T \tag{1.24e}$$

Here, L and L' denote Langmuir waves and back-scattered Langmuir waves, respectively, S is an ion-sound wave, and T is a transverse EM wave (Melrose, 1987; Tsytovich & ter Haar, 1995). Equation 1.24a leads to backscattered Langmuir waves, which may coalesce with Langmuir waves to produce harmonic emission (equation 1.24e). Equations 1.24b and 1.24c are associated with fundamental emission, whilst equation 1.24d is of interest to the scattering of transverse waves (Melrose, 1987). Additionally, the scattering of Langmuir waves off thermal ions may also produce EM radiation, analogous to Thomson scattering, where the wave is deflected by the Debye shield of an ion. However, this process may be inadequate for the high brightness temperatures associated with plasma emission (Melrose,

[2]Since $v_s = \sqrt{\gamma\rho/\rho_\mathrm{i}}$ where $\gamma = 5/3$ is the adiabatic index, $\rho = n_e k_B T$ is the thermal pressure, and $\rho_\mathrm{i} = n_i m_i$ is the ion mass density. Since $n_e/n_i \approx 1$, then $v_s = \sqrt{\gamma k_B T/m_i} \approx v_\mathrm{Ti}$, and considering that $\sqrt{m_i/m_e} \approx 43$, then $v_s \approx v_\mathrm{Te}/43$.

1980).

The emission pattern for fundamental emission is dipolar with a maximum perpendicular to k_L and quadrupolar for harmonic emission (Zheleznyakov & Zaitsev, 1970b; Tsytovich & ter Haar, 1995). Electron beams will produce Langmuir waves with wavenumbers parallel to the magnetic field, but as noted above, they are observed in-situ within a small angular spread up to $\sim 30°$(Malaspina & Ergun, 2008; Kellogg et al., 2009). With uniformly generated Langmuir waves within such a distribution, the emission pattern approaches isotropic, as considered for electron beam and Langmuir wave evolution simulations (Ratcliffe & Kontar, 2014) as well as injected radio sources for radio-wave scattering simulations (Kontar et al., 2019). For electron beam speeds at a significant fraction of the speed of light, the emission will be beamed along the tangent to the Parker spiral that the exciter is propagating along (Zheleznyakov & Zaitsev, 1970b; Thejappa et al., 2012).

1.2.2 Electron-cyclotron Maser Emission

An alternative process for generating coherent radio emission is the Electron-cyclotron Maser (ECM). Cyclotron emission refers to emission from electrons deflected by a magnetic field, occurring near the harmonics $\omega \approx s\omega_{\rm ce}$, where s is the harmonic integer. In a plasma where $\omega_{\rm pe} > s\omega_{\rm ce}$, such emission cannot escape directly and so fundamental ECM emission is only possible where $\omega_{\rm pe} < \omega_{\rm ce}$. Additionally, wave dispersion in the plasma further restricts this condition to $\omega_{\rm pe} \ll \omega_{\rm ce}$ (Melrose, 2017). As a result, ECM emission is generally considered for regions of strong magnetic field in the low corona. As noted by Aschwanden (2005), in solar flare conditions, a ratio of $\omega_{\rm pe}/\omega_{\rm ce} \approx 1$ would require a plasma density of $n_e \simeq 10^{10}$ cm^{-3} and $B \simeq 360$ G, corresponding to frequencies of $f_{\rm pe} = f_{\rm ce} \approx 1$ GHz. Such strong magnetic fields are not tenable in the upper corona. ECM emission is dominated by emission in the magneto-ionic extraordinary mode (x-mode) (Aschwanden, 2005), resulting in strongly circularly polarised light.

Whilst plasma emission is beam-driven in the regime $\partial f/\partial v_{\parallel} > 0$, ECM emission is produced via so-called losscones where $\partial f/\partial v_{\perp} > 0$ that develop in magnetic mirror regions. As described by Aschwanden (2005), waves that satisfy the Doppler resonance condition $\omega - s\omega_{\rm ce}/\gamma - k_{\parallel}v_{\parallel} = 0$ (where γ is the Lorentz factor) may contribute to growth or absorption. Gyroresonant waves grow exponentially due to the energy of resonant particles by quasilinear diffusion. The particles lose energy, and drift into the losscone until the distribution forms a plateau, and the maser is quenched. Losscone masers are expected to have short lifetimes with small spatial scales, producing short, narrowband emission with high brightness temperatures. An estimation of the relative bandwidth produced via ECM emission is given by Hewitt et al. (1982) as

$$\frac{\Delta\omega}{\omega} \approx \left(\frac{v}{c}\right)^2, \tag{1.25}$$

where v is the speed of the responsible fast particles. However, Fleishman (2004a) found that this relation may overestimate the bandwidth by an order of magnitude; instead suggesting that the natural width of maser emission is strongly dependent on the angle between the direction of wave emission and the magnetic field direction at the source. They find that typical ECM bandwidths lie in the range of 0.1–0.4%, similar to the minimum observed bandwidths of millisecond spikes as determined by Messmer & Benz (2000), although this limit could be lower as the minimum observed bandwidths were 1.5 MHz ($f = 900$ MHz) and 1.2 MHz at ($f = 300$ MHz), close to the IKARUS radio spectrometer spectral resolution of 1 MHz.

1.3 Solar Radio Bursts

1.3.1 Radio Burst Overview

The signatures of plasma and ECM emission manifest as a variety of structures in dynamic spectra. The idealised morphology of some of these burst types are shown in Figure 1.5.

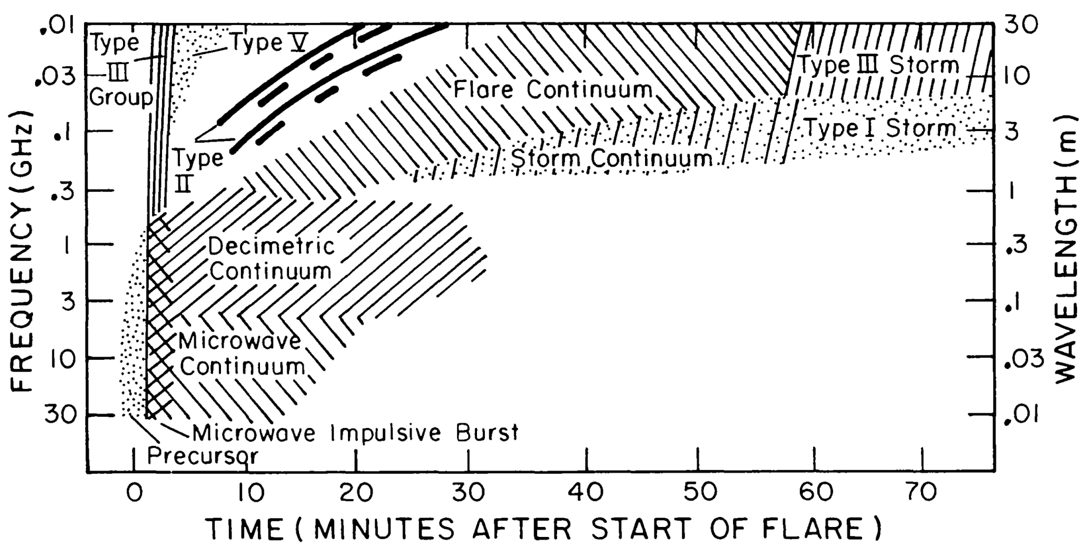

Figure 1.5: Schematic of radio burst signatures after a solar flare in a dynamic spectrum. Used with permission of Annual Reviews, Inc., from Dulk (1985); permission conveyed through Copyright Clearance Center, Inc.

The first observations of solar radio emission led to the classification of Type I, II, and III bursts (Wild & McCready, 1950), with the later addition of Type IV and V. In this thesis, the main focus is on fine structures of radio emission that can be embedded in or separate from these broadband bursts; in particular, radio spikes and striae, which are discussed in detail in chapter 2. Type I, IV, and V bursts form continuum emission—Type I bursts, or storms, consist of many narrow-band (few MHz) bursts ~ 1 s in duration distributed over hundreds of MHz superimposed on a continuum that can last a few hours to days. Type

IV bursts comprise different varieties that may be moving or stationary continuum and are associated with trapped electrons in post-eruption flare loops, with emission via plasma or gyrosynchrotron processes. The emission mechanism has also been shown to change over time for a given observation Morosan et al. (2019). Finally, Type V bursts are continuum emission lasting a few minutes following a Type III burst, suggested to be caused via trapped electrons oscillating between magnetic mirror points in a magnetic trap (Weiss & Stewart, 1965; Zheleznyakov & Zaitsev, 1968). As noted in section 1.1.4, the large-scale coronal density decreases with increasing distance from the Sun. Radio emission produced via plasma emission is emitted near the local plasma frequency (section 1.2.1), and so the EM signature of a propagating electron beam through the corona presents as a fast drifting structure with a drift rate of $\mathrm{d}f/\mathrm{d}t$. A positive drift rate would imply an exciter that is propagating towards the Sun through increasing density, and a negative drift rate implies propagation away from the Sun. The drift rate is therefore a useful diagnostic of the exciter velocity and the coronal environment that it propagates through. These burst types are described in the following sections.

1.3.2 Type II Bursts

Type II bursts are associated with the propagating shock fronts driven by CMEs. They are observed to have frequency drift rates between $\sim 0.1-1$ MHz s^{-1} and last for around 10 minutes (Cliver et al., 1999), implying exciter speeds on the order of 10^3 km s^{-1} (McLean & Labrum, 1985; Pick & Vilmer, 2008), covering a distance of $\sim 0.8\ R_\odot$. Interplanetary CME driven shocks exist out to 1 AU and beyond, and interplanetary Type II emission is observed with starting frequencies near a few MHz, as well as kilometre Type II bursts observed at kilohertz frequencies. Such emission can have durations that last for many hours (Cane & Stone, 1984; Cane & Erickson, 2005), and this can make Type II emission at low frequencies difficult to discern from overlying Type III emission in dynamic spectra (e.g. Schmidt et al., 2014). Nevertheless, Bisi et al. (2010) show the harmonic branch of a Type II burst that lasts for tens of hours and was visible down to 40 kHz, close to the plasma frequency at 1 AU. A decametric Type II burst is shown in Figure 1.6, observed by the CALLISTO station at Birr Observatory, Ireland, and analysed in detail by Maguire et al. (2021).

The lower frequency structure is identified as fundamental emission, with the higher frequency structure as the second harmonic. An often observed phenomena is that each component is further separated into individual sub-bands known as 'band splitting'. Numerous models have tried to explain such a phenomena; for example, that the sub-band emission arose from regions upstream and downstream of the shock front (Smerd et al., 1975), or in different regions of the shock front (Holman & Pesses, 1983). Imaging observations have shown that each sub-band appears to be spatially separated (e.g. Zimovets et al., 2012), however, recent imaging of a 0.2 $R_\odot$ spatial separation between sub-bands has been

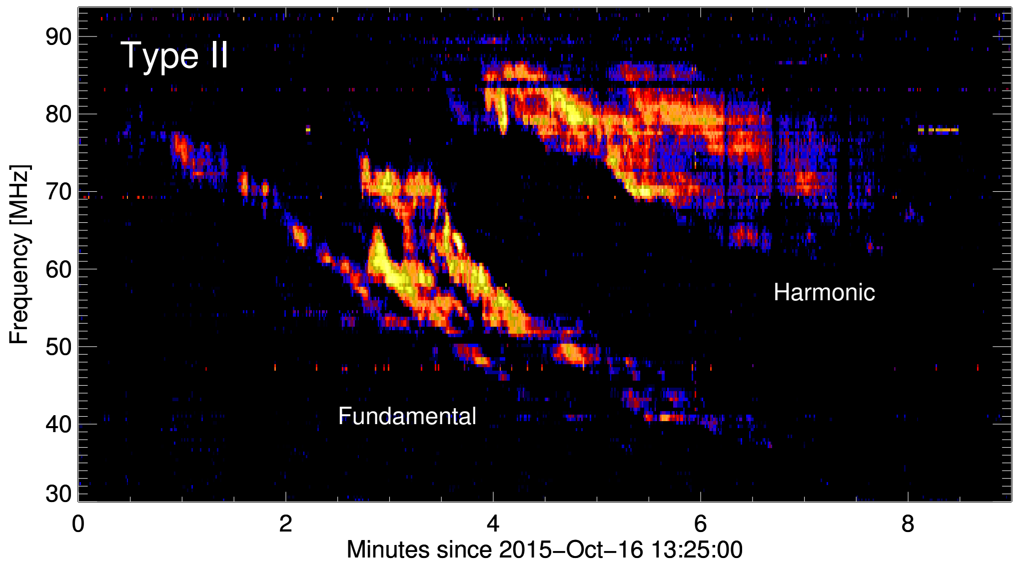

Figure 1.6: Dynamic spectrum of a Type II burst observed by CALLISTO (Birr station, Ireland).

explained via a radio-wave scattering model, implying that the sub-band sources arise from almost co-spatial locations (Chrysaphi et al., 2018).

Whilst the mechanism that produces Type II bursts is well agreed upon, the location of the exciter in relation to the shock front is inconclusive. Zimovets et al. (2012) observe a Type II source to appear above the shock apex, yet other studies have shown the emitter to be located along the CME flank (e.g. Zucca et al., 2018). Claßen & Aurass (2002) find an equal number of events with Type II emission associated with the leading edge or the flanks of the CME-driven shocks; however, a statistical study by Krupar et al. (2019) find that flank-generated Type II bursts are more probable from interplanetary CMEs, with an average deviation from the CME propagation direction of 62°. They note that interactions between adjacent CMEs or between CMEs and streamers are more likely to occur near the flanks, which could be a source of magnetic reconnection and subsequent energy release. Moreover, shocks near CME flanks have been observed in white light images (Vourlidas et al., 2003), which would lead to enhanced compression and increased density in these regions which could lead to Type II emission (Reiner et al., 2003).

1.3.3 Type III Bursts

Type III bursts are prolific, and appear as broadband emission in dynamic spectra with circular polarisation that can vary from weak to strong (McLean & Labrum, 1985), and even vary across the lifetime of an individual burst (Dulk & Suzuki, 1980). Figure 1.7 shows a group of Type III bursts from 80 MHz down to below 100 kHz. At the higher frequencies, numerous individual bursts can be seen that present as almost vertical bands on the timescale shown.

Below 1 MHz, the emission overlaps into one structure.

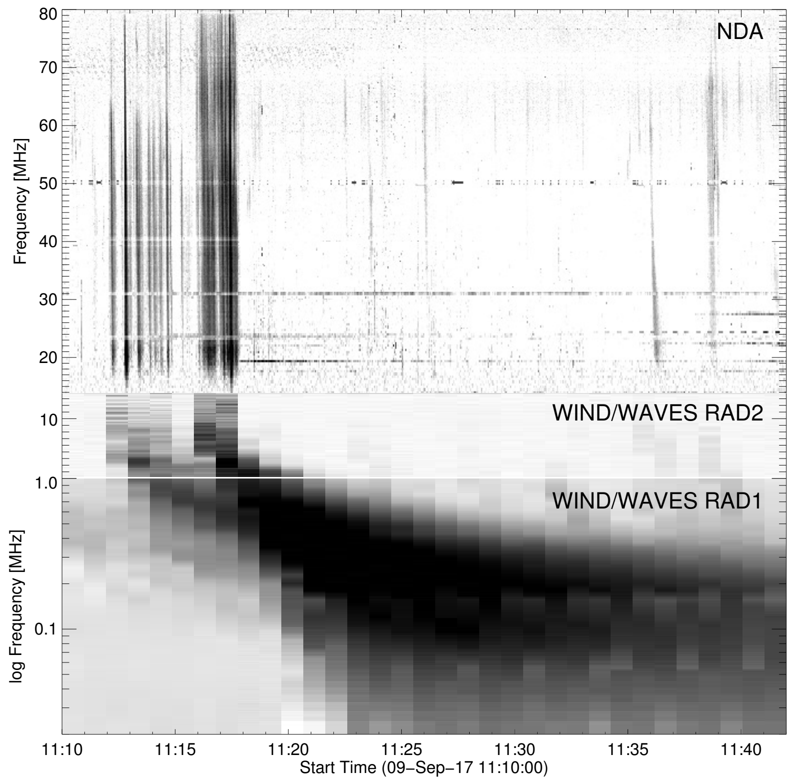

Figure 1.7: Dynamic spectrum of numerous Type III bursts observed by both NDA (section 1.5.2) and the WAVES instrument aboard the WIND spacecraft (Bougeret et al., 1995). The gap near 15 MHz is due to the ionospheric cut off for ground based instruments. The horizontal bands are due to terrestrial radio interference. The RAD1 frequency scale is shown logarithmically.

The bulk drift rates are faster than that of Type II bursts at a few MHz s^{-1} at frequencies of tens of megahertz (e.g. Melnik et al., 2011) and a few GHz s^{-1} at low gigahertz frequencies (Benz et al., 1992a), implying typical beam velocities near $c/3$ (McLean & Labrum, 1985). A statistical survey by Alvarez & Haddock (1973) found a frequency dependency on the Type III drift rate to follow

$$\frac{\mathrm{d}f}{\mathrm{d}t} = -0.01 f^{-1.84}\ \mathrm{MHz\ s^{-1}}, \tag{1.26}$$

from 75 kHz to 550 MHz. Between 200–3000 MHz, Aschwanden et al. (1995) derive a relation of $|\mathrm{d}f/\mathrm{d}t| = 0.1 f^{1.4}$ MHz s^{-1}. From the frequency drift rate, the exciter velocity can be estimated. Since $f_{\mathrm{pe}} \propto \sqrt{n_e}$ (equation 1.13), then $\mathrm{d}f/\mathrm{d}n_{\mathrm{e}} \sim 1/(2\sqrt{n_{\mathrm{e}}})$, and using the chain rule we have

$$\frac{1}{f}\frac{\mathrm{d}f}{\mathrm{d}t} = \frac{1}{\sqrt{n_{\mathrm{e}}}}\frac{\mathrm{d}f}{\mathrm{d}n_{\mathrm{e}}}\frac{\mathrm{d}n_{\mathrm{e}}}{\mathrm{d}t} = \frac{1}{2n_{\mathrm{e}}}\frac{\mathrm{d}n_{\mathrm{e}}}{\mathrm{d}r}\frac{\mathrm{d}r}{\mathrm{d}t} = \frac{1}{2}\frac{\mathrm{d}\ln(n_{\mathrm{e}})}{\mathrm{d}r}\frac{\mathrm{d}r}{\mathrm{d}t}, \tag{1.27}$$

where the introduction of $\ln(n_e)$ comes from $\mathrm{d}\ln(n_e)/\mathrm{d}r = 1/n_e(\mathrm{d}n_e/\mathrm{d}r)$, and $(1/f)(\mathrm{d}f/\mathrm{d}t)$

normalises the drift rate in order to remove any frequency dependence. Here, the beam velocity is $v_{\mathrm{b}} = \mathrm{d}r/\mathrm{d}t$, and $r_n = (\mathrm{d}\ln(n_{\mathrm{e}})/\mathrm{d}r)^{-1}$ is the density scale height, such that

$$v_{\mathrm{b}} = \frac{\mathrm{d}f}{\mathrm{d}t}\frac{2r_n}{f}. \tag{1.28}$$

Near 30 MHz, $r_n \simeq 2\times10^{10}$ cm giving $v_{\mathrm{b}} \simeq 0.3c$ for a drift rate of -7 MHz s^{-1} (e.g. Kontar et al., 2017b). The extent of the observed frequency range and inferred exciter speed is consistent with the interpretation that Type III emission is caused by electron beams propagating along open magnetic field lines. The speed of the exciter has also been shown to decrease as it propagates out into interplanetary space from the loss of beam energy due to Langmuir wave refraction reducing the reabsorption level of the beam-plasma structure (Krupar et al., 2015). Moreover, faster electron beams are associated with brighter emission yet the beam structure does not have a constant velocity across its length, with the front propagating faster than the rear, causing elongation over time (Reid & Kontar, 2018a).

Figure 1.8 shows an example of an in-situ electron beam detected at 1 AU by the 3D Plasma and Energetic Particle (3DP) detector onboard the WIND spacecraft (Lin et al., 1995). Each coloured time profile is associated with an electron energy band centred on the value indicated in the figure. The higher energy electrons propagating at faster speeds arrive at the detector first, followed by lower energy electrons. Such observations show the beam structure as it propagates past the spacecraft (e.g. Krucker et al., 2007). The upper panel shows an associated Type III burst likely emitted from the same electron beam. The bright features just above the local plasma frequency of 10 kHz are signatures of in-situ Langmuir waves. Similar local Langmuir waves have been observed by Parker Solar Probe (PSP; Fox et al., 2016) spacecraft closer to the Sun at a distance of $r \sim 35.7$ $\mathrm{R}_\odot$ (0.17 AU) (Pulupa et al., 2020).

Attempts at identifying the location of a Type III radio source at a given frequency have been performed via triangulation using multiple spacecraft observations. Using the two antennas mounted perpendicular and parallel to the spacecraft spin axis on Helios 2, IMP 8, and Hawkeye 1, Gurnett et al. (1978) were able to find the angle between the spacecraft and radio source in three different planes that defined the source position at 86 $\mathrm{R}_\odot$ and 129 $\mathrm{R}_\odot$ for observed frequencies of 178 and 100 kHz, respectively. Stone (1980) used the ISEE-3 and Helios spacecraft to trace a Type III source between 36.5 $\mathrm{R}_\odot$ (732 kHz) and 157 $\mathrm{R}_\odot$ (62.8 kHz), and Reiner et al. (1998) used Ulysses and WIND spacecraft to track the source from 22.3 $\mathrm{R}_\odot$ (940 kHz) to 91.5 $\mathrm{R}_\odot$ (148 kHz), noting a propagation speed of $c/3$. The three studies find that the Type III sources propagate along a Parker spiral as it moves out into the heliosphere. With the recent launch of Parker Solar Probe and Solar Orbiter joining the WIND and STEREO spacecraft, we are now in the unique position of having four spacecraft situated around the Sun. This was exploited by Musset et al. (2021) by using the radio flux measurements by four spacecraft to determine the emission pattern, directivity, and source location. The flux measured at each spacecraft is corrected as though they were observed at 1 AU. By fitting the resultant intensity curves with an assumed directivity function, the source is localised to a particular longitude. The radial distance is then estimated with a density model. The study concludes that the directivity shape varies from one event to another, consistent with anisotropic scattering of the radio-waves.

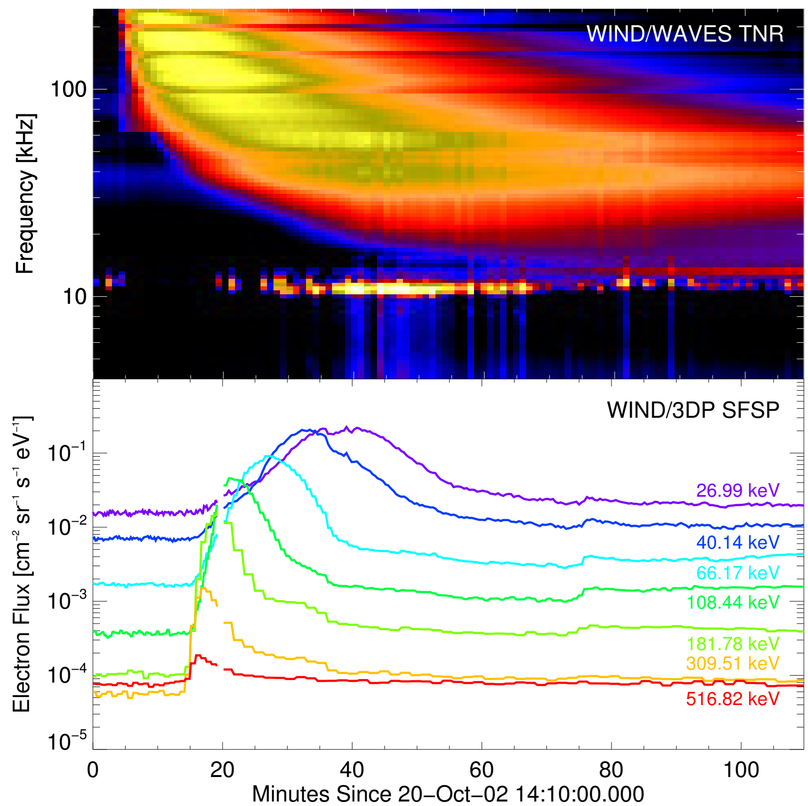

Figure 1.8: *Top:* Dynamic spectrum of the low frequency tail of a Type III burst observed by the WIND/WAVES TNR receiver between 12–245 kHz. *Bottom:* Electron flux detected by the WIND/3DP SFSP instrument between 27–517 keV energies.

The onset of Type III burst emission typically occurs below 1 GHz (McLean & Labrum, 1985). Above 1 GHz, collisional damping of the electrons and Langmuir waves make radio emission difficult to generate, and absorption in the low corona means that a Type III burst must be very bright to be observed at these frequencies (Reid & Ratcliffe, 2014). The observed Type III burst flux also varies with frequency. Statistical analysis of Type III burst flux show an increase with decreasing frequency up to a peak between 1–2 MHz (Weber, 1978; Krupar et al., 2014; Sasikumar Raja et al., 2022). The density models in Figure 1.2 show little variation at this height, and corresponding to a distance from the Sun between $5-8$ $R_\odot$. An explanation for this peak is not well defined, but suggestions pose that this emission is harmonic and saturated (Krupar et al., 2014), as well as considering that Langmuir wave growth, and radio intensity, are affected by density fluctuations—the 8 $R_\odot$ distance that corresponds to 1 MHz is near the region where the solar wind becomes super-Alfvénic, and is essentially, decoupled from the Sun (Sasikumar Raja et al., 2022).

Type III burst durations vary inversely with frequency. At 30 MHz, the full-width at half-maximum (FWHM) durations can be between a few seconds to 10 s (e.g. Reid & Kontar, 2018b, see Figure 4). The decay times follow a trend of $\tau \propto f^{-1}$ with a statistical relation from multiple studies given by

$$\tau(f) = (72.23 \pm 0.05) f^{-0.97 \pm 0.03}\,\mathrm{s}, \tag{1.29}$$

where f is in MHz between 0.1–300 MHz (Kontar et al., 2019). Additionally, the Type III source sizes also vary as $S \propto f^{-1}$, with a statistical relation composed from multiple studies of

$$S(f) = (11.78 \pm 0.06) f^{-0.98 \pm 0.05}\,\mathrm{degrees}, \tag{1.30}$$

between 0.5–500 MHz (Kontar et al., 2019). At fixed frequencies, the source sizes have been observed to increase over time from the peak of the time profile onwards (Raoult & Pick, 1980).

Type III emission may also present positive frequency drift rates produced via electron beams streaming towards the Sun through increasing density, named reverse-drift Type III bursts. It is possible for both a normal-drift and reverse-drift burst to be produced simultaneously, resulting in a bi-directional Type III burst in dynamic spectra, yet these events are uncommon (Meléndez et al., 1999). Additional variants of Type III bursts are labelled as Type U and J bursts owing to their shapes in dynamic spectra (e.g. Leblanc & Hoyos, 1985; Reid & Kontar, 2017) originate from electron beams propagating along coronal loops. The former arise from electron beams propagating along the ascending (decreasing density) and then descending (increasing density) leg of the loop, and the latter from beams that emit radio emission up to the loop apex only. However, due to the difficulty of generating sufficient Langmuir waves with a positive density gradient, as well as the higher densities contributing to increased damping from collisions (Reid & Ratcliffe, 2014), such bursts (whilst not uncommon) are rarer than Type III bursts. Embedded within the broadband Type III emission are often observed narrowband fine structures called striae, connected to coronal density fluctuations (section 1.4.1) and detailed in section 2.1.

1.4 Radio-wave Propagation Effects

The solar corona's turbulent nature has a significant impact on the propagation of radio-waves from the source location to the observer. The effects are evident in several ways, including the broadening of time profiles and source sizes, as well as a shift of the observed emission location away from the source location. Additionally, the angular broadening of radio sources can dilute the observed brightness, resulting in decreased brightness temperature estimations from observations (Bastian, 1994). Early observations of Taurus A, also known as the Crab Nebula or Tau A, made while passing within a small angular distance from the Sun (Hewish, 1958), revealed that the radiation is considerably scattered as it passes through the corona, leading to broadened angular sizes of extra-solar point sources. A compilation of such measurements from numerous studies, normalised to the same observing frequency, presents an increase in source size closer to the Sun approximately as $1/f^2$ (Figure 1.9).

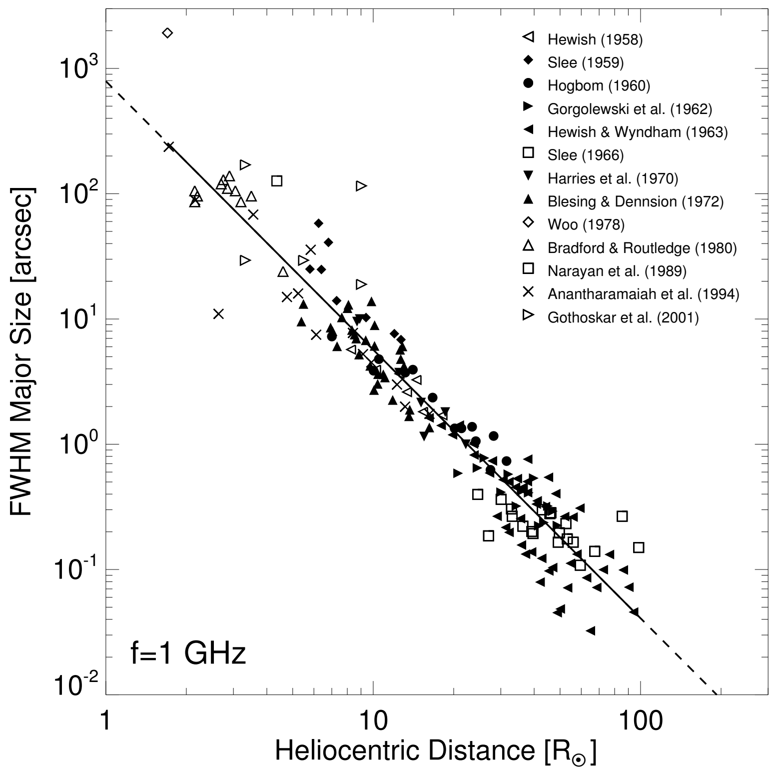

Figure 1.9: Observed FWHM extra-solar source sizes along the major axis from Hewish (1958); Slee (1959); Högbom (1960); Gorgolewski et al. (1962); Hewish & Wyndham (1963); Slee (1966); Harries et al. (1970); Blesing & Dennison (1972); Woo (1978); Bradford & Routledge (1980); Narayan et al. (1989); Sakurai et al. (1992); Anantharamaiah et al. (1994); Gothoskar et al. (2001). Data from Hewish (1958) shows points where the detector baseline orientation was specified, taking the larger of the measurements as the assumed major axis size. Woo (1978) reports broadening of the Helios 1 spacecraft signal. Data is scaled to 1 GHz from the observed frequency f_{obs} as $\theta = \theta_{\mathrm{obs}}(f_{\mathrm{obs}}\,[\mathrm{MHz}]/1000\,\mathrm{MHz})^2$.

Variations in the coronal density, including both the large scale decreases (as described in section 1.1.4) and changes due to structures such as streamers and shock fronts, as well as small-scale fluctuations, can alter or guide the ray path. Generally, the effect of observable features such as streamers cause the rays to refract, whilst fibrous structures aligned along the magnetic field act as waveguides to 'duct' the radiation along the structure. The small oscillations of plasma density act to scatter the radiation. In an unmagnetised plasma, the refractive index is given by

$$n_{\mathrm{ref}} = \left(1 - \omega_{\mathrm{pe}}^2/\omega^2\right)^{1/2}. \tag{1.31}$$

Near the plasma frequency, n_{ref} can vary significantly due to density inhomogeneities (remembering that $\omega = 2\pi f$ and $n_e \propto f^2$). This also implies that the radio-wave propagation effects subside as the radiation propagates far from the emission site, as the wave frequency is no longer close to the local plasma frequency. Additionally, due to the dispersion relation of EM waves (equation 1.22), the plasma frequency acts as a cut-off

$$k^2 = \frac{\omega^2 - \omega_{\mathrm{pe}}^2}{c^2}, \tag{1.32}$$

such that an EM wave will not propagate in the plasma when $\omega = \omega_{\mathrm{pe}}$, and will be reflected if $\omega < \omega_{\mathrm{pe}}$.

Numerous studies proposed different models to explain the effects of radio-wave propagation. Under the geometrical optics approximation, which ignores diffraction effects, the radiation can be considered as propagating rays (Bastian, 2000). This approach has enabled ray-tracing simulations to investigate radio-wave scattering on weak density inhomogeneities (e.g. Fokker, 1965; Steinberg et al., 1971; Robinson, 1983; Thejappa & MacDowall, 2008; Kontar et al., 2019). Alternative methods consider the coronal plasma confined to magnetic flux tubes, utilising these cylindrical, over-dense 'fibres' aligned in bundles to explain the size and directivity of Type I bursts Bougeret & Steinberg (1977), although such structures are not always present or visible in the corona. Duncan (1979) suggests ducting of the radio emission along flux tubes to explain observed source positions as the location where the radiation escapes the flux tube. However, a satisfactory explanation should be able to predict all observed radio source properties simultaneously for any event, an issue that is discussed in section 1.4.1.1.

1.4.1 Density Inhomogeneities

Small-scale fluctuations of plasma density, quantified by $\delta n_e/n_e$, have been studied in connection with scintillation of extra-solar sources, and spectral broadening of spacecraft signals (e.g. Woo & Armstrong, 1979). At 1 AU, in-situ observations from spacecraft provide direct measurement of the density oscillations. For example, Celnikier et al. (1983) measured the phase shift of radio signals due to density changes in the intervening plasma when transmitted between two spacecraft in near-Earth orbit. The measured power spectrum of density fluctuations $P(f)$ can be integrated over all observation frequencies as $\delta n_e/n_e = [1/n_e^2 \int f P(f)\,\mathrm{d}f]^{1/2}$, where $n_e = 8\ \mathrm{cm}^{-3}$ is the measured average density at the spacecraft, resulting in an average fluctuation level of approximately 10 % over the 3 hour observation window.

Closer to the Sun, remote sensing observations can be used to probe the turbulence level. For instance, observations of the point source Taurus A as it passed through the outer corona were used by Hewish (1955); Sasikumar Raja et al. (2017). The latter find $\delta n_e/n_e \approx 0.19-0.77\,\%$ between 9–20 $R_\odot$. Investigation into radio burst fine structures (chapter 2) suggested values ranging from $\delta n_e/n_e \approx 0.2-0.32\,\%$ between 30–70 MHz ($r \approx 1.45-1.75\ R_\odot$) (Sharykin et al., 2018). Near 30 MHz, Kolotkov et al. (2018) find $\delta n_e/n_e \approx 0.35\,\%$, and interpret the density oscillations as a fast magneto-acoustic wave guided along the open magnetic field. Between frequencies of 0.1–1 MHz ($r \approx 5-55\ R_\odot$ using the density model of equation 1.10), Krupar et al. (2018) find a range of $\delta n_e/n_e$ between 6–7% in Monte Carlo simulations can reproduce the decay times of Type III radio bursts observed by the STEREO spacecraft. Marsch & Tu (1990) found that $\delta n_e/n_e$ grows in amplitude with increasing distance from the Sun using in-situ data from the Helios spacecraft at 0.1 and 0.3 AU, which supports the aforementioned turbulence levels at various distances from the Sun.

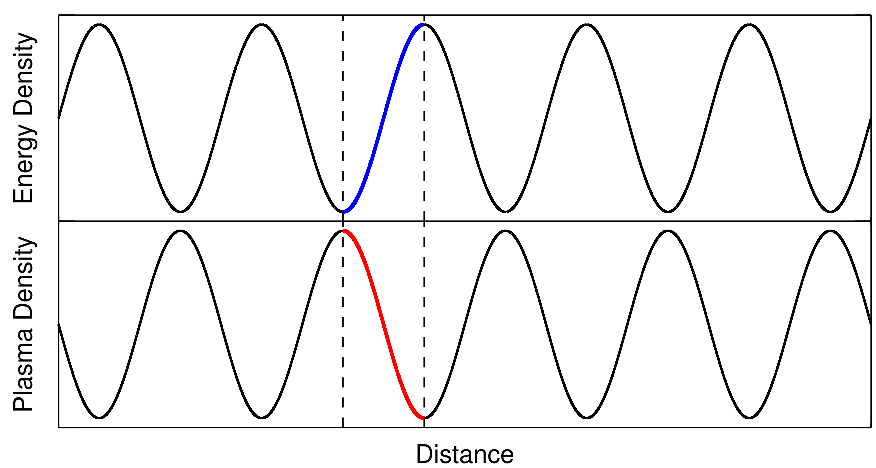

Figure 1.10: Diagram of plasma density fluctuations and corresponding Langmuir wave energy density growth (blue) during negative decreasing density regions (red).

Plasma inhomogeneities may also influence the distribution of Langmuir waves by suppressing growth in some regions. Smith & Sime (1979) hypothesise that the clumping of Langmuir waves in Type III burst sources results from such quenching, with the size of the inhomogeneity on the order of 50–200 km at 0.5 AU. On scales of 50–100 km, they note that significant clumping occurs with amplitudes between 0.06–0.48%. Simulations of electron beam propagation in an inhomogeneous plasma show that the beam propagates as a continuous stream, whilst the clumpy distribution of Langmuir waves is wholly determined by the plasma density inhomogeneities (Kontar, 2001b). In this sense, when the density increases within a particular fluctuation, Langmuir wave growth decreases, as illustrated in

Figure 1.10. This can lead to modulation of the radio emission, observed as fine structures discussed in section 2.

1.4.1.1 Anisotropic Turbulence

Over the past few decades, investigations into coronal density fluctuations have considered either isotropic fluctuations where the inhomogeneities are on average the same in all directions, or anisotropic fluctuations where the fluctuations may be stronger in one particular direction. In both early and recent scattering models that have assumed isotropy, radio-wave scattering simulations were able to reproduce the observed source sizes (Steinberg et al., 1971) and decay times (Krupar et al., 2018). However, the isotropic models were not sufficient to explain both these characteristics simultaneously. In addition, as noted in section 1.4, large-scale structures were sometimes invoked to explain burst sizes and directivity (Bougeret & Steinberg, 1977; Duncan, 1979), but these structures are not always present and so fail to explain radio burst characteristics from every event.

A recent study into radio burst fine structures by Kontar et al. (2017b) found that anisotropic fluctuations were required. The approach is rather simple; the observed fine structure FWHM durations were typically on the order of $\Delta t \simeq 1$ s after broadening due to the radio-wave propagation effects, yet the observed sizes in the sky plane were ~ 20 arcmin. Since $c\Delta t \simeq 3\times10^{10}$ cm $\simeq 8$ arcmin, the turbulence causing the scattering is likely to be anisotropic, with the dominant scattering contribution perpendicular to the line-of-sight (LOS). This arises from the density fluctuating more strongly along the magnetic field direction such that a ray will be refracted towards the perpendicular direction. This causes the scattering power to be stronger in the perpendicular direction, and the easiest route of photon escape to be parallel to the magnetic field. The observed result of this is a source that is broadened along the perpendicular axes, and shifted along the parallel axis, as depicted in Figure 1.11. A by-product of this is that sources at a non-zero heliocentric angle associated with radial magnetic fields will appear narrower along the x-direction of the sky-plane, and displaced from the emitters location. Such source directivity at a given frequency has been observed in numerous studies (e.g. Wild et al., 1959b; Bougeret & Steinberg, 1977; Kontar et al., 2017b; Kuznetsov & Kontar, 2019).

Inclusion of anisotropy in radio-wave scattering numerical simulations was conducted recently by Kontar et al. (2019). They assume that the density fluctuations are axially symmetric with a radial magnetic field, and parametrise the spectrum of density fluctuations S as

$$S(\boldsymbol{q}) = S\left(\left[q_\perp^2 + \alpha^{-2} q_\parallel^2\right]^{1/2}\right), \tag{1.33}$$

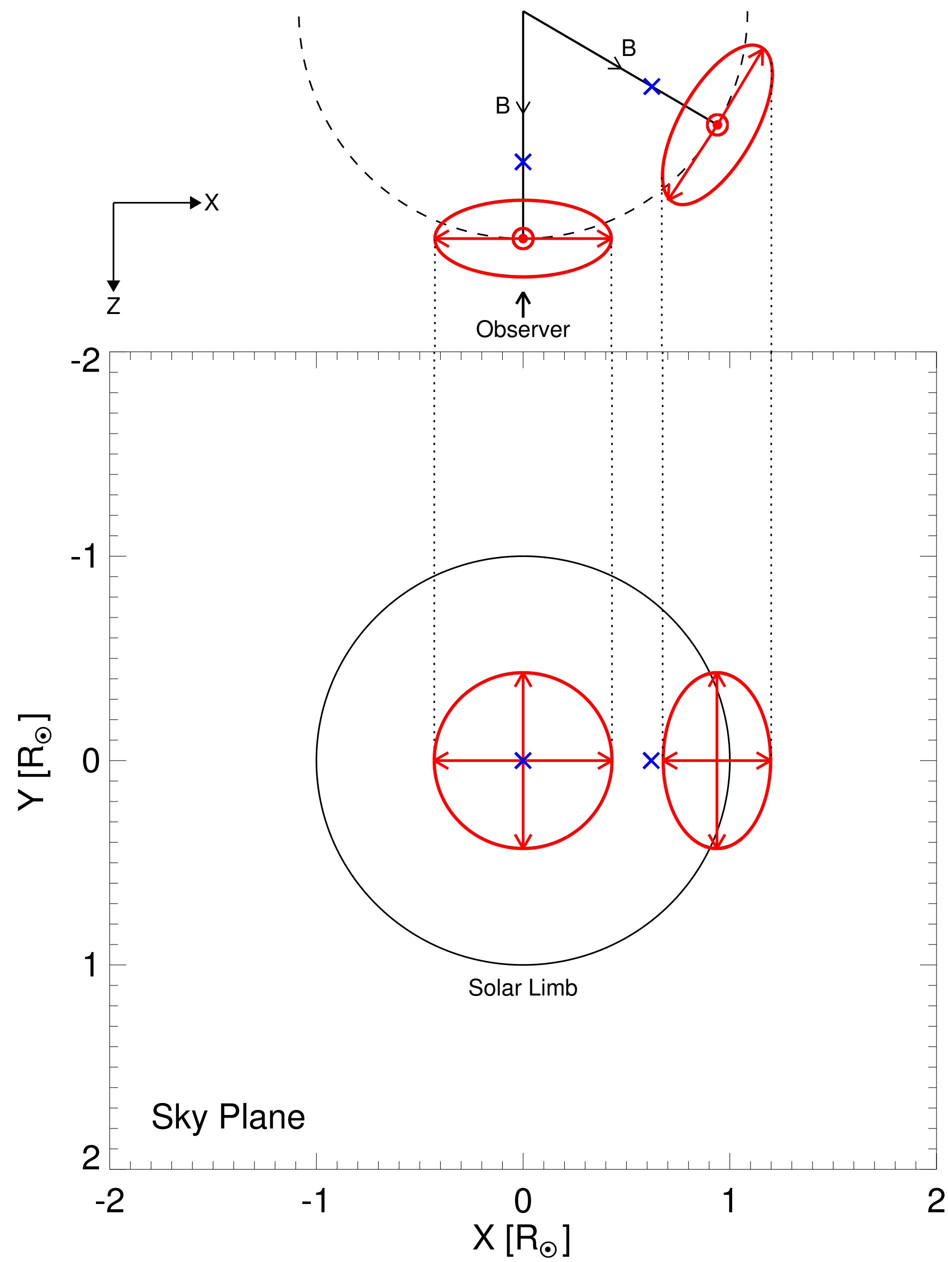

Figure 1.11: Illustration of the effect of anisotropy of the density fluctuation spectrum on the observed source sizes and position. The upper section shows the *zx*-plane with the observer along the positive *z*-axis. Two emitting sources (blue crosses) are placed at the same radius but along different radial magnetic field directions; one along the LOS and one at some heliocentric angle. The red ovals represent sources broadened tangentially to the field direction. The red arrows designate the direction of broadening. The lower panel shows the sky plane and the projected source positions, shapes, and sizes superimposed onto the solar disk. Due to preferential photon escape along the field direction, the observed sources are shifted away from the true source location in the sky-plane for sources located away from the disk centre.

where $\boldsymbol{q}$ is the wavevector of electron density fluctuations, and

$$\alpha = h_{\perp}/h_{\parallel} \tag{1.34}$$

is the anisotropy factor with $h_{\perp}$, $h_{\parallel}$ are the perpendicular and parallel correlation lengths. The isotropic case is given when $\alpha = 1$, and anisotropic when $\alpha \ll 1$. Through comparison with radio burst observational data, an anisotropy factor of 0.3 was required to reproduce the decay times and source sizes simultaneously near 30 MHz, which the isotropic case could not do.

Varying the anisotropy factor affects the decay times, sizes, and position of the simulated sources. Strong anisotropy leads to shorter decay times, reducing to ~ 0.1 s near 30 MHz when $\alpha = 0.2$, and rising to ~ 1 s for $\alpha = 1$ when the same level of density fluctuations are considered. In the absence of anisotropy, the time profile is broadened to a greater extent (Kontar et al., 2019), owing to a lack of directivity of the emission. Conversely, strong anisotropy has a focusing effect that directs the radio-waves along the field direction and produces shorter pulses of emission that arrive at a given position in space. Although Kontar et al. (2019) show a weak variation of source size with α, the strongest anisotropy factor considered was limited to 0.3. Kuznetsov et al. (2020) used the same simulation code to demonstrate that the peak source sizes decrease for anisotropy $\alpha \leq 0.2$. They also show the short time profiles observed with strong anisotropy produce a visible radio echo component which is observed in drift pair fine structures (section 2.2). Weak anisotropy masks the echo because it merges into the tail of the primary burst component. The directivity induced by anisotropy can be significant—Kontar et al. (2019) show that an observed radio source is displaced from the emission site up to 0.6 $R_{\odot}$ for sources injected at a height of 1.75 $R_{\odot}$ above the limb with $\alpha = 0.3$. Such a displacement depends on the source angle with respect to the observer. In a radial magnetic field, sources at the disk centre will display no visible displacement since such a shift occurs along the LOS. Kuznetsov et al. (2020) go on to show that the centroid shift over time as seen in drift pair bursts and other radio emissions (cf. section 2.1) can be explained by including anisotropy. Specifically, they show that a source located at a heliocentric angle of 30° presents a centroid shift of ~ 120 arcsec when $\alpha = 0.2$. Additionally, the study found that the burst size increases by ~ 30 arcmin^2 during the decay phase for the same parameters. These results are consistent with the fixed frequency, temporal evolution observed in drift pair bursts (Kuznetsov & Kontar, 2019) and striae (e.g. Kontar et al., 2017b). Moreover, the striae observations by Kontar et al. (2017b) were replicated in position and size for both the fundamental and harmonic components by (Chen et al., 2020). Providing the specific time in relation to the burst profile is therefore essential when reporting the position and size of radio emission.

A long-standing and puzzling dilemma regarding fundamental and harmonic burst pairs is often observed, where the frequency ratio between the two components at a given time is less than the theoretical ratio of 2, sometimes as low as 1.6. Recent research by Chen et al. (2023a) provide a resolution to this issue by showing that anisotropic radio-wave scattering can induce a delay of the fundamental emission with respect to the harmonic. Their simulations demonstrate that strong anisotropy with a factor of $\alpha \sim 0.25$ can replicate the observed frequency ratios due to delayed fundamental emission. This finding is consistent with the required anisotropy factor for reproducing the decay times and sizes of the bursts.

1.4.1.2 Inner and Outer Scales

The power spectra of solar wind density fluctuations are observed to follow a Kolmogorov-like spectral slope in the inertial range between the inner and outer scales with $P(f) \propto f^{-5/3}$. Energy is thought to cascade from the larger outer scales, to the smaller inner scales (Alexandrova et al., 2013). The outer scale marks where the spectral slope changes from near -1 to $-5/3$ at $l_o = 2\pi/q_o$ where q_o gives the wavenumber of the density fluctuation at this scale. Power spectra measurements by Wohlmuth et al. (2001) from the Galileo spacecraft between 7–80 $R_\odot$ suggest that $l_o(r) = (0.23 \pm 0.11) r^{(0.82\pm0.13)}$. The inner scale is given by $l_i(r) = 2\pi/q_\mathrm{i}$ which marks the point where the spectral slope steepens from $-5/3$ to approximately -2.5, and is thought to vary with distance from the Sun as $l_i(r) = r/R_\odot$ [km] between 2–70 $R_\odot$ (Coles & Harmon, 1989) based on observations from numerous studies. Beyond this scale, the fluctuations likely dissipate.

1.4.2 Ionospheric Refraction

Solar radio emission detected by ground based instruments must first propagate through the ionosphere, which is the ionised upper region of Earth's atmosphere. The ionisation exists due to solar ultra-violet (UV) radiation, producing an irregular shell of charged particles around the Earth. The ionosphere has direct implications on radio communication, as it allows signals to be refracted and received beyond the transmitter's local horizon. Changes in the ionospheric density lead to radio-wave refraction due to variations in the refractive index (equation 1.31). These density changes occur in the form of stratified layers, causing the refractive index to vary with height, as well as density irregularities. Ionospheric refraction can be measured using ionosondes, which transmit radio frequency signals as they move through the ionosphere.

For incident radio emission, the effect of ionospheric refraction is a frequency variable shift of the observed source. Galactic radio-sources have been found to experience displacements of a few arcminutes and fluctuations in intensity (e.g. Ryle & Hewish, 1950). For instance, Gordovskyy et al. (2019) showed that observations of Taurus A can be displaced by up to 25 arcmin. The displacement is dependent on the source zenith angle with greater displacements near the local horizon (Thompson et al., 2017). The fluctuating amplitude of

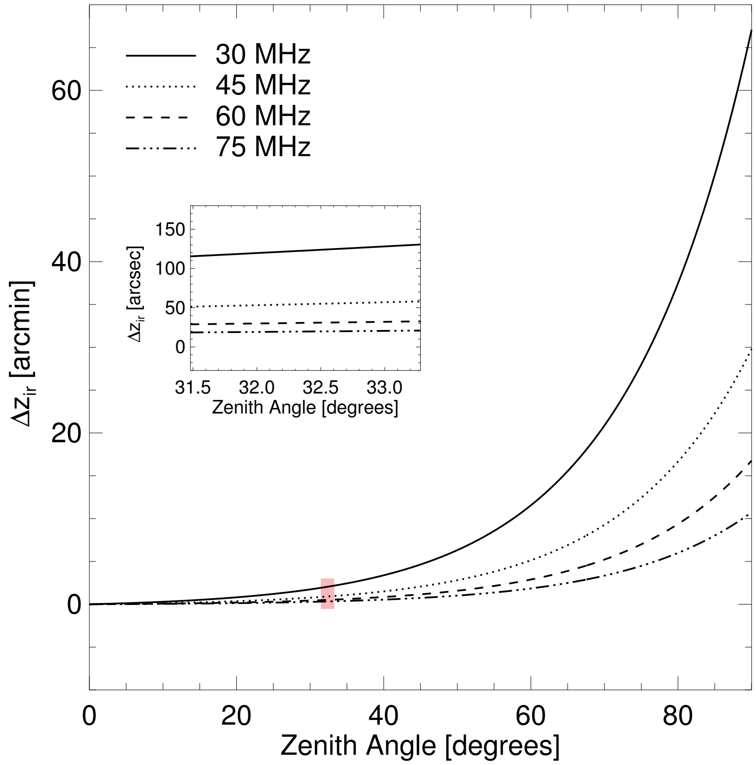

Figure 1.12: The shift in zenith angle of low frequency ratio sources due to ionospheric refraction as given by equation 1.35. Each curve corresponds to a different observing frequency. The inset displays the zoomed in region denoted by the light red box corresponding to the solar position as viewed from the latitude and longitude of the LOFAR core (section 1.5.1) between 10:40 UT and 11:40 UT on 15-Jul-2017. The solar zenith angle at this location was found from National Oceanic and Atmospheric Administration (NOAA) data.

radio emission received from a star were linked to ionospheric irregularities with a size of 2–10 km, causing fluctuations on timescales of around 30 s for small-scale fluctuations, while large-scale fluctuations can last for $\sim$ 10 minutes (Hewish, 1952). To quantify the effect of ionospheric refraction, Gordovskyy et al. (2019) measured the angular deviation in zenith position Δz of Taurus A observed at different zenith distances, and provide an empirical relation for the average source shift Δz_{ir}, presented in Gordovskyy et al. (2022) as

$$\Delta z_{\mathrm{ir}}(f,z) = \frac{5.59}{f^2}\left[13.01\exp\left(\frac{z-44.417}{17.313}\right)-1\right], \tag{1.35}$$

where f is in MHz, and both Δz_{ir} and z are in degrees. Equation 1.35 ignores effects of any seasonal and daily variation, and consequently can be used to correct for the average effects of ionospheric refraction only. Figure 1.12 shows the dependence of Δz_{ir} on the source zenith angle for different frequencies between 30–75 MHz. At lower frequencies, there is a steep increase in Δz above 60°, whereas at 75 MHz, little change is observed up to 80°. For example, at a source zenith angle of $z \sim 30°$, which corresponds to the solar zenith position of LOFAR in the Netherlands at noon in July, a 30 MHz source may experience a shift of $\Delta z_{\mathrm{ir}} \sim 2$ arcmin. Although this may seem small, it corresponds to ~ 100 arcsec, more than 10 % of a solar radius. Therefore, when trying to determine the location of radio sources relative to other solar phenomena, such a shift is substantial. This empirical relation is used in sections 4 and 5 of this thesis.

For decades, solar radio observations have revealed the effects of ionospheric refraction. Wild et al. (1959a) used relatively stable, long duration Type I emission to probe these effects, observing deviations up to 20 arcmin, with stronger deviation at lower frequencies. More recently, Koval et al. (2017) found that travelling ionospheric disturbances can cause spectral perturbations known as 'spectral caustics' in solar dynamic spectra, using 129 low frequency radio observations over 16 years. These disturbances were found to occur primarily during the winter months, with only 5% occurring during summer, and the majority occurring during the active phases of solar cycles.

1.5 Instrument Overview

1.5.1 The Low Frequency Array

The LOw Frequency ARay (LOFAR, van Haarlem et al. (2013)) is an advanced radio interferometer that serves as a pathfinder towards the Square Kilometre Array (SKA). Its sophisticated antenna design and digital signal processing enable high temporal and spectral resolution observations, facilitated by the telescope's vast computing power. LOFAR is designed as a phased-array with fixed antennas, which means that signal delays are inserted to each antenna to achieve coherence across the array for a specific region in the sky, effectively 'pointing' the telescope. Observations are then made using a combination of antennas in groups called stations. The telescope has 24 core and 14 remote stations located in the Netherlands, as well as 14 international stations throughout Europe. Its operating frequency range is from 10–240 MHz, with 10–90 MHz for the Low Band Antennas (LBA) and 120–240 MHz for the High Band Antennas (HBA). The core stations consist of 96 LBAs and 48 HBAs. The design of LOFAR allows simultaneous output of both spectroscopic and imaging data with the same temporal and spectral resolution. This unique feature enables a two-dimensional radio image to be generated for every pixel in a LOFAR dynamic spectrum.

1.5.1.1 Phased-Array Interferometry and Digital Beam-forming

When using an interferometer with antennas spaced apart by a baseline distance D, the incoming radiation from a distant source can be approximated as a plane wave. As illustrated in Figure 1.13, this radiation arrives at antenna two before reaching antenna one, causing a geometric delay that can be expressed as

$$\tau_{\text{delay}} = D \sin z / c, \tag{1.36}$$

where z represents the zenith angle of the source. The signal from each antenna is passed

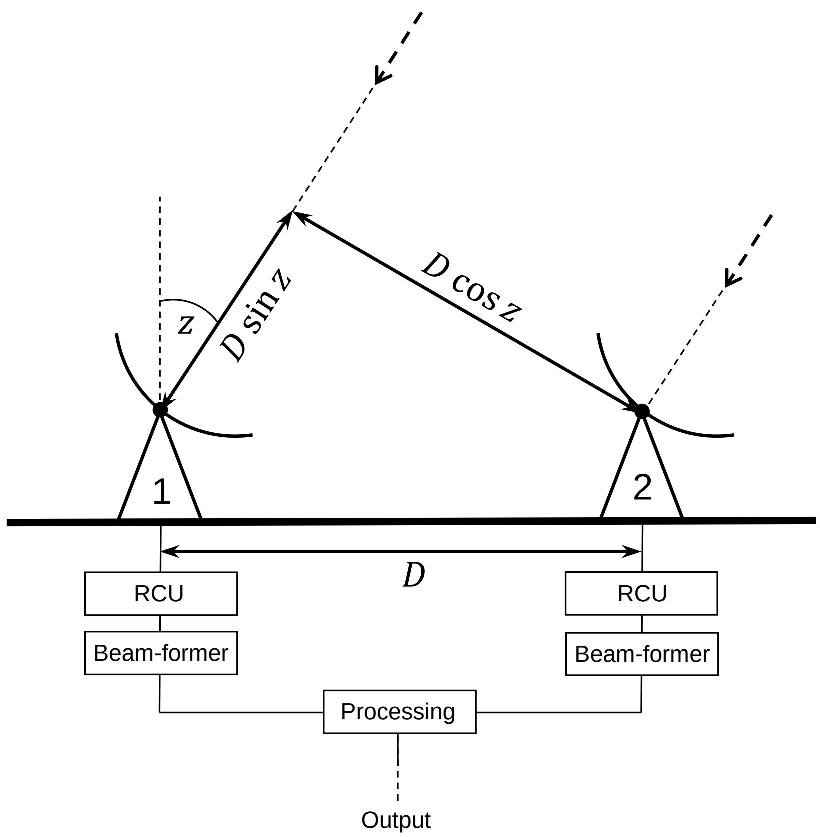

Figure 1.13: Geometry of an interferometer with two antennas spaced apart by baseline D. The diagonal, dashed arrows represent the incoming radiation from a source at zenith angle z. Figure based on that by Thompson et al. (2017). Analogue signals from each antenna pass through the Receiver Unit (RCU) where they are digitized, with the beam-former introducing artificial phase delay to each signal (van Haarlem et al., 2013).

through a Receiver Unit (RCU) where it undergoes filtering and digitisation. A polyphase filter then divides the digitised signal into 512 sub-bands with 195 kHz bandwidth (if the 200 MHz clock is selected), as detailed in van Haarlem et al. (2013). The beam-former applies a phase correction in real-time based on the baseline and source direction allowing the beam to be pointed at a specific source. Furthermore, each sub-band is divided into 16 channels, resulting in a bandwidth of 12.2 kHz per channel.

1.5.1.2 Low-band Antenna

The LBAs are simple dipoles as shown in Figure 1.14, and are sensitive to two polarisations. They are designed to operate from the ionospheric cut-off of 10 MHz up to 90 MHz. Above 90

MHz, strong radio frequency interference (RFI) exists from commercial FM broadcasting, and similarly between a few megahertz to 26.1 MHz from short-wave radio. In practice, the antennas are used above 30 MHz, with an analogue filter used to suppress the response below 30 MHz. This noise can be seen as sharp peaks in average spectral power as shown in Figure 1.14. The spectrum peak at 58 MHz denotes the frequencies at which the LBA is most sensitive. The dipole length of 1.38 m corresponds to a resonance frequency of 52 MHz, which is shifted to 58 MHz from interaction between the antenna and low noise amplifiers (van Haarlem et al., 2013). The increased response at this frequency can cause observations to appear artificially brighter and must be corrected for during calibration.

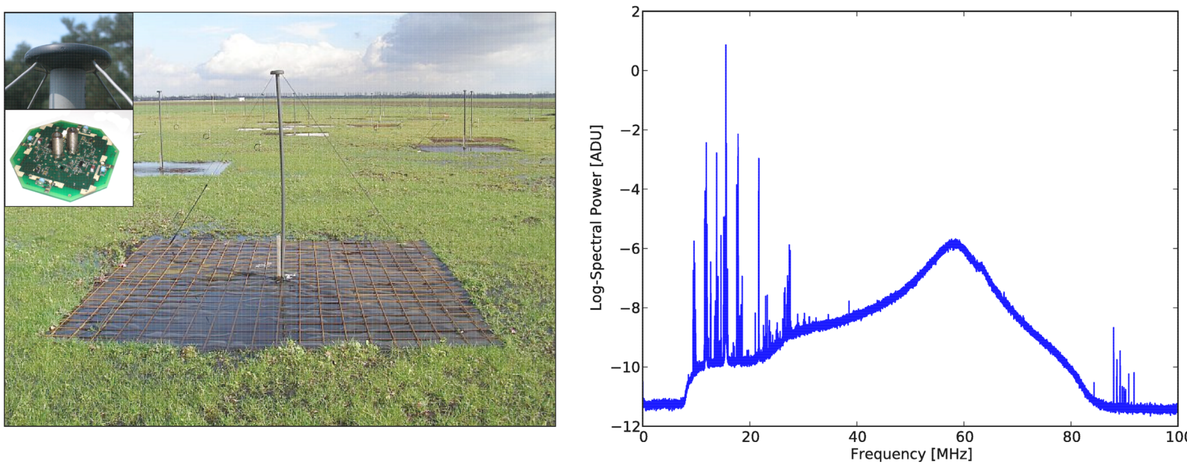

Figure 1.14: (*left*) A LOFAR low band antenna dipole. (*right*) Averaged spectral power for all LBA dipoles in a single station van Haarlem et al. (2013). Reproduced with permission ©ESO.

1.5.1.3 Tied-Array Beam Imaging

LOFAR offers two major observing modes depending on the research goal. Interferometric imaging mode provides visibility data like a traditional aperture synthesis radio telescope with an antenna array, providing high spatial resolution. In this work, we utilise the tied-array imaging mode from the core stations, which are centred at an Earth latitude of 52.914610° and longitude of 6.871362°, with a maximum baseline of $D \sim 3.5$ km (Figure 1.15). The tied-array mode offers increased temporal resolution of 10 ms at the expense of decreased spatial resolution.

Each LBA beam covers the full sky, although sensitivity is reduced below an elevation of 30°. The individual LBA beams that form a given station are coherently summed to form a station beam pointing towards a selected location. The coherence is achieved by the aforementioned artificially introduced delay to compensate for the geometric and instrumental phase delay of radio signals. Each station beam is further coherently combined to form tied-array beams, with each pointing in a different location of the sky. The beams form an

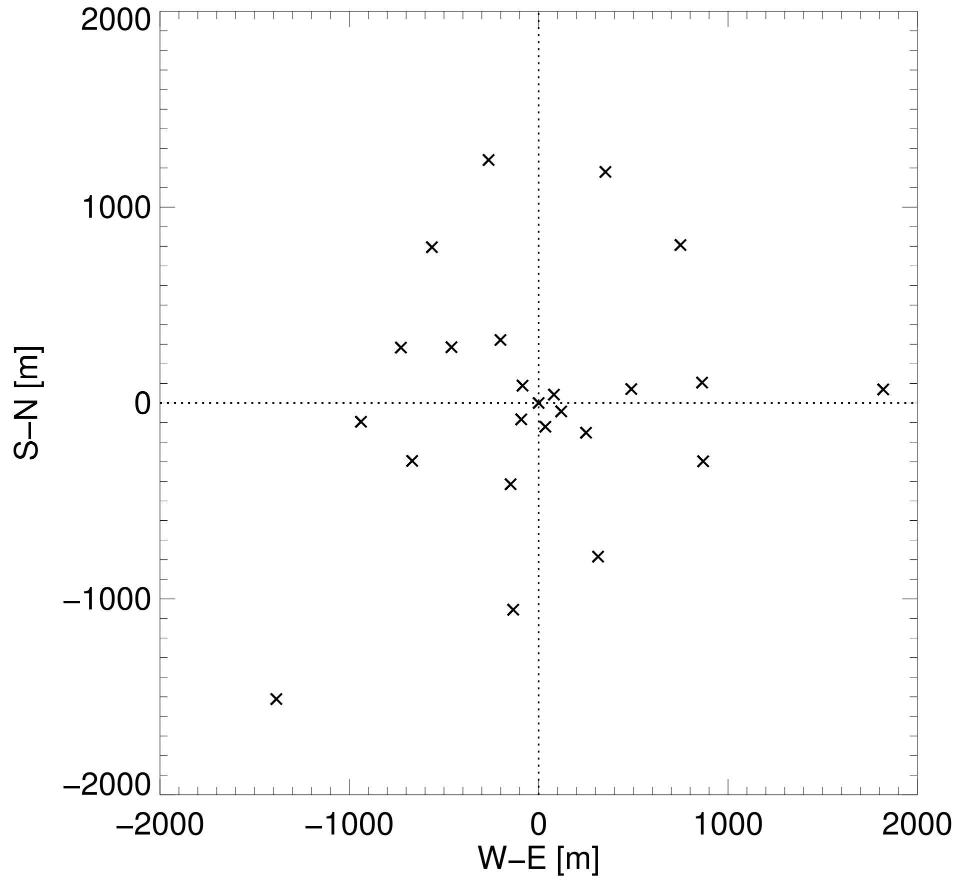

Figure 1.15: Relative distribution of the 24 LOFAR core stations.

overlapping hexagonal honey-comb pattern across the solar disk out to approximately 3 $R_\odot$. The beam coordinates relative to the solar disk centre are calculated as shown in Reid & Kontar (2017) using

$$\begin{aligned} x_b &= -(\alpha - \alpha_\mathrm{s})\cos\delta_\mathrm{s}\cos\theta_\mathrm{pa} + (\delta - \delta_\mathrm{s})\sin\theta_\mathrm{pa} \\ y_b &= (\alpha - \alpha_\mathrm{s})\cos\delta_\mathrm{s}\sin\theta_\mathrm{pa} + (\delta - \delta_\mathrm{s})\cos\theta_\mathrm{pa}, \end{aligned} \tag{1.37}$$

where α, δ are the right ascension and declination beam coordinates in radians, $\alpha_\mathrm{s}, \delta_\mathrm{s}$ are the solar centre right ascension and declination, and θ_pa is the angle of the solar north pole to celestial north.

Each beam has an angular width θ_b given by

$$\theta_\mathrm{b} = a\frac{\lambda}{D}, \tag{1.38}$$

where $\lambda = c/f$ is the wavelength corresponding to observing frequency f, and a depends on the imaging weighting scheme with a value of ~ 1 (van Haarlem et al., 2013). This corresponds to a FWHM beam area A_{b} given by

$$A_{\mathrm{b}} = \pi \left(\frac{\theta_{\mathrm{b}}}{2}\right)^2 \tag{1.39}$$

Figure 1.16 shows both the angular resolution and FWHM beam area between 30–80 MHz for a nominal, spherical beam as shown distributed across the solar disk in Figure 1.17(left). The spacing of the beam centres of ~ 6 arcmin ensures partial overlap of each beam. In practice, the array baseline will not reach the maximum of 3.5 km if the source is located away from the local zenith. For example, if the source has an elevation from the horizon of 60°, corresponding to zenith angle $z = 30°$, then the effective baseline will contract by a factor of $\cos z$ due to the projection effect (Figure 1.13), leading to a larger angular resolution (equation 1.38) and elongated beam shape. Figure 1.17 (right) shows the synthesised beams for a solar observation on 15 July 2017 where the Sun was located 57.6° above the horizon.

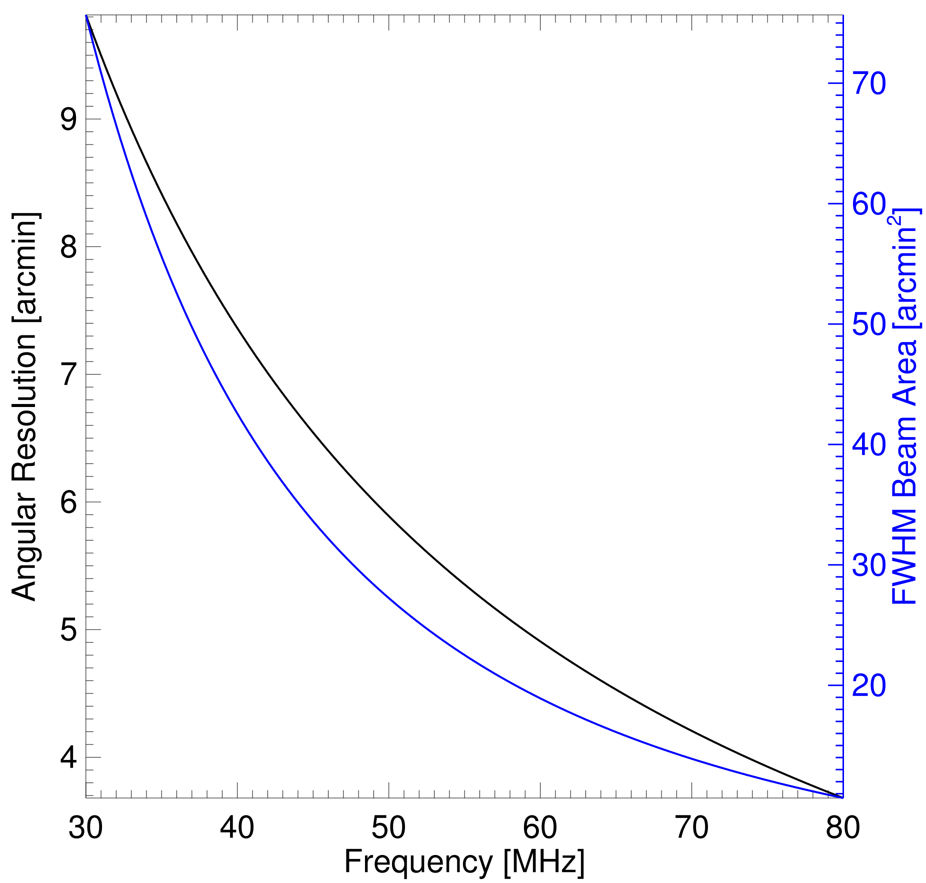

Figure 1.16: The angular resolution (black curve and vertical axis) and FWHM nominal beam area (blue curve and vertical axis) for the LOFAR LBAs.

An individual, synthesised LOFAR beam image that represents the point-spread function (PSF) is shown in Figure 1.18. The elongated main lobe is clearly visible centred on

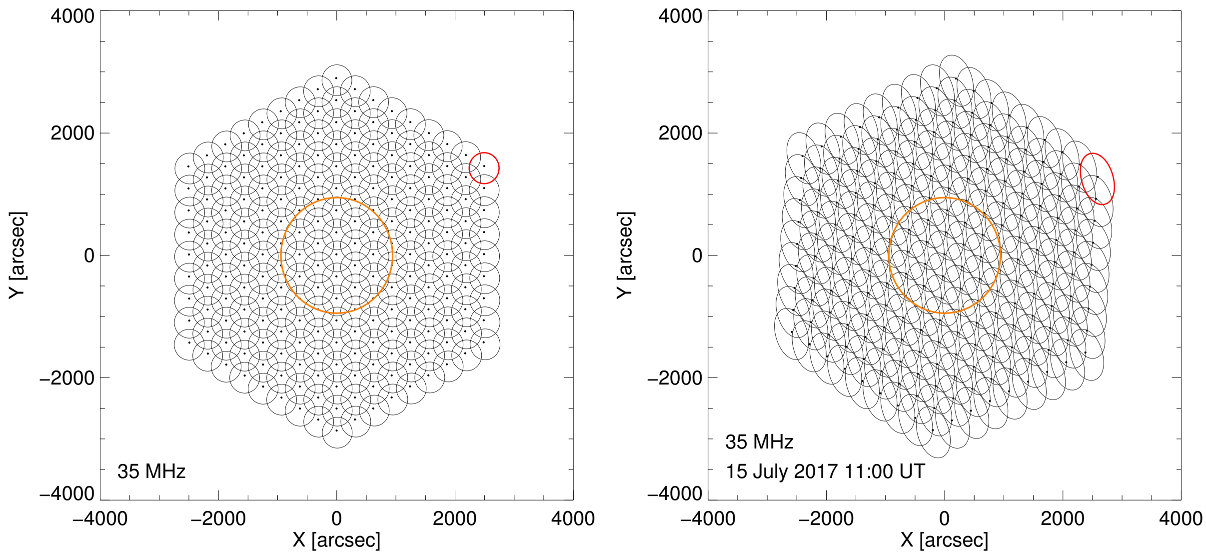

Figure 1.17: (*left)* Honey-comb pattern formed by 217 tied-array beams with nominal angular width of 8.4 arcmin at 35 MHz (grey circles) distributed across the centre beam coordinates (black dots) across the solar disk (orange). The red contour highlights a single beam. (*right)* As in the left panel but showing a beam size and shape synthesised for an observation on 15 July 2017 at 11:00 UT when the Sun had an elevation of 57.6°.

$x = y = 0$ arcsec, with sidelobe intensity approximately 10% of the peak. To minimise the effect of low source elevation, solar observations are best conducted near local noon around the summer solstice. In the northern hemisphere, this means observations are best conducted around the month of June.

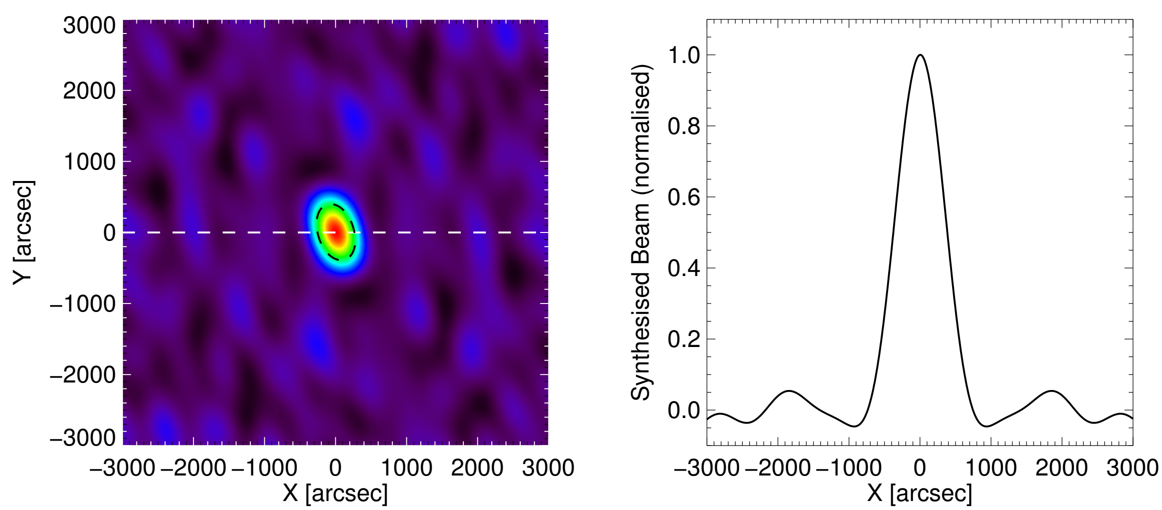

Figure 1.18: (*left*) Synthesised LOFAR PSF at 35 MHz, generated using code written for Kontar et al. (2017b). The black dashed outline represents the half-max contour. (*right*) A slice of the PSF along the white dashed line in the left panel.

Each individual beam records a dynamic spectrum (e.g. Morosan et al., 2014) that are then summed over the full tied-array. Similarly, the full-disk image is an interpolation of the intensities recorded by each beam at a given time, frequency, and location across the solar disk, as done in Reid & Kontar (2017); Kontar et al. (2017b) using 169 and 127 beams, respectively. Figure 1.19 shows an example LOFAR image at 30.0 and 44.3 MHz corresponding to the dynamic spectrum shown in Figure 2.1. At higher frequencies, the sidelobes can become comparable in brightness to the main lobe (e.g. Gordovskyy et al., 2019), as seen in panel (a) here. Therefore, in this thesis, LOFAR imaging is conducted at frequencies below 45 MHz.

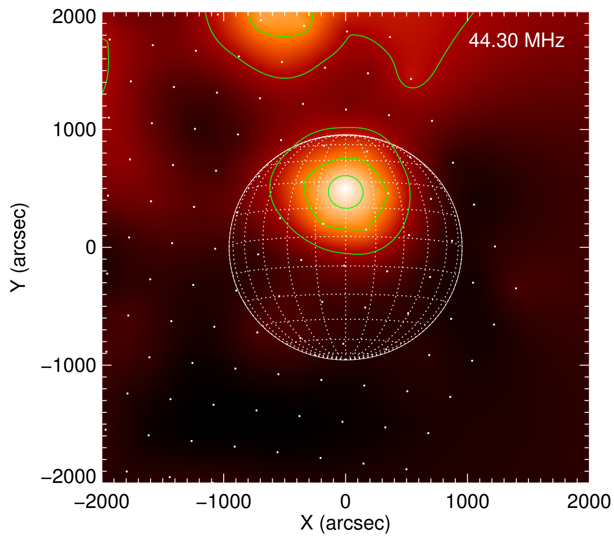

Figure 1.19: LOFAR images at 44.3 MHz (left) and 30.0 MHz (right) on 16 April 2015 at 11:56:56.170 and 11:56:57.743 UT, respectively. The white dots represent the individual beam pointing, and the green contours are shown at the 50%, 75% and 90% intensities.

1.5.1.4 Flux Calibration

The raw LOFAR data can be calibrated to flux density in solar flux units by utilising Taurus A as a calibrator. Tau A is a well-observed point-source with high flux density (Apparao, 1973). It is located sufficiently far from the Sun to avoid solar contamination. The main lobe of radio emission from Tau A is centred on a right ascension of 83.63° and declination of 22.01° (Figure 1.20). To record the Tau A flux, the full tied-array can be used before and after the solar observation, or one beam can be directed at Tau A throughout the solar observation. By normalising the LOFAR data with the known Tau A flux, the flux density of the observed radio emission can be determined (e.g. Kontar et al., 2017b).

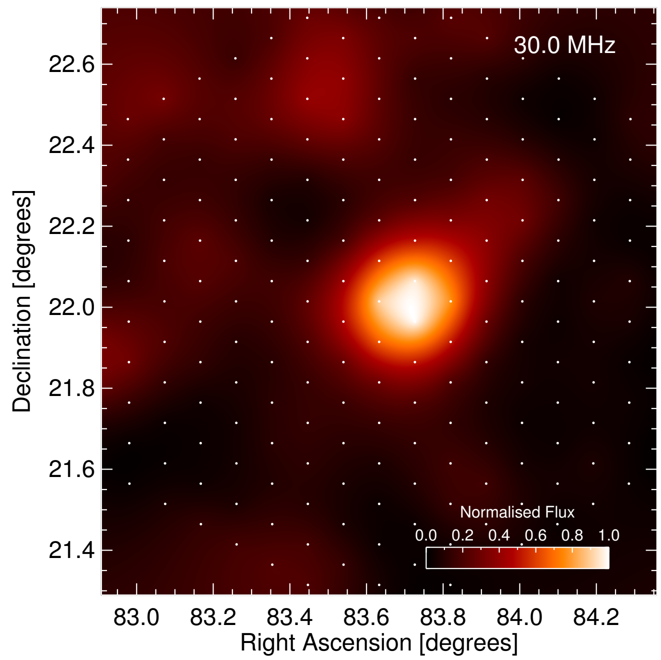

Figure 1.20: LOFAR image of Tau A at 30 MHz on 15-July-2017 11:54:59.7 UT. The white dots represents the beam pointing.

1.5.2 Nançay Decametre Array

The Nançay Decametre Array (NDA, Lecacheux, 2000) is composed of two phased antenna arrays located in Nançay, France with a longitude of 2° East, and latitude of 47° North, built between 1975–1977. Each array has 72 conical 9 m high by 5 m wide antennas angled at 20° south of the meridian. The antennas are sensitive to opposite senses circular polarisation. The fixed antennas are steerable via a system of phase delays. Originally built to observe Jovian radio emission (Boischot et al., 1980), the NDA also observes solar radio emission for approximately 8 hours a day, providing dynamic spectra with time and frequency resolution of 0.5 s and 175 kHz, respectively. For solar observations, the NDA operates between 10–80 MHz with an effective aperture of ~ 4000 m^2 at 30 MHz.

Since 1990, multiple additional receivers have been connected to the NDA. The MEFISTO receiver observes the Sun between 10–35 MHz with time and frequency resolution of 0.1 s and 80 kHz, simultaneously measuring left and right hand circularly polarised flux densities. The data are processed with on-the-fly median filtering, which reduces the RFI (Lamy et al., 2018). Data from the MEFISTO receiver is used in chapter 3.

1.5.3 Solar Dynamics Observatory

NASA's Solar Dynamics Observatory (SDO, Pesnell et al., 2012) is a spacecraft launched in 2010 into a circular geosynchronous orbit inclined by 28°. The onboard instrumentation consists of the Atmospheric Imaging Assembly (AIA, Lemen et al., 2012), the EUV Variability Experiment (EVE, Woods et al., 2012), and the Helioseismic and Magnetic Imager (HMI, Scherrer et al., 2012). The spacecraft transmits $\sim$ 150000 high-resolution full-Sun images and 9000 EUV spectra to Earth per day (Pesnell et al., 2012), providing images, magnetograms, dopplergrams, and spectra.

1.5.3.1 Atmospheric Imaging Assembler

The SDO/AIA instrument is an array of four telescopes that provides full-disk images of the solar atmosphere using a 20 cm primary mirror, providing a pixel size of 0.6 arcsec and field of view of 41 arcmin, with a maximum synoptic cadence of 12 s (Lemen et al., 2012), although higher cadence is possible for special campaigns. The telescope filters are optimised to ten narrowband EUV wavelengths (Table 1.2), specifically chosen to probe different regions of the solar atmosphere, owing to the primary ions and characteristic emission temperatures within a given region. Of interest to the corona are the passbands centred on wavelengths 171 Å and 193 Å, where the main ion contributions are Fe IX and Fe XII, respectively, corresponding to temperatures of 1–1.25 MK. The former is particularly useful for highlighting coronal loops. At hotter temperatures of 2 MK, the primary ions are Fe XIV, correlating to a wavelength at 211 Å, useful for probing active regions. Data from AIA are used in chapters 3, 4, and 5.

Wavelength [Å]	Atmosphere Region
94	Flaring corona
131	Transition region, flaring corona
171	Quiet corona, upper transition region
193	Corona and hot flare plasma
211	Active region corona
304	Chromosphere, transition region
335	Active region corona
1600	Transition region, upper photosphere
1700	Temperature minimum, photosphere
4500	Photosphere

Table 1.2: SDO/AIA wavelength channels. Adapted from Lemen et al. (2012).

1.5.3.2 Helioseismic and Magnetic Imager

The SDO/HMI instrument maps the magnetic and velocity fields on the solar surface. The photospheric surface velocity is mapped across the solar disk by measuring the Doppler shift of the Fe I spectral line. To determine magnetograms, HMI uses the splitting of the spectral line of Fe I in the presence of a magnetic field (the Zeeman effect, section 1.1.3). The spatial pixel size is 0.5 arcsec and the cadence is 45 s, although a 12 minute average provides improved noise levels (Scherrer et al., 2012). The magnetograms can act as an input for coronal magnetic field modelling, for example, in Potential-Field Source-Surface (PFSS) extrapolations. A PFSS extrapolation is used in chapter 4.

1.5.4 Solar and Heliospheric Observatory

The Solar and Heliospheric Observatory (SOHO) is a spacecraft launched in 1995 as a collaborative mission from NASA/ESA, in orbit around the first Lagrangian point, providing an unobscured view of the Sun. The spacecraft includes twelve instruments to observe various aspects of the Sun such as EUV imaging, Doppler imaging, and a coronagraph. The latter is named the Large Angle and Spectrometric Coronagraph Experiment (LASCO, Brueckner et al., 1995), and currently provides two different coronagraphs labelled C2 and C3 (C1 is no longer operational) with overlapping fields of view, imaging the corona between 1.1–3 $R_{\odot}$, 1.5–6 $R_{\odot}$, and up to 30 $R_{\odot}$. This allows for tracking of large-scale structures as they propagate through the corona such as CME shock fronts. Data from LASCO is used in chapter 4.

1.5.5 Geostationary Operational Environmental Satellite

The Geostationary Operational Environmental Satellite (GOES) is a system of spacecraft in geostationary orbit, providing continuous imaging and atmospheric observations of Earth, as well as solar activity. GOES includes an X-ray instrument called the X-ray Sensor (XRS; Garcia, 1994) that measures the X-ray emission from the Sun. XRS consists of two detectors that measure different energy bands with wavelengths of 0.4–4 Å and 1–8 Å in real-time, corresponding to soft X-ray flare emission. The data is provided as 1 minute averages, and used in chapter 3.

2

Fine Structures and Spikes

Solar radio bursts often display fine structures embedded within or separate to broadband emission. The term fine structures is referring to the narrow spectral width and short time scales of such emission as observed in dynamic spectra. The structures are of interest to solar radio astronomy to help refine the emission process of solar radio bursts and improve our understanding of the coronal environment through which their exciter propagates. The following sections detail some of the different types of fine structure that were previously observed, along with their interpretation.

2.1 Type IIIb Striae

Type III bursts present as as smoothly drifting broadband emission (section 1.3.3), yet often there are numerous narrowband structures embedded within them called 'striae'. These fine structures have been observed as low as 20 MHz (Baselian et al., 1974; Melnik et al., 2010; Kontar et al., 2017b) to near 200 MHz (Stewart, 1975). When striae structures are present, the burst envelope is called a Type IIIb burst (de La Noe & Boischot, 1972). Figure 2.1 shows an example of a Type IIIb burst observed by LOFAR between 30–70 MHz, which has been well studied by Kontar et al. (2017b); Chen et al. (2018); Sharykin et al. (2018). Each distinct striae can be identified as a fluctuation of the Type III envelope intensity, in this case, peaking between 100–200 sfu. The lower panel shows the light curve of an individual striae at 32.5 MHz with a duration of 0.68 s. The figure shows the fundamental component where the striae are well defined, as well as the more diffuse and dimmer harmonic component where the striae are difficult to observe, if at all present. Typically, striae are visible in the fundamental, and rarely observed in the harmonic emission. Kontar et al. (2017b) show that the fundamental striae are 15% circularly polarised, whilst the harmonic is $< 5\%$, consistent with statistical observations of fundamental and harmonic Type III emission (e.g. Dulk & Suzuki, 1980).

The bulk frequency drift of the Type IIIb is typically a few to ten MHz s^{-1} (e.g. de La Noe

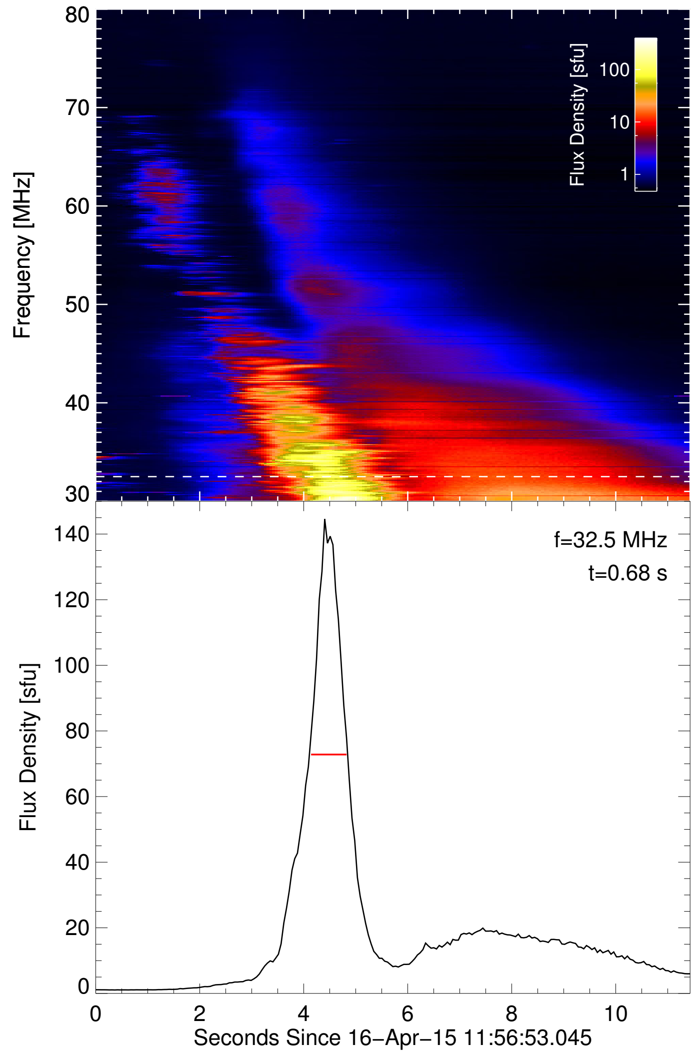

Figure 2.1: Dynamic spectrum of a Type IIIb burst observed by LOFAR between 30–70 MHz on 16-Apr-2015. The data is downsampled to a time resolution of 52 ms, and normalised to the background spectrum taken prior to the burst. The lower panel shows the light curve at 32.5 MHz where the red line denotes the FWHM striae duration. Data provided courtesy of E. Kontar, University of Glasgow.

& Boischot, 1972; Chen et al., 2018), similar to that of Type III bursts. On the other hand, in the decametre range, individual striae usually show much lower drift rates on the order of ten to hundreds of kHz s^{-1} (e.g. Baselian et al., 1974; Sharykin et al., 2018; Reid & Kontar, 2021), with bandwidths typically on the order of few tens to 100 kHz (de La Noe & Boischot, 1972; de La Noe, 1975; Melnik et al., 2010; Sharykin et al., 2018). The duration of type IIIb bursts, and individual striae, is shorter than the duration of Type III emission. For example, de La Noe & Boischot (1972) find Type IIIb durations on the order of 1–2 s, rather than 3–10 s for Type III bursts at similar frequencies (Aubier & Boischot, 1972). Similar short striae duration is shown in Figure 2.1 at 32.5 MHz.

Recently, Type IIIb striae source sizes have been observed with LOFAR. According to

Kontar et al. (2017b), a disk centred striae was found to be spherical in the sky-plane, with a peak area of 400 arcmin^2 at 32.5 MHz. Striae observations by Murphy et al. (2021) for sources located off-disk found a peak area of 150.6 arcmin^2 at 34.76 MHz with linear sizes of 18.8 and 10.2 arcmin; hence, the source was elliptical. These observed sizes are larger than estimations from the striae bandwidth, which is an indication of the distance the exciter has propagated whilst emitting. In consideration of this, Kontar et al. (2017b) noted that striae bandwidths of $\Delta f \sim 0.3$ MHz correspond to a distance of $\Delta r \simeq 2r_n(\Delta f/f) \simeq 4\times 10^8$ cm, where $r_n \simeq 2\times 10^{10}$ cm is the density scale height near 30 MHz (see section 1.3.3). This size extends over a solid angle of 10^{-2} arcmin^2, four orders of magnitude smaller than the observed areas. In addition, observations showed that areal expansion was most pronounced during the decay phase. Meanwhile, the fundamental centroid shifted radially by hundreds of arcsec, whereas the harmonic presented slower motion in no clear direction (Kontar et al., 2017b). These broadening and drift effects were suggested to be caused via anisotropic scattering (as described in section 1.4.1.1). The expansion and motion of the striae was replicated through anisotropic scattering simulations by Chen et al. (2020). Moreover, to reproduce the slower harmonic expansion rate and motion, the harmonic source required a finite time opposed to an instantaneous injection, which was suggested to be caused by time-of-flight spread of the electrons.

The emission mechanism of Type IIIb bursts is believed to be similar to that of Type III bursts which is plasma emission due to fast electron beam propagation and subsequent Langmuir growth (section 1.2.1). However, Type IIIb bursts exhibit modulation in intensity, resulting in the formation of the striae structures. In-situ observations have shown that the spatial distribution of Langmuir waves is clumpy rather than smoothly distributed (e.g. Gurnett & Anderson, 1976; Lin et al., 1981; Robinson et al., 1993; Chaizy et al., 1995). These clumps of Langmuir waves are thought to arise due to the background density fluctuations (e.g. Melrose et al., 1986), as Langmuir wave growth is promoted in regions of local density decrement (Figure 1.10). The clumps of Langmuir waves may then propagate as fast magneto-acoustic waves (Kolotkov et al., 2018). Simulations of Langmuir wave growth due to a propagating electron beam in an inhomogeneous plasma by Kontar (2001b) have shown that small scale density inhomogeneities of about 0.1% at a coronal height of 200 MHz can significantly alter the Langmuir wave spatial distribution, while the electron beam remains a continuous, smooth structure. Additionally, the Langmuir spectral energy density peaks in regions of density minima, with clump sizes related to the regional size of the negative density gradient—such coupling is illustrated in Figure 1.10. Therefore, the striae structures observed in Type IIIb bursts are expected to be visible at frequencies corresponding to the spatial regions where the Langmuir wave energy density peaks (Kontar, 2001b; Reid & Kontar, 2021).

The spatial distribution of the Langmuir waves changes due to the refraction induced by the background inhomogeneities (Melrose et al., 1986). This refraction can cause some Langmuir waves to move out of phase with the beam-plasma structure leading to energy loss from the system (Kontar, 2001b). Recent simulations by Reid & Kontar (2021) have revealed that the clumps of Langmuir waves drift at the group velocity v_{gr} of around 500–4000 km s^{-1} (0.0017–0.013c), which is substantially slower than the electron beam at $c/3$. This motion acts as the driver of the striae drift rates that are much lower than the Type IIIb bulk drift rate.

2.2 Drift Pairs

Drift pair bursts were first identified by Roberts (1958), described as a solar radio burst echo. Drift pairs are identified as two elements in dynamic spectra with the second a repetition of the first structure delayed by 1–2 s with no change in frequency; contrary to other drifting stripe emission such as Type II bursts (section 1.3.2). Each band has a narrow, instantaneous spectral width in the range of hundreds of kHz to a few MHz (Moller-Pedersen et al., 1978), described as 'sharp' for small bandwidths around 400 kHz, and 'diffuse' for larger bandwidths around 1 MHz. They typically cover a few MHz in total bandwidth (e.g. Melnik et al., 2005), with both positive and negative drift at rates of $\sim$1–8 MHz s^{-1} (Roberts, 1958; Melnik et al., 2005). Figure 2.2 shows numerous drift pair bursts between 30–70 MHz with both positive and negative drifts embedded within a Type III storm. The zoomed in panel highlights a single drift pair burst that was analysed in detail by Kuznetsov & Kontar (2019). Clear primary and echo components are both visible, with the lightcurve showing a slightly reduced intensity for the echo.

Both drifting directions present similar parameters in time delay, duration, and bandwidth (Melnik et al., 2005), although the reverse-drift bursts are typically more diffuse (Moller-Pedersen et al., 1978; Kuznetsov & Kontar, 2019). They occur at decametre frequencies between 10–100 MHz (e.g. Ellis, 1969; Melnik et al., 2005; Kuznetsov & Kontar, 2019) and are often associated with Type III storms (e.g. Melnik et al., 2005; Kuznetsov & Kontar, 2019), with each drift pair element typically sharing the same sense of polarisation as each other and the storm itself (Suzuki & Gary, 1979; McLean & Labrum, 1985). Imaging observations show that each drift pair element has similar position, and are approximately the same size, typically between 100–300 arcmin^2 (Suzuki & Gary, 1979; McLean & Labrum, 1985; Kuznetsov & Kontar, 2019). Moreover, Kuznetsov & Kontar (2019) show that each component propagates in the same direction over time at a given frequency, suggesting radio-wave scattering effects are at play as the radiation escape through the same region of turbulence.

Explanation of these structures has been explained in terms of either a single source or two correlated sources. An example of the latter by Moller-Pedersen et al. (1978) concerns magnetohydrodynamic (MHD) shocks propagating in opposite directions perpendic-

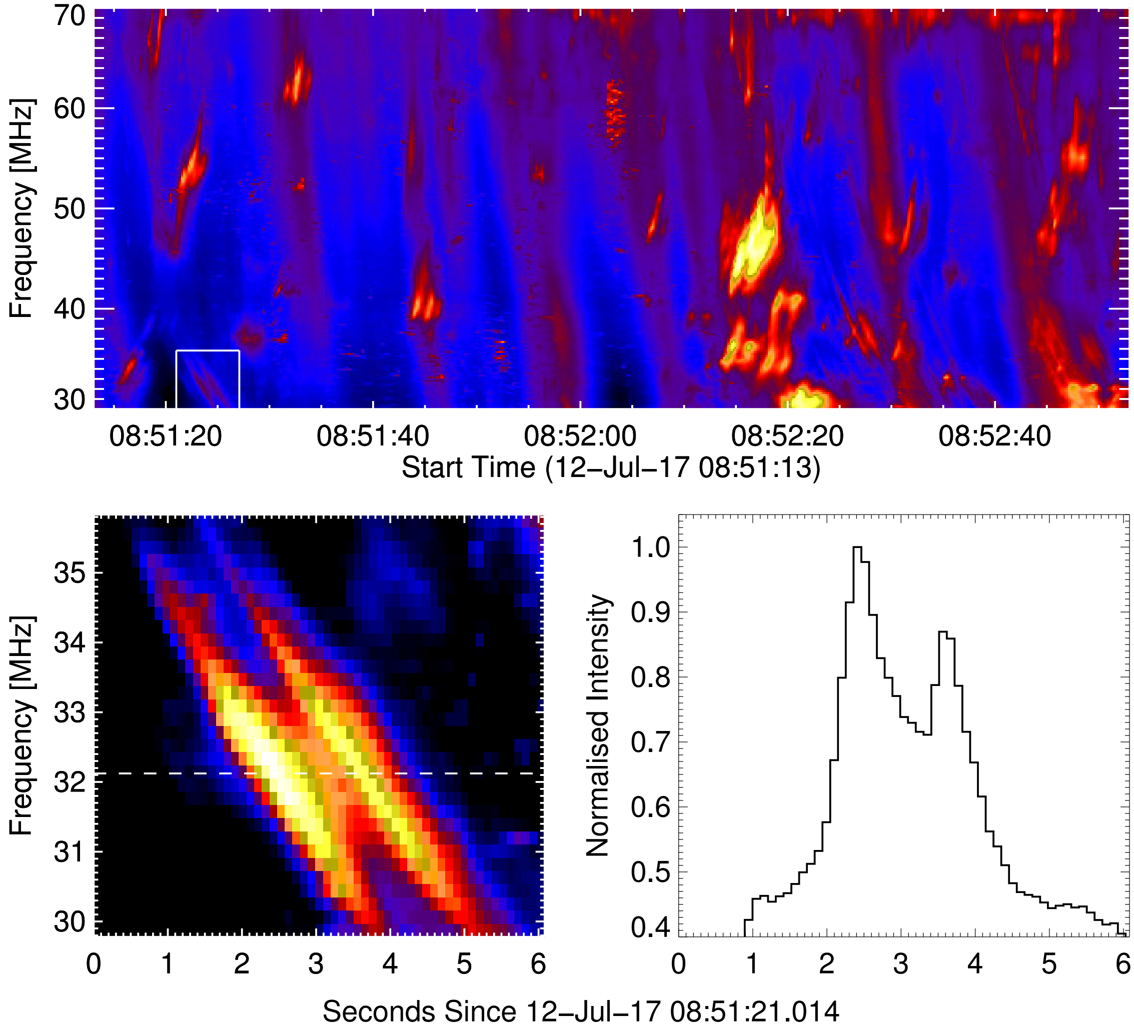

Figure 2.2: *Top:* Dynamic spectrum between 30–70 MHz observed by LOFAR on 12 July 2017 with numerous drift pair bursts visible. *Bottom left:* Zoomed in dynamic spectrum of a single drift pair burst of the region bounded by the white box in the top panel. *Bottom right:* Time profile along the dashed line in the lower left panel. The data are reduced to a time and frequency resolution of 0.1 s and 195 kHz, respectively.

ular to the magnetic field of a coronal streamer. However, the co-spatial observations of each component favours a single source producing both drift pair elements. Roberts (1958) has previously suggested a model where the second component is a radio echo—i.e. the emission is generated some distance away from a reflective layer (such as harmonic emission), and the radiation is received via two paths with different propagation times. These echoes were deemed possible by Jaeger & Westfold (1950) (considering 'double-humped' solar noise) where a ray would propagate to the observer with a time delay due to reflection from lower in the corona. However, Riddle (1974) suggest that a reflected ray shouldn't display the same spectral characteristics as the direct component since the radiation is scattered over a longer period than the direct ray, and the polarisation of drift pairs are more consistent with fundamental emission (Suzuki & Gary, 1979). A further complication noted by Roberts (1958) is that such an echo should be visible for other burst types too, which is not observed.

Recently, radio-wave scattering simulations with anisotropic turbulence were able to replicate the observed motion, size, source speed, and echo delay of drift pair bursts (Kuznetsov et al., 2020). The inclusion of anisotropic scattering provides high emission directivity, so when combined with a reflection will produce near exact echoes due to the focusing of the emission. The scattering simulation results by Kuznetsov et al. (2020) are also able to reproduce the fixed frequency source motion, as well as the decrease of the delay time between each component with emission frequency, in agreement with observations (Melnik et al., 2005). Kuznetsov et al. (2020) also show that the echo will only be observed if the decay time of the first component is short enough so that the echo is not 'absorbed' into the tail of the first. Consequently, drift pair bursts are likely associated with regions of strong anisotropy, which produces narrower emission peaks. This also explains why radio echoes are not observed for longer duration emission such as Type III bursts.

2.3 Spikes

Explosive solar events frequently produce a variety of radio signatures, e.g. Type II (section 1.3.2) and Type III (section 1.3.3) bursts, with some of these emissions further modulated with fine structures such as Type IIIb bursts (section 2.1). However, spikes are of particular interest due to their often observed independence from any other broadband emission and very short, impulsive lifetime. Spikes are the shortest radio signatures observed from the Sun usually < 1 s in duration at decametre frequencies, and milliseconds at decimetre frequencies and above. Therefore, they provide a valuable diagnostic to study the fastest processes in the solar corona. As detailed below, spikes are often suggested to be a manifestation of the energy release process itself (section 2.3.2), and can be a driver of certain space weather phenomena (section 2.3.3), yet their origin is not fully understood. Owing to their fine spectral widths and short durations, they pose a challenge in solar physics to resolve with instrumentation. With the addition of the latest high resolution telescopes, advances will begin to shed light on this interesting phenomena.

2.3.1 Previous Spike Observations

Solar radio spikes manifest as short duration (tens to hundreds of milliseconds) radio signatures with narrow spectral widths from $\Delta f/f \simeq 0.02\% - 1\%$ where f is the spike central frequency. They are observed over a few orders of magnitude in frequency from tens of megahertz (e.g. Barrow & Saunders, 1972; Barrow et al., 1994; Melnik et al., 2014; Shevchuk et al., 2016), hundreds of megahertz (e.g. Tarnstrom & Philip, 1972a; Chernov, 1977; Bakunin &

Chernov, 1985; Barrow et al., 1984; Guedel & Benz, 1990; Bouratzis et al., 2016) and gigahertz frequencies (e.g. Staehli & Magun, 1986; Benz et al., 1992b; Cliver et al., 2011; Krucker & Benz, 1994; Dabrowski et al., 2011; Chernov et al., 2012)—see Figure 2.3 for example spike observations across various frequency ranges. They are often distributed chaotically in dynamic spectra, and can be embedded within or near to other broadband burst types in time and frequency such as Type II (Armatas et al., 2019), Type III (Tarnstrom & Philip, 1972b; Barrow & Saunders, 1972) and Type IV (Bouratzis et al., 2016) bursts. Benz (1986) noted that spikes are most abundant between 300–3000 MHz, yet relatively fewer observations have been made at decametre frequencies.

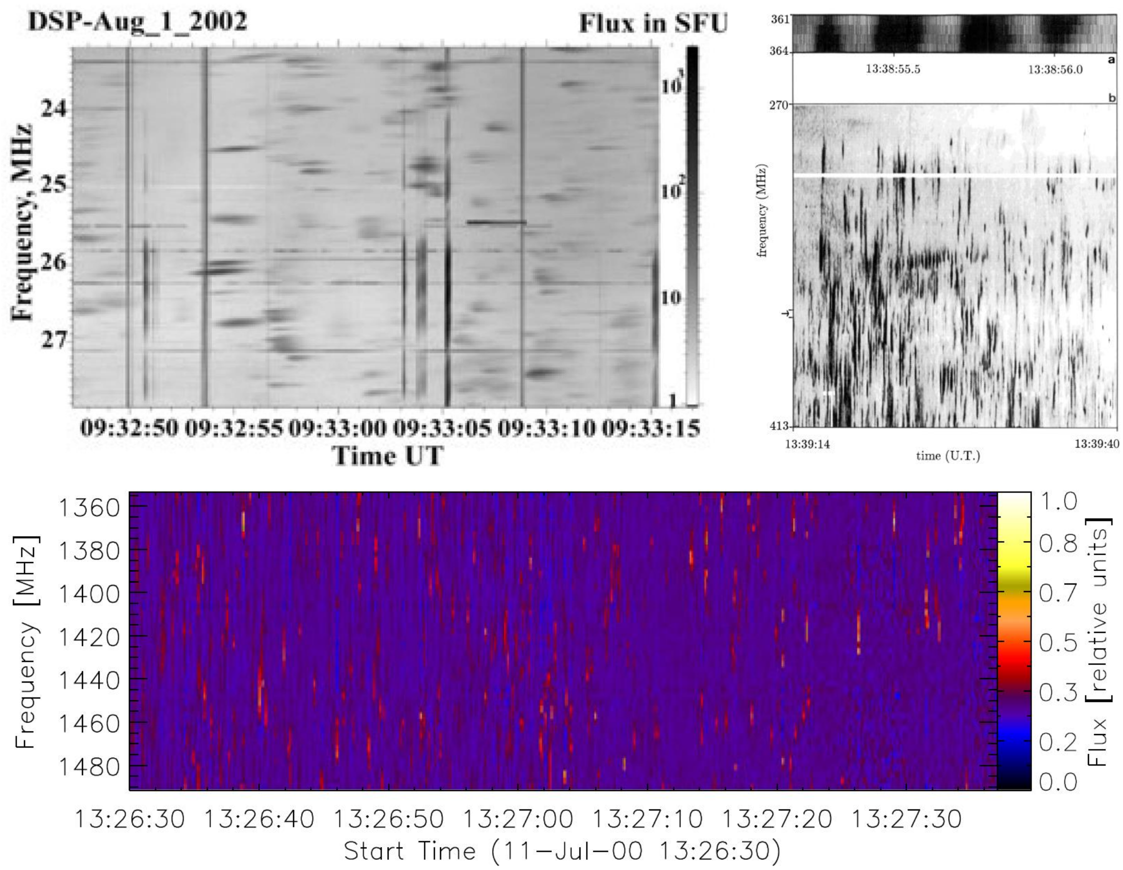

Figure 2.3: Example spike dynamic spectra observations at various frequency ranges. *Top left:* Decametric spikes between $23-28$ MHz observed with the UTR-2 radio telescope (Melnik et al., 2014). *Reproduced with permission from Springer Nature*. *Top right:* Decimetric spikes between $270-413$ MHz observed with the frequency-agile radio spectrometer IKARUS. The upper panel shows spikes between $361-364$ MHz with a 2 ms time resolution. Figure taken from Guedel & Benz (1990). *Bottom:* Decimetric spikes between $1360-1480$ MHz observed with the Toruń radio spectrograph (Dabrowski et al., 2011). *Reproduced with permission from Springer Nature.*

Spike characteristics as measured in dynamic spectra are typically defined as in Figure 2.4, which represents a frequency drifting spike with short duration and narrow bandwidth.

Specifically, the spike central frequency is defined as the centre frequency of the total spike bandwidth. The time profile is measured across the central frequency and calculated at the FWHM. The FWHM bandwidth is measured at the time of the peak defined along the FWHM time profile, and the drift rate is measured across the times and frequencies corresponding the FWHM duration. The spike characteristics used in this thesis for chapters 3 and 4 are measured according to this definition.

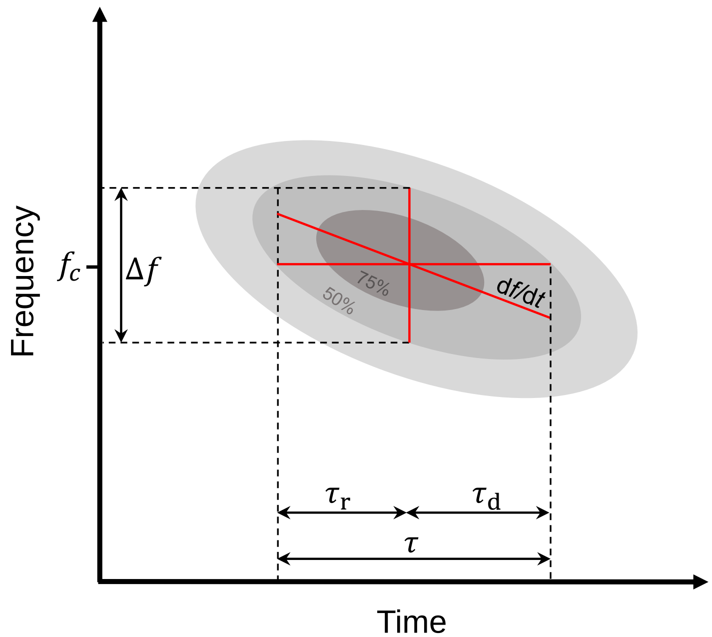

Figure 2.4: Cartoon showing spike burst characteristics as measured in dynamic spectra. The solid oval represents the total visible spike emission with central frequency f_c, with darker contours representing higher intensity at 50% and 75%. The red lines represent the duration (split into rise t_r and decay t_d separated at the peak intensity), bandwidth at the time of peak intensity, and drift rate as measured across the FWHM duration.

2.3.1.1 Duration

Spike durations τ are found to follow an inverse power-law as $\sim 1/f$. For example, Guedel & Benz (1990) find the duration at the $1/e$ level to vary with frequency as

$$\tau(f) \approx 0.0348 \left(\frac{f\,[\mathrm{MHz}]}{661} \right)^{-1.34 \pm 0.13} \mathrm{s}, \tag{2.1}$$

with a decay relation of

$$\tau_\mathrm{d}(f) = 0.0165 \left(\frac{f\,[\mathrm{MHz}]}{661} \right)^{-1.06 \pm 0.06} \mathrm{s}, \tag{2.2}$$

between 362–1010 MHz. Compared to Type III bursts (see equation 1.29), the spike decay times share the same trend yet are almost an order of magnitude shorter. Converting equation 1.29 from the FWHM level to the $1/e$ level by a factor of $1/\sqrt{\ln 2}$, the typical Type III decay time at 1 GHz is 74 ms, whilst using equation 2.2 for spikes gives 10 ms at the same frequency. At decametre frequencies near 30 MHz, the FWHM spike durations are observed to be < 1 s (Melnik et al., 2014). At 25 MHz, Shevchuk et al. (2016) present an average spike FWHM duration across three events of 0.6 s, with a rise time of 0.27 s and decay time of 0.32 s. At 35 MHz, these values are 0.43 s, 0.20 s, and 0.22s, respectively.

2.3.1.2 Bandwidth

The spectral shape of spikes is typically found to be Gaussian with a FWHM bandwidth Δf that varies with frequency. Csillaghy & Benz (1993) present a weak frequency dependence of

$$\Delta f = 0.66 f^{0.42}, \ \ 300 \text{ MHz} \le f \le 8.5 \text{ GHz}, \tag{2.3}$$

where f is in MHz. The data used are a compilation of observations from different events, with individual events presenting a spread of a factor of 2–3. The combined data are distributed over an order of magnitude at a given frequency; hence, the observed mean bandwidths differ significantly from event to event. At 1 GHz, equation 2.3 gives a bandwidth of ~ 10 MHz, or $\Delta f / f \simeq 1\%$, similar to the mean bandwidth of 9.96 MHz between 0.8–2 GHz found by Dabrowski et al. (2011). Csillaghy & Benz (1993) noted that the results suggest no intrinsic spike bandwidth, with the observed bandwidth dependent on the individual source parameters. At 300 and 900 MHz, Messmer & Benz (2000) report *minimum* observed bandwidth ratios of 0.4% (1.2 MHz) and 0.17% (1.5 MHz), respectively, which were close to the instrumental resolution (1 MHz) of the IKARUS spectrometer (Perrenoud, 1982). Rozhansky et al. (2008) investigate a spike cluster between 4.5–6 GHz, finding that the bandwidth distribution is asymmetrical. They use a deconvolution technique to decompose overlapping spikes within the cluster. The bandwidth distribution peaks at 0.6% with a tail approaching $\sim 3\%$. For context, the instrument (Purple Mountain Observatory (PMO); Xu et al., 2003) spectral resolution is 10 MHz, correlating to 0.13–0.2% across the observing frequency range. Between 18–29 MHz, Melnik et al. (2014) also find the bandwidth to increase with frequency, with a linear relation of $\Delta f \approx A f$, where f is in MHz and A varies from different events between 1.4×10^{-3} and 2.5×10^{-3}. This gives a range of 25–45 kHz at 18 MHz and 40–70 kHz at 29 MHz. At both frequencies, $\Delta f / f$ ranges between 0.14–0.24%.

2.3.1.3 Frequency Drift Rates

A range of fast and slow spike frequency drift rates are reported, as well as both positive (reverse-drifting) and negative. Early observations between 135–255 MHz by Tarnstrom &

Philip (1972a) categorised spikes into those with fast drifts where $\mathrm{d}f/\mathrm{d}t \geq 100$ MHz s^{-1}, medium drift with $\mathrm{d}f/\mathrm{d}t < 100$ MHz s^{-1}, and simple spike bursts with no apparent drift. The majority of spikes they observed were of the fast drift type, followed by those with no apparent drift. Between 190–220 MHz, Markeev & Chernov (1971) noted drift rates between 20–40 MHz s^{-1}. Spikes observed from 490–545 MHz by Elgaroy & Sveen (1979) where found to have average drift rates of -23 MHz s^{-1}. Between 0.8–2 GHz, Dabrowski et al. (2011) find average drifts of -776 MHz s^{-1}, and reverse-drifting rates of 1608 MHz s^{-1}. Whilst not calculated in the study, the decametre spike observations by Melnik et al. (2014) and Shevchuk et al. (2016) show very low drift rates of spikes between 18–42 MHz, with the latter study noting that spikes below 100 MHz tend to have low drift rates between 20–150 kHz s^{-1} or 'practically zero'.

2.3.1.4 Polarisation and Flux

Spikes are often observed with strong circular polarisation (e.g. Markeev & Chernov, 1971; Chernov, 1977, 1978; Slottje, 1978), although intermediate polarisation degrees that may change sense between spikes in a given event have been observed (Slottje, 1980; Benz et al., 1982), with average values later suggested between 25–30% (Benz, 1986). Chernov (1977) noted that spikes had the same sense of polarisation as a Type I burst in a particular event. Additionally, spikes associated with a Type III burst had strong circular polarisation, whilst the Type III itself had weak polarisation—an observation also noted by Benz et al. (1982); Paesold et al. (2001). Spike peak flux distributions have been observed to display exponential trends (Aschwanden et al., 1998; Mészárosová et al., 2000; Rozhansky et al., 2008) and power-law trends (Nita et al., 2008). The spike deconvolution method by Nita et al. (2008) is noted to do an improved job of recovering low amplitude spikes, such that the exponential flux distribution for the same data set in Rozhansky et al. (2008) could be an artefact of missing weaker spikes, thus producing a distribution with a concave form. There seems to be no clear dependence on spike flux with frequency: near 30 MHz, Melnik et al. (2014) report spike fluxes that don't exceed 200–300 sfu, and were often below 100 sfu, with no clear dependence on frequency. Similar values (20–100 sfu) were found by Shevchuk et al. (2016) at the same frequencies, and ~ 60 sfu by Benz et al. (1992b) up to 8.5 GHz, yet at 0.6 GHz, Droege (1977) report peak fluxes of 5×10^4 sfu, and 2.5×10^4 sfu at 1.4 GHz.

2.3.1.5 Sizes

Whilst solar radio spikes have been observed and studied in some detail in dynamic spectra, imaging observations of spikes are relatively sparse, and generally limited to imaging of spike clusters where individual spikes are not resolved. The available studies that provide two dimensional imaging of spikes have used either the Nançay Radio Heliograph (NRH) (Heyvaerts et al., 1978; Paesold et al., 2001; Benz et al., 2002; Khan & Aurass, 2006; Battaglia

& Benz, 2009; Bouratzis et al., 2016) at 164, 236.6, 327, and 432 MHz; the Very Large Array (VLA) at 0.333, 1.446, and 4.866 GHz (Krucker et al., 1995, 1997), and 1–2 GHz (Battaglia et al., 2021; Luo et al., 2021), or the Nobeyama Radio Heliograph (NoRH) at 17 GHz (Huang & Nakajima, 2005). One dimensional spatial imaging has been conducted using the Siberian Solar Radio Telescope (SSRT) at 5.7 GHz (Altyntsev et al., 1995, 1996), and the Owens Valley Frequency-Agile Interferometer at 1.4 and 2.8 GHz (Gary et al., 1991).

Few papers have managed to sufficiently resolve the spike source areas which can be below, or close to, the size of the instrumental beam. Moreover, the effects of radio-wave scattering will cause significant broadening of the sources, and so the reported source sizes lend themselves as upper limits only. One-dimensional observations constrain the source size upper limit to be $<$ 28 arcsec at 2.8 GHz (Gary et al., 1991), and 5–50 arcsec at 5.7 GHz (Altyntsev et al., 1995, 1996). They find that spike source sizes reach unexpectedly high values that increase towards the solar limb, and remain constant throughout the event with no dependence on the intensity. This centre-to-limb variation is explained by scattering of the radio-waves due to plasma turbulence, and is consistent with the broadening of compact sources observed through the corona (e.g. Bastian, 1994). Krucker et al. (1995) find an observed source size of 90 arcsec deconvolved from the instrument beam to 68 arcsec assuming a spherical source (this was necessary as the source ellipse was not resolved along the major axis). From recent VLA observations, Battaglia et al. (2021) use 2D Gaussian fits to spike images to provide a FWHM size of 20 arcsec at 1.1 GHz, although they note that this size should only be considered as a lower limit due to the larger instrument beam size of 60 arcsec, such that the spike sources are not spatially resolved. Clearly, there is a need for resolved imaging of individual spikes that will allow imaging spectroscopy observations to explore their evolution—this forms a major part of the work in this thesis within chapters 3 and 4.

2.3.1.6 Spatial Location

The majority of instruments are dedicated to fixed frequencies and thus have no ability to perform spectroscopy over broad frequency ranges that coincide with the bandwidth of the spike emission. Therefore, the imaging information provides a general snapshot of the events, without any specific detail in the motion of the spike sources across small spatial and temporal scales. Nevertheless, Gary et al. (1991) manage to localise the spike sources to a separate region to an underlying gyrosynchrotron radio burst source, with the spikes arising from the same one dimensional location to within ± 1 arcsec, even through the spikes showed rapid evolution of the sense and degree of polarisation. The spike source sizes were not well constrained, yet they could be located above an active region with strong magnetic field strength. Both Altyntsev et al. (1995) and Altyntsev et al. (1996) determine the height of the spike sources at 5.7 GHz to coincide with the that of a microwave continuum burst observed at the same time to within 12 arcsec at approximately 0.05–0.057 $R_\odot$ above the photosphere; although in some cases, the spike source centroids were shifted relatively by up to 10 arcsec.

From two-dimensional imaging, Krucker et al. (1995, 1997) found spike source heights to lie at $\sim 0.6\ R_\odot$ above the photosphere at 333 MHz. Whilst individual spikes are not spatially resolved, the centroid positions are stable within a region of $\sim$ 20 arcsec. The heights were estimated from magnetic field lines that crossed the spike sources in the projection from PFSS models, assuming that they were associated with the nearby active region. The spike sources therefore occurred near open field lines, although in the later study, Krucker et al. (1997) note the possibility of weak-field loops cannot be dismissed due to suppression below 20 G in their PFSS code. Even so, the spikes were connected to regions of enhanced SXR flux relative to the ambient plasma. At NRH frequencies, Benz et al. (2002) found the spike sources to be 20–400 arcsec away from the flare site, and generally located near loop tops. They noted that on some occasions, different clusters of spikes from the same event were spatially separated by up to 140 arcsec. Khan & Aurass (2006) found decimetric spikes to be located a distance of 167 and 210 arcsec above X-ray sources of a near-limb flaring region. They were able to place the spike emission region near the site and time of magnetic loop compression induced along the flank of a CME as it expanded outwards. Decimetric spikes were also associated with a CME by Battaglia & Benz (2009). They report the average centroid positions of the decimetric spikes were displaced from the SXR and HXR emission associated with the flaring site by 79–97 arcsec, and a distance of 108–137 arcsec from the loop foot-points, giving a projected height of the radio sources above the limb of 0.056 $R_\odot$ at 432 MHz, and 0.079 $R_\odot$ at 327 MHz. Additionally, Bouratzis et al. (2016) found a separation between the SXR flare and the spike radio source to be 100 arcsec at 432 MHz, and 240 arcsec at 164 MHz. Recent VLA imaging spectroscopy of a spike cluster by Luo et al. (2021) show that the burst centroids form a 10 arcsec long structure in frequency-space across the corona, 60 Mm above the flare arcade where many plasma down-flows are present. There is a gradual movement of the structure towards lower frequencies. The observations suggest that the spikes are located above the loop top, in conjunction with the region where a termination shock could form, at a radial height above the solar surface of 120 arcsec. It seems that spike imaging observations at decimetric frequencies place the source location some distance from the flaring site, suggesting that they do not originate from X-ray flare sources.

2.3.2 Spike Origins & Emission Theory

The origin of spike emission is not fully understood. As noted above, in some cases spikes are associated with Type III bursts with the spike cluster appearing at frequencies higher than the starting frequency of the Type III, or in some cases below. Benz et al. (1982) suggest that spikes arising at frequencies higher than the Type III starting frequency could be a signature of the acceleration process. In this case, the acceleration may occur in numerous small sites, a concept further developed in Benz (1985). In this scenario, the spike emission is thought to originate in close proximity to the energy release region. Consequently, the fragmentation or discontinuous energy release in this region may be responsible for the fragmentation of the spike exciter. However, Fleishman & Mel'nikov (1998) argue that the appearance of spikes is not directly due to the primary fragmentation, but due to secondary fragmentation that results from magnetic field inhomogeneities. At decametre frequencies, such an inhomogeneity could be density fluctuations that act as the catalyst for spike generation associated with plasma emission in a given region (Benz et al., 2009). Such magnetic and density inhomogeneities are shown to affect the spectral properties of ECM emission by Fleishman (2004b), with typical bandwidth values found to be consistent with that of spike observations. Since the localisation of spike emission as discussed in section 2.3.1.6 tends to place spikes away from the flaring region, Benz et al. (2002) suggest that the spike sources could be associated with secondary, post-flare acceleration sites high in the corona. The observations by Khan & Aurass (2006) are supportive of this in the context of magnetic field compression along the CME flanks.

Between 400–1000 MHz, Benz (1985) also noted that the spike bandwidths suggest a source dimension equal to $l = L_{\mathrm{B}}\Delta\omega/\omega \leq 200$ km, where $L_{\mathrm{B}} \sim 10^4$ km is the magnetic scale length—an order of magnitude smaller than the size derived from the spike durations. The appearance of spike clusters across a range of frequencies suggests that the energy release occurs across many different sites, each releasing energies on the order of 10^{26} erg. In the events considered, there are on the order of 10^4 spikes, meaning a similar number of energy release sites occurring over tens of seconds (Benz, 1985). Temporal association of spike emission in time with HXR flare emission (e.g. Guedel et al., 1991) may then suggest that a flare could be comprised of an ensemble of 'micro-flares' (Benz & Aschwanden, 1992), and that radio emission in the form of spikes is a manifestation of such a process.

The high brightness temperatures of spike emission suggest a coherent emission mechanism. Whether ECM or plasma emission is suggested can depend on the region (frequency) at which the spikes are observed. Given the requirement for ECM emission requires a strong magnetic field (section 1.2.2), below 100 MHz it is difficult to reconcile such a mechanism for spikes, even for some of the most powerful events recorded, as Cliver et al. (2011) noted in regards to the 6 December 2006 event discussed in section 2.3.3. As such, high frequency (decimetric) spike emission is typically attributed to ECM emission (e.g. Melrose & Dulk, 1982; Benz et al., 1992b; Cliver et al., 2011), although this is not always the case (see Krucker et al., 1995, for example), whereas low frequency (decametric) spikes are associated with plasma emission (e.g. Tarnstrom & Philip, 1972b; Melnik et al., 2014). Concerning plasma emission, Tarnstrom & Philip (1972b) suggest that the acceleration of weak electron beams with low densities between 1–10 cm^{-3} and small spatial sizes less than $10^3 - 10^4$ km could produce spike emission, rather than Type III emission. This proposal is consistent with observations of spikes and Type III sources arising from the same region of energy release (Krucker et al., 1995).

Tarnstrom & Philip (1972b) compared the short spikes durations to the plasma collision time using the approximation

$$\tau_{\rm coll}(f, T_e) \approx \frac{1.92 \times 10^3 T_e[\mathrm{MK}]^{3/2}}{f[\mathrm{MHz}]^2} \ \mathrm{s}, \tag{2.4}$$

shown in Figure 2.5 for 0.5–8 MK. Whilst such an assumption for Type III bursts would require very high coronal temperatures ($\sim 10^7$ MK), the similarity to spike durations between 1–2 MK led to suggestions that their short duration was the result of damping in the plasma (McKim Malville et al., 1967; Tarnstrom & Philip, 1972b; Melnik et al., 2014). However, whilst the temperatures are consistent with that expected in the corona, the slopes are not exactly the same in Figure 2.5. This could be due to a multi-thermal corona or there could be an additional, underlying factor that governs the time profile.

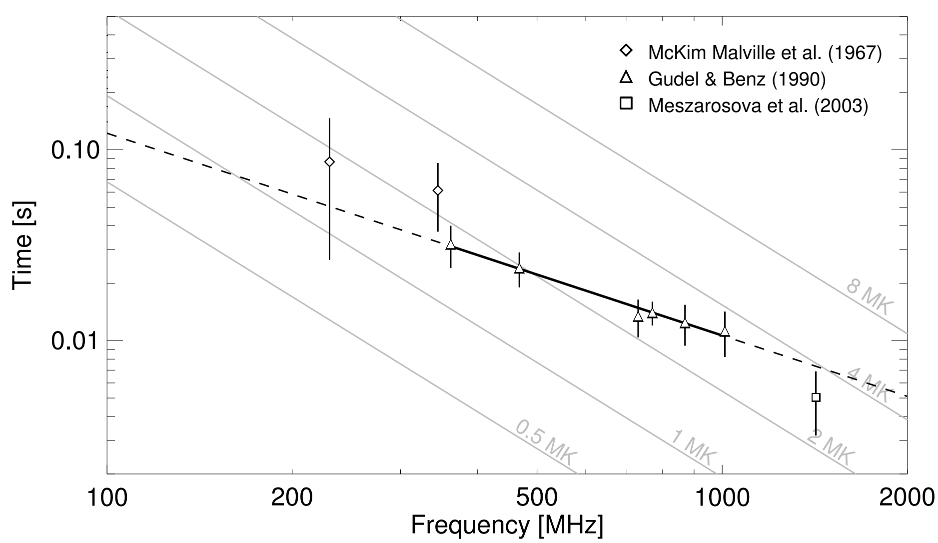

Figure 2.5: Plasma collision time as given by equation 2.4 for coronal temperatures between 0.5–16 MK. Average spike decay $1/e$ decay times are overlaid from McKim Malville et al. (1967); Guedel & Benz (1990); Mészárosová et al. (2003). The solid black line denotes the fit to the data by Guedel & Benz (1990) given by equation 2.2. The black, thick line denotes the observed frequencies, and the dashed line an extrapolation.

2.3.3 Radio Jamming

Radio jamming refers to interference with wireless communication which can be achieved through the presence of other radio signals that decrease the signal-to-noise (SNR) ratio.

Among the first published reports of solar radio emission concerns the jamming of military radars between 50–75 MHz (Hey, 1946). The radiation was described to be '...continuous, with some variations of intensity...' that '...extended over the whole receiver tuning range of about 4–6 metres'. The disturbance was always located to within a few degrees of the Sun from measurements at various sites throughout the United Kingdom. Such communication interference has been attributed to solar radio bursts on many occasions, particularly causing disruption to the GNSS (Chen et al., 2005; Cerruti et al., 2008; Carrano et al., 2009; Afraimovich et al., 2009; Kintner et al., 2009; Demyanov et al., 2012; Sreeja et al., 2013; Muhammad et al., 2015; Sato et al., 2019), and wireless communications (Bala et al., 2002; Redmon et al., 2018; Marqué et al., 2018).

The maximum power flux density allowed for satellite communication is set by the International Telecommunication Union (ITU) regulations (ITU, 2020), and varies with frequency and elevation angle. At low gigahertz frequencies, this threshold is set to near -142 dBW m^{-2} within any 4 kHz frequency band, also styled as dBW/(m^2 4kHz), between 25–90° with specific values given in small frequency ranges. At lower angles, this value may decrease by $\sim 10\%$. For context, Earth's surface temperature of $T_\oplus \simeq 273$ K correlates to a thermal noise of $L_P = 10\log_{10}(P/P_0) = -168.21$ dBW/(m^2 4kHz) where $P = k_B T_\oplus \Delta f$ for a bandwidth $\Delta f = 4$ kHz and using a reference power of $P_0 = 1$ W.

The impact of excess radio noise on GPS receivers was hypothesised by Klobuchar et al. (1999). They noted that a sufficiently large solar radio burst could raise the background noise level, decreasing the SNR of GPS signals. This is often measured using the carrier-to-noise ratio $C/N_0 = C/(N_0 + W)$, where C is the carrier power of the satellite signal, N_0 is the system noise level, and W is the wideband noise power from the solar radio burst in sfu (Cerruti et al., 2008). Following Klobuchar et al. (1999), the equivalent system noise power of a typical GPS receiver is

$$P_n = k_B T_{\text{sys}} \tag{2.5}$$

where k_B is the Boltzmann constant in decibels with a value of -228.6 dB. Using a GPS antenna system temperature of $T_{\text{sys}} \simeq 513$ K or 27.1 dB gives $P_n = -201.5$ dBW Hz^{-1}. GPS receivers have low gain ($g = 1$ dB) and a correspondingly small effective antenna area of

$$A_\text{e} = \frac{g\lambda^2}{4\pi}. \tag{2.6}$$

At the L1 frequency of 1575 MHz (wavelength $\lambda = 0.19$ m), $A_{\text{e,L1}} = 3.62 \times 10^{-3}$ m$^2 = -24.4$ dB m^2. Thus, the flux density required to reach the antenna noise floor is $I = -201.5 + 24.4 = -177.1$ dB m^{-2} Hz^{-1}. Considering that 1 sfu $= -220$ dBW Hz^{-1}, then $I = 42.9$ dB sfu. For a solar radio burst to meet the GPS noise floor at the L1 frequency, it would require a flux density at Earth of $I = 10^{42.9/10} \simeq 2 \times 10^4$ sfu. (note that more recent system noise temperature estimates are approximately 260 K (e.g. , xxx) leading to $I \simeq 10^4$ sfu). Klobuchar et al. (1999)

also note that GPS receivers are generally right hand circularly polarised, and their value of I is doubled to 4×10^4 sfu and noted to be the value that would have a 'just noticeable' effect on a GPS receiver, correlating to a C/N_0 reduction of 3 dB. A more severe reduction of 10 dB would require a flux density of 2×10^5 sfu. Further, Chen et al. (2005) suggest the threshold depends on the type of receiver—when using codeless or semi-codeless dual-frequency GPS receivers that do not require the signal code, a lower threshold of 1.2×10^4 sfu should be adopted. This limit was also calculated to be 1.03×10^4 sfu by Cerruti et al. (2006). According to Demyanov et al. (2012), different solar flux density limits apply to GPS and GLONASS. For codeless GPS receivers, they suggest that L2 signal failures are expected at solar flux densities exceeding $\sim 4 \times 10^3$ sfu and $\sim 10^4$ sfu at L1, while for GLONASS, the limit is higher at 10^4 sfu and 1.35×10^4 sfu at L1 and L2, respectively.

A statistical study by Bala et al. (2002) used 40 years of solar radio burst data to present the peak solar radio burst flux distribution over multiple solar cycles. They noted that the number of bursts per day with flux densities $> 10^3$ sfu forms an approximate power-law between 1–10 and 10–20 GHz, occurring approximately every 10–20 days. During solar maximum periods, it's reported that several solar events per year may occur that cause severe interference in wireless cell sites. Using the same data set and accounting for missed events, Nita et al. (2002) suggest the average occurrence rate is every 3.5 days at solar maximum, and 18.5 days at solar minimum.

On 6 December 2006, a significant radio burst associated with an X6-class solar flare near 18:40 UT (Balasubramaniam et al., 2010) caused significant disruption of GPS signals in the sunlit hemisphere. The flux density within the L-band (1.0–1.6 GHz) varied between $\sim 10^3 - 10^6$ sfu with the peak of 10^6 sfu at 1.4 GHz near the GPS L1 frequency which was recorded by the Owens Valley Solar Array (OVSA) near 19:30 UT (Cerruti et al., 2008; Kintner et al., 2009). This was the strongest flux recorded at this frequency. Moreover, and unexpectedly, this powerful burst manifested during solar minimum. The substantial flux density occurred after the flare impulsive phase and was associated with the evolution of a post-eruption loop system (Cliver et al., 2011). Indirect evidence of a CME was noted by Balasubramaniam et al. (2010) due to impulsive magnetic field change in magnetographs, and was suggested to be the driver of a Moreton wave (shock wave) across the solar surface. The emission appears broadband between 1–5 GHz, yet there is rapid variation of flux intensity (Cerruti et al., 2008). Indeed, observations using the Frequency Agile Solar Radio Telescope Subsystem Testbed (FST; Liu et al., 2007) which uses three modified antennas of OVSA recorded hundreds of millisecond radio spikes per second between 1.0-1.5 GHz, with each less than 20 ms in duration (Cliver et al., 2011). When observed with low resolution instruments, such a rapid ensemble of spikes can appear like continuous, broadband emission, particularly if the individual spikes overlap in time and frequency. Figure 2.6 shows the FST dynamic spectrum over small time intervals where a vast number of millisecond duration, right-hand polarised intensity peaks form the broadband emission. During the earlier phase (upper panel), the spikes overlap and are difficult to identify. However, ten minutes after (lower panel) the number of spikes per second has reduced and are individually identifiable. The decimetric spikes in this event were suggested to be produced via ECM emission from electrons trapped in the post-eruption loop system (Cliver et al., 2011).

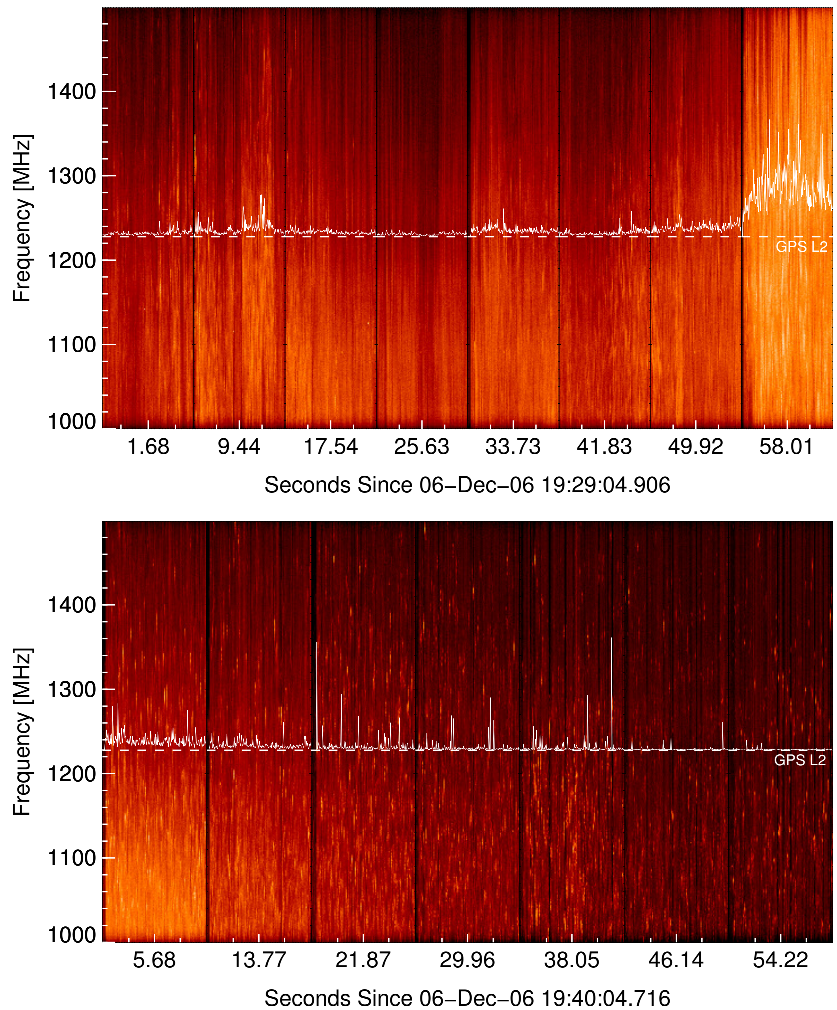

Figure 2.6: Dynamic spectra observed by FST on 6 December 2006. Each vertical panel is right-hand circularly polarised and 4 s in duration, separated by a 4 s left-land circularly polarised data which are not shown. The x-axis labels are centred within each spectra, with the preceding and following minor tick marks 1 s apart. The horizontal dashed lines show the L2 GPS frequency (1227.7 MHz), with the intensity at this frequency channel overlaid. Data provided courtesy of D. Gary, New Jersey Institute of Technology.

Investigating the impact on GPS receivers, Cerruti et al. (2008) use data from the ZHU1 Federal Aviation Administration (FAA) Wide Area Augmentation System (WAAS) receiver and report severe drops in C/N_0 over a period of 30 minutes, with the largest degradation aligned with the time of peak burst intensity near 19:30 UT (see the right hand side of the upper panel of Figure 2.6). Measurements from the previous day at the same time during a quiet period of solar activity shows an average C/N_0 at L1 of $\sim$ 52 dB, compared to 35 dB near the burst peak. In comparison, the L2 C/N_0 was reduced from ~ 45 dB to ~ 25 dB. The signal degradation at both frequencies is oscillatory and rapid. They note that the largest 17 dB C/N_0 reduction at the L1 frequency '...would endanger the operation of many GPS receivers, and similar fades were observed at all sunlit WAAS receivers'. Using their estimated minimum flux density of 1.03×10^4 sfu to meet the GPS receiver noise floor, they suggest that a 17 dB reduction would equate to a radio burst of 5×10^5 sfu. Similarly, the largest L2 reduction was 18–20 dB correlating to $\sim 6.5 \times 10^5$ sfu, although it's noted that this may be underestimated as tracking C/N_0 below 30 dB is problematic. A direct impact of such GPS signal loss across the sunlit hemisphere meant that many receivers were tracking fewer than four satellites and so were unable to obtain accurate tracking data (Cerruti et al., 2008). An additional study by Carrano et al. (2009) reported complete loss of lock of GPS positioning information for several minutes, and peak positioning errors of 20 m and 60 m in the horizontal and vertical directions, respectively. The theoretical burst flux density limits suggested by Demyanov et al. (2012) were found to be associated with L1 and L2 loss of signal lock when the radio flux exceeded just 10^3 sfu during the 6 December burst.

It should be noted that this event was not isolated to 6 December; in fact, the same active region produced further GPS signal disruption following solar radio burst activity on 13 and 14 December. Although the impact was less severe, Afraimovich et al. (2009) reported partial disruption of GPS positioning in the sunlit hemisphere for 12–15 minutes on 13 December attributed to the wideband solar radio noise that reached $\sim 10^5$ sfu, observed by the Nobeyama Radio Polarimeters in the L-band. They also noted that GPS failure depends on the Sun zenith angle—at high zenith angles, a greater number of signal failures are present.

With the rise of modern radio telescopes with improved spectral and temporal resolution, solar radio observations are increasingly displaying fine structures within broadband emission. Observations of a radio burst on 4 November 2015 using the Humain Solar Radio Spectrometer (HSRS) between 300–3000 MHz with frequency and time resolution of 98 kHz and 0.25 s, respectively, presented broadband radio emission between 600–1400 MHz peaking at 10^5 sfu with a significant number of fine structures that appear as pulsations, spikes, and fibre bursts (Marqué et al., 2018). Figure 2.7 shows the dynamic spectrum of the burst. The lower panels show numerous short duration fine structures over 100 MHz in bandwidth that overlap to form the broadband emission. The burst occurred after the impulsive phase of the flare around 30 minutes after the soft X-ray peak, similar to the 6 December 2006 burst, and is associated with fast evolving magnetic field activity (Marqué et al., 2018). The radio emission was linked to coherent processes, suggested to be ECM emission. The emission correlated in time with radar disturbances of air traffic control (ATC) across Europe. Several critical radar systems are employed by ATC. As detailed by Marqué et al. (2018), in order to locate aircraft, the time difference of an emitted radio signal received after reflection off the aircraft operates in the L-band. To gain additional information about the aircraft, coded queries are sent by radar at 1030 MHz (uplink) and 1090 MHz (downlink). Additional radio requirements in the VHF band are used by pilots to operate the aircraft in poor visibility in order to align with the appropriate descent approach. Marqué et al. (2018) report that Belgian ATC observed false echoes that represented non-existing planes in the direction of the Sun between 14:19–14:33 and 14:45–14:49 UT, corresponding to the time of enhanced radio emission observed by HSRS near 1 GHz. Additionally, Swedish radar systems could not display correct information to ATC beginning at 14:19 UT, leading to partial closure of their airspace.

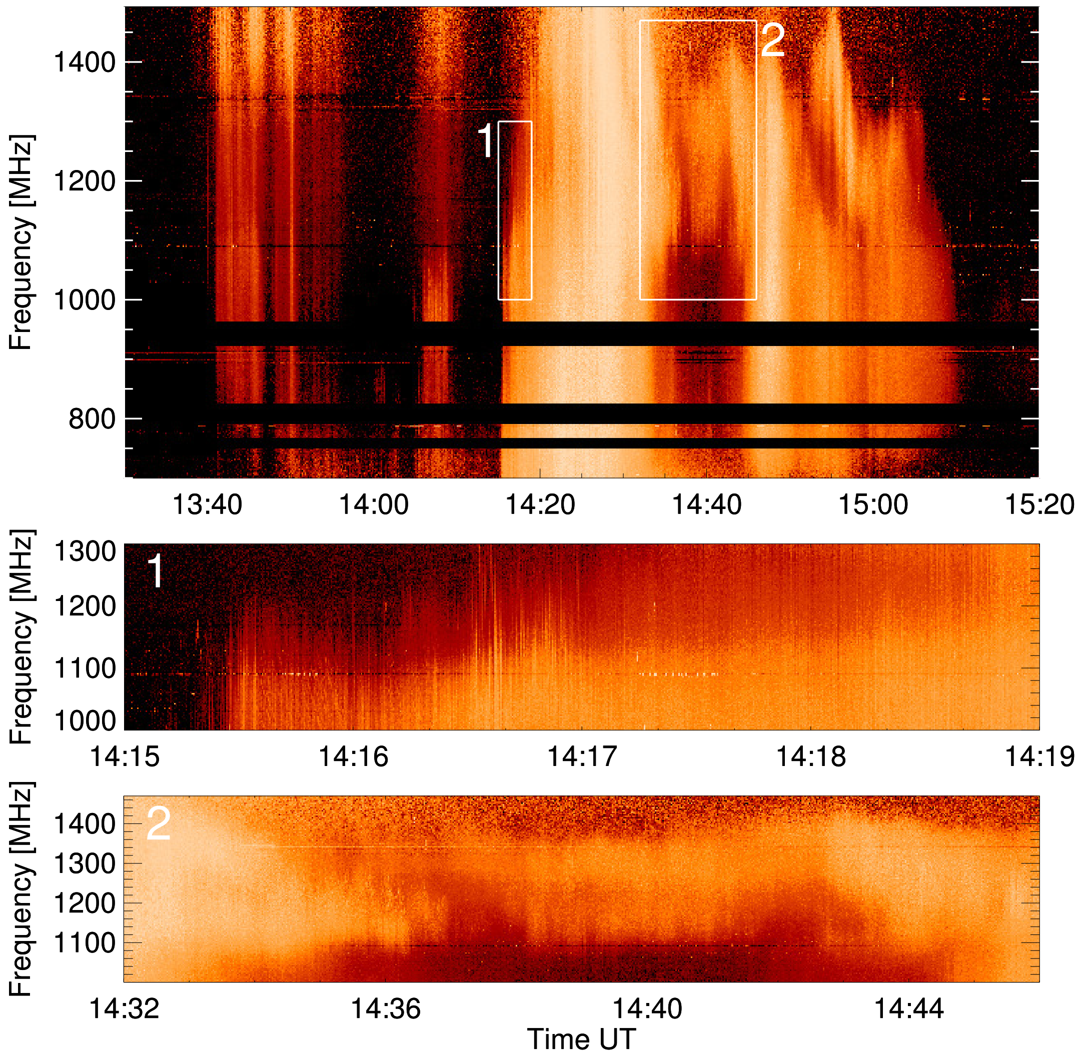

Figure 2.7: Dynamic spectra observed by HSRS on 4 November 2015, with the background subtracted. The horizontal black stripes are bands of RFI that have been removed. The white boxes show the zoomed in regions in the lower panels. Data provided courtesy of C. Marqué, Royal Observatory of Belgium.

2.4 Conclusion

The observations of fine structures in solar radio emission can provide crucial insights into the underlying emission process and the dynamics of the coronal environment. These structures, such as striae and drift-pair bursts, can reveal important information about the plasma dynamics in the solar corona. However, it is important to note that these small-scale structures are often modulated by various radio-wave propagation effects, which can complicate their interpretation and analysis.

One particularly intriguing phenomenon in solar radio emission is the occurrence of radio spikes. These spikes represent the fastest processes in the corona and thus offer unique diagnostic potential for understanding the underlying physics of particle acceleration and energy release. However, despite decades of research, the exact mechanisms responsible for the generation of radio spikes are still not fully understood. Furthermore, the rapid and unpredictable nature of spike bursts poses a potential threat to communication systems on Earth. Therefore, it is important to have new observations using advanced instrumentation to better understand their origin and behaviour. In particular, resolved imaging observations of individual spikes would provide a powerful tool for studying the spatial and temporal evolution of these structures.

Overall, the study of fine structures in solar radio emission, including radio spikes, is crucial for advancing our understanding of the dynamics and physics of the solar corona, as well as for improving our ability to predict and mitigate the potential impact of these phenomena on Earth.

3

Frequency-time-resolved Imaging of Decametre Solar Radio Spikes

These results were published in Clarkson et al. (2021).

Section 2.3 presents a wide range of solar radio spike observations, however, the detailed evolution of individual spikes in time, space and frequency have not been reported in the literature before. In this chapter, the frequency and time-resolved evolution of individual radio spikes is presented using LOFAR imaging to track the spike source motion over time between 30–45 MHz. The observations reveal superluminal source motion and source size expansion at 100 ms scales consistent with strong anisotropic scattering of radio-waves in a turbulent corona. The results also confirm not only the similarity of the observed spike properties with Type IIIb striae, but the co-spatial character of the Type IIIb and spike sources.

3.1 Overview of the Observations

The active region responsible for the emission is labelled AR12665, and located on the western solar limb. A C1.4 class solar flare erupted from this active region between 10:50 to 10:55 UT on 15 July 2017, with the ejection of a jet that was well analysed by Chrysaphi et al. (2020). The jet is bifurcated into two components which Chrysaphi et al. (2020) estimated to propagate at speeds of ~ 650 km s^{-1} and ~ 660 km s^{-1}. Figure 3.1 shows the soft X-ray flux recorded by GOES in panel (a), the radio flux dynamic spectrum between 30–70 MHz observed by LOFAR in panel (b), and polarisation dynamic spectrum observed by NDA/MEFISTO in panel (c) during the eruptive event. The degree of polarisation P_d is given by $P_\mathrm{d} = (P_\mathrm{r} - P_\mathrm{l})/(P_\mathrm{r} + P_\mathrm{l})$, where P_r and P_l are right and left hand circularly polarisation, respectively. The GOES lightcurves show three peaks, with the latter two strongly correlating with the onset of the two jet components with a gap between each jet of around two minutes (Chrysaphi et al., 2020)—in Figure 3.1(a), the jet onset times are shown by the two vertical dashed lines, shortly after two of the X-ray peaks. The brightest feature in the radio dynamic spectrum is a series of Type III bursts that overlap below 40 MHz, and occur during the rise of increased X-ray flux. A Type II burst is visible near 11:03 UT drifting between $\sim$ 55 MHz to 30 MHz which signifies the presence of a CME that was analysed in detail by Chrysaphi et al. (2020), and further discussed in chapter 4. Throughout the event are many Type IIIb bursts, too short in time to be apparent in Figure 3.2(b), as well as numerous short duration intensity points that are clusters of spikes. Some spikes are chaotically distributed in the spectrum, whilst others form chains similar to Type IIIb bursts. The lower panels (d–f) show the polarisation lightcurves at 34.5 MHz for the Type III, Type II, and two examples of spikes (the spikes are too short in time to be visible in the one hour NDA polarisation overview). All three burst types are left hand circularly polarised—the Type III and Type II bursts with a degree of approximately -0.4 and -0.2, respectively, and the spikes slightly weaker at around -0.15 and -0.1.

43 isolated solar radio spikes between 10:40 to 11:36 UT are analysed using LOFAR tied-array beam-forming mode (van Haarlem et al., 2013) using 24 core Low Band Antenna stations in the outer LBA configuration as described in section 1.5.1.2. The temporal and spectral resolution of 10 ms and 12.2 kHz enabled spikes with durations <1 s and spectral widths greater than $\sim$24 kHz to be individually resolved. The spike observations were temporally decreased in resolution to 20 ms to reduce noise at the intensity peaks. The flux was calibrated using observations of Taurus A (section 1.5.1.4). A single beam at the northern outer edge recorded no data, and was discarded during analysis.

Figure 3.2 shows zoomed-in versions of some of the fine structures. Panels (b,e) show examples of two Type IIIb bursts with starting frequencies of 40 MHz and 47 MHz, that drift down to at least 30 MHz. The flux density of individual striae for each burst peaks near 100 and 200 sfu. Panel (c) shows a cluster of spikes over a period of 10 seconds. The spikes appear sporadically over a range of 10 MHz, with maximum flux just tens of sfu, and many weaker spikes below 10 sfu. A single, isolated spike is shown in panel (d) covering 10 frequency channels and hundreds of temporal points. Each frequency-time point can be used to create a radio map, allowing the first resolved imaging spectroscopy of individual spikes as detailed below.

3.2 Measurement of Fine Structure Characteristics

The characteristics of the individual spikes are described below for the duration, bandwidth, frequency drift rate, area, and centroid motion, following the definition provided in Figure 2.4. For each parameter, the single spike displayed in Figure 3.2(d) is used an example, as shown in Figure 3.3. These methods also apply to the determination of individual striae

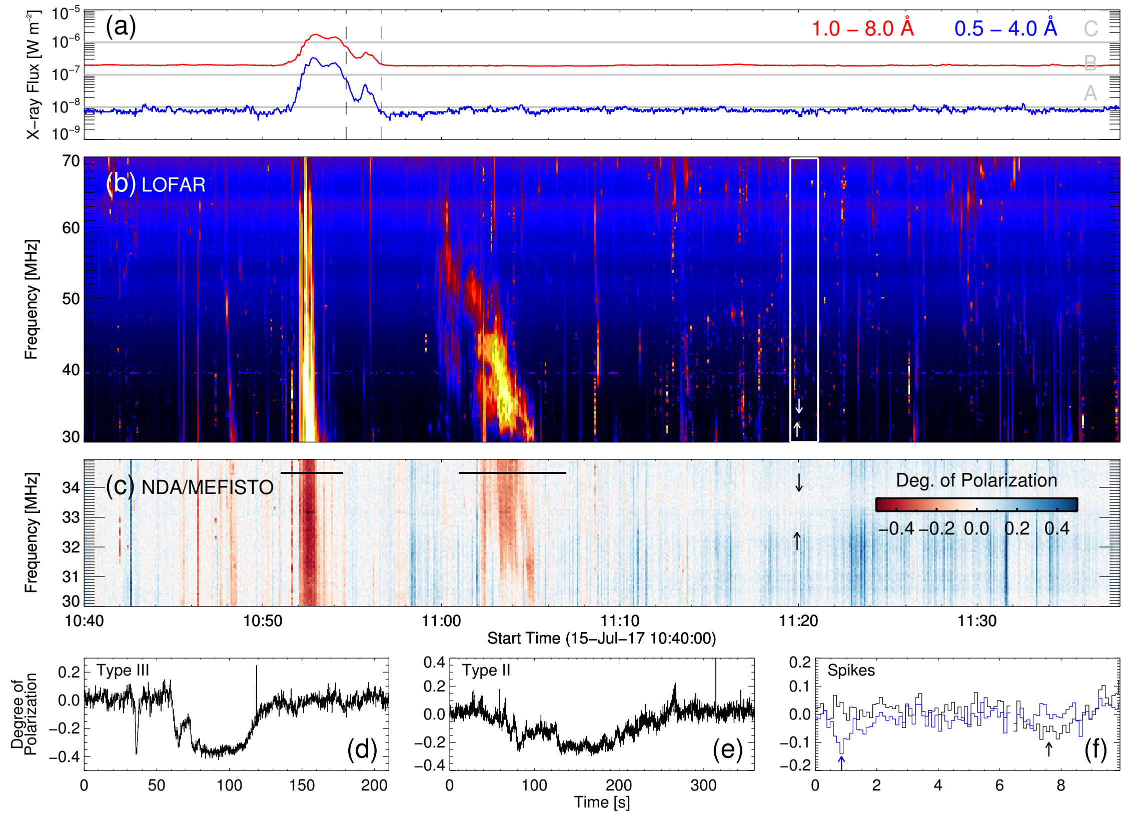

Figure 3.1: X-ray and radio emissions between 10:40 and 11:40 UT. **(a)** X-ray lightcurves from the GOES spacecraft (Garcia, 1994). The vertical black dashed lines represents the jet onset times as given by Chrysaphi et al. (2020). **(b)** Dynamic spectrum of the LOFAR observation. A series of bright Type III bursts can be seen near 10:52, with a Type II burst near 11:03. Spikes are distributed across the dynamic spectrum with a cluster between 11:10 and 11:21. The white box represents the region shown in Figure 3.2(a). The two white arrows show the locations of the spikes highlighted in panel (f). **(c)** Dynamic spectrum of the circular polarization from the NDA/MEFISTO receiver. The two black arrows show the locations of the spikes highlighted in panel (f). **(d-f)** Polarization from the NDA/MEFISTO receiver of the Type III and Type II bursts, respectively, at 34.5 MHz indicated by the solid black lines in panel (c), and polarization of two spike bursts within the region shown in Figure 3.2(c) at 32.50 and 33.88 MHz. The spikes are highlighted by the arrows.

characteristics.

3.2.1 Time Profile

The spike durations were analysed at the burst central frequency (Figure 2.4). The time τ_0 of peak flux I_0 at the central frequency is defined at the location of average flux within 15% of the maximum, which allows for spurious intensity peaks. The half-maximum intensity level $I_{\rm fwhm}$ is then defined as $I_{\rm fwhm} = I_0 - (I_0 - I_{\rm bg})/2$, where $I_{\rm bg}$ is the average background flux level recorded prior to the burst. Due to the variation between the time profiles of each spike

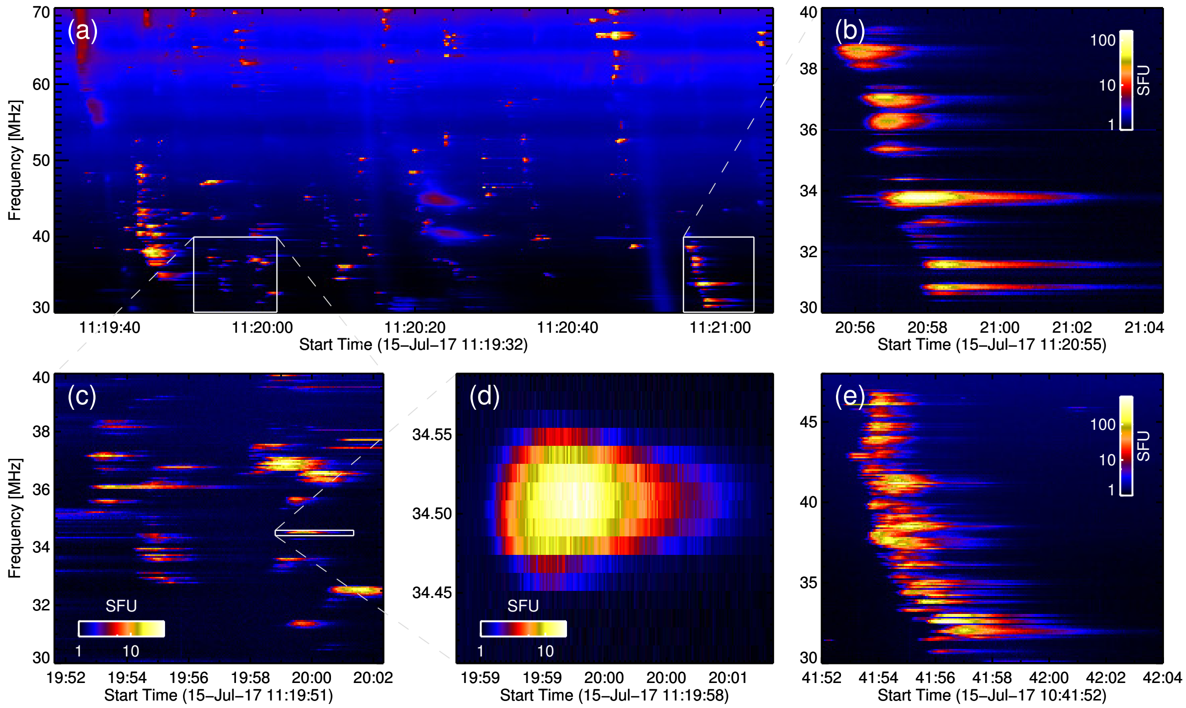

Figure 3.2: Zoomed in dynamic spectra of numerous spike and Type IIIb features within Figure 3.1. **(a)** Numerous spikes between 11:19:32 and 11:21:06 UT from the region bounded by the white box in Figure 3.1. **(b)** Type IIIb burst near 11:21 UT. **(c)** Spike cluster between $30-40$ MHz. **(d)** An individual radio spike. **(e)** Type IIIb burst observed near 10:42 UT.

burst (i.e. they are not all well described by a single Gaussian or asymmetrical Gaussian shape), there is ambiguity in approximating all bursts with a single model. As such, the rise and decay times are measured directly from the data. The rise time $\tau_{\rm r}$ is defined as the time elapsed between the first point above $I_{\rm fwhm}$ to τ_0, and the decay time $\tau_{\rm d}$ is defined as the time elapsed from τ_0 to the final value above $I_{\rm fwhm}$. The FWHM duration is then simply $\tau = \tau_{\rm r} + \tau_{\rm d}$ (Guedel & Benz, 1990; Barrow et al., 1994; Reid & Kontar, 2018b). Figure 3.3(b) shows the lightcurve of the single spike presented in Figure 3.2(d) with a duration of 0.65 s formed from a rise and decay time of 0.34 and 0.31 s, respectively.

The spike peak fluxes range from $4-66$ sfu, averaging at $I_0 \sim 18$ sfu. As noted above, the peak flux of the Type IIIb striae are an order of magnitude brighter than the average spikes at ~ 200 sfu. Of the sample of spikes considered here, their durations fall between $0.2-1.1$ s, and average at 0.48 s with a rate of change of $\mathrm{d}\tau/\mathrm{d}f = -5 \pm 1.8$ ms per MHz between 30–70 MHz given by a linear fit of the form $\tau(f) = (\mathrm{d}\tau/\mathrm{d}f)f + C$ where C is a constant (Figure 3.4). The spike time profiles at a given frequency resemble that of Type III bursts; usually a prompt rise time followed by a longer decay; however, the duration of spikes near 30 MHz are shorter up to a factor of ~ 20. Typically, the rise time is shorter than the decay time (Figure 3.5), averaging at 0.22 and 0.26 s, respectively, although in a

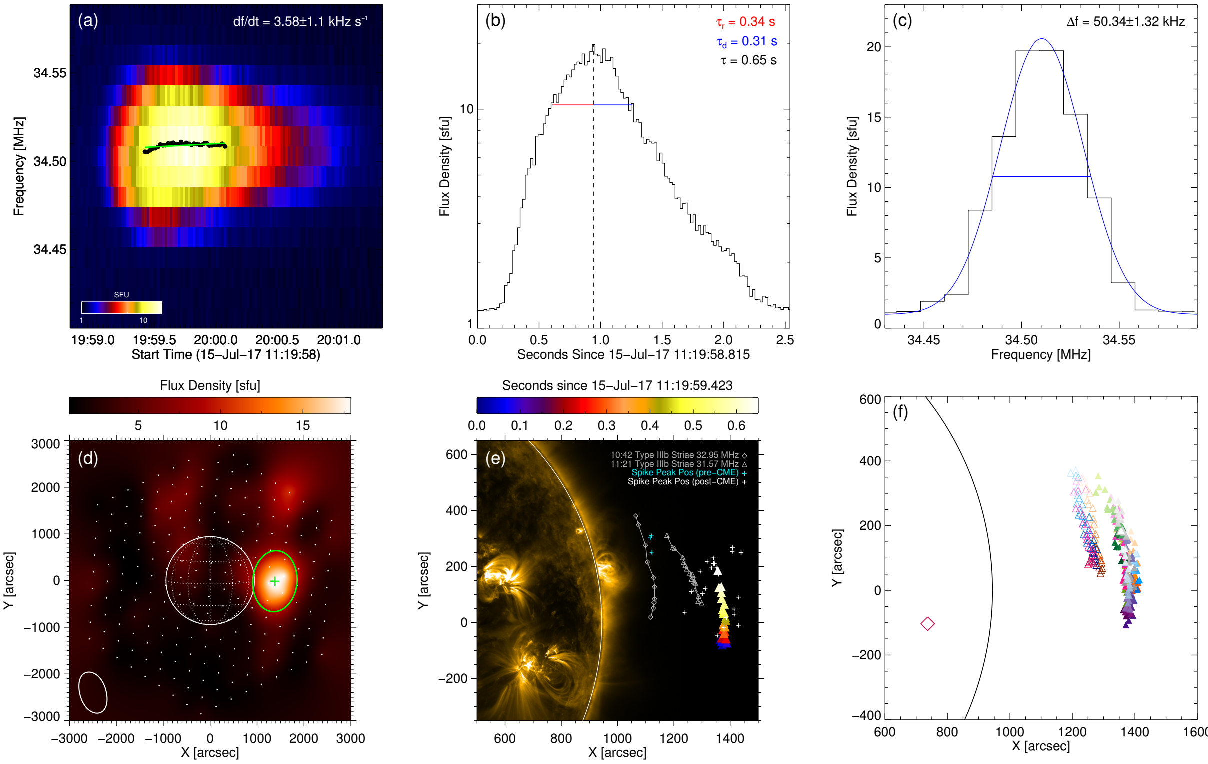

Figure 3.3: **(a)** Dynamic spectrum of the single spike shown in Figure 3.2(d). The black points show the peak of the Gaussian fit to the flux profile at each time bin. The green line shows the linear fit to these points to derive the frequency drift rate. **(b)** Spike flux profile at 34.5 MHz. The dashed vertical line shows the burst peak time, with the horizontal red and blue lines showing the rise and decay time, respectively. **(c)** Flux profile at the time of the burst peak (black) with a Gaussian fit (blue). The horizontal line marks the FWHM spectral width. **(d)** LOFAR image at the peak intensity of the spike at 34.5 MHz near 11:19:59.8 UT. The green contour marks the 2D Gaussian fit at the FWHM level with the centroid marked by the green cross. The white dots represent the phased-array beam pointing, and the white oval shows the half-maximum synthesized LOFAR beam. **(e)** Spike centroid motion in time at a fixed central spike frequency of 34.5 MHz represented by the colored triangles overlaid on an SDO/AIA 171 Å image at 11:20:57 UT. The blue plus symbols show the peak centroid position of the spikes between 30 – 45 MHz before the CME, whilst the white plus symbols show the spike peak centroid positions after the CME. The grey lines with diamond markers represent the centroid motion of a single Type IIIb striae near 10:42 UT at 32.95 MHz, whereas the open grey triangles represent a striae near 11:21 UT at 31.57 MHz. **(f)** Motion of 10 individual spikes. The open triangles represent frequencies between 43 – 45 MHz and closed triangles between 33 – 35 MHz. The color gradients represent time increasing from dark to light. The red diamond shows the approximate location of the active region.

few cases they are of similar duration as in Figure 3.3(b)—this may depend on the method of peak time identification. The durations are comparable with the Type IIIb striae as well as the collision time for a plasma for temperatures between $(0.5-2)\times10^6$ K shown by the curves in Figure 3.4.

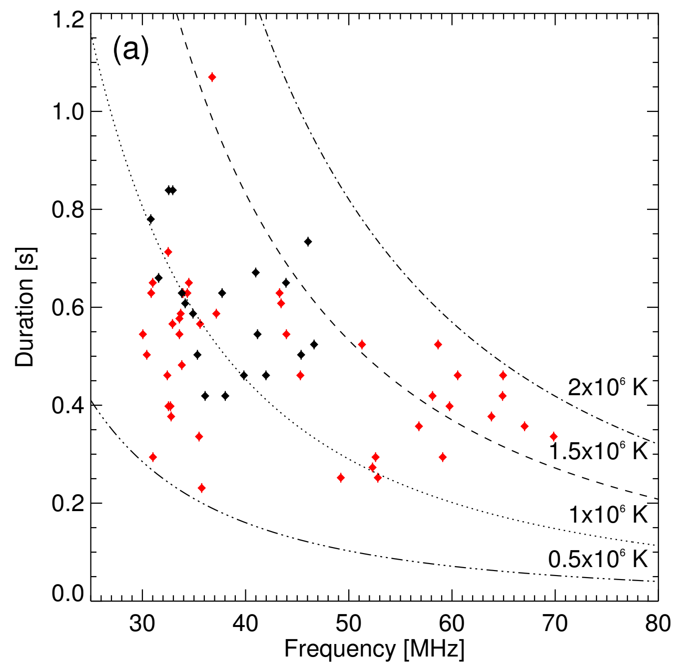

Figure 3.4: Spike (red) and striae (black) FWHM durations. The thin-line curves show the collision time $\tau_{\text{coll}} \approx T^{3/2}/110n$ (McKim Malville et al., 1967) for a plasma of the temperatures T, where n is the plasma density. The errors represent the uncertainty due to the temporal resolution.

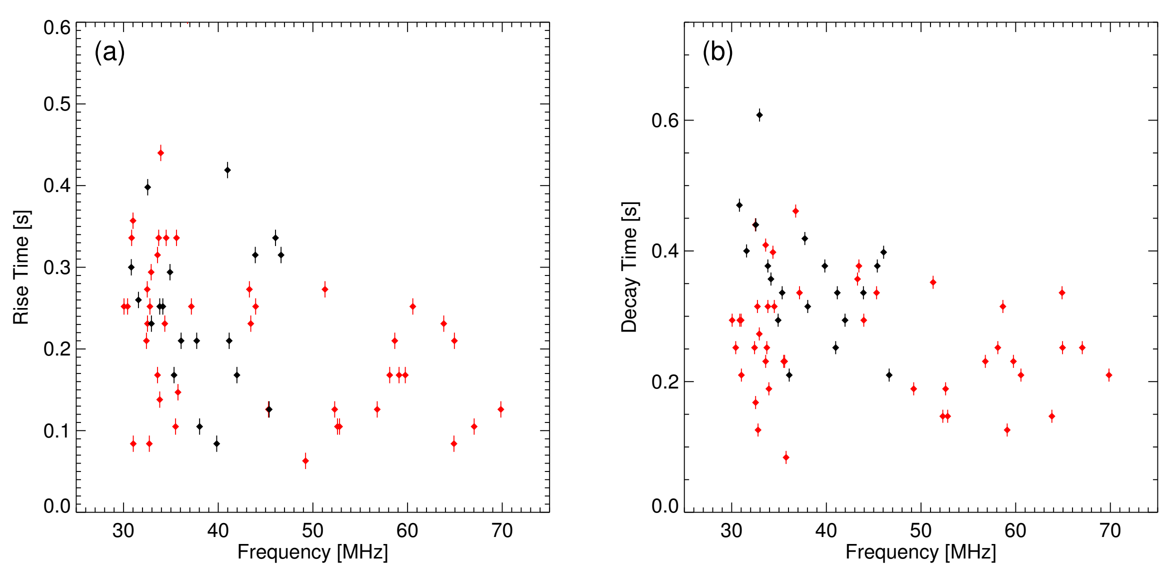

Figure 3.5: Spike (red) and striae (black) HWHM rise (left) and decay (right) times. **(a)** FWHM durations. The errors represent the uncertainty due to the temporal resolution.

3.2.2 Bandwidth

The instantaneous frequency flux profile of the spikes at the burst peak time is symmetrical and well approximated by a Gaussian of the form

$$I(f) = I_0 \exp\left(-\frac{(f - f_c)^2}{2\sigma^2}\right) + I_{\text{bg}}, \tag{3.1}$$

where I_{bg} is the flux offset due to the background level, and σ gives the standard deviation. The FWHM bandwidth is then $\Delta f = \sigma \cdot 2\sqrt{2\ln 2}$. For the spike in Figure 3.2(d), $\Delta f = 50.34 \pm 1.32$ kHz as shown in Figure 3.3(c). The collection of spikes have an average bandwidth of 76.1 kHz between $30-70$ MHz that tends to increase with frequency (Figure 3.6), with some spike widths reaching up to 250 kHz near 70 MHz. Spike spectral widths overlap with that of Type IIIb striae between $30-46$ MHz from the same event, with striae widths also observed up to 174 kHz. Figure 3.6 also presents spike bandwidths measured by Melnik et al. (2014). The grey region presents the bounds of the linear fits applied to data over several events, with the black line showing the average. The trend from 18–29 MHz is consistent with that observed with LOFAR between 30–70 MHz. Also included are the linear fits to striae bandwidths measured by Sharykin et al. (2018). The average striae bandwidths overlap with the spikes presented here, yet the trends differ with frequency.

3.2.3 Frequency Drift Rate

The narrow bandwidths of the spike sample, typically around ~25–150 kHz, mean that measuring the frequency drift rate is challenging with a spectral resolution of 12.2 kHz. Therefore, the drift rate $\mathrm{d}f/\mathrm{d}\tau$ is measured following the method employed by Sharykin et al. (2018) for individual striae. This involves fitting a Gaussian to the intensity profile at each time throughout the FWHM period, and fitting a linear model $f(\tau) = (\mathrm{d}f/\mathrm{d}\tau)\tau + C$ to the Gaussian peaks in time and frequency. This process is illustrated in Figure 3.7 using the fastest drifting striae in this sample at $\mathrm{d}f/\mathrm{d}\tau \simeq -75.2$ kHz s^{-1}, and an example for a spike with minimal drift is shown in Figure 3.3(a), resulting in $\mathrm{d}f/\mathrm{d}\tau = 3.58 \pm 1.1$ kHz s^{-1}.

The majority of spikes have negative drift rates between zero and -75 kHz s^{-1} with an outlier near -123 kHz s^{-1} and eight spikes that have a positive drift rate (Figure 3.8). The linear fit of drift rate against frequency indicates no significant frequency dependence. The spike drift rates are comparable with striae drift rates ranging between 50 to -70 kHz s^{-1}. In comparison, the fine structure drift rates are markedly different from that of the bulk Type IIIb structures shown in Figure 3.2(b,e). These have drift rates of -3.14 ± 0.21 MHz s^{-1} and -2.31 ± 0.26 MHz s^{-1} measured by a linear fit to the peak flux position at the central frequency of each striae. The light grey points in Figure 3.8 represent striae drift rates measured by Sharykin et al. (2018).

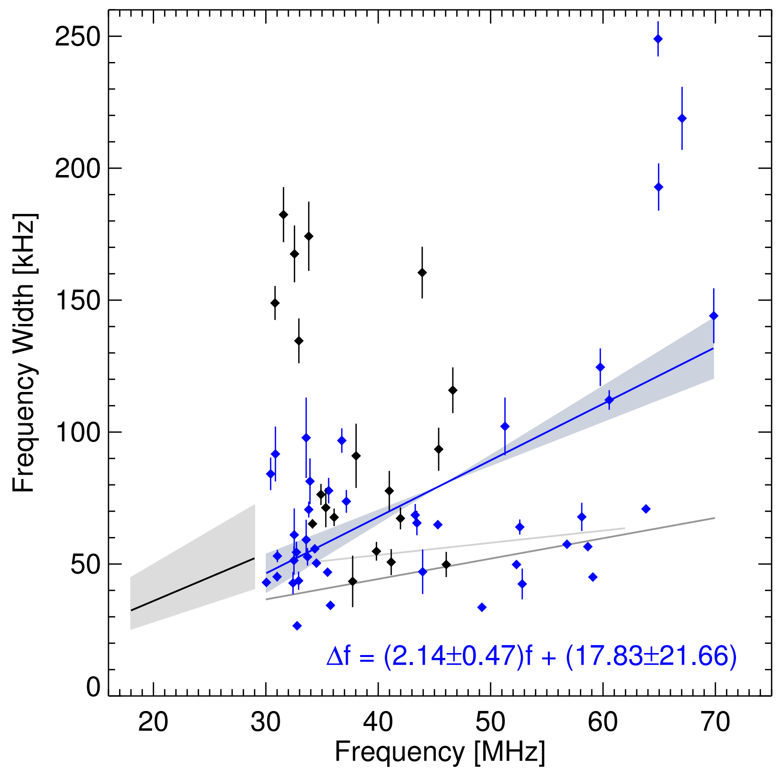

Figure 3.6: Spike (blue) and striae (black) spectral widths. The individual data uncertainty represents the 1-sigma error provided by the Gaussian fitting procedure. The blue line shows a linear fit to the spike data with the blue shaded region representing the fit uncertainty. The black solid line shows the average fit to spike spectral widths from Melnik et al. (2014) with the grey region showing the upper and lower bounds. The two grey lines show fits to striae widths from two different Type IIIb bursts by Sharykin et al. (2018).

3.2.4 Source Area

The spike source areas are measured at the peak time τ_0 of the central frequency by constructing a radio map from LOFAR tied-array data (section 1.5.1.3). The maps are generated from the interpolation of the scattered intensity points of the 217 beams distributed across the solar disk and immediate surrounding area into a regular grid. Figure 3.3(d) shows an example image at 34.5 MHz at the peak of the spike presented in Figure 3.2(d). The centre of each beam is located at the white dots in a hexagonal pattern. The interpolated source is seen as a bright ellipse near the western solar limb. The white oval in the lower left corner gives the half-maximum synthesised LOFAR beam. The faint emission mostly observed towards the northern solar limb are sidelobes. To estimate the source area and centroid location, the image is fit with a 2D elliptical Gaussian as in Kontar et al. (2017b) with the form

$$I(x,y) = I_0 \exp\left(-\frac{x'^2}{2\sigma_x^2} - \frac{y'^2}{2\sigma_y^2}\right), \tag{3.2}$$

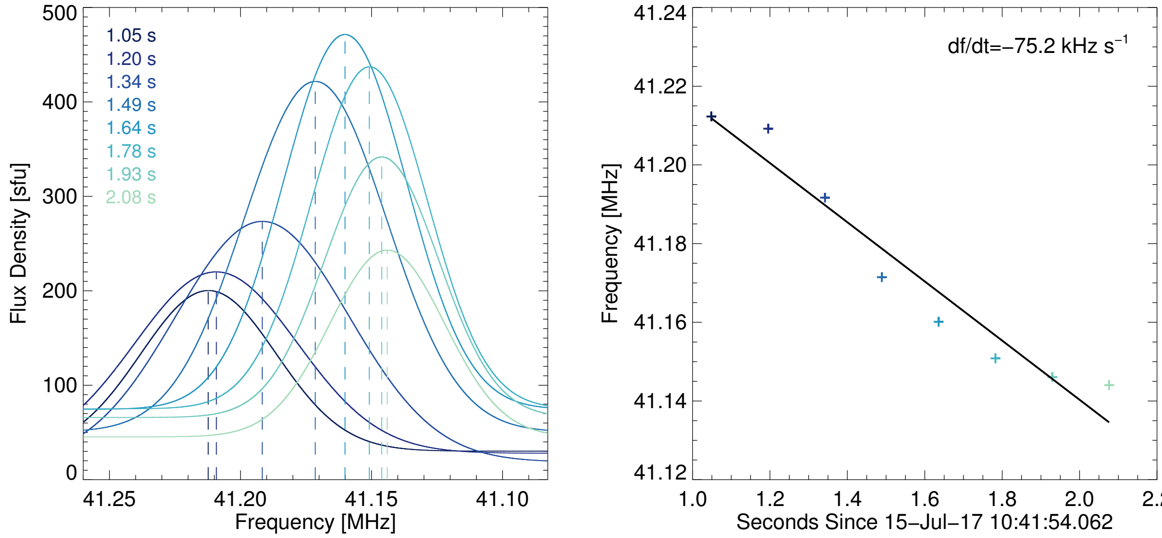

Figure 3.7: The procedure of estimating the fine structure frequency drift rate for an individual striae from the Type IIIb burst in Figure 3.2e. The left panel shows the Gaussian fits to the intensity profiles at different time intervals, with the dashed line marking the frequency of the peak. Note that not all time indices were used here, for clarity. The right hand panel shows the time and frequency position of each peak with a linear fit where the gradient provides the frequency drift rate $\mathrm{d}f/\mathrm{d}\tau$ of the fine structure.

where

$$\begin{aligned} x' &= (x - x_c)\cos\beta - (y - y_c)\sin\beta \\ y' &= (x - x_c)\sin\beta + (y - y_c)\cos\beta, \end{aligned} \tag{3.3}$$

and β is the anti-clockwise rotation from the x-axis, x_c, y_c are the source centroid coordinates, and $\sigma_\mathrm{x}, \sigma_\mathrm{y}$ is the standard deviation along major and minor axes, giving FWHM linear sizes of $S_\mathrm{x} = \sigma_\mathrm{x} \cdot 2\sqrt{2\ln 2}$ and $S_\mathrm{y} = \sigma_\mathrm{y} \cdot 2\sqrt{2\ln 2}$ which are described as the major S_maj or minor S_min axis length as shown in Figure 3.9.

The FWHM area is then

$$A = \frac{\pi}{4} S_\mathrm{maj} S_\mathrm{min}. \tag{3.4}$$

The uncertainty of the fitted parameters of equation 3.2 is as defined in Kontar et al. (2017b). Note the misprint in the equation for δx_s and δy_s where $\sqrt{2/\pi}\sigma_x/\sigma_y$ should be $\sqrt{2\sigma_x/\pi\sigma_y}$—the uncertainties are derived in Condon (1997) (see equation 11). As such, the uncertainty on the centroid location $\delta x_c, \delta y_c$ is given as

$$\begin{aligned} \delta x_c &\approx \sqrt{\frac{2\sigma_\mathrm{x}}{\pi\sigma_\mathrm{y}}} \frac{\delta I}{I_0} \theta_b, \\ \delta y_c &\approx \sqrt{\frac{2\sigma_\mathrm{y}}{\pi\sigma_\mathrm{x}}} \frac{\delta I}{I_0} \theta_b, \end{aligned} \tag{3.5}$$

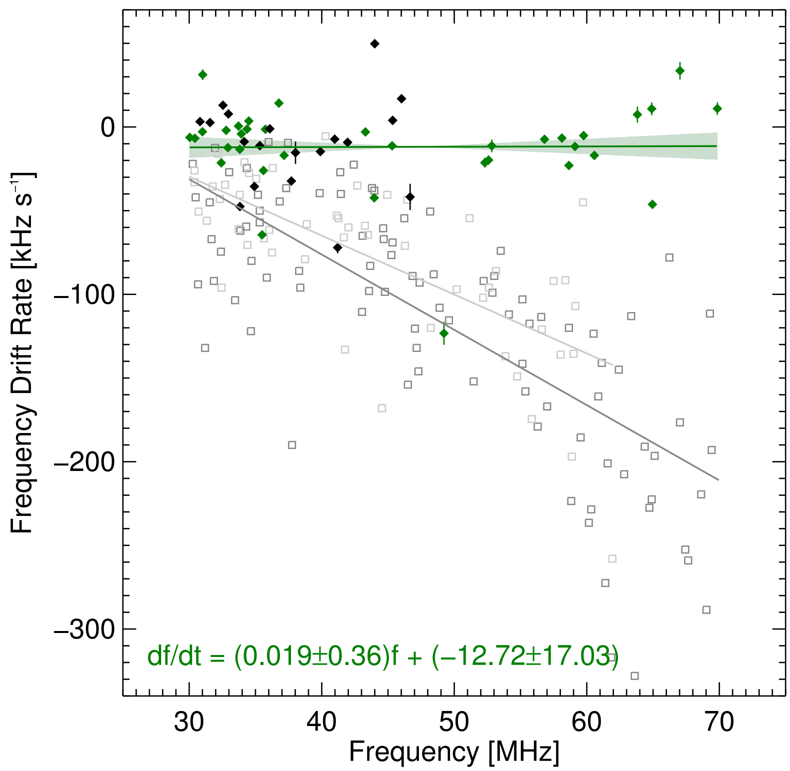

Figure 3.8: Frequency drift rates of spikes (green) and striae (black) between 30 − 70 MHz. The individual data uncertainty represents the 1-sigma error provided by the Gaussian fitting procedure. The solid green line represents a linear fit to the spike data with the green shaded region showing the fit uncertainty. The light and dark grey squares show the striae drift rates from two different Type IIIb bursts by Sharykin et al. (2018) with corresponding linear fits.

where θ_b is the angular resolution (equation 1.38), I_0 is the peak flux, and δI is the flux uncertainty which is typically ~ 1 sfu (Kontar et al., 2017b). The areal uncertainty is given as

$$\delta A \approx 2\frac{\delta I}{I_0}\frac{A}{\sqrt{A}}\theta_{\mathrm{b}}. \tag{3.6}$$

Therefore, brighter spikes and striae will have smaller uncertainty on their positions and sizes. The example spike in Figure 3.2(d) has an observed FWHM area at the peak of the central frequency of 202.19 ± 16.3 arcmin^2 at 34.5 MHz (Figure 3.3d). The ensemble of observed spike areas decrease with increasing frequency from 297 to 122 arcmin^2 between 30–45 MHz (Figure 3.10) in a similar manner to drift-pair bursts (Kuznetsov & Kontar, 2019), and is approximated with a power law $A \sim f^{-\gamma}$ where $\gamma = 1.85$ and 1.92 for spikes and striae, respectively. The synthesised LOFAR beam area over this frequency range is $A_{\mathrm{beam}} \simeq 50 - 113$ arcmin^2, so the LOFAR beam-corrected source areas are up to $A \simeq 72 - 184$ arcmin^2. Importantly, the spike areas at a fixed frequency increase over time at tens of millisecond scales (Figure 3.11d) with expansion rates between 18–108 arcmin^2 s^{-1} that are most pro-

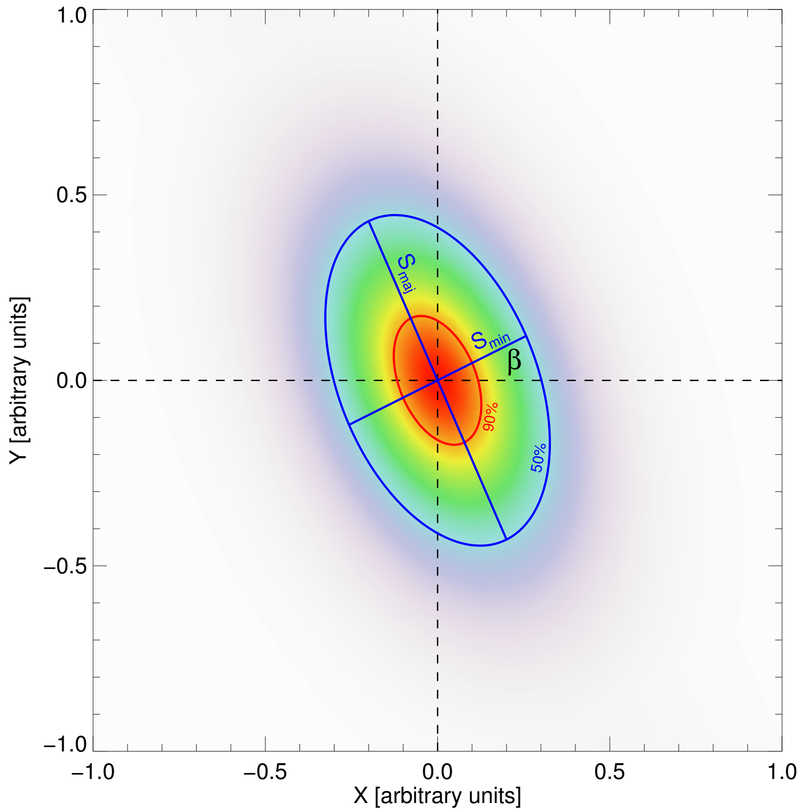

Figure 3.9: Diagram of a 2D elliptical fit with a 2D Gaussian given by equation 3.2. The ellipse is tilted by 25°. The fitted parameters provide the FWHM area given by the blue contour, and the corresponding FWHM major S_{maj} and minor S_{min} axis lengths, shown by the straight blue lines. The tilt angle of the fit is labelled as β, marking the angle between the horizontal, dashed white line and the minor axis. The red oval marks the 90% fit contour.

nounced during the decay phase, similar to Type IIIb observations (Kontar et al., 2017b).

3.2.5 Centroid Location

One of the intriguing observations is the variability of the radio spike sources (positions and areas) with time at tens of millisecond scales. The spike centroid position moves vertically in the plane-of-sky image over 0.65 s crossing the solar equator (Figure 3.3d) and covering 262 arcsec $\simeq$ 0.28 $R_\odot$ in the image plane across the FWHM duration. Since 1 $R_\odot$ = 944 arcsec as viewed from Earth at the time of the event, this centroid speed corresponds to the speed of light c across the FWHM. The frequency drift rate inferred exciter velocity is estimated following that in Kontar et al. (2017b), and as shown in section 1.3.3 using

$$v = \frac{2r_n}{f}\frac{\mathrm{d}f}{\mathrm{d}t}, \qquad \textbf{(??)}$$

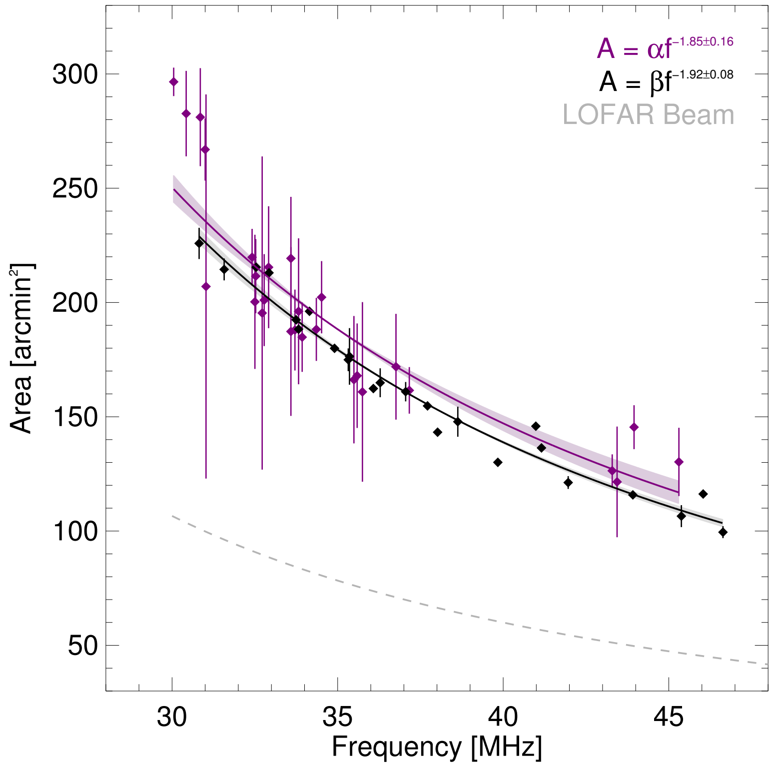

Figure 3.10: Observed FWHM area of spikes (purple) and striae (black) at their peak intensity. The data uncertainties are given by equation 3.6. The solid lines show the power-law fits to the data, with the shaded regions representing the fit uncertainties. The coefficients α and β of the fits are 1.34×10^5 and 1.64×10^5, respectively. The light-grey dashed line shows the LOFAR beam area.

where $r_n \simeq 2\times10^{10}$ cm is the density scale height near 30 MHz using the Newkirk density model (Table 1.1). For $\mathrm{d}f/\mathrm{d}t = 3.58$ kHz s^{-1}, equation **??** gives $v \sim 42$ km s^{-1}. Spikes with higher frequency drifts such as 60 kHz s^{-1} at 35.5 MHz infer speeds of up to 680 km s^{-1} using this method. The spikes observed $\sim$10 mins before the flare and CME eruption appear closer to the disk centre, while the spikes in the wake of the CME are further away (Figure 3.3e). The spike source motion follows a trajectory parallel to the Type IIIb striae observed prior to the CME. Post-CME Type IIIb striae show motion that originates within the same region as the post-CME spikes (Figure 3.3f), suggesting a common exciter. It is interesting to note that the FWHM spike source areas are comparable to Type IIIb areas in this event, but smaller than observed before (e.g. Kontar et al., 2017b).

Figure 3.11(a–c) shows the spike centroid motion in the image plane for the radial, x, and y positions. During the time where the signal (shown by the normalised red curves) is sufficiently bright, we find that each parameter has a most pronounced change during the decay phase, similar to the Type IIIb striae observed by Kontar et al. (2017b). Each set of data is fit with a linear model across the decay phase—the radial distance changes weakly since the bulk motion is in the y-direction with a superluminal apparent plane-of-sky speed of 10.4 arcmin s^{-1} $\simeq$ 1.5c. This vertical motion is typical for all observed spikes during this period (see Figure 3.3f), with x and y drift rates between -0.44 to -2.27 arcmin s^{-1} and 5.25 to 11.18 arcmin s^{-1}, respectively. In the y-direction, this corresponds to apparent speeds between 0.76–1.8c.

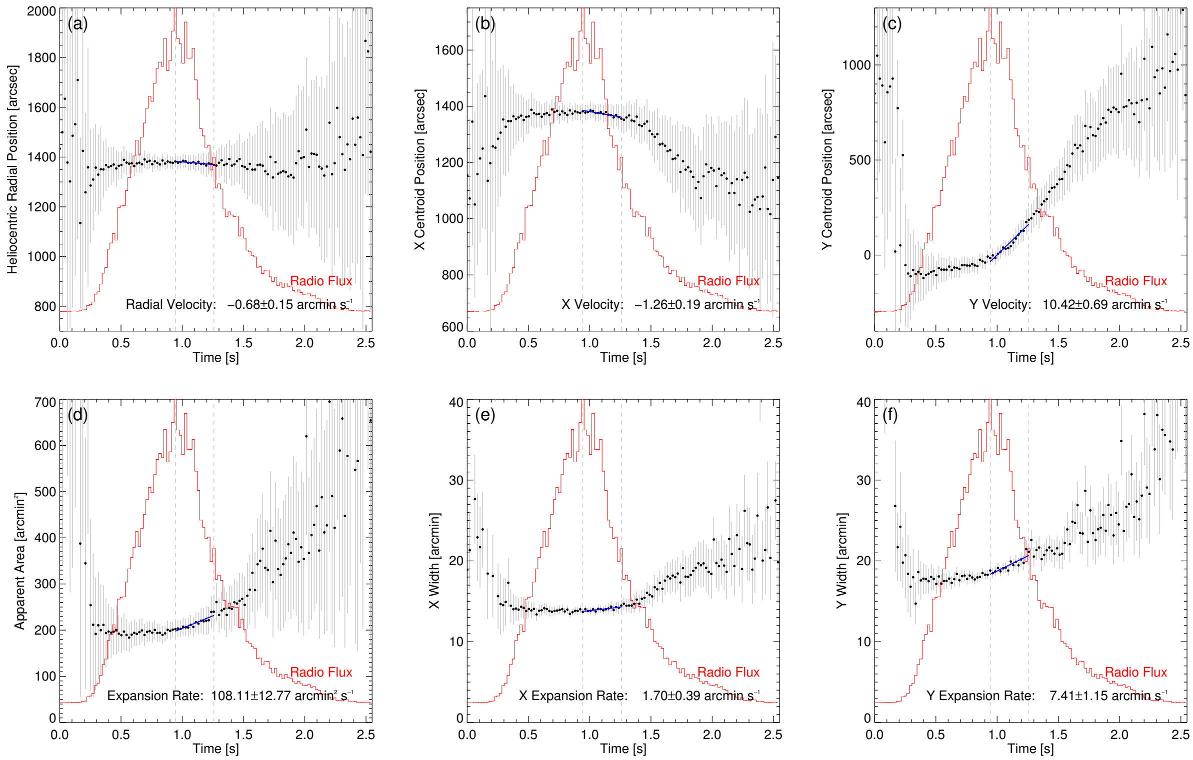

Figure 3.11: Spike source motion and expansion over the duration of the dynamic spectrum shown in Figure 3.2(d) at 34.5 MHz. The red curve shows normalised radio flux at the same frequency, with the vertical grey dashed lines at the peak and FWHM decay time. The blue lines show linear fits over the decay period. The errors are given as in Kontar et al. (2017b). **(a)** Heliocentric radial position. **(b)** Spike centroid velocity in the X direction. **(c)** Spike centroid velocity in the Y direction. **(d)** Observed area and **(e, f)** widths in the X and Y direction over time.

3.3 Discussion

The spectral and temporal characteristics of the observed spikes are consistent with those previously reported at similar frequencies (Melnik et al., 2014; Shevchuk et al., 2016). There is a tendency for longer durations and shorter bandwidths towards lower frequencies, although from the small sample size and spread of the time profile measurements, identifying a clear frequency dependence is not possible. However, from a larger sample size, one would expect the time profile to shorten with increasing frequency, considering that observations at gigahertz frequencies are significantly shorter (see section 2.3.1.1). The spike areas also decrease with increasing frequency, as typically observed for solar radio bursts (see section 1.3.3, for example).

For spikes near 30 MHz, where the Newkirk density model (Table 1.1) gives a height of $\sim 1.78\ R_\odot$, the average magnetic field strength estimated by equation 1.6 (Dulk & McLean, 1978) is 0.73 G. This is similar to estimates using LOFAR Type IIIb observations by Kolotkov et al. (2018) who found a value of 1.1 ± 0.2 G at a plasma frequency of 34 MHz, inferred from deduction of the Alfvén speed of a fast magneto-acoustic wave. The electron cyclotron frequency (equation 1.13) for this field strength is $f_{\mathrm{ce}} \simeq 2.0$ MHz which is sufficiently less than the plasma frequency of $f_{\mathrm{pe}} \sim 30$ MHz for the ECM criteria that $\omega_{\mathrm{ce}} \gg \omega_{\mathrm{pe}}$ (section 1.2.2) to not be satisfied. Moreover, NDA/MEFISTO measurements indicate that the Type III and Type II bursts both show left-handed circular polarization up to -0.4 and -0.3, respectively (Figure 3.1). The spikes within the region shown in Figure 3.2(c) are also left-hand polarized at -0.15 and -0.1, indicating that the spikes are produced by the same emission mechanism. Therefore, we suggest plasma emission as the source of the radio spikes similar to Type IIIb bursts, but likely from electrons beams with lower densities and velocities, as previously suggested by Tarnstrom & Philip (1972b); Melnik et al. (2014). Turbulence within the plasma will also change the spatial distribution of Langmuir waves (seen in the numerical simulations by Kontar, 2001b), creating regions of enhanced Langmuir waves that manifest as electromagnetic emission seen as striae or more sporadically as spikes.

The radio spike positions are observed before and after the onset of the solar eruptive event at 10:50 UT. The location of radio spikes and Type IIIb striae after the CME are 1250–1450 arcsec away from the Sun centre, compared to ~ 1100 arcsec prior to the CME eruption, showing a shift away from the Sun. For the first time, the time-resolved observations of individual spikes reveal source motions and source size changes at 100 ms scales. The spike sources (both before and after the CME) follow trajectories approximately parallel to the solar limb, which contrasts the previously observed radial motions of Type IIIb bursts (Kontar et al., 2017b; Zhang et al., 2019), and the corresponding spherically symmetric coronal simulations (Chen et al., 2020) that replicated their motion.

The motion of the spike sources is superluminal (0.76–1.8c) and accompanied by the superluminal FWHM source size expansion of 7.4 arcmin $\mathrm{s}^{-1} \sim 1.1c$. In particular, such characteristic evolution occurs during the decay phase, suggesting strong scattering of the emitted radiation as similarly observed for striae (section 2.1) and drift pair (section 2.2) fine structures. For scatter-dominated sources, the observed source velocity depends on the angle between the line-of-sight and the direction from the Sun centre to the source location (since sources shifted along the LOS have a masked velocity component; see section 1.4.1.1), as well as the anisotropy of plasma turbulence (Kontar et al., 2019; Chen et al., 2020; Kuznetsov et al., 2020). Stronger anisotropy will focus the emission, increasing the directivity in the direction of the magnetic field, which presents as faster source motion across the sky plane. Large heliocentric angles such as that observed by spikes in this observation are subject to larger displacements along the direction of the guiding magnetic field and increased apparent velocities. Superluminal motions are, in fact, observed in radio-wave propagation simulations (see Figure 5 by Kuznetsov et al., 2020), suggesting 1.0–1.1c speeds for sources located at heliocentric angles of 30 and 50 degrees. For the data in this study, the associated active region on the solar disk has a heliocentric angle of approximately 50 degrees; that is, the angle between the radial line connecting the solar centre and observer, and the radial line connecting the solar centre and the active region.

The previously unobserved non-radial superluminal motion of spike and Type IIIb sources in this event suggests a different magnetic configuration to what was simulated by Chen et al. (2020). In anisotropic density turbulence that is aligned with the magnetic field, radio waves propagate preferentially along the magnetic field direction (Kontar et al., 2019, and section 1.4.1.1). The observed spike and Type IIIb sources are located within the region where the magnetic field is likely forming loop-like structures, so radio-wave scattering in the region with the magnetic field lines parallel to the limb could induce the observed direction of the source motion. The extended post-reconnection closed loops are likely formed within the CME wake and are the location of weak electron beam acceleration, resulting in Langmuir wave generation and subsequent spike emission. The simulations of radio-wave transport by Kuznetsov et al. (2020) show that stronger anisotropy leads to smaller observed peak source sizes and superluminal velocities. Thus, the spikes and Type IIIb striae source properties are consistent with the simulations with anisotropy $\alpha = 0.1 - 0.2$ (Kuznetsov et al., 2020), which is higher than the anisotropy $\alpha = 0.25 - 0.3$ required in open configurations to explain Type III burst properties (e.g. Kontar et al., 2019; Chen et al., 2020). Consequently, the anisotropy of density turbulence in closed loop configurations should be higher than that along open field lines.

Many similarities between spike and Type IIIb striae characteristics such as duration, spectral width, velocities and observed area suggest a common physical mechanism. The spike durations decrease on average with increasing frequency, with bandwidths ranging between 20–100 kHz, covering a similar range reported in Sharykin et al. (2018) for striae. The spike and striae drift rates show little dependence on frequency, and indicate velocities of 10–50 km s^{-1}. Spike drift rates close to 30 MHz overlap with the striae drift rates presented by Sharykin et al. (2018), however the comparison diverges above 40 MHz. The drift rate inferred velocities of our observed spikes and striae are much less than the bulk speeds of Type III bursts that propagate at characteristic speeds of $\sim 10^5$ km s^{-1} $\simeq c/3$ (Suzuki & Dulk, 1985). The motion of Langmuir waves is believed to be responsible for Type IIIb striae drift (Reid & Kontar, 2021), and so could be the explanation for the individual spike drift. However, since the spikes have on average shorter duration, such drift is likely to be diluted by scattering effects since the spike emission will be broadened in time in dynamic spectra, yet persist across the same frequency range. As a result, any measurable value of $\mathrm{d}f/\mathrm{d}\tau$ will be reduced due to increased τ. The disparity between the measured spike and striae drift rates in this work and the striae drift rates by Sharykin et al. (2018) could be a combination of these effects; i.e., different coronal temperatures leading to varied Langmuir wave group velocities, as well as different coronal turbulence levels leading to different levels of drift dilution. The latter effect is explored in more detail in chapter 5.

As was noted before (e.g. Melnik et al., 2014), the spike duration is comparable to the plasma collision time. However, a spread of temperatures from 0.5–2 MK are required for the same cluster of spikes to explain the characteristic decay time (Figure 3.4). Radio spikes above 100 MHz (e.g. Guedel & Benz, 1990) would need even higher plasma temperatures of 2–4 MK within the collisional damping hypothesis (Figure 2.5). While damping of plasma oscillations should be present, the large source sizes, the superluminal motion of spike sources, and the aforementioned morphological similarity to Type IIIb striae implies that scattering is an important factor in determining spike profiles. Therefore, we suggest that the scattering of radio waves rather than collisional damping alone determines the time profile. This is statistically analysed in chapter 4.

Spike durations are often used to constrain the shortest energy release time in flares, with the bandwidth equating to the size of the acceleration region itself (section 2.3.2). Following the approach previously used for estimating Type IIIb bursts (Kontar et al., 2017b; Sharykin et al., 2018), the size of the emitting spike source region can be estimated as $\Delta r \simeq 2L_n(\Delta f/f) \simeq 10^8$ cm, and corresponds to a subtended solid angle of $\sim 10^{-2}$ arcmin^2. Therefore, the effect of radio-wave propagation has increased the observed source area by four orders of magnitude to the $\sim 10^2$ arcmin^2 observed areas. This means that the brightness temperatures of the spike (and striae) sources in this sample corrected for scattering could be up to $10^{12} - 10^{13}$ K, well above the values $10^8 - 10^9$ K when radio-wave scattering is ignored. With scattering as the determining factor of the duration and higher resulting brightness temperature, the energy release responsible for electron acceleration would be much shorter and more intense than previously assumed in the literature when determined from observations alone. The characteristic emission timescale is approximately reduced by the ratio of the observed size to the emitting region, and could be two orders of magnitude shorter, i.e. tens of milliseconds instead of ~ 1 s as observed at decametre frequencies.

3.4 Conclusion

Using the LOw Frequency ARray (LOFAR), frequency and time resolved observations of individual radio spikes are presented for the first time, associated with a coronal mass ejection (CME). Individual radio spike imaging demonstrates that the observed area is increasing in time and the centroid positions of the individual spikes move superluminally parallel to the solar limb. Comparison of spike characteristics with that of individual Type IIIb striae observed in the same event show similarities in duration, bandwidth, drift rate, polarization, and observed area, as well as the spike and striae motion in the image plane. It suggests that spike emission is fundamental plasma emission with the spike emission region on the order of $\sim 10^8$ cm, with brightness temperature as high as 10^{13} K. The observed spatial, spectral, and temporal properties of the individual spike bursts are also suggesting that the radio emission observed as spikes escapes through anisotropic density turbulence in closed loop structures with scattering preferentially along the guiding magnetic field oriented parallel to the limb in the scattering region. The dominance of scattering on the observed time profile suggests the energy release time is likely to be shorter than what is often assumed. The observations also imply that the density turbulence anisotropy along closed magnetic field lines is higher than along open field lines.

4

Manifestations of Sub-second Electron Acceleration Triggered by a Coronal Mass Ejection

These results were published in Clarkson et al. (2023).

The initial results presented in Chapter 3 considered a small sample of spikes. In this chapter, 1076 spikes are individually analysed occurring between 10:17 and 11:39 UT on 15 July 2017 (the same event discussed in Chapter 3), allowing a much needed statistical determination of the various spike characteristics between 30–45 MHz from imaging observations (421 spikes) and 30–70 MHz from dynamic spectra (1076 spikes). The spikes are compared with 250 individual striae (207 were imaged) from six Type IIIb bursts from the same event. The data also provide insight into the acceleration region using the centroid locations of both spikes and striae within the closed magnetic loop in conjunction with the CME.

Figure 4.1a shows the LASCO C2 field of view at 11:36 UT where two narrow CME fronts, one of which is a streamer-puff CME (section 1.1.2.3), are traced back to the aforementioned jet eruption near 10:52 UT (section 3.1). Also shown is an SDO/AIA 171 Å image of the Sun at 11:21 UT, and a PFSS extrapolation showing open and closed magnetic geometry at 12:00 UT. The closed field lines show the possible configuration of trans-equatorial, extended coronal loops that bridge the two active regions on the western hemisphere. Panels (b–d) show three dynamic spectra consisting of spike clusters at different times. Of the six Type IIIb bursts, an example is presented in Figure 4.1e. There is a clear fundamental branch with a starting frequency of 45 MHz that extends down to 30 MHz, and a possible harmonic branch between 60–66 MHz. As described in Chapter 3, the data were reduced to 20 ms temporal resolution. Contrary to the imaging measurements in Chapter 3, all centroid data in this chapter are corrected for ionospheric refraction using equation 1.35 for the solar zenith angle of $z = 32.4°$. This results in a reduction of the vertical sky plane position by around 50–100 arcsec depending on the frequency (Figure 1.12).

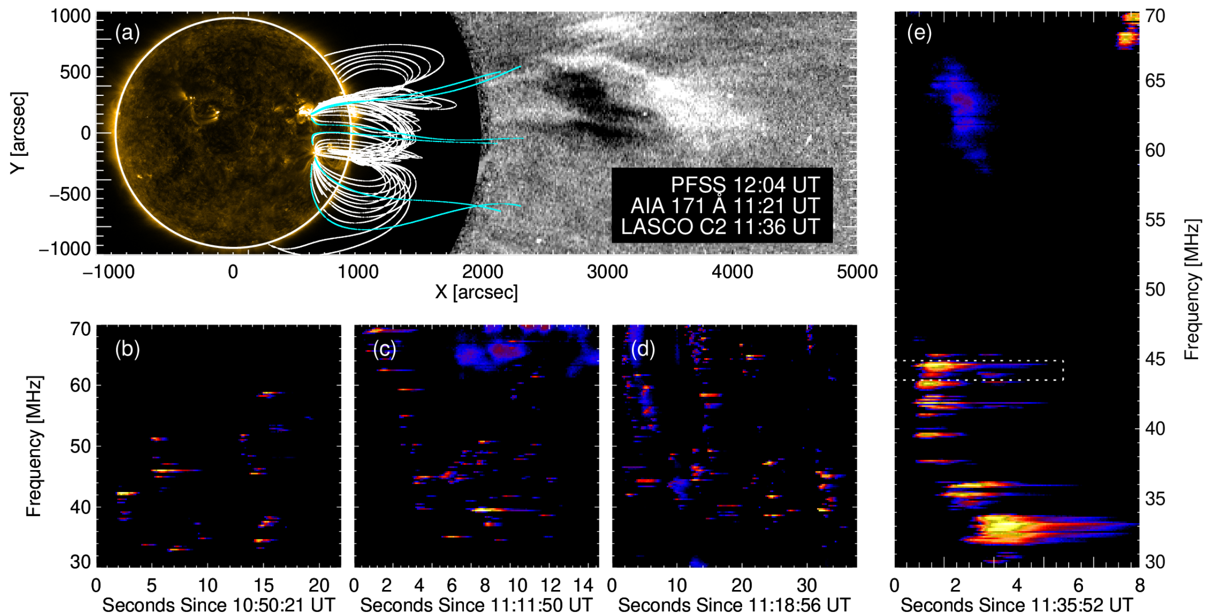

Figure 4.1: An overview of the event. **(a)** SDO/AIA 171 Å image at 11:20:57 UT, superimposed with a PFSS extrapolation at 12:00 UT showing both open (blue) and closed (white) field lines within region surrounding the active region and northern sunspot, and a LASCO C2 difference image showing the streamer-puff (above) and narrow (below) CME fronts at 11:36:05 UT, as shown in Chrysaphi et al. (2020). LASCO difference data provided courtesy of N. Chrysaphi. **(b-d)** Dynamic spectra showing samples of the spike emission. **(e)** Dynamic spectra of a Type IIIb J-burst. The dotted box highlights the region shown in Figure 4.7. All dynamic spectra are background subtracted where the background is defined using a region at the start of each dynamic spectra containing no bursts at all frequencies.

4.1 Acceleration Region

4.1.1 Type IIIb Bi-Directional Exciter Motion

As described in section 1.3.3, the Type IIIb bursts of this event appear as J-bursts, suggesting that their sources partially trace the coronal loop, making them a useful diagnostic of the loop environment. Moreover, these bursts present an interesting property—within the burst envelope, there are two bulk components with a drift rate of opposite sign. The bulk drift rates are estimated by fitting the peak positions in time at each frequency channel of the individual striae. The example shown in Figures 4.1(e) and 4.2(a) has a negative bulk drift of -6.1 MHz s^{-1} near 40 MHz, comparative to previously reported Type IIIb drift rates (Sharykin et al., 2018; Chen et al., 2018). Towards 32 MHz, the drift rate reduces to -1.1

MHz s^{-1} as the exciter approaches the loop apex, similar to other decametre J-bursts (Reid & Kontar, 2017). Above these frequencies, the burst exhibits a reverse-drift at 4.9 MHz s^{-1} signifying electrons that are propagating towards the footpoints. Figure 4.2 shows the peak centroid locations for the J-burst as a function of time, separated by the bulk drift direction. The bi-directional burst exciter motion (Aschwanden et al., 1995; Tan et al., 2016) suggests that the acceleration region of the Type IIIb is at a radius corresponding to ~ 40 MHz where the opposing centroid motions (bulk drifts) emanate, implying that in general, the site of acceleration for this event is high in the corona.

4.1.2 Inferred Loop Density Model

Figure 4.2(b) displays the frequency position according to an exponential loop density model (e.g. Aschwanden et al., 1999) given by equation 1.12, repeated here

$$n_e(l) = A_n \exp\left(-\frac{r(l)}{r_n}\right), \tag{1.12}$$

where $A_n = 10^{11}$ cm^{-3} is the density at the base of the footpoints, $r_n = 1.57 \times 10^{10}$ cm is density scale height similar to values found by Reid & Kontar (2017) for Type III U and J bursts, and $r(l)$ is the height along the loop from the solar surface. The latitude and longitude $(\lambda_{1,2}, \phi_{1,2})$ of each active region on the solar disk is (-6°, 52°) and (20°, 44°), denoted by the red symbols in the inset of Figure 4.2. The angle formed between them and the solar north is $\Phi \sim -27°$ as given by the spherical law of cosines of the form

$$\Phi = \cos^{-1}(\cos\lambda_1 \cos\lambda_2 \cos(\phi_1 - \phi_2) + \sin\lambda_1 \sin\lambda_2). \tag{4.1}$$

The density model is then rotated around the x and y axes as

$$\begin{aligned} x' &= x\cos\theta \\ y' &= y\cos\Phi + x\sin\theta\sin\Phi, \end{aligned} \tag{4.2}$$

producing the dashed lines representing the frequencies of the density model. The value of r_n was then chosen to best represent the centroid locations at a given frequency. The inset of Figure 4.2(b) displays the applied rotation on the solar disk.

4.1.3 Type IIIb Beam Velocities

The centroid positions of the reverse-slope component of the Type IIIb J-burst are distributed across 80.6 ± 11 arcsec of the sky-plane over 0.9 s. The distance uncertainty is derived from the average centroid uncertainties $\overline{\delta x_c}, \overline{\delta y_c}$ as $\delta r = \left[(\partial r/\partial x \overline{\delta x_c})^2 + (\partial r/\partial y \overline{\delta y_c})^2\right]^{1/2}$. This correlates to a beam velocity of $v_{\mathrm{rev,obs}} = (0.22 \pm 0.03)c$. For the negative drift component,

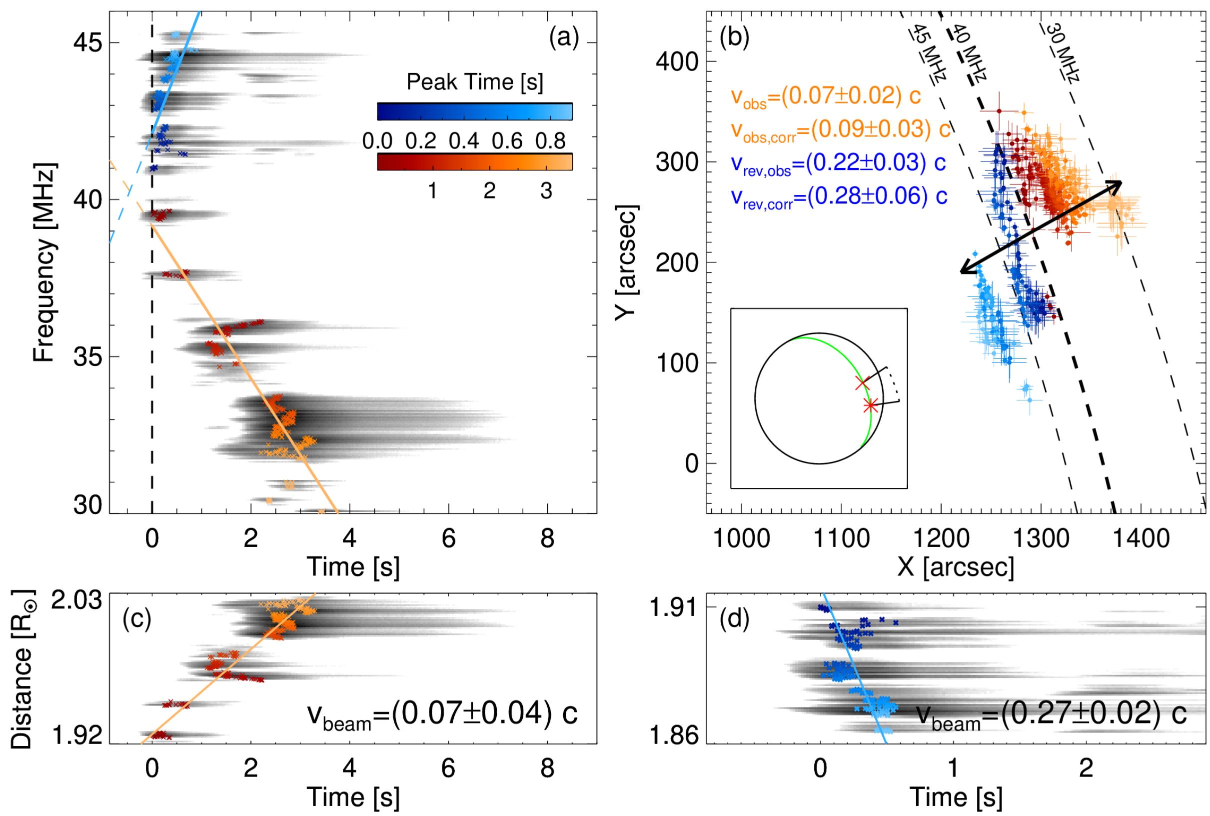

Figure 4.2: Centroid positions at the striae peaks of the Type IIIb J-burst, marked by the coloured points in the dynamic spectrum of panel (a). The orange and blue lines in panel (a) highlight the opposite sign bulk drift rates. In all panels, the orange points relate to the negative drifting burst segment, and the blue points relate to the reverse-drifting section. The colour gradients show the elapsed time from the earliest striae peak, represented by the vertical black dashed line in panel (a). Panel (b) shows the centroid locations of each striae with the arrows representing the observed trajectories and radial distances used to estimate the centroid velocities v_{obs}, v_{rev} of each component across the plane-of-sky. A velocity estimate with a correction for the projection effect is given as $v_{obs,corr}$ and $v_{rev,corr}$ assuming the sources propagate along the sun-centre and active region plane with an uncertainty corresponding to a magnetic field spread of 30°. The black dashed curves show the exponential loop density model of equation 1.12 rotated as demonstrated in the inset of panel (b). Panels (c) and (d) show the distance-time spectra of each burst component with the distance obtained from the density model of equation 1.12. The gradient of the linear fits to the striae peaks provides the beam velocities.

the observed radial spread is 103.0 ± 9 arcsec over 3 s, giving $v_{obs} = (0.07 \pm 0.02)c$. Due to the projection effect, these observed values are likely to be larger as a component of motion is masked in the 2D plane. The actual velocities can be estimated as $v_{obs}/\sin 52°$ assuming that the sources propagate along the plane connecting the sun-centre and active region. The uncertainty in this velocity is increased since we do not know the spread in angle that the magnetic field geometry makes with the active region, and thus the actual trajectory of the beam. Here we assume a spread of 30°. The projection corrected beam velocities are then

$v_{\mathrm{corr}} = (0.09 \pm 0.03)c$ and $v_{\mathrm{rev,corr}} = (0.28 \pm 0.06)c$. The beam velocities can also be estimated via the assumption of a density model (equation 1.12). Panels (c-d) of Figure 4.2 show the distance-time spectra of each burst component where the striae peaks are fit with a linear model. The gradient then provides the beam velocity through space as $(0.07 \pm 0.04)c$ and $(0.27 \pm 0.02)c$ for the normal and reverse drifting components, respectively. Whilst each method to determine the beam velocity requires some assumption (projection effect or density model), the determined velocities agree within their uncertainties.

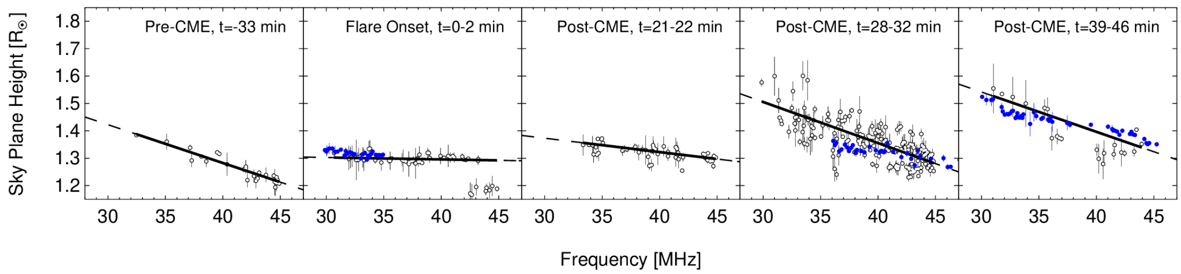

Figure 4.3: Observed centroid radial heights with frequency in the sky-plane for spikes (black, open circles) and striae (blue, closed circles). Each panel shows bursts that are close in time, with the second panel near the time of the flare, such that the prior panel shows pre-CME spikes. The spike data are fit with linear models.

4.1.4 Acceleration Site Location

Figure 4.3 shows the observed spike and striae centroid heights in the sky-plane as a function of frequency, with each panel showing a period progressively later in time. For the bursts pre-CME, the heights vary linearly with frequency between 30–45 MHz. After the onset of the flare and passage of the CME, the observed sky-plane heights from the Sun at a given frequency are reduced. In panel 2, the variation with frequency is minimal and then progressively increases over ~ 45 minutes. The increase in the observed sky-plane height at 30 MHz over time is shown in Figure 4.4 from 1.30–1.54 $R_{\odot}$. The variation is linear, and correlates to a velocity of $v_{\mathrm{H,obs}} = (81 \pm 5)$ km s^{-1}. The actual radial heights can be estimated by correcting for the projection effect as presented in section 4.1.3, leading to a corrected velocity of $v_{\mathrm{H,rad}} = (90.2 \pm 24)$ km s^{-1}.

4.2 Statistical Spike Characteristics

4.2.1 Comparison of Spike & Striae Centroid Positions

The centroid position of both spikes and striae differs greatly depending on the point in time that is used to generate the radio image. Figure 4.5 shows centroid motion across the FWHM

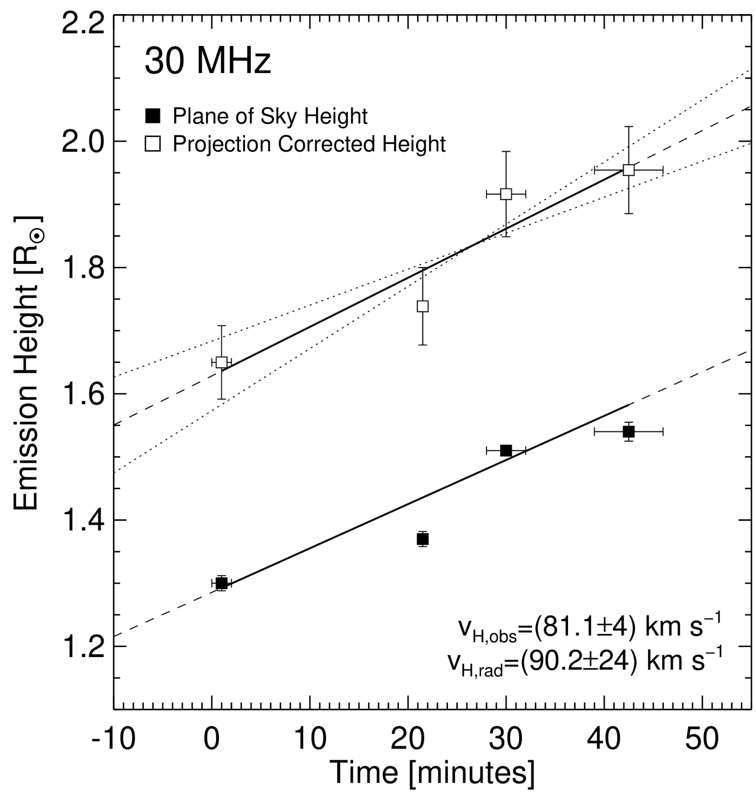

Figure 4.4: Observed sky-plane heights (solid squares) and estimated radial heights of the spike bursts over time at 30 MHz extrapolated from the linear fits in Figure 4.3. The horizontal error denotes the width of the time interval in each panel of Figure 4.3. The vertical error of the plane-of-sky heights is derived from the linear fits in Figure 4.3. The projection corrected heights assume a spread in angle of the loop magnetic field of 30°, contributing to the increased uncertainty. These data are fit with a linear model (solid lines) where the gradient describes the velocity at which the emission height at 30 MHz increases over time. The dotted lines demonstrate the fit uncertainty for the projection corrected heights.

of the time profile of individual striae from the Type IIIb at various fixed frequencies. There are two visible components of motion—a frequency drift away from the Sun associated with the path of the exciter, and a displacement over time at fixed frequencies almost parallel to the solar limb towards the solar north, which is typically increased during the decay phase compared to the rise phase. The frequency drift and exciter trajectory does not correlate to the local field line direction of an inferred coronal loop that the scattered centroid locations trace. Given that the beam will propagate along the magnetic field direction, it implies that the actual emitter location is farther down the loop leg in a region where the field line trajectory matches the observed frequency drift direction, as indicated by the green arrow in the inset of Figure 4.5.

The fixed frequency centroid motion evolution of spikes across the FWHM time duration are shown in Figure 4.6. The individual and collective motion exhibits a displacement

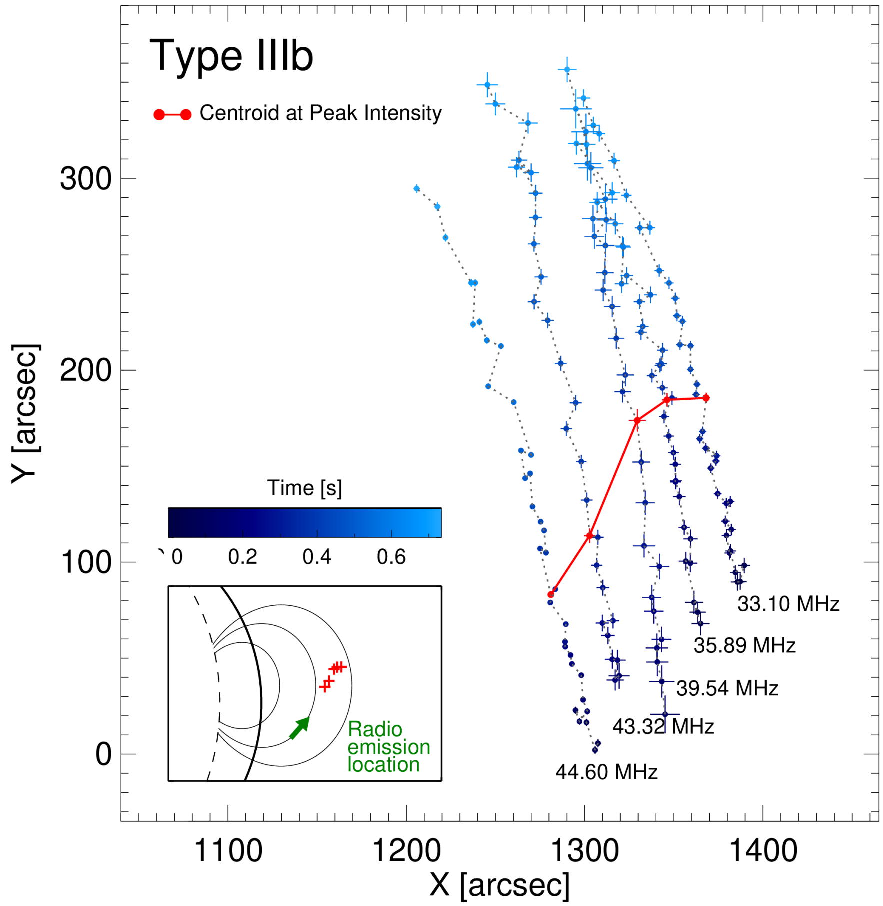

Figure 4.5: Type IIIb J-burst centroid locations of individual striae throughout the FWHM of the time profile at fixed frequencies. The red points and connected line represent the centroid at the peak intensity of each striae. The inset depicts coronal loop field lines with the likely location and path of the radio source (green arrow) corresponding to where the peak trajectory matches the field line direction. The red plus symbols mark the peak centroid locations.

trajectory consistent with that shown by the striae—almost parallel to the limb, as found in section 3.2.5, correlating in position with the closed magnetic field lines implied from the PFSS extrapolation. At a given frequency between 40–45 MHz, the spikes and striae centroids appear to drift linearly, yet at lower frequencies there is a curvature in their motion.

Figure 4.7 compares an individual spike and striae separated by 1.82 s and 207 kHz. The contours represent the intensity of the radio main-lobes, overlaid on the apparent images of the spike emission. The burst contours are aligned in time at their respective peaks, and each panel shows the contour locations in intervals of 0.2 s before and after the peak. During the rise phase, the contour 90% levels overlap almost entirely with the average peak intensity locations above the 90% level separated by tens of arcsec. At the 50% level, the spike contours are varied in shape compared to the striae towards the top left of the image. This is likely

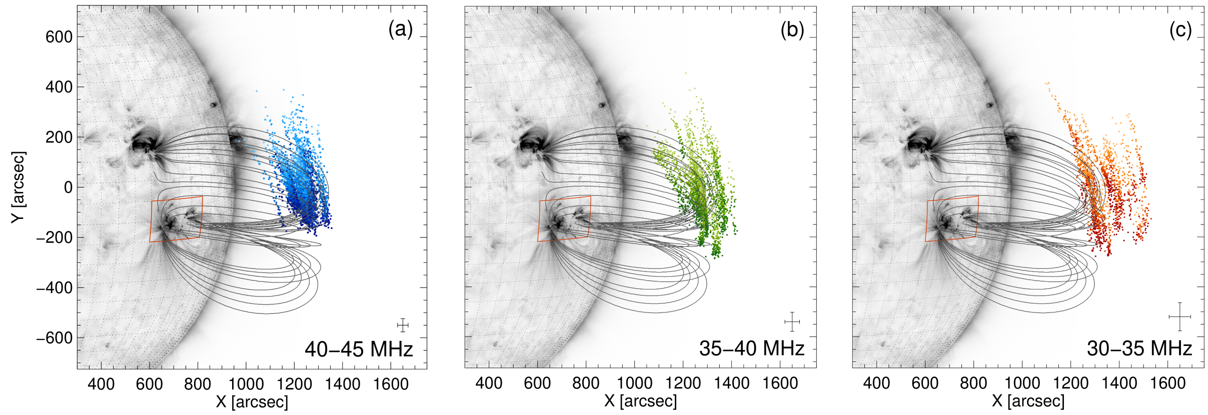

Figure 4.6: Centroid positions of post-CME spikes across the FWHM intensity. Each individual spike is measured along its central frequency, with the collective motion grouped between **(a)** 40 − 45 MHz, **(b)** 35 − 40 MHz, and **(c)** 30 − 35 MHz, and overlaid on an SDO/AIA image at 171 Å. The colour gradients represent time increasing from dark to light. The average centroid error within each frequency band is indicated at the bottom right of each panel. The thin grey lines show the closed magnetic field lines from a PFSS extrapolation. The red box on the solar surface bounds the active region.

a secondary lobe of the PSF (see Figure 6d in Gordovskyy et al., 2022, where observations of Tau A have an irregular ellipse shape) combined with the lower intensity of the spike emission. During the decay phase, the contours are shifted vertically and rotated towards the limb by a similar angle, with the location of peak intensity becoming separated. The shifted distance shown here is greater than that displayed in Figures 4.5 and 4.6 which only show the FWHM period, rather than the full rise and decay phase.

4.2.2 Spike Centroid Velocity, Source Area, & Expansion

From the observed centroid motion in time at fixed frequencies, the spike plane-of-sky centroid velocity can be measured as $v = \sqrt{v_x^2 + v_y^2}$, where $v_x = \mathrm{d}x_c/\mathrm{d}\tau$ is obtained from linear fits to the x centroid position over time, and similarly for v_y. The velocities are often superluminal with an average of 1.27c (Figure 4.8). The measured centroid velocities from radio-wave scattering simulations (Kontar et al., 2019; Kuznetsov et al., 2020) are consistent with the median observed spike velocities, and both data sets show no frequency dependence between 30–45 MHz. The simulated data shown in Figure 4.8 is generated from the code developed in Kontar et al. (2019) for sources placed at a heliocentric angle of 52° corresponding to the lower active region, with varied anisotropy factors (equation 1.34) between 0.1–0.2.

The area of the radio source is measured at the FWHM level using equation 3.4, with uncertainty using equation 3.6. At 30 MHz, the angular resolution of LOFAR is ∼ 9 arcmin (Figure 1.16), and the beam size at the time of observation is 115 arcmin^2, reducing to 64 arcmin^2 at 45 MHz. The areal and linear expansion rates are given by fitting the change

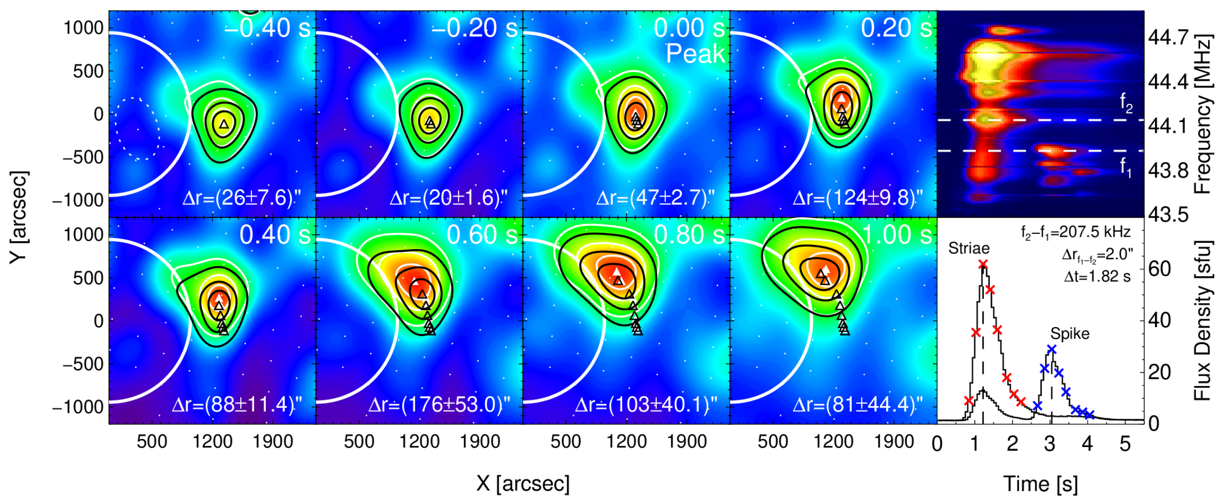

Figure 4.7: Comparison of spike and striae image contours with time. The left panels display contours of spike (white) and striae (black) emission from bursts at 44 MHz that have a peak flux 1.82 s apart, overlaid on the spike images with the background (average intensity of the faintest ten beams) subtracted. The contour levels are given at 90, 75 and 50% of the maximum image flux. The peak of the each burst is set to $t = 0.0$ s, with each panel showing the image at intervals of 0.2 s before or after the peak. The triangle symbols track the motion of the spike (filled white) and striae (black) main lobes, with each symbol marking the average position of the image peak within 10% of the maximum flux at each time. The separation distance of the peak locations in each panel is given by Δr with the uncertainty given as $\delta r = \Delta r[(\Delta x_{\mathrm{err}}/\Delta x)^2 + (\Delta y_{\mathrm{err}}/\Delta y)^2]^{1/2}$ where $\Delta x_{\mathrm{err}}, \Delta y_{\mathrm{err}} \propto \delta I/I_0$, and the peak intensity I_0 uncertainty is $\delta I \sim 1$ sfu. The white dots show the LOFAR beam locations, with the dotted oval in the first panel representing the beam size. The right two panels show the dynamic spectrum with the time profiles of the striae and spike sources along the white dashed lines. The red and blue crosses mark the time positions correlating to the images. $\Delta r_{\mathrm{f_1-f_2}}$ represents the distance in space between ~ 200 kHz according to the density model of equation 1.12.

in area and ellipse axes widths over time during the decay phase with a linear model as in section 3.2.5. The individual spike characteristics between 30–45 MHz measured from imaging can be seen in Figure 4.9. With a larger number of spikes analysed, the median and interquartile range within 3 MHz bands is considered to fit the data. The peak area presents a power-law dependence on frequency with an index of -1.79 ± 0.2, compared to -2.3 ± 0.12 using a smaller sample size in Figure 3.10. The major and minor axis sides decrease with increasing frequency with a power-law index of -0.98 ± 0.2 and -0.83 ± 0.1, respectively. The median areal expansion rate has a power-law relation with frequency, but the spread of data is large at a given frequency. Consequently, the uncertainty in the power-law index is large at -2.70 ± 1.4. Along the major and minor axes, the expansion rates seem to show no frequency dependence, with a median value between 30–45 MHz of approximately 3.5 arcmin s^{-1} and 2 arcmin s^{-1}, respectively.

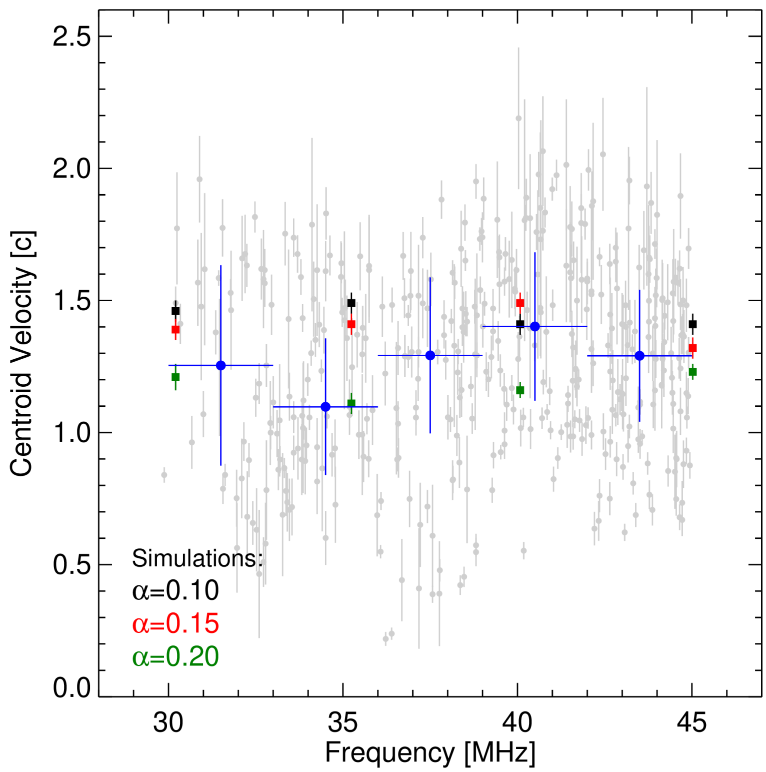

Figure 4.8: Spike plane-of-sky centroid velocities. The light grey points show the data with associated uncertainties. The blue points show the median values across 3 MHz bins with the vertical error as the interquartile range representing the 25th and 75th percentiles. The squares show the centroid velocity calculated from scattering simulations of an initial point source injection located at $\theta = 52°$, anisotropy of the density fluctuation spectrum between $\alpha = 0.1 - 0.2$, and a density fluctuation variance of $\epsilon = 0.8$.

4.2.3 Spike Temporal & Spectral Profiles

The spike time profiles, bandwidth, and drift rates between 30–70 MHz are measured using the same method in section 3.2 and the full set of data can be seen in Figure 4.10, with the mean and median across the same frequency range shown in Table 4.2.3. Some characteristic average values show an oscillation with frequency that correlates with an oscillation in the observed flux from Tau A (Figure 4.10a). Therefore, we regard this as an instrumental artefact and not the result of a physical solar process, as Tau A was not located near the Sun at this time. The uncertainty on the rise and decay times is a combination of the background (~ 1 sfu at 30 MHz, rising to 3–4 sfu at 70 MHz) and flux uncertainty that is typically ~ 1 sfu (Kontar et al., 2017b). Each characteristic shows a wide spread at a given frequency. Nonetheless, the duration, rise, decay times, and bandwidths are fit with power-laws that decrease with increasing frequency. The drift rate, and flux density are better fit with linear models. The statistical sample of spike measurements show that the median decay time is increased by 16% over the rise time.

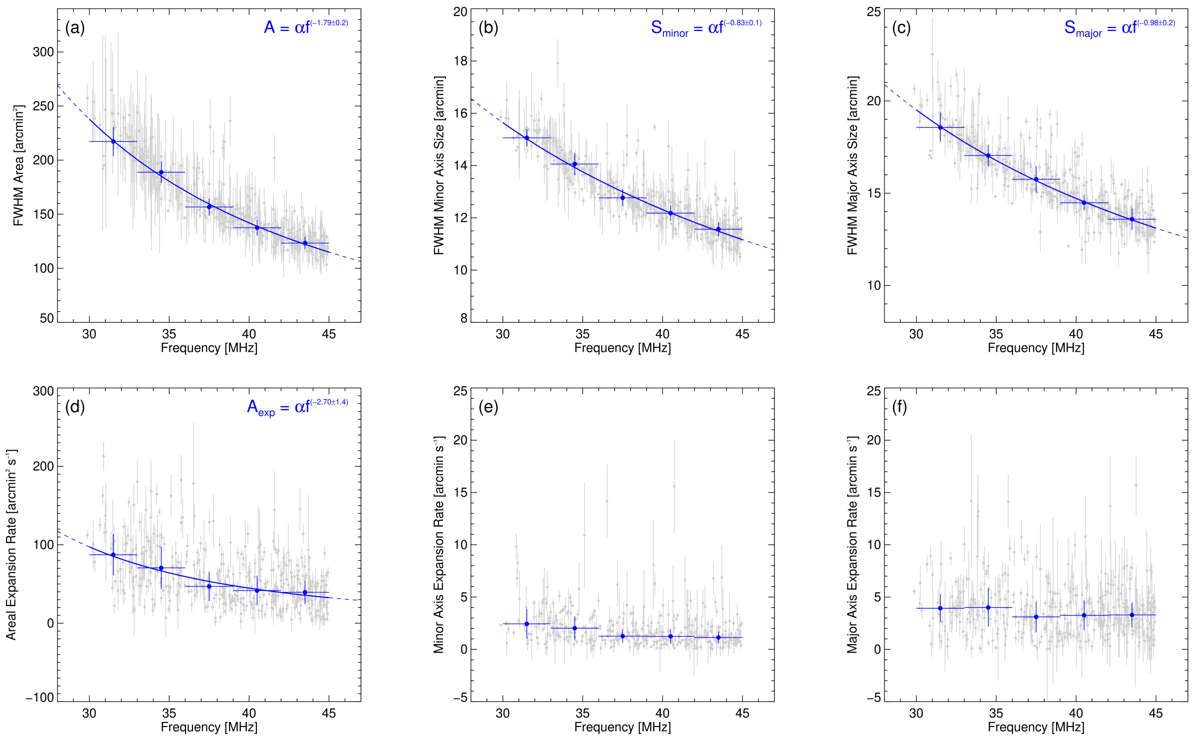

Figure 4.9: Spike characteristics derived from imaging observations. The grey data show the observed quantity and associated uncertainties. The blue points show the median values across 3 MHz bins, with the vertical error as the interquartile range between the 25th and 75th percentiles, and a power-law fit given by the solid blue line. **(a)** Observed FWHM area. **(b)** FWHM minor axis size. **(c)** FWHM major axis size. **(d)** Areal expansion rate. **(e)** Minor axis expansion rate. **(f)** Major axis expansion rate.

Figure 4.11 shows the histogram of spike bandwidth ratios within this event. The distribution is asymmetrical, with a peak near 0.1% followed by a tail that extends up to 0.6%. The peak is similar to that reported by Melnik et al. (2014) between 0.2–0.3% at 20–30 MHz, yet lower than GHz observations by Rozhansky et al. (2008) at 0.7%, although this latter value is decreased to 0.5% by Nita et al. (2008) using an updated spike deconvolution technique that allowed for overlapping spikes to be measured individually. Both aforementioned distributions at GHz frequencies extend up to 3%, a factor of five above that observed by LOFAR in this study, perhaps due to the employed algorithms ability to deconvolve overlapping spikes with larger bandwidths, or differing emission mechanisms. Figure 4.11 also includes the bandwidth ratio for individual striae that share a similar peak and spread to the spikes in this event. The slopes of the two distributions are comparable at the smallest bandwidth ratios, whilst the trends differ above $\Delta f/f \approx 0.0035$, potentially due to overlapping striae broadening the measured bandwidth at lower frequencies. The spike absolute frequency drift rates are typically a few tens of kHz per second, with a weak tendency to increase with frequency. Similarly, the flux density, with a median of ~ 19 sfu, also has a weak frequency dependence in this event.

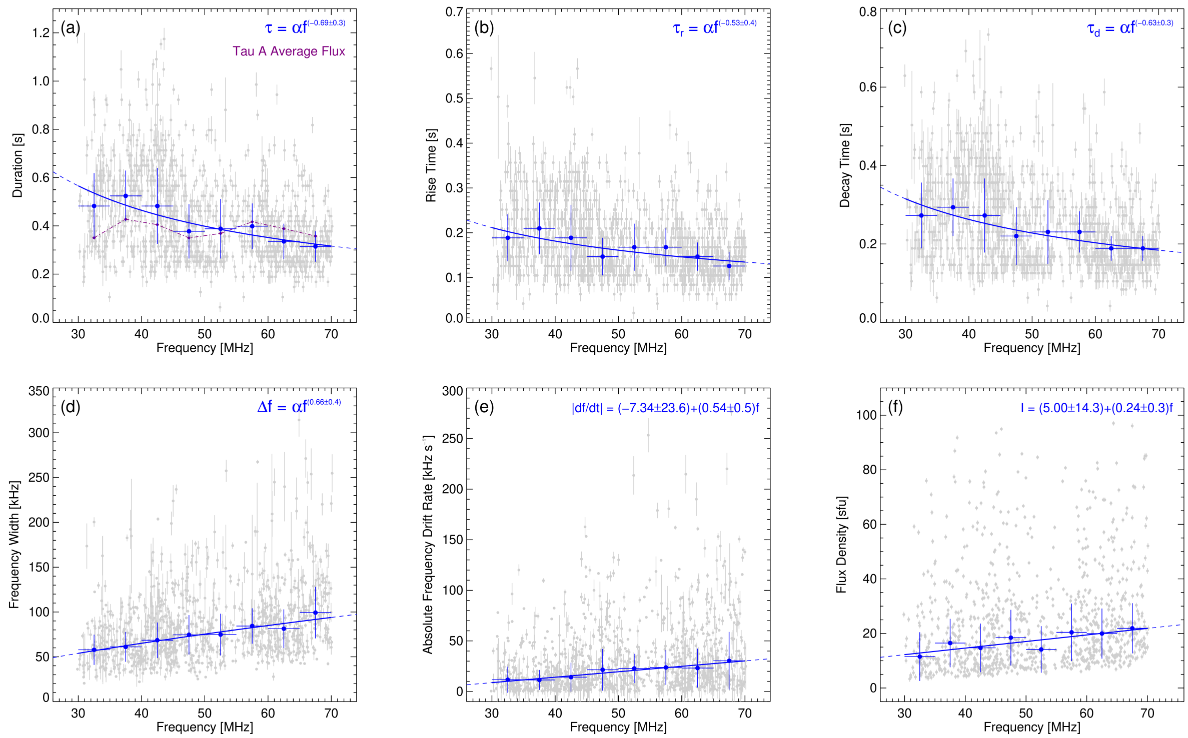

Figure 4.10: Spike characteristics derived from dynamic spectra observations. The light grey points show the data with associated uncertainties. The blue points show the median values across 5 MHz bins, with the vertical error as the interquartile range representing the 25th and 75th percentiles, and a power-law or linear fit shown by the blue line. **(a)** FWHM Duration. The purple points show the median Tau A flux on the day of observation. **(b)** Rise Time at the half-maximum intensity level. **(c)** Decay time at the half-maximum intensity level. **(d)** FWHM bandwidth. **(e)** Absolute frequency drift rate. **(f)** Flux at the lightcurve peak.

4.3 Comparison of Decametre & Decimetre Spikes

4.3.1 Image Sizes

The limited image measurements from previous studies (Krucker et al., 1995; Battaglia et al., 2021) are compared with the median linear spike sizes observed by LOFAR in Figure 4.12. The trend is consistent between each frequency range with a power-law index of $\sim f^{-1}$. However, the decimetre measurements are not resolved along the major axes. Krucker et al. (1995) observes the half-max contour sizes of 110 arcsec (major) and 90 arcsec (minor), yet the instrument beam is 112 arcsec (major) and 59 arcsec (minor), such that the source is resolved only along the minor axis—in Figure 4.12, only the minor axis size is shown with the error set to the upper and lower sizes of the instrument beam. Battaglia et al. (2021) note that the bursts are not spatially resolved, such that the FWHM of the fitted 2D Gaussian is a lower limit. The uncertainty presented in Figure 4.12 represents the instrument beam size.

Characteristic	Units	Mean	Median	Min	Max
Duration, τ	s	0.42	0.38	0.06	1.20
Rise Time, τ_{r}	s	0.18	0.17	0.02	0.57
Decay Time, τ_{d}	s	0.24	0.21	0.04	0.86
Bandwidth, Δf	kHz	83.90	74.86	20.48	314.30
Drift Rate, $\mathrm{d}f/\mathrm{d}\tau$	kHz s^{-1}	30.64	18.93	0.03	276.63
Flux Density, I_0	sfu	32.81	19.05	3.31	1480.71

Table 4.1: Spike characteristics averages and limits from across 30–70 MHz measured from dynamic spectra as defined in Figure 2.4. Note that the maximum observed flux is not shown in Figure 4.10f.

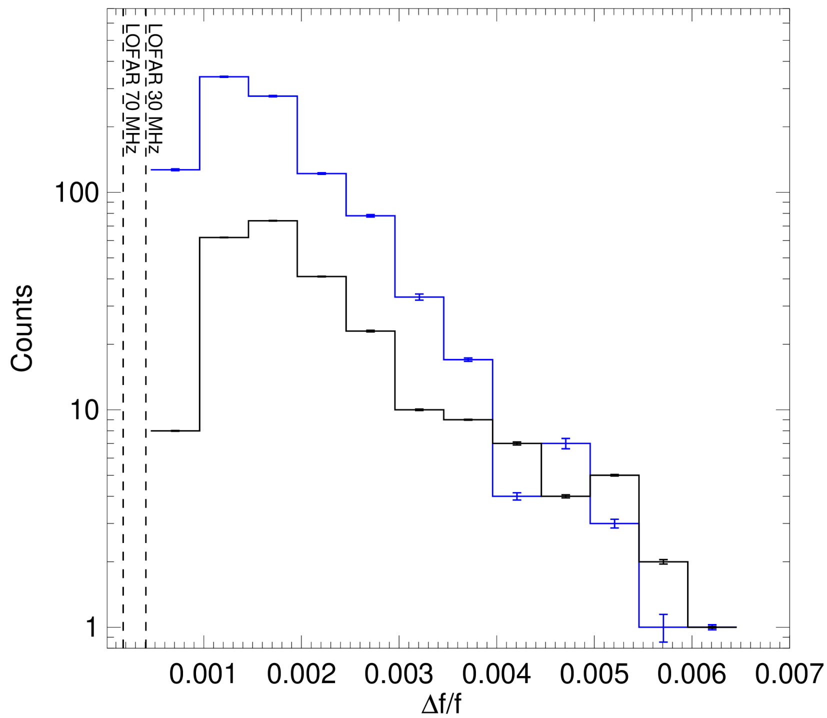

Figure 4.11: Histogram of the spike (blue) and striae (black) bandwidth ratio $\Delta f/f$ distributions with a bin size of 0.05%. The bin errors are given as $\delta N = N\left(\sum_i \delta f_i^2 / \sum_i \Delta f_i^2\right)^{0.5}$, where N is the bin count and δf is the error on the measured bandwidth. The vertical dashed lines show the LOFAR frequency resolution (12.2 kHz) at 30 and 70 MHz.

4.3.2 Decay Times

Figure 4.13 combines spike average $1/e$ decay time measurements between 25 MHz and 1.42 GHz from several authors (McKim Malville et al., 1967; Guedel & Benz, 1990; Barrow et al., 1994; Mészárosová et al., 2003; Shevchuk et al., 2016). The linear fit in log-space indicates a

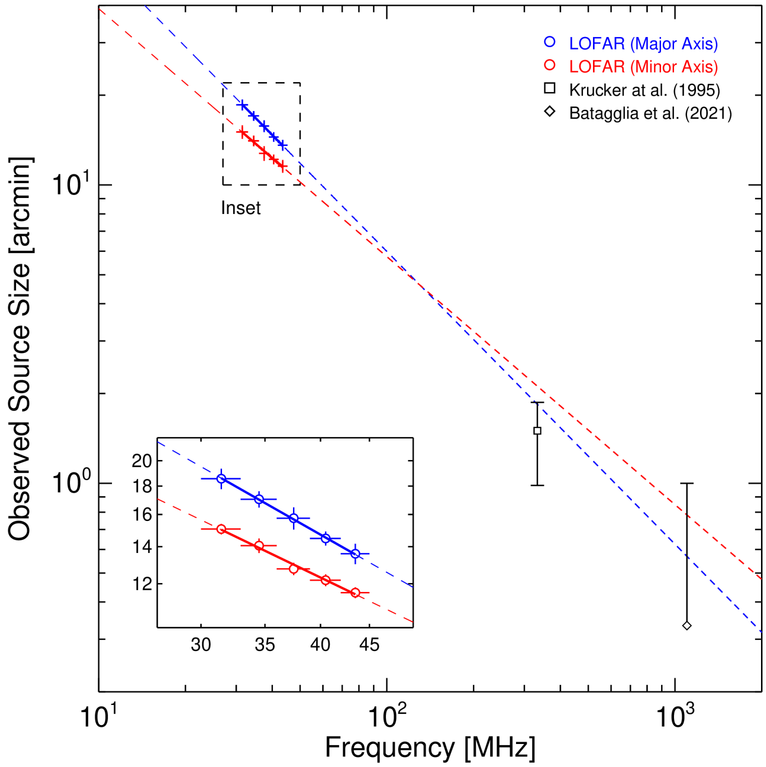

Figure 4.12: Observed source sizes of spikes. The blue and red points show the median major and minor axes FWHM sizes observed by LOFAR from Figure 4.9(b,c), along with higher frequency data from Krucker et al. (1995) and Battaglia et al. (2021).

f^{-1} dependence as

$$\tau_d(f) = (11.22 \pm 1.9) f^{(-1.01 \pm 0.03)}\ \text{s}, \quad 25 \leq f \leq 1420\ \text{MHz}. \tag{4.3}$$

The collisional damping time is included using the form $\tau_\gamma = 1/\gamma_c$ for various coronal temperatures T_e where

$$\gamma_c = \frac{\pi n_e e^4 z_p^2 \ln \Lambda}{m_e^2 v_{Te}^3}, \tag{4.4}$$

as defined in Reid et al. (2011) but with an additional term $z_p = 1.18$ giving the average atomic number in the photosphere (Jeffrey & Kontar, 2011), and with the Coulomb logarithm $\ln \Lambda \approx 23$ (Holman et al., 2011). The density is derived from the frequency using equation 1.15 as $n = (f[\text{MHz}]/8.93 \times 10^{-3})^2$, and the parameters e, m_e, v_{Te} are the electron charge and mass, and thermal velocity, respectively.

Also shown is the inhomogeneity time which is the characteristic time for Langmuir waves to drift in velocity space (e.g. Kontar, 2001b) as

$$\tau_{\text{inh}} = \frac{|L|}{v_b} = \frac{2n_e(r)}{v_b}\left(\frac{\mathrm{d}n_e(r)}{\mathrm{d}r}\right)^{-1} = \frac{2n_e(r)}{v_b}\frac{\lambda}{\delta n_e}, \tag{4.5}$$

where v_b is the electron beam velocity, and λ is the inhomogeneity scale. Here, L is given by

$$L = \omega_{\text{pe}}\left(\frac{\partial \omega_{\text{pe}}}{\partial r}\right)^{-1}, \tag{4.6}$$

and describes the size of ambient plasma density fluctuations (e.g. Kontar, 2001b). Using the chain rule, $\partial\omega_{\text{pe}}/\partial r$ can be described as a function of ω_{pe} that varies with n_e, and n_e that varies with distance r as

$$\frac{\partial \omega_{\text{pe}}}{\partial r} = \frac{\partial \omega_{\text{pe}}}{\partial n_e}\frac{\partial n_e}{\partial r}. \tag{4.7}$$

Considering the term $\partial\omega_{\text{pe}}/\partial n_e$ and substituting equation 1.14, then

$$\frac{\partial \omega_{\text{pe}}}{\partial n_e} = \left(\frac{2\pi e^2}{m_e}\right)\frac{1}{\sqrt{n_e}} \tag{4.8}$$

Substituting $\partial\omega_{\text{pe}}/\partial n_e$ and ω_{pe} into L then gives

$$L = 2n_e\left(\frac{\partial n_e}{\partial r}\right)^{-1}. \tag{4.9}$$

For the density profile $n(r)$, equation 1.10 is considered with the additional chromospheric term of equation 1.11 due to the inclusion of high frequency (low coronal height) data. The electron beam velocity is set to $v_b = 10^{10}$ cm s^{-1}, and the scale λ is set to vary linearly from 2 km at 1.03 R$_\odot$ ($f_{\text{pe}} = 1.4$ GHz) to 100 km at 2 R$_\odot$ ($f_{\text{pe}} = 20$ MHz), with fixed density fluctuation amplitudes of $\delta n_e/n_e = 0.003$ and 0.01. This gives $|L| \sim (0.04-2)\times10^4$ km when $\delta n_e/n_e = 0.01$ and $|L| \sim (0.1-6)\times10^4$ km when $\delta n_e/n_e = 0.003$, where the upper values of $|L|$ are similar to that considered by Kontar (2001b) for electron beam dynamics with a fluctuating background density. As noted in Kontar (2001b), $\tau_{\text{inh}} > \tau_{\text{ql}}$ where τ_{ql} is the quasilinear time (equation 1.16), and so the plasma inhomogeneities can be considered as an evolution of the final stage of quasilinear relaxation.

4.3.3 Bandwidth

Combined average spike bandwidth observations as a function of frequency between 10 MHz and 8 GHz are shown in Figure 4.14 with data from Markeev & Chernov (1971); Tarnstrom & Philip (1972a); Benz et al. (1982); Benz (1985); Staehli & Magun (1986); Benz et al. (1992b); Csillaghy & Benz (1993); Benz et al. (1996); Wang et al. (1999); Messmer & Benz

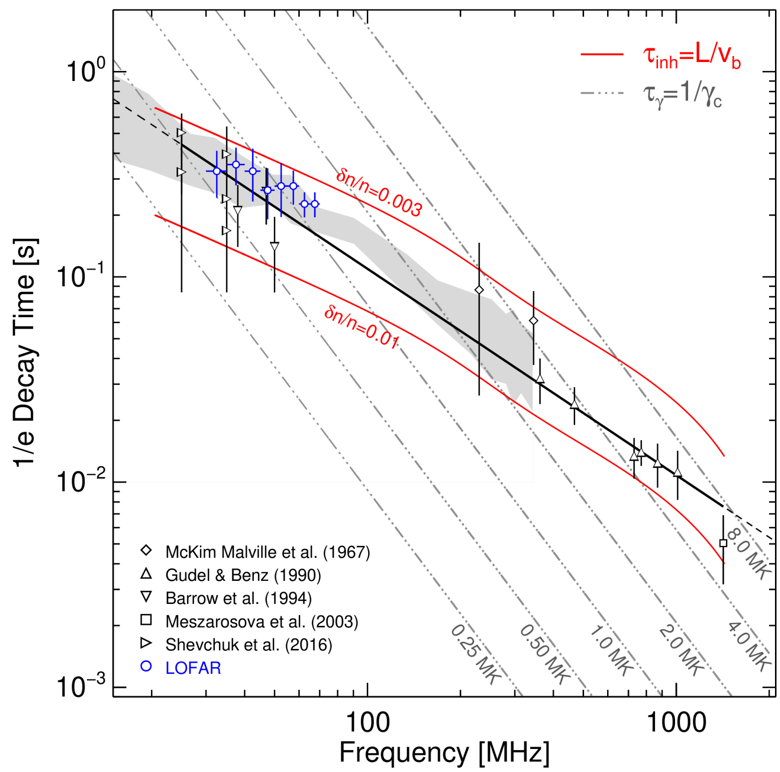

Figure 4.13: Average spike $1/e$ decay times against frequency. LOFAR data show the median from Figure 4.10(c) adjusted from the FWHM by a factor of $\sqrt{\ln 2}$. The solid black line represents a power-law fit to the data given by equation 4.3. The grey dash-dotted lines represent the plasma collision time for various coronal temperatures. The grey region shows the scattering decay time contribution for $\alpha = 0.2$ between $\epsilon = 0.5$ (lower bound) and 2.0 (upper bound). The scattering simulation data was provided courtesy of E. Kontar. The red curves show the inhomogeneity time as defined by equation 4.5 for fixed values of $\delta n/n$ as shown. For each curve, the inhomogeneity scale varies from 2 km at 1.03 $R_\odot$ to 100 km at 2 $R_\odot$.

(2000); Wang et al. (2008); Nita et al. (2008); Rozhansky et al. (2008); Wang et al. (2002); Dabrowski et al. (2011); Melnik et al. (2014); Shevchuk et al. (2016); Tan et al. (2019). The instrument spectral resolutions are included as solid diagonal lines. At high frequencies above 200 MHz, the average values are close to the instrumental limit in many cases. Despite the possibility of over-estimated average bandwidths at the higher frequencies due to these limited spectral resolutions, the increase of $\Delta f/f$ above 200 MHz is expected via consideration of the Langmuir wave dispersion relation in a weakly magnetized plasma (Melrose, 1985; Pécseli, 2012; Melnik et al., 2014; Shevchuk et al., 2016) as given by equation 1.20 and repeated here

$$\omega = \omega_{\rm pe} + \frac{3k^2 v_{\rm Te}^2}{2\omega_{\rm pe}} + \frac{\omega_{\rm ce}^2}{2\omega_{\rm pe}} \sin^2\psi, \tag{1.20}$$

where ψ is the angle between the plasma wave direction and the magnetic field, and $\omega_{\mathrm{ce}} = eB/m_e c$ is the electron cyclotron frequency. Equation 1.20 is valid under the condition that $\omega_{\mathrm{ce}} \ll \omega_{\mathrm{pe}}$ for electron beams where the spatial size is $< 10^8$ cm (Melnik et al., 2014). Figure 4.14 shows the expected bandwidth $\Delta\omega = \omega(\psi) - \omega(0)$ for varied magnetic field strengths based on the model by Gary (2001) shown in equation 1.7 with terms B_f varied between 100–800 G as shown in panel (b), and the density model of equation 1.10 and 1.11, shown in panel (c). A value of $B_f = 500$ G gives a magnetic field strength of ~ 300 G at a height of 0.02 $\mathrm{R}_\odot$ from the solar surface, as estimated by Kontar et al. (2017a). We choose $\psi = 23°$ to provide the best match to the low frequency spike population trend when $B_f = 100$ G, similar to the angle of 20° by Zaitsev (1975) for Type III bursts.

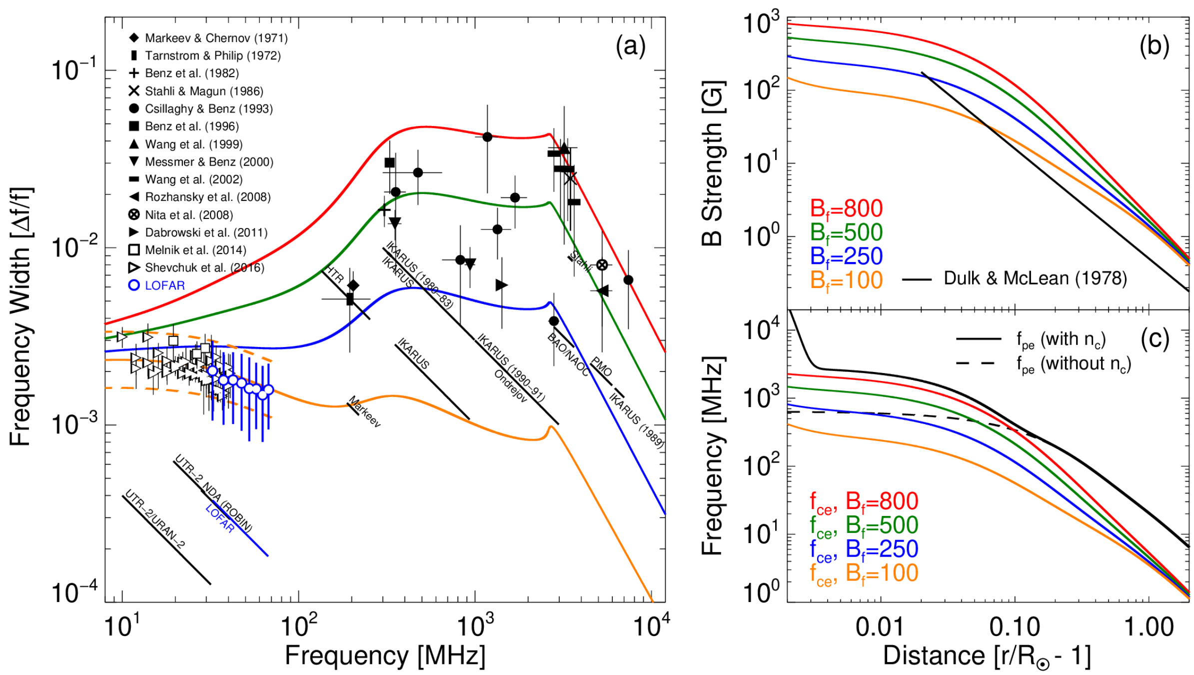

Figure 4.14: (a) Average spike bandwidth ratio $\Delta f/f$ (where Δf is given at the FWHM level) against frequency combining observations as indicated in the legend. LOFAR data show the median from Figure 4.10(d). The diagonal lines represent the instrument resolutions. The coloured curves denote the bandwidth derived from the Langmuir wave dispersion relation in a magnetized plasma (equation 1.20) with $\psi = 23°$. Each colour uses a the magnetic field model of Gary (2001) with the constant B_f varied. The orange dashed curves vary ψ from 19° (lower) to 28° (upper). (b) The magnetic field models with distance. Also shown is the magnetic field model from Dulk & McLean (1978) as $B(r) = 0.5(r/\mathrm{R}_\odot - 1)^{-1.5}$. (c) The plasma and cyclotron frequencies from the density and magnetic field models.

4.4 Discussion

1076 solar radio spikes were analysed to statistically retrieve their characteristics in the decametre range. The spike centroid locations were compared with individual Type IIIb striae within a coronal loop structure. The apparent radio map contours of each burst type that are close in time (less than a few seconds) and frequency overlap with little variation in position and shape, with any clear separation occurring during the decay phase. Both burst types experience comparable and significant displacement along the loop direction at fixed frequencies with substantial broadening over time, predominantly along the major axis.

4.4.1 Beam Velocities & Emission Heights

From the Type IIIb bulk frequency drift, the electron beam velocity can be estimated. The reverse-slope component corresponds to a beam velocity of $0.3c$, whilst the outward propagating beam has a velocity of $0.1c$, which could indicate an asymmetry in the energy injected in each direction. Pre-CME, the spikes show an increase of height with decreasing frequency. After the CME ejection at approximately 10:52 UT (indicated by the Type III burst onset as shown in Figure 3.1 and jet (Chrysaphi et al., 2020)), the observed spike and Type IIIb striae heights weakly vary with frequency. This could be caused by the magnetic field being distorted from the passing CME shock such that the density gradient and loop trajectory is along the line of sight. The loop may then restore over tens of minutes towards the prior configuration with a velocity of ~ 90 km s^{-1} (Figure 4.4). The bursts near 45 MHz seem to retain an approximately constant height, whilst those towards 30 MHz experience the bulk of the shift, which implies the bulk of the rotation and/or expansion of the magnetic field occurs at the lower frequencies towards the loop top, possibly due to the decreased magnetic pressure with increasing height.

4.4.2 Anisotropic Scattering

The spike and striae centroids present two components of motion: an exciter-driven frequency dependent radial motion resulting from the electron beam motion, and a shift perpendicular to the radial direction over time at fixed frequencies. The latter is assumed to be independent of the exciter motion since variations in the ambient density or magnetic field will be stable over the time periods of 0.1–0.5 s, meaning that the plasma frequency corresponding to a given spatial location will not vary whilst the beam propagates through a given location. For example, in-situ electron density measurements using PSP show density fluctuations on scales of tens of minutes (Moncuquet et al., 2020, see Figure 7 that uses a temporal cadence of 57 s); and Krupar et al. (2020) show that the density fluctuations $\delta n_e/n_e$ decrease with decreasing time interval, reducing down to $\delta n_e/n_e \approx 0.05$ across 10 s intervals (see their Figure 10) when PSP was 35.7 $R_{\odot}$ from the Sun. Moreover, the fluctuations within the Earth's ionosphere are not expected to change over such short timescales (section 1.4.2). Therefore, any positional change due to ionospheric refraction will not cause variation in the observed source position over the short time periods considered here. The fixed frequency displacement is then attributed to radio-wave scattering in an anisotropic turbulent medium (section 1.4.1.1). The centroid locations therefore provide insight into the magnetic field structure: above 40 MHz, the displacement is linear, becoming arced towards the limb at lower frequencies such that the field structure may have greater curvature farther from the Sun.

We show that the median fixed frequency centroid velocities present no frequency dependence between 30–45 MHz, and are replicated with radio-wave scattering simulations using strong levels of anisotropy ($\alpha = 0.1 - 0.2$). Whilst varying the anisotropy factor causes a small change in the centroid velocity, the major influence is the magnetic field angle to the observer—for a field aligned perpendicularly to the observer's line of sight, the observed centroid velocity will be maximal. The spread in observed velocities at a given frequency for spikes at different times suggests that the source locations are distributed across a range of angles within the loop, and that the anisotropy and turbulence levels may fluctuate over time.

4.4.3 Event Interpretation

The interpretation of the event is shown in the cartoon of Figure 4.15. Beam acceleration most likely occurs along the ascending loop leg towards the lower flank of the CME, at a region closer to the Sun where the magnetic field geometry has a radial trajectory, inferred from the peak frequency drift in Figure 4.5. Interestingly, the Type II observed during this event is suggested to have occurred towards the opposite CME flank (Chrysaphi et al., 2020). The passage of the CME perturbs the magnetic geometry, rotating the loops towards the observer, causing any frequency dependence of emission to be masked in the sky-plane. Post-CME, repeated magnetic reconnection and subsequent electron beam acceleration produces a greater number of spikes than in the pre-CME case. Interestingly, the greatest number of spikes used in this work occurs approximately 30 minutes after the soft X-ray peak (Figures 3.1 and 4.4) similar to the spike events analysed in Cliver et al. (2011) and Marqué et al. (2018), although it should be noted that the spikes in this event were manually selected from select time periods and will not include all spikes throughout the event. Nonetheless, the increased spike density tens of minutes after the flare is apparent. As the field restores towards its original configuration, a sky-plane drift of the imaged emission source locations is observed at a speed of almost 100 km s^{-1} (Figure 4.4). The distance from the acceleration region and location where the source begins emitting will depend on the beam density, velocity, and turbulence that determine the spatial location of Langmuir wave growth. The emission quickly undergoes radio-wave scattering, with the strongest scattering power perpendicular to the field lines at a given location, such that the likely direction of photon propagation is parallel to the field where the scattering power is weakest. This direction changes over time and distance due to the field geometry. The observed centroids are then displaced along the loop direction at fixed frequencies over time and expanded in area, with the true source location never observed.

The spikes were observed to be spread across many frequencies at a given time, implying that the acceleration heights may vary, and/or the electron beams have differing initial densities and spatial sizes which can increase the onset time and burst starting frequencies (Reid et al., 2011; Reid & Kontar, 2018a). The former agrees with the interpretation of spikes arising from many small sites of magnetic reconnection (Benz et al., 1982; Benz, 1985) which may have been triggered by the CME. The frequency at which a spike is observed could then be an interplay between the acceleration location, the initial beam properties, and the coronal turbulence that will promote Langmuir wave growth at a specific region of space.

4.4.4 Radio-wave Scattering Dominance

The scatter-dominated characteristics of spikes (source size, decay time) present power-law trends between decametre and decimetre observations. At 30 MHz, estimation of the intrinsic source size suggests $l < 2r_n \Delta f/f \approx 1$ arcsec where $\Delta f/f \sim 2\times10^{-3}$ (Figure 4.11). Following the same approach at 333 MHz, Krucker et al. (1995) note a similar intrinsic size of 2 arcsec using a density scale height of 10^{10} cm, rather than 1.57×10^{10} cm considered here. The spike duration and plasma collision time similarity has led to previous suggestions of this damping mechanism to be the dominant factor controlling their short time profiles (section 2.3.2). Using the collision time to infer the coronal temperature gives a range between 0.5–8.0 MK from 25 MHz to 1.4 GHz in Figure 4.13. However, due to significant broadening in time, the inferred temperatures would be reduced. At 30 MHz, typical decay times from simulations are ~ 0.2 s for $\alpha = 0.2$ (Kontar et al., 2019), reducing the median observed decay time in this study to 0.1 s and the coronal temperature to < 0.25 MK, much lower than expected above an active region. Figure 4.13 presents a $1/f$ trend for spike decay times, with a similar power-law index to that for Type III bursts (equation 1.29; Kontar et al., 2019). In addition, it is shown that the inhomogeneity time τ_{inh}, which is the characteristic time for Langmuir waves to drift in velocity space (Kontar, 2001b), can match the observed $1/f$ trend for given input parameters as described in section 4.3.2. We see that varying the value of $\delta n_e/n_e$ can explain the spread in the observed data, where larger fluctuation amplitudes causes the Langmuir waves to drift in velocity space faster, resulting in shorter decay times—and indeed, $\delta n_e/n_e$ would be expected to vary from event to event. However, the trend required to match the observations with frequency is found from the inhomogeneity length scale λ linearly increasing with r—we estimate this to range from

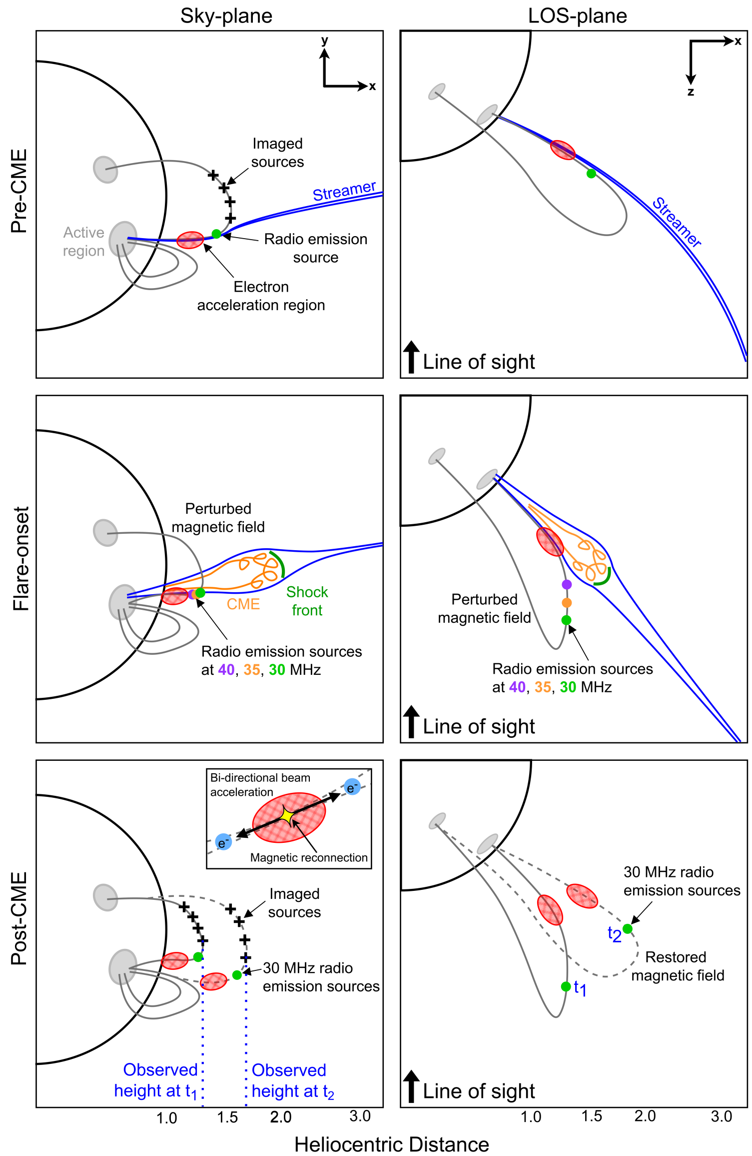

Figure 4.15: A cartoon of the event before and after the CME eruption. The two columns show the x, y sky-plane and z, x line-of-sight (LOS) planes, respectively, with each column showing the configuration pre-CME, during the flaring period, and post-CME. Pre-CME, a smaller number of spikes are observed with source emission locations (coloured circles) and electron acceleration (red hatched regions) likely occurring along the lower loop leg via magnetic reconnection interaction between the loops (grey lines) and streamer (blue lines). At the onset of the flare and eruption of the streamer-puff CME (orange line) caused by a jet at the lower active region, the streamer is inflated due to the CME-driven shock (green line) that also perturbs the magnetic loop geometry towards the observer. The rotation of the loop means that the frequency dependence of the observed spike sources is masked. Throughout the remaining observation window, repeated magnetic reconnection occurs, accelerating electron beams along the loop direction leading to an increased number of spike sources. In the post-CME phase, the magnetic field restores towards its original configuration, such that the observed emission at the same frequency appears at larger sky-plane heights over time, moving across the sky-plane at a velocity of 90 km s^{-1} between t_1 and t_2. The imaged sources are observed to drift along the direction of the magnetic field due to anisotropic radio-wave scattering such that their centroids (black crosses) drift upwards in the sky-plane over time at fixed frequencies. The inset in the lower left panel shows counter-propagating electron beams induced by magnetic reconnection that can then produce the bi-directional Type IIIb. The streamer and shock front are not shown in the lower panels, and the smaller loops connected to the lower active region are excluded from the LOS-plane, for clarity.

2–100 km between 1.03–2.0 $R_\odot$. The inhomogeneity time is also similar to the scattering induced decay time from simulations (grey region in Figure 4.13) using the code described by Kontar et al. (2019), which is dictated by the density fluctuations. Since the observed time profile is a combination of both the intrinsic duration and broadening due to scattering as $\tau = (\tau^2_{\text{source}} + \tau^2_{\text{scat}})^{1/2}$, if $\tau_{\text{source}} \ll \tau_{\text{scat}}$ as the observations suggest, then radio-wave scattering is the dominant contribution, and governs the observed decay time.

4.4.5 Magnetic Field Strength

The spread in $\Delta f/f$ can be predicted via the Langmuir wave dispersion relation (Figure 4.14), which is significantly modified near 400 MHz through variation of the magnetic field strength which could vary substantially between events. It should be noted that the theoretical spectral shape of spikes produced via plasma emission is not described with this relation, which remains an open question outside the scope of this study. For Langmuir wavevectors spread between the magnetic field direction at $\psi = 0°$and $\psi = 23°$, the dispersion relation predicts values of $\Delta f/f$ that match the average trend of the low frequency spikes, with the full set of low frequency data that was considered accounted for by varying the maximum ψ angle between 19–28°. Fixing $\psi = 23°$, then between 0.4–3.5 GHz, the data suggest that the magnetic field strength between events could vary from 30–800 G. In the decametre range, for spikes observed between 20–70 MHz (1.45–2.0 $R_\odot$ for the density model considered), the magnetic field strength varies between 1.2–3.5 G, larger than the model above active regions by Dulk & McLean (1978) of 0.5–1.65 G. However, this model is derived from a compilation of different techniques where the data have a spread within a factor of three. It suggests that decametre spike events are associated with active regions that have stronger magnetic fields than average by a factor of ~ 2.

4.5 Conclusion

Solar radio spikes and Type IIIb bursts are observed to be associated with a trans-equatorial closed loop system, and could be associated with repeated magnetic reconnection in numerous small sites triggered by a streamer-puff CME. The observed bandwidth ratios suggest that the size of the emitting region is less than 1 arcsec, which evolves in position over several tens of minutes owing to a perturbed magnetic geometry caused by the CME and shock propagation. Spikes and striae that are close in time and frequency have 90% intensity contours that almost completely overlap, suggesting the sources emit radio-waves from the same region of space. The emitting location will be determined by an interplay of the electron beam acceleration site, the beam characteristics, and the turbulent conditions. Fixed frequency imaging of both burst types reveals strongly directive, superluminal centroid motion along the guiding magnetic field parallel to the solar limb, consistent with radio-wave scattering in an anisotropic medium. The observed spread in centroid velocity could be due to varying anisotropy, turbulence level, and emission angle within the loop. The strong scattering environment means that the emitting source locations do not correspond to the locations of the observed sources—from the Type IIIb frequency drift, the beam trajectory is likely associated with a region of the loop closer to the Sun along the ascending leg where the field trajectory is closer to the radial direction. Consequently, the region of acceleration and emission could be near the CME flank, and driven by magnetic reconnection with adjacent field lines. The frequency dependence of scattering dominated properties from decametre to decimetre wavelengths present a consistent $1/f$ trend, similar, but not identical to that for type III bursts, suggesting that radio-wave scattering is significant in both domains and governs the observed decay and sizes. Assuming plasma emission, the observed spike bandwidth ratios can be replicated via the Langmuir wave dispersion relation for conditions where $f_{\rm ce} \ll f_{\rm pe}$, with an order of magnitude increase above 400 MHz due to strongly varying magnetic field strength between events at this scale. However, ECM emission can not be discarded as the mechanism for spikes at GHz frequencies. In the decametre range, the compilation of spike observations suggest that the magnetic field strength is stronger than average above active regions by a factor of ~ 2.

5

Radio-wave Propagation Simulations

Recent solar radio burst fine structure observations and simulations have shown that an anisotropic environment is required to reproduce the observed characteristics such as decay time, size, and centroid motion (section 2.1). Moreover, the aforementioned quantitative investigations have studied this source motion using anisotropic simulations of radio-wave scattering, successfully recreating the source positions, sizes, and time profiles simultaneously (Kontar et al., 2019; Kuznetsov et al., 2020; Chen et al., 2020). However, these simulations have considered radially aligned, spherically symmetric coronal magnetic fields; yet, as is shown in chapters 3 and 4, there are instances where radio sources display non-radial, fixed frequency motion over time associated with a coronal loop. So far, the anisotropic turbulent nature and subsequent radio-wave scattering within coronal loops has not been investigated.

In addition to the centroid motion and broadened source sizes due to scattering in radio imaging observations, fine structure morphology in dynamic spectra can be heavily modified. In particular, the broadened time profiles at each frequency channel will smear out the fine structure, leading to a visibly reduced drift rate as suggested in section 3.3. Indeed, solar radio spikes can have distinct drift rates between decametre and decimetre emission, with spikes near 1 GHz typically presenting drift rates on the order of 10^3 MHz s^{-1} (e.g. Dabrowski et al., 2005), while spikes near 30 MHz have drift rates near tens of kHz s^{-1} (e.g. Melnik et al. (2014) and chapter 3), leading to dissimilar morphology in dynamic spectra. The drift rates of individual striae of Type IIIb bursts (on the order of tens of kilohertz per second at decametre frequencies (Sharykin et al., 2018)), are significantly lower than the bulk drift of the Type IIIb structure at ~ 10 MHz s^{-1} (e.g. Chen et al., 2018). Such low drift rates are not consistent with the exciter motion on the order of $c/3$, and thus require a different driving mechanism. Fine structure drift rates have been associated with density fluctuations and propagating MHD waves (Chen et al., 2018; Kolotkov et al., 2018), and as noted in section 2.1, were recently linked to the Langmuir wave drift at the group velocity and the coronal temperature using simulations of electron beam propagation (Reid & Kontar, 2021). Consequently, if the drift rate is considered without correcting for the dilution due to scattering effects, then the Langmuir wave group velocity and coronal temperature estimate will be underestimated. Combined with the unobserved emitter location due to anisotropic scattering, a complete picture of the source location and accompanying intrinsic characteristics is challenging without decoupling the scattering component.

In this chapter, the role of anisotropic scattering on radio source motion and fine structure drift rates in closed magnetic fields is investigated. The scattering model by Kontar et al. (2019) is extended to account for the magnetic field configuration of coronal loops approximated as a dipole. The directivity of the escaping radiation is analysed through analysis of the simulated image centroid motion, and the fine structure drift rates in dynamic spectra for simulated narrowband radio pulses convolved with a scattering function.

5.1 Ray-tracing Simulation Set-up

The numerical code is based on that described in Kontar et al. (2019) which uses a kinetic approach to simulate the propagation of radio waves in a turbulent medium based on the Fokker-Plank and Langevin equations. The initial source heights r_s are set to $r_s = 1.75\ R_\odot$, corresponding to a plasma frequency of $f_{pe} = 32$ MHz and emission frequency of $f = 35.2$ MHz, assuming an emission ratio of $f = 1.1 f_{pe}$ (fundamental emission). This frequency is chosen in order to compare to both the fine structure observations in chapters 3 and 4, as well as previous simulations using a radial magnetic field (Kontar et al., 2019; Kuznetsov et al., 2020; Chen et al., 2020). At this height, the magnetic field is relatively weak on the order of ~ 1 G (e.g. Dulk & McLean, 1978; Kolotkov et al., 2018), and the unmagnetised plasma dispersion relation for radio waves is considered by equation 1.22 as $\omega^2 = \omega_{pe}^2 + k^2c^2$ where ω_{pe} is the plasma frequency (equation 1.14). The background density $n_e(r)$ is modelled as in Kontar et al. (2019) as given by equation 1.10, and repeated here

$$n_e(r) = \frac{4.8\times10^9}{r^{14}} + \frac{3\times10^8}{r^6} + \frac{1.4\times10^6}{r^{2.3}}, \tag{1.10}$$

where r is expressed in solar radii. The group velocity of the turbulence is far less than the speed of light such that the density fluctuations are considered to be static over the transit time of the photons. Near the plasma frequency, the small-scale density fluctuations cause the refractive index (equation 1.31) to vary such that the photons experience small angular deflections and are rapidly scattered. The scattering is elastic such that the photon frequency is conserved. In addition, the numerical code simulates the effects of refraction due to the large-scale variation of the plasma density, as well as free-free absorption of propagating electromagnetic waves with a rate given by

$$\gamma = \frac{\omega_{\mathrm{pe}}^2}{\omega^2}\gamma_c, \tag{5.1}$$

where

$$\gamma_c = \frac{4}{3}\sqrt{\frac{2}{\pi}}\frac{e^4 n_e(\boldsymbol{r})\ln\Lambda}{m_e^2 v_{\mathrm{Te}}^3}. \tag{5.2}$$

The thermal speed is $v_{\mathrm{Te}} = \sqrt{T_e/m_e}$ with $T_e = 129$ eV, equivalent to an average coronal temperature of 1.5 MK (McLean & Labrum, 1985), and the Coulomb logarithm is set to $\ln\Lambda \simeq 20$ as used in Kontar et al. (2019).

The density fluctuation spectrum is parametrised by

$$S(\boldsymbol{q}) = S\left[\left(q_\perp^2 + \alpha^{-2}q_\parallel^2\right)^{1/2}\right], \tag{5.3}$$

where $\alpha = q_\parallel/q_\perp$ defines the anisotropy of the density fluctuation spectrum, and $\boldsymbol{q}$ is the wavevector of the density fluctuations with components in the parallel $q_\parallel$ and perpendicular $q_\perp$ directions. When $\alpha = 1$, the density fluctuation spectrum is isotropic, and anisotropic when $\alpha < 1$. Correspondingly, when $\alpha \ll 1$, the density fluctuation spectrum is dominated by fluctuations with smaller wavenumber in the parallel direction. The angular scattering frequency ν_s is set to

$$\nu_s = \frac{\pi}{8}\overline{q\epsilon^2}\frac{\omega_{\mathrm{pe}}^4 c}{\omega(\omega^2 - \omega_{\mathrm{pe}}^2)^{3/2}}, \tag{5.4}$$

with units of radians^2 s^{-1} where

$$\epsilon^2 = \frac{\langle \delta n_e{}^2\rangle}{n_e^2} = \int S(\boldsymbol{q})\frac{d^3q}{(2\pi)^3}. \tag{5.5}$$

and the heliospheric model of the spectrum-averaged mean wavenumber $\overline{q\epsilon^2}(r)$ is defined as in Kontar et al. (2023, submitted) given by

$$\overline{q\epsilon^2}(r) = 2\times 10^3\alpha\left(\frac{R_\odot}{r}\right)^{0.7}\left(1 - \frac{R_\odot}{r}\right)^{2.7}\eta^2, \tag{5.6}$$

with an extra factor η that acts as a scaling factor to reduce ($\eta < 1$) or increase ($\eta > 1$) the scattering rate. The scattering frequency is then proportional to the spectrum averaged mean wavenumber $\overline{q\epsilon^2}$. Figure 5.1 shows the variation in the model of $\overline{q\epsilon^2}$ with distance from the Sun, normalised as a dimensionless quantity by 1 $R_\odot$. The scattering rate increases with increasing distance from the Sun to a peak between a heliocentric distance of 4 to 7 $R_\odot$, before decreasing further into the heliosphere.

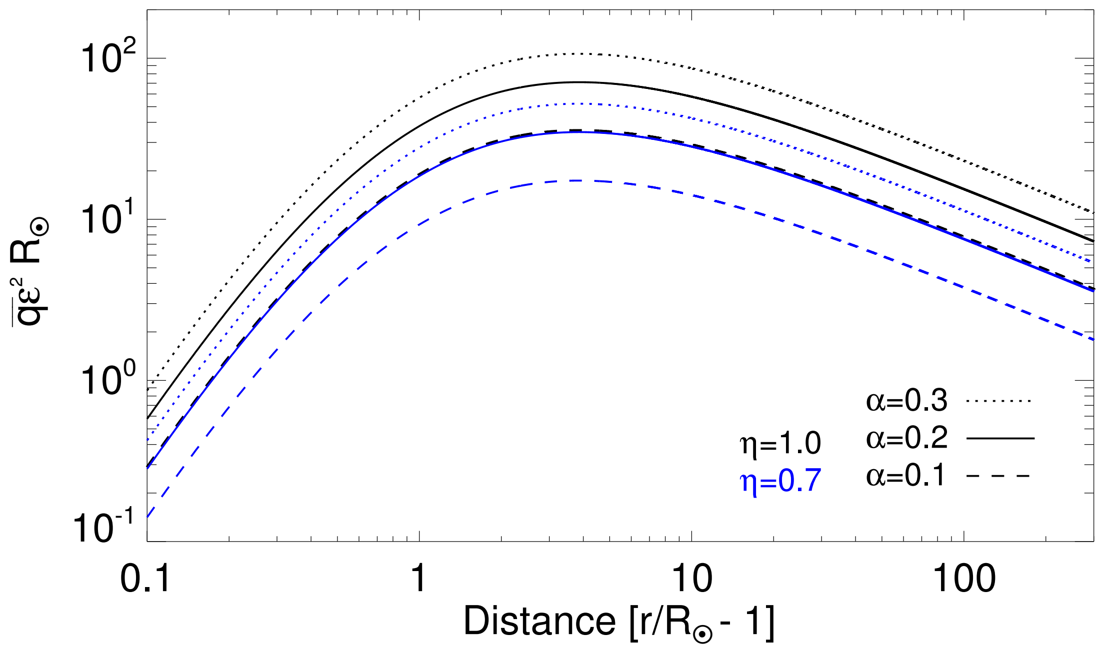

Figure 5.1: The model of $\overline{q\epsilon^2}(r)$ given by equation 5.6 for different values of η and α.

Figure 5.2 shows the spherical coordinate system (r, θ, ϕ) where θ is the azimuthal angle from the z-axis in the range $-\pi \leq \theta \leq \pi$, and ϕ is the polar angle between $-\pi/2 \leq \phi \leq \pi/2$ with $\phi > 0$ towards the solar north. The presence of a coronal loop is approximated with a dipolar magnetic field model where the dipole centre is shifted to a location given by $(r_\mathrm{d}, \theta_\mathrm{d}, \phi_\mathrm{d})$. The radio source is assumed to be a point source given by the coordinates $(r_\mathrm{s}, \theta_\mathrm{s}, \phi_\mathrm{s})$. In the Sun-centred coordinate system (x, y, z), the observer lies along the $+z$-axis such that the x, y axes form the plane-of-sky.

The dipole magnetic field equations are

$$\boldsymbol{B}(\boldsymbol{r}) = \frac{B_0}{r^3}\left(2\cos\theta\hat{\mathbf{r}} + \sin\theta\hat{\boldsymbol{\theta}}\right), \tag{5.7}$$

where $B_0 = (B_r^2 + B_\phi^2 + B_\theta^2)^{1/2}$, set such that at $\sim 2\,\mathrm{R}_\odot$ the strength is comparable to the Parker spiral (approximately 0.8 G) according to the $1/r^3$ scaling. Despite being a simple model for the field above an active region, the approximation is reasonable far from the photosphere (e.g. Bandiera, 1982; Kundu & Alissandrakis, 1984; Ryabov et al., 1999).

5.2 Numerical Simulation Results

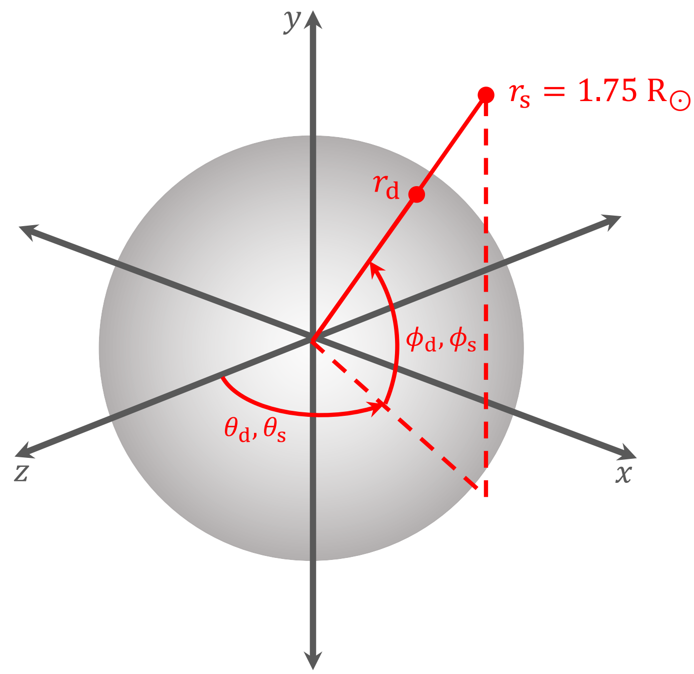

Figure 5.2: Coordinate system (r,θ,ϕ) for an observer located along the positive z-axis where $\theta = 0°$ and $\phi = 0$.

5.2.1 Methodology

Each simulation is run with 10^5 photons (unless otherwise noted) with the frequency conserved, injected as a radio pulse modelled by a delta function with isotropic wavevector distribution. In this sense, all photons are emitted simultaneously. Consequently, if no scattering were present, the photons propagating in the direction of the observer would arrive at the same instance, with the arrival time $t = t_0 + \Delta t$ where $\Delta t = \Delta r/c$, and t_0 and Δr is the injected time and propagation distance, respectively. The photons experience scattering until they cross a sphere with a radius where the scattering rate becomes negligible, i.e., when $\omega_{pe} \ll \omega$. In the simulations used here at $f_{pe} = 32$ MHz, this distance was 17.9 R$_\odot$. The photons are then collected at a scattering 'screen' whose k vectors are directed towards the observer; that is, those where k is between $0.9 < k_z/k < 1$. These photons are then back-projected to the source plane in order to generate an x, y photon position map. This process is similar to that used for X-ray imaging simulations in Kontar & Jeffrey (2010), as noted by Kontar et al. (2019). The observed photon locations are binned into a weighted 2D histogram with a bin-size of 50 arcsec. The weighting w of each photon i is given as

$$w_i = e^{-\tau_a}, \tag{5.8}$$

where

$$\tau_a = \int \gamma(\mathbf{r}(t))\,\mathrm{d}t \tag{5.9}$$

is the Coulomb collision depth. As noted by Kontar et al. (2019), absorption is stronger at frequencies higher than that considered here ($\gtrsim$ 50 MHz), yet the effect is also important when photons are trapped near the source location for a duration greater than the free-free absorption time given by $1/\gamma$. The 2D images are fit with an elliptical Gaussian of the form of equation 3.2

$$I(x,y) = I_0 \exp\left(-\frac{x'^2}{2\sigma_{\mathrm{x}}^2} - \frac{y'^2}{2\sigma_{\mathrm{y}}^2}\right), \tag{3.2}$$

where I_0 is the maximum intensity, σ_x, σ_y are the major and minor ellipse lengths, β is the ellipse rotation angle anti-clockwise from the x-axis, and

$$\begin{aligned} x' &= (x - x_c)\cos\beta - (y - y_c)\sin\beta, \\ y' &= (x - x_c)\sin\beta + (y - y_c)\cos\beta. \end{aligned} \tag{3.3}$$

Equation 3.2 provides the centroid locations (x_c, y_c) of the observed emission, full-width at half-maximum (FWHM) major and minor sizes as $S_{\mathrm{x,y}} = \sigma_{\mathrm{x,y}} 2\sqrt{2\ln 2}$, and FWHM area as $A = \pi/4 \cdot S_{\mathrm{x}} S_{\mathrm{y}}$, as used in chapters 3 and 4.

5.2.2 Simulated Images

To demonstrate the presence of a non-radial magnetic field in an anisotropic environment, Figure 5.3 shows the centroid trajectories measured from multiple images at times throughout the FWHM time profile from many simulations with initial sources distributed across the solar disk. Panel (a) uses a spherically symmetric radial magnetic field, and panel (b) uses a dipole field located at the solar centre. In the radial case, the anisotropy causes photon cloud motion outwards from the Sun, with the largest component of motion visible for sources closer to the limb. In the dipole case, the motion is complex, and depends on the source polar angle. At large ϕ_{s} and θ_{s}, the observed centroid shift is more than double that for disk-centred sources. Figure 5.3(b) also shows an absence of any clear centroid trajectory for sources location at $\phi_{\mathrm{s}} = 0°$.

Figure 5.4 shows the results of a single simulation for a source located at $\theta_{\mathrm{s}} = 0°$ and $\phi_{\mathrm{s}} = -5°$, and a solar disk centred dipole at $r_{\mathrm{d}} = 0.9\ \mathrm{R}_{\odot}$. Throughout the FWHM duration of the main peak, the centroid shifts along the field direction (which here is projected vertically in the sky-plane) by $\sim$ 160 arcsec over 0.65 s. The bulk of this motion (100 arcsec) occurs throughout the decay phase. The FWHM linear size is larger in the x-direction by a ratio of 2.2 and 2.5 at the peak and decay respectively. The FWHM area increases almost at a constant rate from 14 to 22 and 32 arcmin^2 at the three time intervals shown. Near 3 s,

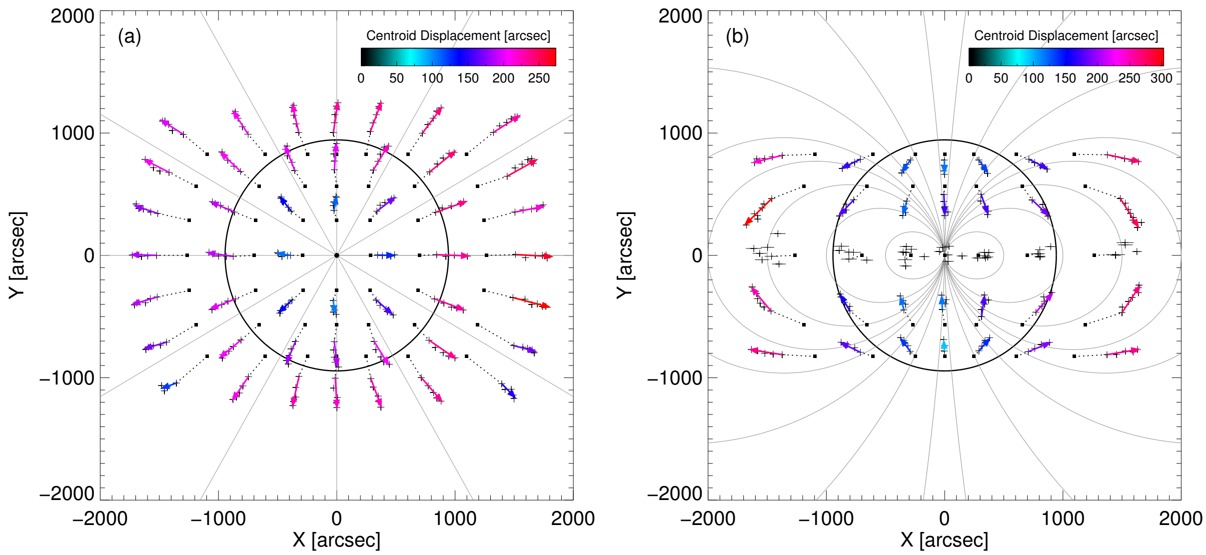

Figure 5.3: Centroid trajectories across the FWHM for sources distributed across the solar disk in a (a) radial and (b) dipole magnetic field, with $\eta = 0.7$ and $\alpha = 0.2$. The dipole is located at the solar centre. The vectors are coloured according to the centroid displacement distance. The black squares give the source injection locations, and the dotted line connects the corresponding centroid locations (black plus symbols). The grey lines provide an indication of the magnetic field direction in a single plane and will not be representative of the local field direction at every presented source.

the major size stops increasing, with a sharp increase in the minor size, likely caused by the arrival of the echo (e.g. Kuznetsov et al. (2020), and section 2.2) as seen in the lightcurve, superimposed onto the main burst component. This causes the centroid location to jump to a lower position in the sky plane as the image is now composed of two sources (the primary and reflected components), which consequently causes the measured source area to be enlarged, and of different shape and orientation. As the echo begins to shift in the same manner as the primary component, the centroid increases along y, and the area begins to reduce as photons that formed the main burst component are no longer visible.

5.2.3 Comparison with Observations

Figure 5.5 presents the simulation results for a configuration similar to Figure 5.4, yet with $\theta_s = \theta_d = 50°$ and $r_d = 0.7\ R_\odot$. Panel (a) includes the centroid locations of a solar radio spike source observed by LOFAR as shown in Figure 3.3(e). For the observed event, the active region is located at approximately 50° from the observers line-of-sight (LOS). The simulated and observed centroids are in agreement with the start location, and their trajectory across the sky-plane. From the simulations, we see a radial distance of 0.13 $R_\odot$ between the photon injection position and the first centroid of the rise phase. The simulated FWHM peak area is $A = 29.7$ arcmin^2 compared to the observed spike peak area in Figure 3.11(d)

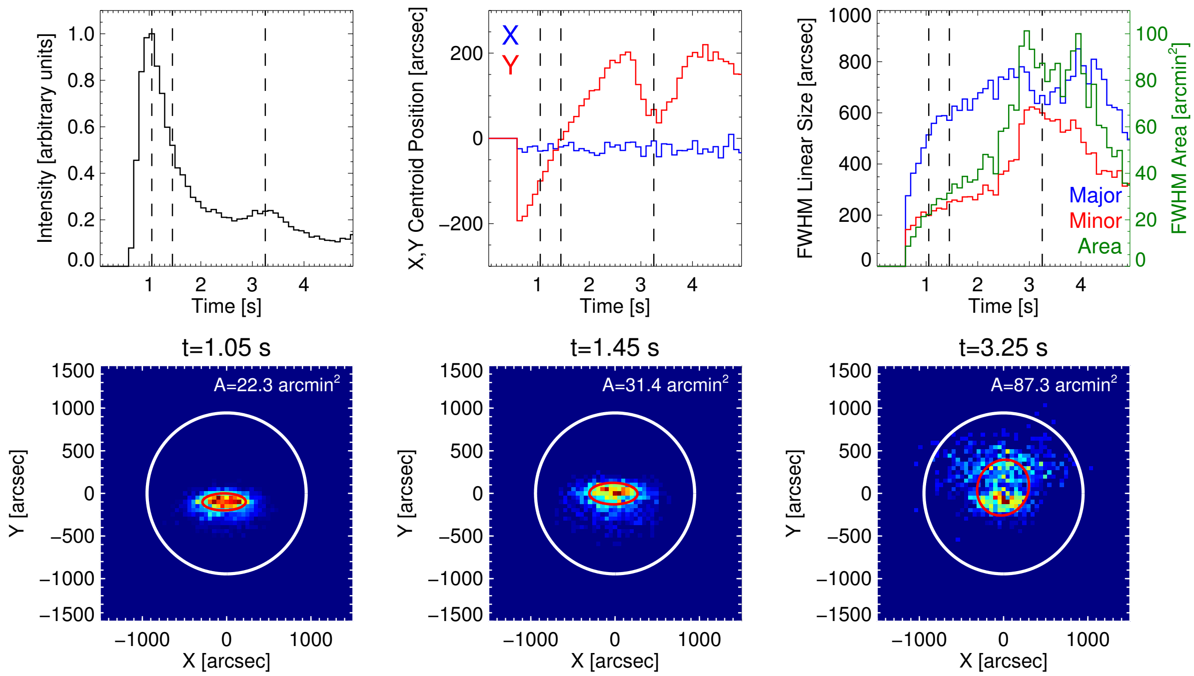

Figure 5.4: Simulation results for an injected source of $N = 10^6$ photons at $\theta_s = 0°$ and $\phi_s = -5°$, with density fluctuation level $\eta = 0.7$ and anisotropy $\alpha = 0.2$. The dipole located at $\theta_d = 0°$, $\phi_d = 0°$, and $r_d = 0.9\ R_\odot$. The top panels show the intensity time profile, the X (blue) and Y (red) centroid positions, and the major (blue), minor (red) sizes with the area (green) respectively. The dashed lines mark the times of the images (weighted 2D histograms) presented in the lower panels from left to right, generated from the observed photon x, y locations with a bin-size of 50 arcsec. The centroid position, sizes, and area are determined from a 2D Gaussian fit to the images. The FWHM area is shown by the red oval.

of $A_{obs} = 200$ arcmin^2 at 34.5 MHz. The simulated and observed images also have different orientation of the emission lobes. Convolving the simulated images with a PSF similar to that of a LOFAR beam on the date of observation (15 July 2017 at 11:00 UT, see Figure 1.18) increases the simulated peak area to 148.7 arcmin^2. This value can be scaled to 34.5 MHz to match the observational frequency as $1/f^2$, giving 154.8 arcmin^2). The convolved areas and orientation are closer to that observed, but not identical, and could be due to a larger and differently shaped PSF. For example, analysis of Tau A observations with LOFAR from numerous observations in tied-array mode show a PSF area of ~ 170 arcmin^2, compared to ~ 75 arcmin^2 for the nominal beam at 30 MHz (Gordovskyy et al., 2022).

5.2.4 Apparent Source Bifurcation

For the same configuration presented in Figure 5.5, yet with anisotropy $\alpha = 0.1$, the imaged source appears as a single source in the vicinity of the emission site at the time of the peak, yet 0.8 s after the peak the apparent source branches into two distinct components. One component shifts upwards in the sky-plane along the field direction, while the other shifts

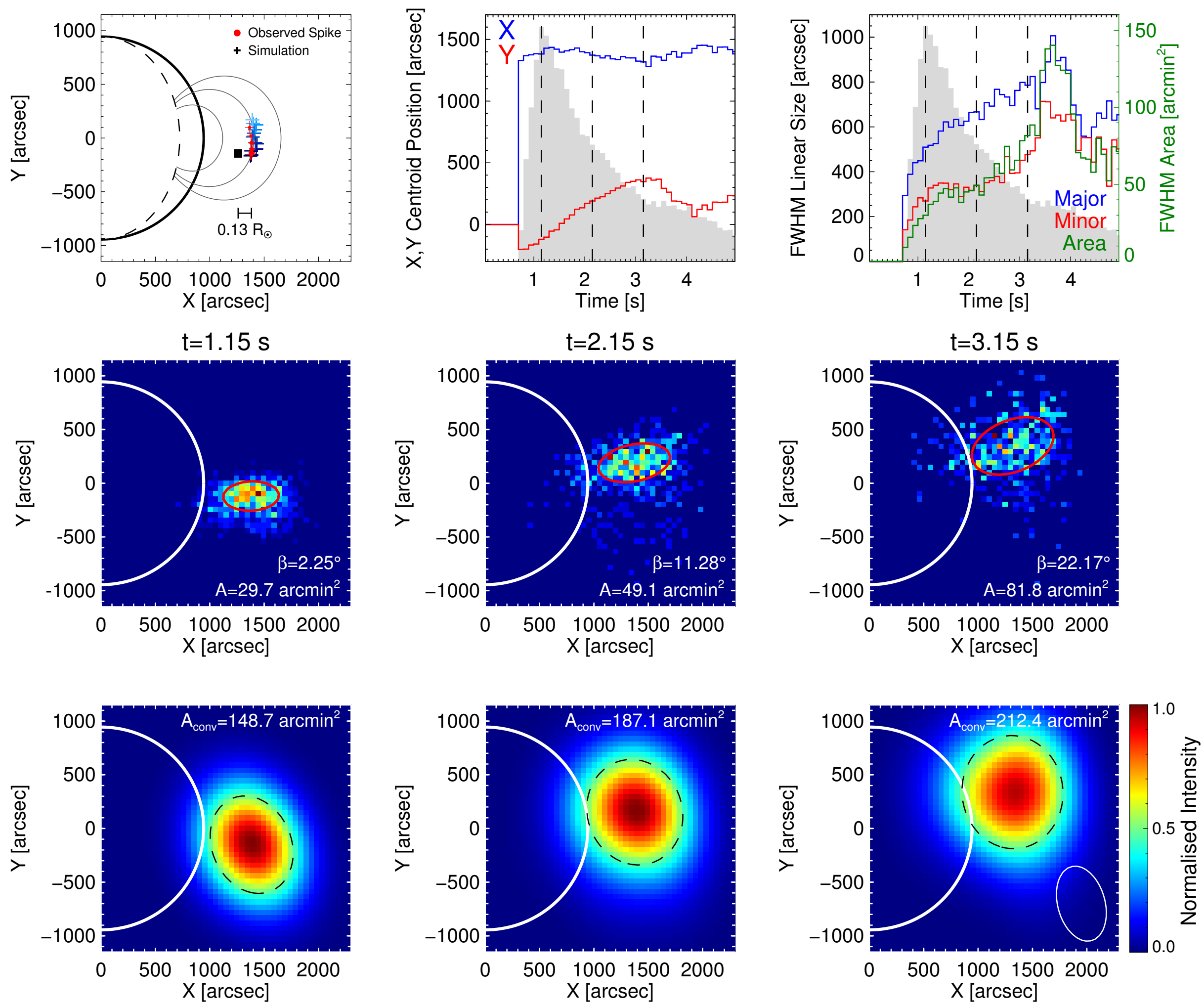

Figure 5.5: Simulation results for an injected source of $N = 10^6$ photons at $\theta_s = 50°$ and $\phi_s = -5°$, with the dipole located at $\theta_d = 50°$, $\phi_d = 0°$ and $r_d = 0.7\ R_\odot$, and density fluctuation level $\eta = 0.7$ with anisotropy $\alpha = 0.2$. The top panels show simulated centroids in the sky-plane, the centroid time profiles, the FWHM major and minor axis sizes, and FWHM area, overlaid onto the normalised intensity time profile (grey). The observed centroids of a radio spike from Clarkson et al. (2021) is included in the top left panel, corrected for average ionospheric refraction as in equation 6 of Gordovskyy et al. (2022). The black square gives the initial source location, with the distance indicator corresponding to the sky-plane distance between the photon injection point and the first observed centroid. The dashed lines mark the times of the images (weighted 2D histograms) presented in the centre panels from left to right. The centroid position, sizes, and area are determined from a 2D Gaussian fit to the images. The FWHM area is shown by the red oval. The fitted ellipse tilt angle is given by β. The lower panels show a convolution of each image with an instrument beam shown in the lower right corner. The black dashed oval marks the 50% intensity level with the FWHM convolved area given by A_{conv}.

downwards, with both components of similar size. Towards the end of the decay phase 1.4 s after the peak, the brighter source has shifted to a higher position in the sky-plane, whilst the lower source is significantly fainter. The lower panels of Figure 5.6 show the simulated images at $t = 1.7$ s convolved with PSFs of different sizes. Panel (e) shows that an instrument PSF of size 8.5 arcmin is not sufficient to resolve the two sources. Panel (f) shows that a PSF with a size of 3 arcmin can spatially resolve the two sources at the 50% intensity level, according to the Rayleigh criterion.

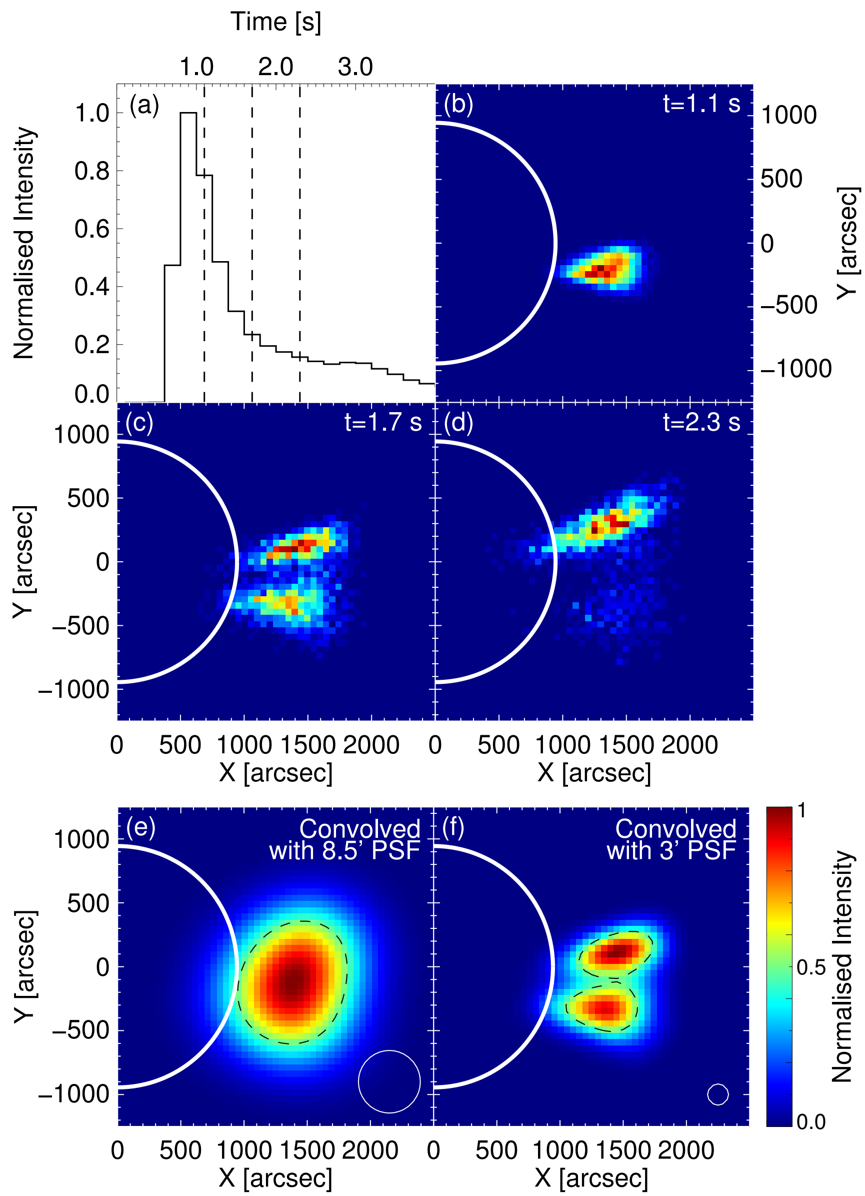

Figure 5.6: Simulated time profile (a) and images presented as weighted 2D histograms (b-d) for a source and dipole located as in Figure 5.5 with a dipole depth of $r_{\mathrm{d}} = 0.9\ \mathrm{R}_{\odot}$, using 10^6 photons and anisotropy $\alpha = 0.1$. The dashed lines in panel (a) give the time of the images in panels (b-d). Panels (e,f) show the sources at $t = 1.7$ s convolved with a PSF of FWHM size 8.5 and 3 arcmin, represented by the white circular contours in the lower right corners. The black dashed lines show the 50% contour levels.

5.2.5 Centroid Motion

In a radially symmetric magnetic field configuration, a source located and imaged along the LOS at the disk centre will display no measurable shift in the sky-plane over time as the scatter-induced shift is along the LOS vector (Kontar et al., 2019). In a dipolar model positioned at the disk centre, the field direction is no longer along the LOS and varies along the polar angle ϕ. Correspondingly, a disk-centred source can display more complex motion arising from the anisotropic scattering. Moreover, displacing the dipole centre outwards towards the solar surface provides a different magnetic field direction for a fixed region of space. Figure 5.7 shows that for a source in a fixed location, increasing the dipole centre height from 0.2 to 0.8 $R_\odot$ causes the centroid trajectory to differ by 45°, quantified by the angle ζ where

$$\zeta = \cos^{-1}\left(\frac{\mathbf{r_c} \cdot \mathbf{r}}{|\mathbf{r_c}||\mathbf{r}|}\right) \tag{5.10}$$

where $\mathbf{r_c}$ is the centroid trajectory and $\mathbf{r}$ is the radial line from the solar centre through the initial source location.

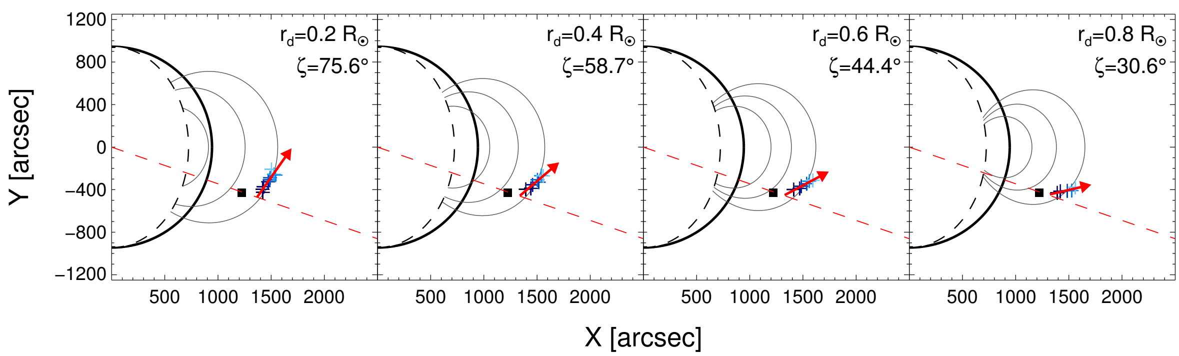

Figure 5.7: Centroid motion across the *xy*-plane through the FWHM of the time profile for an initial source at $\phi_s = -5°$, and $\theta_s = 50°$ with $\eta = 0.7$ and $\alpha = 0.2$. In each successive panel, the dipole radius is increased from 0.2–0.8 $R_\odot$. The angle that the centroid trajectories (red arrows) make with the radial line passing from the solar centre through the source location (dashed red lines) is given by ζ.

Figure 5.8 shows that the centroid trajectory can vary depending on the orientation of the dipole with respect to the solar surface. The lower panels shows the default configuration at $\theta_d = 50°$, and rotated anticlockwise about the normal to the solar surface by $\psi = 90°$. The centroid trajectories vary in each case due to the anisotropic scattering-induced motion along the field direction, showing that motion along the radial line yet towards the Sun is possible for certain configurations. The upper panel presents a rotation anticlockwise about the normal to the solar surface by $\psi = 35°$ such that the field lines that connect the sky-plane region of interest emerge from the solar surface aligned with the two active regions in the AIA image. The simulated centroid trajectories now have a component of motion towards the solar limb, matching that of an observed Type IIIb striae presented in Figure 3.3(e). The striae was observed at 31.6 MHz, whilst the simulation has an observed frequency of 35 MHz. Assuming that the observed striae emission originated within a coronal loop, the density profile could differ from that used here, in such a way that the observed frequency resides at a higher altitude.

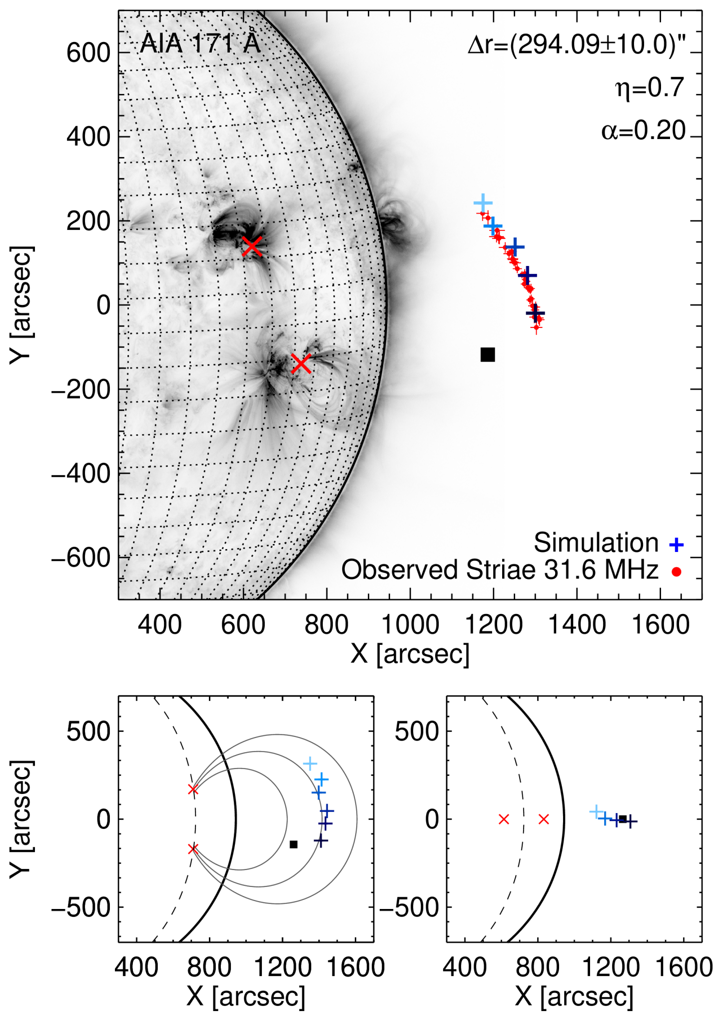

Figure 5.8: FWHM Centroid motion across the *xy*-plane for an initial source at $\theta_s = 50°$and $\phi_s = -5°$(black square) with $\eta = 0.7$ and $\alpha = 0.2$. The top panel overlays an SDO/AIA 171 Å image from 15 July 2017 at 11:20 UT with the simulated centroids (blue crosses) where the dipole has been rotated anticlockwise by $\psi = 35°$to align the dipole footpoints (red crosses) with active regions in the AIA image. The observed distance that the centroids are shifted by throughout the FWHM of the time profile is given by Δr. The closed red circles show the observed Type IIIb striae centroids from an observation at 31.6 MHz at the time of the AIA image (Clarkson et al., 2021, see Figure 3e), corrected for ionospheric refraction as in Clarkson et al. (2023). The lower panels show a rotation of $\psi = 0°$and $\psi = 90°$, respectively.

5.2.6 Observed Characteristics with Source Polar Angle

For a fixed dipole magnetic field perpendicular to the ecliptic, the local magnetic field direction varies for sources located at different polar angles ϕ. Figures 5.9 and 5.10 present the decay times, centroid displacement distances, and centroid velocities for a dipole centre at $\theta_\mathrm{d} = 0°$, $\phi_\mathrm{d} = 0°$, and $r_\mathrm{d} = 0.9\ \mathrm{R}_\odot$, and sources located at polar angles between $\phi_\mathrm{s} = 0 - 30°$ at $\theta_\mathrm{s} = 0°$. The velocities were calculated as $v = \sqrt{v_\mathrm{x}^2 + v_\mathrm{y}^2}$ where $v_\mathrm{x,y}$ are determined via the gradient of a linear fit to the x, y centroid positions over time throughout the decay phase. For comparison, the above source characteristics simulated with a radial magnetic field are also included. For ϕ close to 0°, the source centroids exhibit reduced motion and prolonged decay times. Between 5–10°, the decay time is halved, and the source centroids have increased displacement and velocity in the sky-plane. At 17.5°, the latter two quantities reduce towards zero as the field is oriented along the LOS. At $\phi = 22.5°$, the field direction matches that of the local radial direction and the characteristics are similar to the radial case. As the field direction approaches perpendicular to the observer at larger ϕ angles, the displaced distance and velocities continue to increase.

5.3 Convolution of Simulated Radio Bursts with a Scattering Function

To evaluate the effect of radio-wave scattering on short duration burst fine structures observed in dynamic spectra, a radio pulse with intensity I is modelled by a 2D Gaussian of form

$$I(t, f) = I_0 \exp\left(-\frac{(t - t_0)^2}{2\sigma_t^2} - \frac{(f - f_0)^2}{2\sigma_f^2}\right), \tag{5.11}$$

where t_0 gives the time of peak intensity I_0 and f_0 is the central frequency of the burst, with standard deviation $\sigma_{t,f}$. Figure 5.11(a) shows the initial Gaussian pulse, and rotated in panel (e), along with the measured characteristics (decay time, frequency drift rate, and bandwidth) in the remaining panels as determined as in chapter 3 for radio spikes. The initial duration is set as 140 ms which is consistent with the inferred duration of decametre radio spikes and striae in the absence of scattering, and a bandwidth of 47 kHz at a central frequency of 34.5 MHz (e.g. Figure 3.3). A Gaussian bandwidth is chosen to match the symmetrical spectral shape of fine structures (e.g. Csillaghy & Benz (1993), and Figure 3.3(c)), and for the time profile assuming an initial Gaussian electron distribution function for plasma emission (Mel'nik et al., 1999; Kontar, 2001a; Reid & Kontar, 2021). The dashed curve in panels (c, g) represent a scattering function simulated with a radial magnetic field from Chen et al. (2020) (see Figure 3c, where $\alpha = 0.25$). The model used to fit the scattering

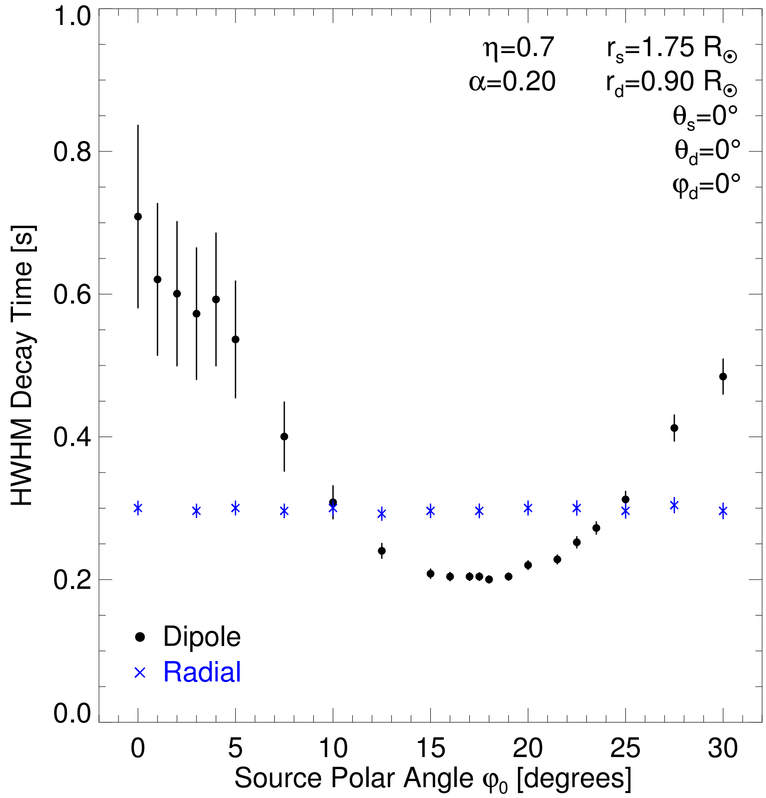

Figure 5.9: Simulated decay times measured from the peak to the FWHM level for sources at polar angles between $\phi_{\rm s} = 0 - 30°$. In all cases, the dipole was offset to $r_{\rm d} = 0.9$ R$_\odot$, at $\theta_{\rm d} = 0°$ and $\phi_{\rm d} = 0°$, with the source azimuth's angle also $\theta_{\rm s} = 0°$. The density fluctuation level is set to $\eta = 0.7$ with anisotropy $\alpha = 0.2$. Data in blue represents the case for a radial magnetic field. The decay uncertainty at lower ϕ results from lower photon counts (two orders of magnitude less than those near 17.5°).

function is an asymmetrical Gaussian given by

$$I_s(t) = I_0 \exp\left[-\left(\frac{t-t_0}{a+t\cdot b}\right)^2\right], \tag{5.12}$$

where I_0, t_0, a, b are free parameters of the fit[1]. The second column (panels b, f) shows a convolution of the intrinsic 2D Gaussian intensity I and the scattering function I_s for each frequency channel as

$$I_c(t) = \int_{-\infty}^{\infty} I(t-\tau) I_s(\tau)\,\mathrm{d}\tau. \tag{5.13}$$

[1]When $b \geq 0$, the standard deviation leads to a HWHM rise $t_{\rm r}$ and decay $t_{\rm d}$ time given by $t_{\rm r,d} = \sqrt{\ln 2}(a + bt_0)/(1 \pm b\sqrt{ln 2})$ for the positive and negative $b\sqrt{\ln 2}$ terms, respectively.

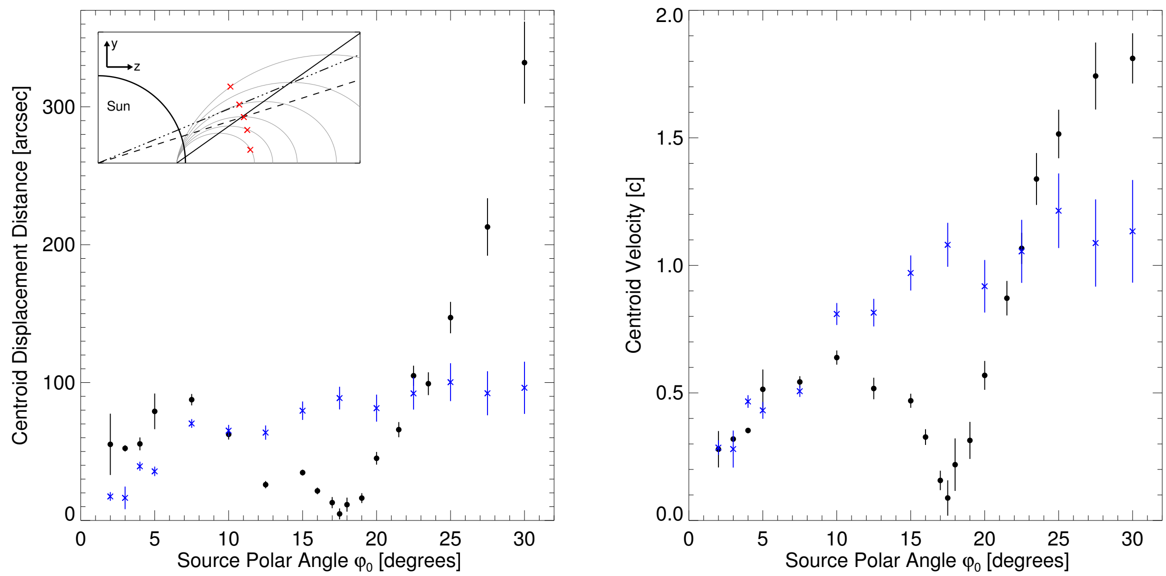

Figure 5.10: Centroid displacement distance (*left*), and centroid velocities (*right*) measured from the peak to the FWHM level for sources at polar angles between $\phi_s = 0 - 30°$. The dipole was offset to $r_d = 0.9$ $R_\odot$, at $\theta_d = 0°$ and $\phi_d = 0°$, with the source azimuth's angle also $\theta_s = 0°$. The density fluctuation level is set to $\eta = 0.7$ with anisotropy $\alpha = 0.2$. Data in blue represents the case for a radial magnetic field. The inset of panel (b) displays zy-plane and the source ϕ locations at 5, 12.5, 17.5, 22.5, and 30 degrees (red crosses) overlaid with the dipole field lines. The solid line gives the angle of 35.3° where each field line reaches a maximum height. The dashed line represents an angle of 17.65° from the solar centre where the displaced dipole reaches a maximum height for that source location, and the dash-dotted line marks an angle of 22.5° from the solar centre where the radial direction matches the field line direction.

5.3.1 Drift Rates

The convolution of the intrinsic burst with the scattering function mimics the time-broadening due to radio-wave scattering at each frequency, whilst leaving the total bandwidth intact. Consequently, the initial short millisecond pulse is observed as smeared emission in dynamic spectra, and the observed frequency drift is diluted. The drift rate reduction level therefore depends on the duration of the scattering function, or physically, the turbulence level, anisotropy factor, and emitter location with respect to a non-radial field (see increased time profiles in Figure 5.9(a) near the loop apex). An additional effect of the convolution is that the observed bursts are delayed from the original peak time by ~ 1 s. The suppression of the observed drift rates has consequences on the determining the characteristics of the physical driver of the drift rate, and as noted earlier, was recently found to result from moving clumps of Langmuir waves and linked to the coronal temperature (Reid & Kontar, 2021). As such, the scatter-reduced drift rates will underestimate these two quantities.

Figure 5.11(f) shows that an intrinsic burst with a drift rate of -100 kHz s^{-1} is reduced to -24 kHz s^{-1}. In Figure 5.12, the convolved drift rates are presented using scattering

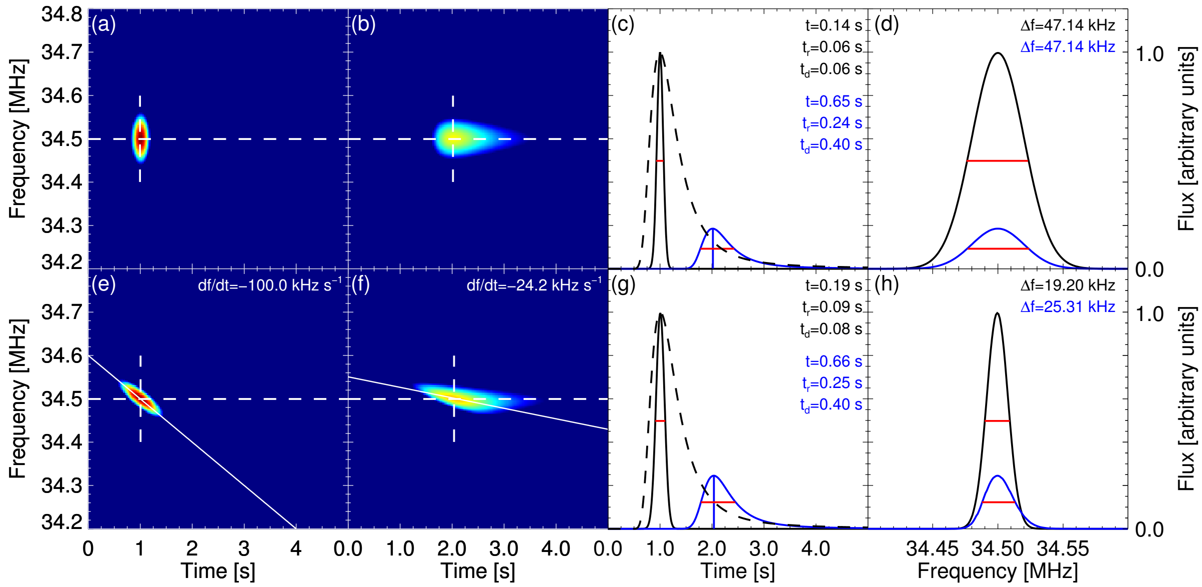

Figure 5.11: Simulated radio burst dynamic spectra with and without the effects of radio-wave scattering. The first column shows a radio pulse pre-scattering, assuming a Gaussian time and frequency profile. The top row (a-d) considers a burst emitted instantaneously across all frequencies, and the bottom row (d-g) consider a burst emitted with a frequency drift rate of -100 kHz s^{-1}, represented by the solid white line in panels (e). The second column shows the results of the convolution between the 2D Gaussian and the scattering function I_s for $\alpha = 0.25$ (dashed curve in panels (c, g)). The white dashed lines in the dynamic spectra show the locations of the time and frequency-flux profiles that cross at the maximum intensity. The profiles are displayed in the third and forth columns, respectively. The solid black curves represent the intrinsic Gaussian profiles, and the blue curves represent the convolved Gaussian. The red horizontal lines denote the FWHM.

functions from various anisotropy values as presented in Chen et al. (2020) along radial magnetic fields. The intrinsic fine structure drift rates are chosen such that the estimated coronal temperature is near $1-2$ MK, typical for coronal plasma. The relation between the thermal temperature and drift rate is given by (Reid & Kontar, 2021) as

$$\frac{\mathrm{d}f}{\mathrm{d}t} = \frac{f_{\mathrm{pe}}}{2n_e}\frac{\mathrm{d}n_e}{\mathrm{d}r}v_{\mathrm{gr}} \tag{5.14}$$

where $v_{\mathrm{gr}} = 3v_{\mathrm{Te}}^2/v_b$ with $v_{\mathrm{Te}}^2 = k_{\mathrm{B}}T_e/m_e$, m_e and k_{B} are the electron mass and Boltzmann constant, and f_{pe} is the plasma frequency given by the density according to equation 1.15 as $f_{\mathrm{pe}} = 8.93\times10^{-3}\sqrt{n_e}$. Equation 5.14 is analogous to that relating the bulk Type III drift rate to the beam velocity v_{b}, where v_{gr} in equation 5.14 is replaced by v_{b}, as used in Melnik et al. (2011); Reid & Kontar (2018b), for example. We set the electron beam velocity at $v_{\mathrm{b}} = c/3$, and the density model given by equation 1.10, giving $n_e = 1.27\times10^7$ cm^{-3} at $f_{\mathrm{pe}} = 31.86$ MHz. Stronger levels of anisotropy have a weaker reduction effect—for example, at intrinsic drift rates of -40 kHz s^{-1}, the observed burst has a drift rate of -4 kHz s^{-1} for $\alpha =$

0.3, and -12 kHz s^{-1} for $\alpha = 0.2$, a reduction of 90% and 70%, respectively. These observed drift rates would suggest coronal temperatures of $\sim(1-3)\times10^5$ K, rather than $\sim10^6$ K.

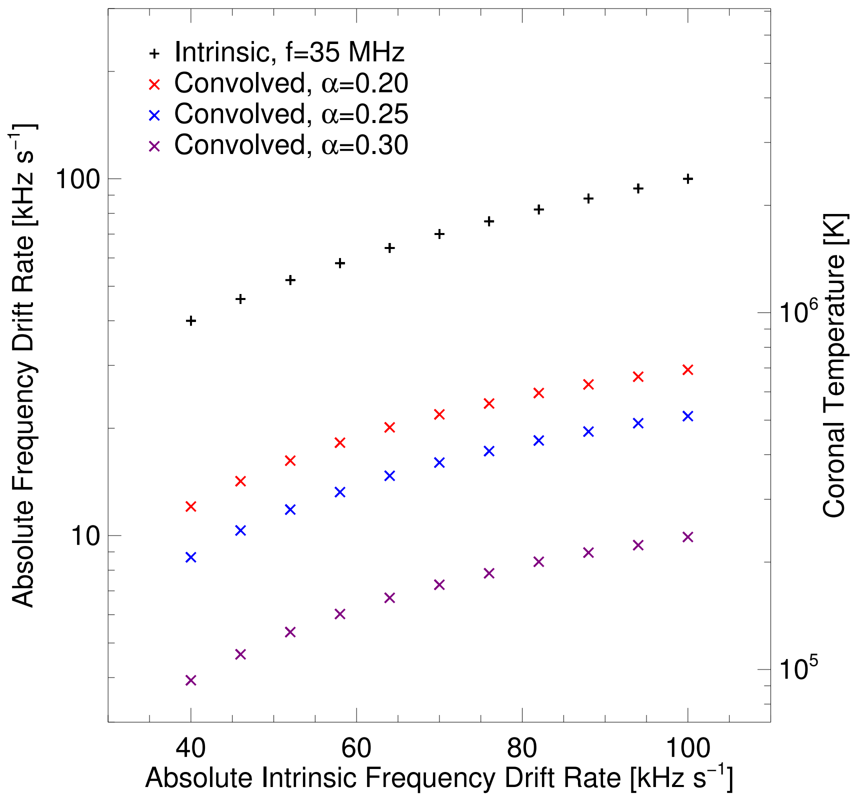

Figure 5.12: Simulated intrinsic and convolved radio burst fine structure frequency drift rates at $f = 35$ MHz. The convolution was performed using scattering functions from radial field simulations with varying values of anisotropy α.

Along dipolar magnetic field lines, the scattering function is extended for sources closer to the loop apex. Figure 5.13 shows three fine structures with intrinsic drift rates matching those in Figure 5.11e. Each is convolved with a scattering function simulated in a dipole for sources located between $\phi_s = 0-20°$. For sources near the loop apex, we find a strong drift rate reduction by 93%, followed by weaker reduction of 73% and 60% for sources at 10° and 20° respectively, as well as peak intensity reduction closer to the loop apex.

5.4 Discussion

In this chapter, the motion of radio sources in dipolar magnetic fields approximating the geometry of anisotropically turbulent coronal loops, as well as the effects of turbulence for radio burst fine structure morphology in dynamic spectra has been investigated.

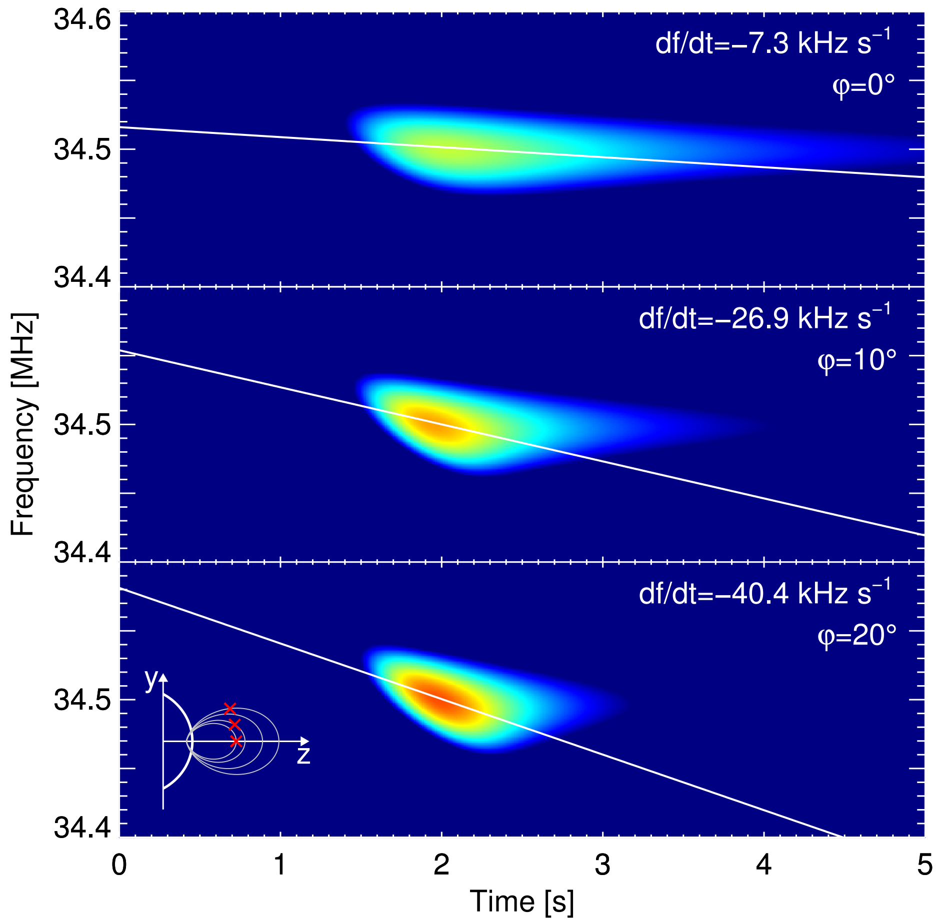

Figure 5.13: Dynamic spectra of radio burst fine structures convolved with a scattering function for sources located at $r_s = 1.75$ R$_\odot$, $\theta_s = 0°$, and ϕ_s of 0°, 10°, and 20°with a dipole magnetic field located at $r_d = 0.9$ R$_\odot$, $\phi_d = 0°$and $\theta_d = 0°$, with $\alpha = 0.2$ and $\eta = 0.7$. The inset shows the source locations (red symbols) for an observer along the $+z$-axis.

5.4.1 Source Evolution

The analysis of a dipole magnetic field configuration and source both near the centre of the solar disk revealed temporal expansion elongated along the x-axis at the time of the peak. In the radial case, this behaviour differs since the field direction is along the LOS, producing stationary sky-plane expansion with a maintained circular shape (see Chen et al., 2020, Figure 1, for example). The time profile and simulated images highlight the emergence of the radio echo, comparable to those observed in drift-pair bursts (Kuznetsov et al., 2020), although not as intense. Despite this, the echo noticeably changes the image morphology by increasing the apparent size and shifting the imaged source centroid due to the combined location of two spatially separated components.

The combination of a dipole field configuration and anisotropic scattering can result in non-radial, fixed frequency centroid motion in images, and in some cases, a complete absence of motion. The latter can happen when sources are located at the loop apex or when the local magnetic field is oriented along the LOS, but the reasons for the lack of centroid motion are disparate in each case. At the loop apex, the photons have no preferential escape direction from the scattering region, resulting in a fixed centroid over time that represents the average position of an extended apparent source. Consequently, the decay times are prolonged while the probability of absorption is increased as the photons remain in the scattering region for longer. Therefore, the model predicts that radio emission emanating from coronal loop tops may appear fainter compared to sources along the loop leg or open field lines. When the magnetic field is aligned with the LOS, the centroid shift is obscured in the image plane, similar to sources at the disk centre in a radial magnetic field. The imaged centroid shift in dipolar fields approximates that in a radial field when the dipole field line tangent approaches the local radial direction. In the dipole model shown in Figures 5.9 and 5.10, this occurs at $\phi = 22.5°$. Figures 5.7 and 5.8 show that for different dipole configurations with respect to a fixed source location, the observed centroid trajectories can propagate away, towards, or parallel to the Sun across the sky-plane. The result shows that peculiar, non-radial centroid trajectories observed in radio emission can be caused by complex magnetic field projections in the sky-plane combined with strong anisotropy of the density fluctuation spectrum. In order to fully interpret the motion of fine structure sources, the time along the burst, location, magnetic field structure, and coronal conditions should be considered simultaneously.

The observations of solar radio spikes and Type IIIb striae presented in chapters 3 and 4 associated with an extended coronal loop presented vertical sky-plane motion and rotation of the observed radio sources over time. In this chapter, this motion is replicated for a source placed at 50° from the observers LOS and $-5°$ below the ecliptic. For anisotropy $\alpha = 0.2$, there is similarity in the observed and simulated centroid locations—both the region at which they originate during the rise phase, and the distance shifted due to scattering effects (Figure 5.5). The 0.13 $R_\odot$ separation in the sky-plane between the injected source and the simulated centroids implies that the source location is not observed in radio images, consistent with the radial magnetic field simulations presented in Kontar et al. (2019). In addition, it is also consistent with the idea that the acceleration region was lower down the loop leg (see Figure 4.15), with the accelerating electron beam propagating some distance along the loop before emitting. As the burst decays, the simulated image undergoes a rotation up to 22° in the sky-plane that is not present for the disk centred simulation. This rotation results from the directivity of the emission along the curved magnetic field and is consistent with that observed for the spike and striae shown in Figure 4.7.

The simulated FWHM peak area convolved with a PSF produces a source shape and orientation similar to that observed by LOFAR, meaning that the true source shape is not observed. The convolved area of ~ 155 arcmin^2 is 30% less than that observed by LOFAR in beam-formed mode (200 arcmin^2 at 34.5 MHz) that could be due to underestimating the LOFAR PSF (Gordovskyy et al., 2022). LOFAR imaging observations in interferometric mode that use larger baselines (and thus improved spatial resolution) measured Type IIIb source areas of 150 arcmin s^{-1} at 34.76 MHz (Murphy et al., 2021), and 205.9 arcmin^2 at 35 MHz (Dabrowski et al., 2023). The former is similar to the convolved area estimated from our simulations for a source at a similar heliocentric angle. The latter area is larger yet located closer to the disk centre where an increased source area would be expected along a radial field line (Kontar et al., 2019).

In environments characterised by a strong anisotropy factor $\alpha = 0.1$, the apparent source can appear to bifurcate into two separate components (Figure 5.6)—a main component that propagates non-radially away from the emission location, and a less intense (lower photon count) source that remains closer to the emission site. The simulations presented in this chapter at a frequency of 35 MHz demonstrate that the separation distance between the two components is a few hundred arcsec at a time they share a similar brightness, requiring an angular resolution ≤ 3 arcmin to spatially resolve. The detection of such events could prove challenging, contingent on the instrument and observing mode. It's possible that this scatter-induced bi-directional apparent source motion in strong anisotropic environments could occur at higher frequencies, and could provide an alternative suggestion for the motion observed in McCauley et al. (2017) (see Figure 10). However, considering the model of $\overline{q\epsilon^2}(r)$, the scattering rate would be decreased by a factor of ~ 3 at 100 MHz compared to 30 MHz, which could lead to a smaller displacement of the two components across the same time interval.

5.4.2 Fine Structure Drift Rate Reduction

To replicate an intrinsic radio burst fine structure in the absence of any scattering effects, a simulated 2D Gaussian with duration approximately an order of magnitude shorter than typical fine structures near 30 MHz is utilized. To mimic the propagation effects, the time profile of the scattering contribution is modelled with an asymmetrical Gaussian. By convolving the intrinsic burst with the scattering function, there are a number of notable effects. Specifically, the resulting time profile exhibits a broadening of the pulse accompanied by a shift in the peak arrival time, and a reduction in the observed fine structure drift rate. The temporal broadening of the intrinsic pulse results in a smearing of the emission in dynamic spectra, leading to a delay in the observed peak by ~ 1 s at decametre frequencies as shown by Chen et al. (2023b) for fundamental emission. Variations in the degree of anisotropy present in the intervening plasma influence the observed drift rate, with a more pronounced reduction evident under conditions closer to isotropy. Moreover, the observed drift rate in an anisotropic turbulent plasma is subject to further alteration by the magnetic field structure by producing an increased scattering contribution dependent on the source location.

Since drift rates observed in radio emission are often used to infer information about the exciting agent, the effect of scattering should be decoupled. For example, considering Type IIIb striae, Sharykin et al. (2018) note that the time of interaction between the electron beam and a particular density inhomogeneity could be estimated via $\tau = \Delta f(\mathrm{d}f/\mathrm{d}t)^{-1}$ where Δf is the striae bandwidth, yet without correcting for the reduction in the observed drift rate, this will overestimate the interaction time. Considering the aforementioned link between the drift rates of radio burst fine structures to both the coronal temperature and moving clumps of Langmuir waves (Reid & Kontar, 2021) (where higher temperatures lead to increased Langmuir wave group velocities and thus increased drift rates), then without a scattering correction, the reduced drift rates at 35 MHz would infer temperatures between $(1-7)\times 10^5$ K for values of $\alpha = 0.2-0.3$, rather than 1–2 MK as typically estimated for coronal plasma. If an observed fine structure drift rate is -20 kHz s^{-1} at 35 MHz in an environment where $\alpha = 0.2$, then a 1.5 MK plasma would infer an intrinsic drift rate of 64 kHz s^{-1}, but the precise magnitude of the drift rate may depend on the relative positioning of the emitter within the magnetic structure. Low drift rates were observed for the spikes presented in chapters 3 and 4, and the typical observed parameters are consistent with an anisotropy factor of $\alpha = 0.2$, implying that their intrinsic drifts were higher by a factor of ~ 3.

If we consider that the scattering contribution to the observed time profile is weaker at higher frequencies (see Figure 5.1) such that a radio pulse is broadened by a smaller amount (see Figure 9 in Arzner & Magun, 1999, for example), then one would anticipate that the fine structure drift rates would be lower for sources observed farther from the Sun. Indeed, observations between 200 MHz and 4 GHz suggest that the rates decrease as the observation frequency decreases with a power-law index of $\mathrm{d}f/\mathrm{d}t \sim f^{-1.84}$ (Figure 5.14). This trend is similar to the drift rate relation observed for Type III bursts below 1 GHz, as reported by Alvarez & Haddock (1973). However, below 100 MHz, the fine structure drift rates deviate from this trend and are approximately one order of magnitude lower (Figure 5.14). It's possible that the increase in scattering contribution at lower frequencies is not linear. However, a further consideration is that the fine structure bandwidth above $\sim 200-400$ MHz is typically an order of magnitude larger than those at lower frequencies, as shown in Figure 4.14. This could cause the amount by which the drift rate is reduced due to broadened time profiles to be suppressed. Furthermore, the steeper density gradient in this environment will produce a larger drift rate for an exciter propagating at a given speed. As a result, a combination of the above factors (bandwidth, density gradient, and scatter-induced drift rate reduction) could contribute to the morphological disparity between spike sources in each frequency domain.

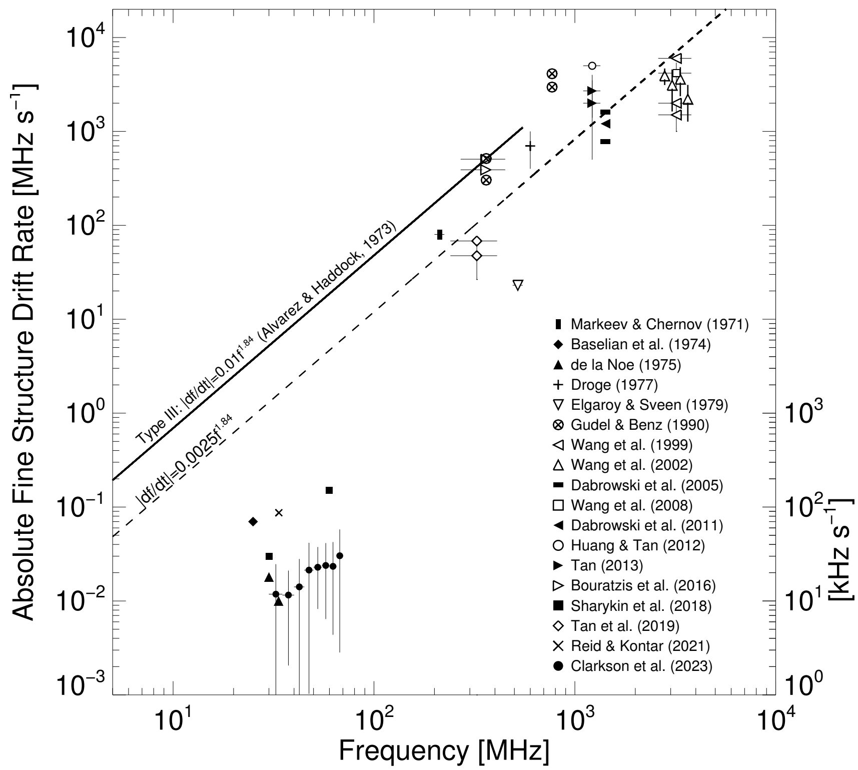

Figure 5.14: Compilation of radio burst fine structure average drift rates from numerous studies (Markeev & Chernov, 1971; Baselian et al., 1974; de La Noe, 1975; Droege, 1977; Elgaroy & Sveen, 1979; Guedel & Benz, 1990; Wang et al., 1999, 2002; Dabrowski et al., 2005; Wang et al., 2008; Dabrowski et al., 2011; Huang & Tan, 2012; Tan, 2013; Bouratzis et al., 2016; Sharykin et al., 2018; Tan et al., 2019; Reid & Kontar, 2021; Clarkson et al., 2023). Note that fine structures that appear vertical in dynamic spectra have no measurable drift rate. The solid line shows the Type III drift rate relation by (Alvarez & Haddock, 1973). The dashed line shows the same slope offset to match the data above 200 MHz. The uncertainty for Clarkson et al. (2023) represents the interquartile range for the median data.

5.5 Conclusion

This chapter presents a quantitative analysis into the spatial and spectral evolution of solar radio burst fine structures as the radiation escapes through an anisotropically turbulent corona. Fine structures associated with a coronal loop that present non-radial centroid motion are replicated by introducing dipolar magnetic field structures to simulations of radio wave scattering. It's inferred that the location of the emitter was 0.13 $R_\odot$ away from the observed centroids, in a loop environment with anisotropy factor of $\alpha = 0.2$. Sources placed within non-radial magnetic field configurations with anisotropic turbulence exhibit a major axis perpendicular to the field direction, which for a field directed towards the solar north is along the x-axis of the sky-plane and may not be discernible due to the instrument PSF. It's demonstrated that strong anisotropy $\alpha = 0.1$ can cause emission from an imaged source to appear to have two components, propagating in different direction over time with different intensities. Radio wave scattering can reduce the observed fine structure drift rate up to an order of magnitude, with weaker anisotropy having a greater effect. Estimations of the Langmuir wave group velocity and coronal temperature that drives the fine structure drift rate can therefore be underestimated from observations. Previous decametre spike absolute drift rates observed at 10 kHz s^{-1} possibly had intrinsic rates of at least 64 kHz s^{-1} in a 1.5 MK plasma with anisotropy factor of $\alpha = 0.2$, yet there could also be a contribution to the drift rate suppression from the source location within the loop structure due to strong scattering near the loop apex. At decimetre frequencies where the scattering contribution to the time profiles is shorter and emission bandwidths larger, the drift rate reduction is weaker, contributing to the morphological disparity when compared to decametre fine structures, in addition to different emission mechanisms and the coronal environment.

6

Conclusions & Final Remarks

The aim of this thesis was to investigate the fine structures of solar radio bursts using the next-generation LOFAR solar radio telescope. The high time and frequency resolution capabilities of LOFAR enabled imaging spectroscopy of *individual* solar radio spikes, which had not been accomplished before. This was particularly intriguing because spikes are the shortest radio signatures observed from the Sun and are not fully understood. Understanding these spikes is important as they may be manifestations of the energy release process. However, scattering of the radio emission significantly affects these sub-second bursts, which can make it challenging to accurately determine the emission site and intrinsic properties unless the scattering effects are decoupled. In addition to interpreting the observed evolution using scattering models, recently developed 3D radio-wave propagation simulations were employed that take into account the anisotropy of the density fluctuation spectrum. These ray-tracing simulations, including a dipolar magnetic field, were able to replicate the peculiar spatial evolution of the radio spikes (and striae), allowing for improved estimation of the emitter location and the coronal environment in which they propagate.

Chapter 2 provides an overview of the typical characteristics and challenges associated with observing radio burst fine structures. This includes a description of Type IIIb striae, which appear as intensity oscillations embedded into the broadband structure of Type III bursts due to an inhomogeneous corona. Their fixed frequency evolution is described from recent imaging spectroscopy studies that show strong modulation due to radio-wave scattering effects. The interpretation of drift pair bursts is presented in the context of a radio echo from observations, as well as simulations that were able to replicate these structures with strongly anisotropic density fluctuations. Previous observations of radio spikes are introduced, highlighting their duration, bandwidth, drift rates, and polarisation over decades in frequency, and the need for resolved imaging observations of this phenomenon. The possible mechanisms for generating spike emission is discussed; that is, plasma emission and electron cyclotron maser emission. Furthermore, a case study into the powerful flare of 6 December 2006 is presented, which caused disruption to communication and GPS receivers across the sunlit hemisphere at Earth, with strong correlation from intense radio spikes across L-band frequencies.

Chapter 3 presents the first frequency and time resolved imaging spectroscopy of individual solar radio spikes between 30–70 MHz using LOFAR. The imaging results show that the observed spike areas and position at fixed frequencies evolve in time in a similar manner to striae in the same event. Throughout the decay phase, the areas increase, whilst the positions shift dramatically parallel to the solar limb at superluminal speeds. These observations suggest that the radiation is escaping through anisotropic density turbulence in closed loop structures with the radio emission scattered preferentially along the guiding magnetic field that may be oriented parallel to the limb in the scattering region. The scattering effects, even on these sub-second bursts, suggest that the intrinsic emission has a brightness temperature approximately four orders of magnitude larger that what is observed. Moreover, comparison of individual spikes and striae reveals similarity in their characteristics, including the sense of polarisation and observed location. Therefore, it is likely that decametre spikes are also produced via plasma emission—accelerated electron beams due to magnetic energy release—but likely from electron beams with weaker properties.

In Chapter 4, the statistical analysis of over 1000 spikes and 250 striae is presented, expanding upon the small sample discussed in Chapter 3. The intensity contours of spikes and striae that occur temporally close to each other overlap at the 90% level, indicating that they are emitted from the same region of space. Their bandwidths suggest that this emitting region is < 1 arcsec, and its location appears to shift in time due to an initial perturbation of the coronal loop from the CME shock front, followed by restoration towards the previous configuration. The centroid velocities of the spikes exhibit no frequency dependence between 30–70 MHz, yet there is a spread at a given frequency that could be due to varying anisotropy across the region, as well as different emission angles within the loop. Analysis of individual striae show that the exciting electron beam of the Type IIIb is propagating tangentially to the scatter-induced motion, along a trajectory that does not correspond to the local field direction at the site of observation. Therefore, consistent with the scattering model, the intrinsic source location is not observed and may be located closer to the Sun along the loop leg at the CME flank. The evolution of the CME and magnetic geometry may have incited frequent magnetic reconnection in numerous sites, producing spikes across a range of decametre frequencies. Comparison of decametre and decimetre spike sizes and decay times show a $1/f$ dependence up to 1 GHz, yet their bandwidth ratios show an abrupt increase above 200–400 MHz which can be replicated using the Langmuir wave dispersion relation. The spread of $\Delta f/f$ at a given frequency suggests varying magnetic field strengths between spike events, which appear to be larger than average by a factor of two.

Chapter 5 analyses the spatial and spectral evolution of fine structures using radio-wave propagation simulations that consider a dipole magnetic field configuration with anisotropic density fluctuations. The simulations replicate the non-radial spike and striae centroid motion presented in chapter 3, and suggest an emission location 0.13 $R_\odot$ away from that interpreted from the sky-plane centroids. The simulations also agree with the interpretation of strong anisotropy in the loop environment with a factor of $\alpha = 0.2$. The simulated images reveal that the source sizes are elongated along the x-direction in the sky-plane when the dipole field direction is vertical. This source shape may not be observed due to convolution with the instrument PSF. Furthermore, with very strong anisotropy of $\alpha = 0.1$, the imaged sources appear to bifurcate into two components, requiring fine spatial resolution to resolve. Through convolution with a scattering function, a radio pulse with millisecond duration and fast frequency drift is broadened to the extent that the observed drift rate is suppressed. As a result, fine structure drift rate observations will underestimate the Langmuir wave group velocity and coronal temperature. Using scattering functions from sources in different positions with respect to the dipole field shows that fine structures arising from different locations can present different drift rates. This drift rate suppression could contribute to the morphological disparity between decametre and decimetre spikes due to the stronger scattering contribution at lower frequencies.

The results presented in this thesis demonstrate that sub-second decametre burst fine structures are significantly modified by radio-wave propagation effects. The evolution of their size and position in time means that measurements of these quantities must be accompanied by the specific time along the burst profile. Moreover, any inference of the intrinsic emission location must decouple the spatial change due to scattering. The results suggest that solar radio spikes generated at high altitudes (low frequencies) share the same morphological characteristics as striae, and can be explained by the plasma emission mechanism. These observations would not have been possible without the excellent time and frequency resolution of LOFAR imaging. With the advent of future interferometric telescopes such as the Square Kilometre Array (SKA), further progress could be made with improved imaging capabilities. In particular, finer spatial resolution whilst maintaining the temporal clarity of LOFAR could enable smaller components of scattered emission to be observed, which could reveal additional details of the coronal environment through which the emission propagates. Combined with improved scattering models, such observations once decoupled from propagation effects, could localise the true source location with greater accuracy.

Bibliography

Abbo, L., Ofman, L., Antiochos, S. K., et al. 2016, Space Sci. Rev., 201, 55, doi: 10.1007/s11214-016-0264-1

Afraimovich, E. L., Demyanov, V. V., & Smolkov, G. Y. 2009, Earth, Planets and Space, 61, 637, doi: 10.1186/BF03352940

Alexandrova, O., Chen, C. H. K., Sorriso-Valvo, L., Horbury, T. S., & Bale, S. D. 2013, Space Sci. Rev., 178, 101, doi: 10.1007/s11214-013-0004-8

Alissandrakis, C. E., & Gary, D. E. 2021, Frontiers in Astronomy and Space Sciences, 7, 77, doi: 10.3389/fspas.2020.591075

Allen, C. W. 1947, MNRAS, 107, 426, doi: 10.1093/mnras/107.5-6.426

Allen, J., Frank, L., Sauer, H., & Reiff, P. 1989, EOS Transactions, 70, 1479, doi: 10.1029/89EO00409

Altyntsev, A. T., Grechnev, V. V., Konovalov, S. K., et al. 1996, ApJ, 469, 976, doi: 10.1086/177844

Altyntsev, A. T., Grechnev, V. V., Zubkova, G. N., et al. 1995, A&A, 303, 249

Alvarez, H., & Haddock, F. T. 1973, Sol. Phys., 29, 197, doi: 10.1007/BF00153449

Anantharamaiah, K. R., Gothoskar, P., & Cornwell, T. J. 1994, Journal of Astrophysics and Astronomy, 15, 387, doi: 10.1007/BF02714823

Andrews, M. D. 2003, Sol. Phys., 218, 261, doi: 10.1023/B:SOLA.0000013039.69550.bf

Apparao, K. M. V. 1973, Ap&SS, 25, 3, doi: 10.1007/BF00648230

Armatas, S., Bouratzis, C., Hillaris, A., et al. 2019, A&A, 624, A76, doi: 10.1051/0004-6361/201834982

Arzner, K., & Magun, A. 1999, A&A, 351, 1165

Aschwanden, M. J. 2005, Physics of the Solar Corona. An Introduction with Problems and Solutions (2nd edition)

Aschwanden, M. J., Benz, A. O., Dennis, B. R., & Schwartz, R. A. 1995, ApJ, 455, 347, doi: 10.1086/176582

Aschwanden, M. J., Dennis, B. R., & Benz, A. O. 1998, ApJ, 497, 972, doi: 10.1086/305484

Aschwanden, M. J., & Freeland, S. L. 2012, ApJ, 754, 112, doi: 10.1088/0004-637X/754/2/112

Aschwanden, M. J., Newmark, J. S., Delaboudinière, J.-P., et al. 1999, ApJ, 515, 842, doi: 10.1086/307036

Aubier, M., & Boischot, A. 1972, A&A, 19, 343

Babcock, H. W. 1961, ApJ, 133, 572, doi: 10.1086/147060

Bakunin, L. M., & Chernov, G. P. 1985, Soviet Ast., 29, 564

Bala, B., Lanzerotti, L. J., Gary, D. E., & Thomson, D. J. 2002, Radio Science, 37, 1018, doi: 10.1029/2001RS002481

Balasubramaniam, K. S., Cliver, E. W., Pevtsov, A., et al. 2010, ApJ, 723, 587, doi: 10.1088/0004-637X/723/1/587

Bandiera, R. 1982, A&A, 112, 52

Barrow, C. H., Flagg, R. S., & Perrenoud, M. 1984, Sol. Phys., 90, 111, doi: 10.1007/BF00153788

Barrow, C. H., & Saunders, H. 1972, Astrophysics Letters, 12, 211

Barrow, C. H., Zarka, P., & Aubier, M. G. 1994, Astronomy and Astrophysics, 286, 597

Baselian, L. L., Goncharov, N. I., Zaitsev, V. V., et al. 1974, Sol. Phys., 39, 213, doi: 10.1007/BF00154982

Bastian, T. S. 1994, ApJ, 426, 774, doi: 10.1086/174114

—. 2000, Washington DC American Geophysical Union Geophysical Monograph Series, 119, 85, doi: 10.1029/GM119p0085

Battaglia, M., & Benz, A. O. 2009, Astronomy and Astrophysics, 499, L33, doi: 10.1051/0004-6361/200912143

Battaglia, M., & Kontar, E. P. 2012, ApJ, 760, 142, doi: 10.1088/0004-637X/760/2/142

Battaglia, M., Sharma, R., Luo, Y., et al. 2021, ApJ, 922, 134, doi: 10.3847/1538-4357/ac2aa6

Bemporad, A., Sterling, A. C., Moore, R. L., & Poletto, G. 2005, ApJ, 635, L189, doi: 10.1086/499625

Benz, A. O. 1985, Sol. Phys., 96, 357, doi: 10.1007/BF00149690

—. 1986, Solar Physics, 104, 99, doi: 10.1007/BF00159950

—. 2017, Living Reviews in Solar Physics, 14, 2, doi: 10.1007/s41116-016-0004-3

Benz, A. O., & Aschwanden, M. J. 1992, in IAU Colloq. 133: Eruptive Solar Flares, ed. Z. Svestka, B. V. Jackson, & M. E. Machado, Vol. 399, 106–115, doi: 10.1007/3-540-55246-4_84

Benz, A. O., Csillaghy, A., & Aschwanden, M. J. 1996, Astronomy and Astrophysics, 309, 291

Benz, A. O., Jaeggi, M., & Zlobec, P. 1982, A&A, 109, 305

Benz, A. O., Magun, A., Stehling, W., & Su, H. 1992a, Sol. Phys., 141, 335, doi: 10.1007/BF00155184

Benz, A. O., Monstein, C., Beverland, M., Meyer, H., & Stuber, B. 2009, Sol. Phys., 260, 375, doi: 10.1007/s11207-009-9455-1

Benz, A. O., Saint-Hilaire, P., & Vilmer, N. 2002, A&A, 383, 678, doi: 10.1051/0004-6361:20011774

Benz, A. O., Su, H., Magun, A., & Stehling, W. 1992b, A&AS, 93, 539

Bisi, M. M., Breen, A. R., Jackson, B. V., et al. 2010, Sol. Phys., 265, 49, doi: 10.1007/s11207-010-9602-8

Blesing, R. G., & Dennison, P. A. 1972, PASA, 2, 84, doi: 10.1017/S1323358000012947

Boischot, A., Rosolen, C., Aubier, M. G., et al. 1980, Icarus, 43, 399, doi: 10.1016/0019-1035(80)90185-2

Bolduc, L. 2002, Journal of Atmospheric and Solar-Terrestrial Physics, 64, 1793, doi: 10.1016/S1364-6826(02)00128-1

Boteler, D. 1994, IEEE Transactions on Power Delivery, 9, 50, doi: 10.1109/61.277679

Bougeret, J. L., King, J. H., & Schwenn, R. 1984, Sol. Phys., 90, 401, doi: 10.1007/BF00173965

Bougeret, J. L., & Steinberg, J. L. 1977, A&A, 61, 777

Bougeret, J. L., Kaiser, M. L., Kellogg, P. J., et al. 1995, Space Sci. Rev., 71, 231, doi: 10.1007/BF00751331

Bouratzis, C., Hillaris, A., Alissandrakis, C. E., et al. 2016, A&A, 586, A29, doi: 10.1051/0004-6361/201527229

Bradford, H. M., & Routledge, D. 1980, MNRAS, 190, 73P, doi: 10.1093/mnras/190.1.73P

Brown, J. C., & Smith, D. F. 1980, Reports on Progress in Physics, 43, 125, doi: 10.1088/0034-4885/43/2/001

Browning, M. K., Miesch, M. S., Brun, A. S., & Toomre, J. 2006, ApJ, 648, L157, doi: 10.1086/507869

Brueckner, G. E., Howard, R. A., Koomen, M. J., et al. 1995, Sol. Phys., 162, 357, doi: 10.1007/BF00733434

Cane, H. V., & Erickson, W. C. 2005, ApJ, 623, 1180, doi: 10.1086/428820

Cane, H. V., & Stone, R. G. 1984, ApJ, 282, 339, doi: 10.1086/162207

Carrano, C. S., Bridgwood, C. T., & Groves, K. M. 2009, Radio Science, 44, RS0A25, doi: 10.1029/2008RS004071

Celnikier, L. M., Harvey, C. C., Jegou, R., Moricet, P., & Kemp, M. 1983, A&A, 126, 293

Cerruti, A. P., Kintner, P. M., Gary, D. E., et al. 2006, Space Weather, 4, S10006, doi: 10.1029/2006SW000254

—. 2008, Space Weather, 6, S10D07, doi: 10.1029/2007SW000375

Chaizy, P., Pick, M., Reiner, M., et al. 1995, A&A, 303, 583

Chandra, R., Gupta, G. R., Mulay, S., & Tripathi, D. 2015, MNRAS, 446, 3741, doi: 10.1093/mnras/stu2305

Chen, F. F. 2016, Introduction to Plasma Physics and Controlled Fusion, doi: 10.1007/978-3-319-22309-4

Chen, N., Ip, W.-H., & Innes, D. 2013, ApJ, 769, 96, doi: 10.1088/0004-637X/769/2/96

Chen, X., Kontar, E. P., Chrysaphi, N., et al. 2020, ApJ, 905, 43, doi: 10.3847/1538-4357/abc24e

Chen, X., Kontar, E. P., Clarkson, D. L., & Chrysaphi, N. 2023a, MNRAS, 520, 3117, doi: 10.1093/mnras/stad325

—. 2023b, MNRAS, doi: 10.1093/mnras/stad325

Chen, X., Kontar, E. P., Yu, S., et al. 2018, ApJ, 856, 73, doi: 10.3847/1538-4357/aaa9bf

Chen, Z., Gao, Y., & Liu, Z. 2005, Radio Science, 40, RS3012, doi: 10.1029/2004RS003066

Chernov, G. P. 1977, Soviet Ast., 21, 612

—. 1978, Soviet Astronomy, 22, 330

Chernov, G. P., Sych, R. A., Meshalkina, N. S., Yan, Y., & Tan, C. 2012, A&A, 538, A53, doi: 10.1051/0004-6361/201117034

Chrysaphi, N., Kontar, E. P., Holman, G. D., & Temmer, M. 2018, ApJ, 868, 79, doi: 10.3847/1538-4357/aae9e5

Chrysaphi, N., Reid, H. A. S., & Kontar, E. P. 2020, ApJ, 893, 115, doi: 10.3847/1538-4357/ab80c1

Clarkson, D. L., Kontar, E. P., Gordovskyy, M., Chrysaphi, N., & Vilmer, N. 2021, ApJ, 917, L32, doi: 10.3847/2041-8213/ac1a7d

Clarkson, D. L., Kontar, E. P., Gordovskyy, M., Chrysaphi, N., & Vilmer, N. 2021, The Astrophysical Journal Letters, 917, L32, doi: 10.3847/2041-8213/ac1a7d

Clarkson, D. L., Kontar, E. P., Vilmer, N., et al. 2023, ApJ, 946, 33, doi: 10.3847/1538-4357/acbd3f

Claßen, H. T., & Aurass, H. 2002, A&A, 384, 1098, doi: 10.1051/0004-6361:20020092

Cliver, E. W., Webb, D. F., & Howard, R. A. 1999, Sol. Phys., 187, 89, doi: 10.1023/A:1005115119661

Cliver, E. W., White, S. M., & Balasubramaniam, K. S. 2011, Astrophysical Journal, 743, 145, doi: 10.1088/0004-637X/743/2/145

Coles, W. A., & Harmon, J. K. 1989, ApJ, 337, 1023, doi: 10.1086/167173

Condon, J. J. 1997, PASP, 109, 166, doi: 10.1086/133871

Csillaghy, A., & Benz, A. O. 1993, A&A, 274, 487

Dabrowski, B., Mikuła, K., Flisek, P., et al. 2023, A&A, 669, A52, doi: 10.1051/0004-6361/202142905

Dabrowski, B. P., Rudawy, P., Falewicz, R., Siarkowski, M., & Kus, A. J. 2005, A&A, 434, 1139, doi: 10.1051/0004-6361:20041798

Dabrowski, B. P., Rudawy, P., & Karlický, M. 2011, Sol. Phys., 273, 377, doi: 10.1007/s11207-011-9756-z

de La Noe, J. 1975, A&A, 43, 201

de La Noe, J., & Boischot, A. 1972, A&A, 20, 55

Demyanov, V. V., Afraimovich, E. L., & Jin, S. 2012, GPS solutions, 16, 411

Droege, F. 1977, A&A, 57, 285

Dulk, G. A. 1985, ARA&A, 23, 169, doi: 10.1146/annurev.aa.23.090185.001125

Dulk, G. A., & McLean, D. J. 1978, Sol. Phys., 57, 279, doi: 10.1007/BF00160102

Dulk, G. A., & Suzuki, S. 1980, A&A, 88, 203

Duncan, R. A. 1979, Sol. Phys., 63, 389, doi: 10.1007/BF00174543

Elgaroy, O., & Sveen, O. P. 1979, Nature, 278, 626, doi: 10.1038/278626a0

Ellis, G. R. A. 1969, Australian Journal of Physics, 22, 177, doi: 10.1071/PH690177

Emslie, A. G., Dennis, B. R., Holman, G. D., & Hudson, H. S. 2005, Journal of Geophysical Research (Space Physics), 110, A11103, doi: 10.1029/2005JA011305

Emslie, A. G., Dennis, B. R., Shih, A. Y., et al. 2012, ApJ, 759, 71, doi: 10.1088/0004-637X/759/1/71

Erickson, W. C. 1964, ApJ, 139, 1290, doi: 10.1086/147865

Feynman, J., & Hundhausen, A. J. 1994, J. Geophys. Res., 99, 8451, doi: 10.1029/94JA00202

Fleishman, G. D. 2004a, Astronomy Letters, 30, 603, doi: 10.1134/1.1795949

—. 2004b, ApJ, 601, 559, doi: 10.1086/380440

Fleishman, G. D., & Mel'nikov, V. F. 1998, Physics Uspekhi, 41, 1157, doi: 10.1070/PU1998v041n12ABEH000510

Fletcher, L., Dennis, B. R., Hudson, H. S., et al. 2011, Space Sci. Rev., 159, 19, doi: 10.1007/s11214-010-9701-8

Fokker, A. D. 1965, Bull. Astron. Inst. Netherlands, 18, 111

Fontenla, J. M., Avrett, E. H., & Loeser, R. 1990, ApJ, 355, 700, doi: 10.1086/168803

Fox, N. J., Velli, M. C., Bale, S. D., et al. 2016, Space Sci. Rev., 204, 7, doi: 10.1007/s11214-015-0211-6

Garcia, H. A. 1994, Sol. Phys., 154, 275, doi: 10.1007/BF00681100

Gary, D. E., Hurford, G. J., & Flees, D. J. 1991, ApJ, 369, 255, doi: 10.1086/169756

Gary, D. E., & Keller, C. U. 2004, Solar and space weather radiophysics: current status and future developments, Vol. 314 (Springer Science & Business Media)

Gary, G. A. 2001, Sol. Phys., 203, 71, doi: 10.1023/A:1012722021820

Ghizaru, M., Charbonneau, P., & Smolarkiewicz, P. K. 2010, ApJ, 715, L133, doi: 10.1088/2041-8205/715/2/L133

Ginzburg, V. L., & Zheleznyakov, V. V. 1958, Soviet Ast., 2, 653

Gordovskyy, M., Kontar, E., Browning, P., & Kuznetsov, A. 2019, ApJ, 873, 48, doi: 10.3847/1538-4357/ab03d8

Gordovskyy, M., Kontar, E. P., Clarkson, D. L., Chrysaphi, N., & Browning, P. K. 2022, ApJ, 925, 140, doi: 10.3847/1538-4357/ac3bb7

Gorgolewski, S., Hanasz, J., Iwaniszewski, H., & Turło, Z. 1962, Acta Astron., 12, 251

Gosling, J. T. 1993, J. Geophys. Res., 98, 18937, doi: 10.1029/93JA01896

Gothoskar, P., Anantharamahaia, K. R., Desai, K., & Rao, A. P. 2001, Ap&SS, 278, 193, doi: 10.1023/A:1013110930964

Grognard, R. J. M. 1985, Propagation of electron streams., ed. D. J. McLean & N. R. Labrum, 253–286

Guedel, M., & Benz, A. O. 1990, A&A, 231, 202

Guedel, M., Benz, A. O., & Aschwanden, M. J. 1991, A&A, 251, 285

Gurnett, D. A., & Anderson, R. R. 1976, Science, 194, 1159, doi: 10.1126/science.194.4270.1159

Gurnett, D. A., Baumback, M. M., & Rosenbauer, H. 1978, J. Geophys. Res., 83, 616, doi: 10.1029/JA083iA02p00616

Harries, J. R., Blesing, R. G., & Dennison, P. A. 1970, PASA, 1, 319, doi: 10.1017/S1323358000012091

Harvey, K. L. 1996, in Astronomical Society of the Pacific Conference Series, Vol. 111, Astronomical Society of the Pacific Conference Series, ed. R. D. Bentley & J. T. Mariska, 9–18

Hewish, A. 1952, Proceedings of the Royal Society of London Series A, 214, 494, doi: 10.1098/rspa.1952.0185

—. 1955, Proceedings of the Royal Society of London Series A, 228, 238, doi: 10.1098/rspa.1955.0046

—. 1958, MNRAS, 118, 534, doi: 10.1093/mnras/118.6.534

Hewish, A., & Wyndham, J. D. 1963, MNRAS, 126, 469, doi: 10.1093/mnras/126.5.469

Hewitt, R. G., Melrose, D. B., & Ronnmark, K. G. 1982, Australian Journal of Physics, 35, 447, doi: 10.1071/PH820447

Hey, J. S. 1946, Nature, 157, 47, doi: 10.1038/157047b0

Heyvaerts, J., Kerdraon, A., Mangeney, A., Pick, M., & Slottje, C. 1978, A&A, 66, 81

Högbom, J. A. 1960, MNRAS, 120, 530, doi: 10.1093/mnras/120.6.530

Holman, G. D., & Pesses, M. E. 1983, ApJ, 267, 837, doi: 10.1086/160918

Holman, G. D., Aschwanden, M. J., Aurass, H., et al. 2011, Space Sci. Rev., 159, 107, doi: 10.1007/s11214-010-9680-9

Howard, R. A., Michels, D. J., Sheeley, N. R., J., & Koomen, M. J. 1982, ApJ, 263, L101, doi: 10.1086/183932

Huang, G., & Nakajima, H. 2005, Ap&SS, 295, 423, doi: 10.1007/s10509-005-6561-x

Huang, J., & Tan, B. 2012, ApJ, 745, 186, doi: 10.1088/0004-637X/745/2/186

ITU. 2020, Radio Regulations. http://handle.itu.int/11.1002/pub/814b0c44-en

Jaeger, J. C., & Westfold, K. C. 1950, Australian Journal of Scientific Research A Physical Sciences, 3, 376, doi: 10.1071/CH9500376

Jeffrey, N. L. S., & Kontar, E. P. 2011, A&A, 536, A93, doi: 10.1051/0004-6361/201117987

Kellogg, P. J., Goetz, K., Monson, S. J., et al. 2009, Journal of Geophysical Research (Space Physics), 114, A02107, doi: 10.1029/2008JA013566

Khan, J. I., & Aurass, H. 2006, A&A, 457, 319, doi: 10.1051/0004-6361:20054034

Kintner, P. M., O'Hanlon, B., Gary, D. E., & Kintner, P. M. S. 2009, Radio Science, 44, RS0A08, doi: 10.1029/2008RS004039

Klimchuk, J. A. 2006, Sol. Phys., 234, 41, doi: 10.1007/s11207-006-0055-z

Klobuchar, J. A., Kunches, J. M., & VanDierendonck, A. 1999, GPS Solutions, 3, 69

Klobuchar, J. A., Kunches, j. M., & VanDierendonck, A. J. 1999, GPS Solutions, 3, 69, doi: 10.1007/PL00012794

Kolotkov, D. Y., Nakariakov, V. M., & Kontar, E. P. 2018, ApJ, 861, 33, doi: 10.3847/1538-4357/aac77e

Kontar, E. P. 2001a, Sol. Phys., 202, 131, doi: 10.1023/A:1011894830942

—. 2001b, A&A, 375, 629, doi: 10.1051/0004-6361:20010807

Kontar, E. P., Hannah, I. G., & MacKinnon, A. L. 2008, A&A, 489, L57, doi: 10.1051/0004-6361:200810719

Kontar, E. P., & Jeffrey, N. L. S. 2010, A&A, 513, L2, doi: 10.1051/0004-6361/201014066

Kontar, E. P., Perez, J. E., Harra, L. K., et al. 2017a, Phys. Rev. Lett., 118, 155101, doi: 10.1103/PhysRevLett.118.155101

Kontar, E. P., Yu, S., Kuznetsov, A. A., et al. 2017b, Nature Communications, 8, 1515, doi: 10.1038/s41467-017-01307-8

Kontar, E. P., Chen, X., Chrysaphi, N., et al. 2019, ApJ, 884, 122, doi: 10.3847/1538-4357/ab40bb

Koval, A., Chen, Y., Stanislavsky, A., & Zhang, Q.-H. 2017, Journal of Geophysical Research (Space Physics), 122, 9092, doi: 10.1002/2017JA024080

Krucker, S., Aschwanden, M. J., Bastian, T. S., & Benz, A. O. 1995, A&A, 302, 551

Krucker, S., & Benz, A. O. 1994, A&A, 285, 1038

Krucker, S., Benz, A. O., & Aschwanden, M. J. 1997, A&A, 317, 569

Krucker, S., Kontar, E. P., Christe, S., & Lin, R. P. 2007, ApJ, 663, L109, doi: 10.1086/519373

Krupar, V., Kontar, E. P., Soucek, J., et al. 2015, A&A, 580, A137, doi: 10.1051/0004-6361/201425308

Krupar, V., Magdalenić, J., Eastwood, J. P., et al. 2019, ApJ, 882, 92, doi: 10.3847/1538-4357/ab3345

Krupar, V., Maksimovic, M., Santolik, O., et al. 2014, Sol. Phys., 289, 3121, doi: 10.1007/s11207-014-0522-x

Krupar, V., Maksimovic, M., Kontar, E. P., et al. 2018, ApJ, 857, 82, doi: 10.3847/1538-4357/aab60f

Krupar, V., Szabo, A., Maksimovic, M., et al. 2020, ApJS, 246, 57, doi: 10.3847/1538-4365/ab65bd

Kundu, M. R., & Alissandrakis, C. E. 1984, Sol. Phys., 94, 249, doi: 10.1007/BF00151317

Kundu, M. R., Raulin, J. P., Nitta, N., et al. 1995, ApJ, 447, L135, doi: 10.1086/309567

Kuznetsov, A. A., Chrysaphi, N., Kontar, E. P., & Motorina, G. 2020, ApJ, 898, 94, doi: 10.3847/1538-4357/aba04a

Kuznetsov, A. A., & Kontar, E. P. 2019, A&A, 631, L7, doi: 10.1051/0004-6361/201936447

Lamy, L., Zarka, P., Cecconi, B., et al. 2018, 1977-2017: 40 years of decametric observations of Jupiter and the Sun with the Nançay Decameter Array, Wien: Verlag der Österreichischen Akademie der Wissenschaften. https://austriaca.at/?arp=0x0039b766

Leblanc, Y., Dulk, G. A., & Bougeret, J.-L. 1998, Sol. Phys., 183, 165, doi: 10.1023/A:1005049730506

Leblanc, Y., & Hoyos, M. 1985, A&A, 143, 365

Lecacheux, A. 2000, The NançAy Decameter Array: A Useful Step Towards Giant, New Generation Radio Telescopes for Long Wavelength Radio Astronomy (American Geophysical Union (AGU)), 321–328, doi: https://doi.org/10.1029/GM119p0321

Leighton, R. B. 1969, ApJ, 156, 1, doi: 10.1086/149943

Lemen, J. R., Title, A. M., Akin, D. J., et al. 2012, Sol. Phys., 275, 17, doi: 10.1007/s11207-011-9776-8

Lin, R. P., Potter, D. W., Gurnett, D. A., & Scarf, F. L. 1981, ApJ, 251, 364, doi: 10.1086/159471

Lin, R. P., Schwartz, R. A., Kane, S. R., Pelling, R. M., & Hurley, K. C. 1984, ApJ, 283, 421, doi: 10.1086/162321

Lin, R. P., Anderson, K. A., Ashford, S., et al. 1995, Space Sci. Rev., 71, 125, doi: 10.1007/BF00751328

Liu, Z., Gary, D. E., Nita, G. M., White, S. M., & Hurford, G. J. 2007, PASP, 119, 303, doi: 10.1086/512825

Luo, Y., Chen, B., Yu, S., Bastian, T. S., & Krucker, S. 2021, ApJ, 911, 4, doi: 10.3847/1538-4357/abe5a4

Maguire, C. A., Carley, E. P., Zucca, P., Vilmer, N., & Gallagher, P. T. 2021, ApJ, 909, 2, doi: 10.3847/1538-4357/abda51

Malaspina, D. M., & Ergun, R. E. 2008, Journal of Geophysical Research (Space Physics), 113, A12108, doi: 10.1029/2008JA013656

Mann, G., Jansen, F., MacDowall, R. J., Kaiser, M. L., & Stone, R. G. 1999, A&A, 348, 614

Markeev, A. K., & Chernov, G. P. 1971, Soviet Ast., 14, 835

Marqué, C., Klein, K.-L., Monstein, C., et al. 2018, Journal of Space Weather and Space Climate, 8, A42, doi: 10.1051/swsc/2018029

Marsch, E., & Tu, C. Y. 1990, J. Geophys. Res., 95, 11945, doi: 10.1029/JA095iA08p11945

McCauley, P. I., Cairns, I. H., Morgan, J., et al. 2017, ApJ, 851, 151, doi: 10.3847/1538-4357/aa9cee

McKim Malville, J., Aller, H. D., & Jensen, C. J. 1967, Astrophysical Journal, 147, 711, doi: 10.1086/149048

McLean, D. J., & Labrum, N. R. 1985, Solar radiophysics : studies of emission from the sun at metre wavelengths

Meléndez, J. L., Sawant, H. S., Fernandes, F. C. R., & Benz, A. O. 1999, Sol. Phys., 187, 77, doi: 10.1023/A:1005110111620

Melnik, V. N., Konovalenko, A. A., Dorovskyy, V. V., et al. 2005, Sol. Phys., 231, 143, doi: 10.1007/s11207-005-8272-4

Melnik, V. N., Konovalenko, A. A., Rucker, H. O., et al. 2011, Sol. Phys., 269, 335, doi: 10.1007/s11207-010-9703-4

Mel'nik, V. N., & Kontar, E. P. 2000, New A, 5, 35, doi: 10.1016/S1384-1076(00)00004-X

Mel'nik, V. N., Lapshin, V., & Kontar, E. 1999, Sol. Phys., 184, 353, doi: 10.1023/A:1005191910544

Melnik, V. N., Rucker, H. O., Konovalenko, A. A., et al. 2010, in American Institute of Physics Conference Series, Vol. 1206, American Institute of Physics Conference Series, ed. S. K. Chakrabarti, A. I. Zhuk, & G. S. Bisnovatyi-Kogan, 445–449, doi: 10.1063/1.3292552

Melnik, V. N., Shevchuk, N. V., Konovalenko, A. A., et al. 2014, Sol. Phys., 289, 1701, doi: 10.1007/s11207-013-0434-1

Melrose, D. B. 1980, Space Sci. Rev., 26, 3, doi: 10.1007/BF00212597

—. 1985, in Solar Radiophysics: Studies of Emission from the Sun at Metre Wavelengths, ed. D. J. McLean & N. R. Labrum (Cambridge and New York, Cambridge University Press), 177–210

—. 1987, Sol. Phys., 111, 89, doi: 10.1007/BF00145443

Melrose, D. B. 2009, in Universal Heliophysical Processes, ed. N. Gopalswamy & D. F. Webb, Vol. 257, 305–315, doi: 10.1017/S1743921309029470

—. 2017, Reviews of Modern Plasma Physics, 1, 5, doi: 10.1007/s41614-017-0007-0

Melrose, D. B., Cairns, I. H., & Dulk, G. A. 1986, A&A, 163, 229

Melrose, D. B., & Dulk, G. A. 1982, ApJ, 259, 844, doi: 10.1086/160219

Messmer, P., & Benz, A. O. 2000, A&A, 354, 287, doi: 10.48550/arXiv.astro-ph/9912502

Mészárosová, H., Karlický, M., Veronig, A., Zlobec, P., & Messerotti, M. 2000, A&A, 360, 1126

Mészárosová, H., Veronig, A., Zlobec, P., & Karlický, M. 2003, A&A, 407, 1115, doi: 10.1051/0004-6361:20030888

Moller-Pedersen, B., Smith, R. A., & Mangeney, A. 1978, A&A, 70, 801

Moncuquet, M., Meyer-Vernet, N., Issautier, K., et al. 2020, ApJS, 246, 44, doi: 10.3847/1538-4365/ab5a84

Morosan, D. E., Kilpua, E. K. J., Carley, E. P., & Monstein, C. 2019, A&A, 623, A63, doi: 10.1051/0004-6361/201834510

Morosan, D. E., Gallagher, P. T., Zucca, P., et al. 2014, A&A, 568, A67, doi: 10.1051/0004-6361/201423936

Muhammad, B., Alberti, V., Marassi, A., Cianca, E., & Messerotti, M. 2015, Journal of Space Weather and Space Climate, 5, A32, doi: 10.1051/swsc/2015034

Mulay, S. M., Tripathi, D., Del Zanna, G., & Mason, H. 2016, A&A, 589, A79, doi: 10.1051/0004-6361/201527473

Müller, D., St. Cyr, O. C., Zouganelis, I., et al. 2020, A&A, 642, A1, doi: 10.1051/0004-6361/202038467

Murphy, P. C., Carley, E. P., Ryan, A. M., Zucca, P., & Gallagher, P. T. 2021, A&A, 645, A11, doi: 10.1051/0004-6361/202038518

Musset, S., Maksimovic, M., Kontar, E., et al. 2021, A&A, 656, A34, doi: 10.1051/0004-6361/202140998

Narayan, R., Anantharamaiah, K. R., & Cornwell, T. J. 1989, MNRAS, 241, 403, doi: 10.1093/mnras/241.3.403

Neupert, W. M. 1968, ApJ, 153, L59, doi: 10.1086/180220

Newkirk, Gordon, J. 1961, ApJ, 133, 983, doi: 10.1086/147104

Nita, G. M., Fleishman, G. D., & Gary, D. E. 2008, ApJ, 689, 545, doi: 10.1086/592191

Nita, G. M., Gary, D. E., Lanzerotti, L. J., & Thomson, D. J. 2002, ApJ, 570, 423, doi: 10.1086/339577

Ogilvie, K. W., Chornay, D. J., Fritzenreiter, R. J., et al. 1995, Space Sci. Rev., 71, 55, doi: 10.1007/BF00751326

Paesold, G., Benz, A. O., Klein, K. L., & Vilmer, N. 2001, Astronomy and Astrophysics, 371, 333, doi: 10.1051/0004-6361:20010358

Parker, E. N. 1955a, ApJ, 122, 293, doi: 10.1086/146087

—. 1955b, ApJ, 121, 491, doi: 10.1086/146010

—. 1957, J. Geophys. Res., 62, 509, doi: 10.1029/JZ062i004p00509

—. 1958, ApJ, 128, 664, doi: 10.1086/146579

—. 1988, ApJ, 330, 474, doi: 10.1086/166485

Pécseli, H. 2012, Waves and Oscillations in Plasmas (CRC Press, Boca Raton), doi: 10.1201/b12702

Perrenoud, M. R. 1982, Sol. Phys., 81, 197, doi: 10.1007/BF00151991

Pesnell, W. D., Thompson, B. J., & Chamberlin, P. C. 2012, Sol. Phys., 275, 3, doi: 10.1007/s11207-011-9841-3

Petschek, H. E. 1964, in NASA Special Publication, Vol. 50, 425

Pick, M., & Vilmer, N. 2008, A&A Rev., 16, 1, doi: 10.1007/s00159-008-0013-x

Pneuman, G. W., & Kopp, R. A. 1971, Sol. Phys., 18, 258, doi: 10.1007/BF00145940

Priest, E. 2014, Magnetohydrodynamics of the Sun, doi: 10.1017/CBO9781139020732

Priest, E. R., & Forbes, T. G. 2002, A&A Rev., 10, 313, doi: 10.1007/s001590100013

Pulkkinen, A., Bernabeu, E., Thomson, A., et al. 2017, Space Weather, 15, 828, doi: 10.1002/2016SW001501

Pulupa, M., Bale, S. D., Badman, S. T., et al. 2020, ApJS, 246, 49, doi: 10.3847/1538-4365/ab5dc0

Raoult, A., & Pick, M. 1980, A&A, 87, 63

Ratcliffe, H., & Kontar, E. P. 2014, A&A, 562, A57, doi: 10.1051/0004-6361/201322263

Reames, D. V. 1999, Space Sci. Rev., 90, 413, doi: 10.1023/A:1005105831781

Redmon, R. J., Seaton, D. B., Steenburgh, R., He, J., & Rodriguez, J. V. 2018, Space Weather, 16, 1190, doi: 10.1029/2018SW001897

Reid, H. A. S., & Kontar, E. P. 2017, A&A, 606, A141, doi: 10.1051/0004-6361/201730701

—. 2018a, ApJ, 867, 158, doi: 10.3847/1538-4357/aae5d4

—. 2018b, A&A, 614, A69, doi: 10.1051/0004-6361/201732298

—. 2021, Nature Astronomy, doi: 10.1038/s41550-021-01370-8

Reid, H. A. S., & Ratcliffe, H. 2014, Research in Astronomy and Astrophysics, 14, 773, doi: 10.1088/1674-4527/14/7/003

Reid, H. A. S., Vilmer, N., & Kontar, E. P. 2011, A&A, 529, A66, doi: 10.1051/0004-6361/201016181

Reiner, M. J., Fainberg, J., Kaiser, M. L., & Stone, R. G. 1998, J. Geophys. Res., 103, 1923, doi: 10.1029/97JA02646

Reiner, M. J., Vourlidas, A., Cyr, O. C. S., et al. 2003, ApJ, 590, 533, doi: 10.1086/374917

Riddle, A. C. 1974, Sol. Phys., 35, 153, doi: 10.1007/BF00156964

Roberts, J. A. 1958, Australian Journal of Physics, 11, 215, doi: 10.1071/PH580215

Robinson, P. A., Cairns, I. H., & Gurnett, D. A. 1993, ApJ, 407, 790, doi: 10.1086/172560

Robinson, R. D. 1983, PASA, 5, 208, doi: 10.1017/S132335800001688X

Rozhansky, I. V., Fleishman, G. D., & Huang, G. L. 2008, ApJ, 681, 1688, doi: 10.1086/588380

Ryabov, B. I., Pilyeva, N. A., Alissandrakis, C. E., et al. 1999, Sol. Phys., 185, 157, doi: 10.1023/A:1005114303703

Ryle, M., & Hewish, A. 1950, MNRAS, 110, 381, doi: 10.1093/mnras/110.4.381

Saito, K., Poland, A. I., & Munro, R. H. 1977, Sol. Phys., 55, 121, doi: 10.1007/BF00150879

Sakurai, T., Spangler, S. R., & Armstrong, J. W. 1992, J. Geophys. Res., 97, 17141, doi: 10.1029/92JA01551

Sasikumar Raja, K., Subramanian, P., Ramesh, R., Vourlidas, A., & Ingale, M. 2017, ApJ, 850, 129, doi: 10.3847/1538-4357/aa94cd

Sasikumar Raja, K., Maksimovic, M., Kontar, E. P., et al. 2022, ApJ, 924, 58, doi: 10.3847/1538-4357/ac34ed

Sato, H., Jakowski, N., Berdermann, J., et al. 2019, Space Weather, 17, 816, doi: 10.1029/2019SW002198

Schatten, K. H., Wilcox, J. M., & Ness, N. F. 1969, Sol. Phys., 6, 442, doi: 10.1007/BF00146478

Scherrer, P. H., Schou, J., Bush, R. I., et al. 2012, Sol. Phys., 275, 207, doi: 10.1007/s11207-011-9834-2

Schmidt, J. M., Cairns, I. H., & Lobzin, V. V. 2014, Journal of Geophysical Research (Space Physics), 119, 6042, doi: 10.1002/2014JA019950

Schwenn, R. 2006, Living Reviews in Solar Physics, 3, 2, doi: 10.12942/lrsp-2006-2

Sharykin, I. N., Kontar, E. P., & Kuznetsov, A. A. 2018, Sol. Phys., 293, 115, doi: 10.1007/s11207-018-1333-2

Shen, Y., Liu, Y., Su, J., & Deng, Y. 2012, ApJ, 745, 164, doi: 10.1088/0004-637X/745/2/164

Shevchuk, N. V., Melnik, V. N., Poedts, S., et al. 2016, Sol. Phys., 291, 211, doi: 10.1007/s11207-015-0799-4

Shibata, K., Nakamura, T., Matsumoto, T., et al. 2007, Science, 318, 1591, doi: 10.1126/science.1146708

Slee, O. B. 1959, Australian Journal of Physics, 12, 134, doi: 10.1071/PH590134

—. 1966, Planet. Space Sci., 14, 255, doi: 10.1016/0032-0633(66)90125-5

Slottje, C. 1978, Nature, 275, 520, doi: 10.1038/275520a0

Slottje, C. 1980, in Radio Physics of the Sun, ed. M. R. Kundu & T. E. Gergely, Vol. 86, 195–203, doi: 10.1017/S0074180900036846

Smerd, S. F., Sheridan, K. V., & Stewart, R. T. 1975, Astrophys. Lett., 16, 23

Smith, D. F., & Sime, D. 1979, ApJ, 233, 998, doi: 10.1086/157463

Sreeja, V., Aquino, M., & de Jong, K. 2013, Space Weather, 11, 306, doi: 10.1002/swe.20057

Staehli, M., & Magun, A. 1986, Solar Physics, 104, 117, doi: 10.1007/BF00159952

Steinberg, J. L., Aubier-Giraud, M., Leblanc, Y., & Boischot, A. 1971, A&A, 10, 362

Stewart, R. T. 1975, Sol. Phys., 40, 417, doi: 10.1007/BF00162388

Stone, R. G. 1980, in Radio Physics of the Sun, ed. M. R. Kundu & T. E. Gergely, Vol. 86, 405–411, doi: 10.1017/S0074180900037153

Sturrock, P. A. 1964, in NASA Special Publication, Vol. 50, 357

Suzuki, S., & Dulk, G. A. 1985, Bursts of type III and type V., ed. D. J. McLean & N. R. Labrum, 289–332

Suzuki, S., & Gary, D. E. 1979, PASA, 3, 379, doi: 10.1017/S1323358000026151

Sweet, P. A. 1958, in Electromagnetic Phenomena in Cosmical Physics, ed. B. Lehnert, Vol. 6, 123

Tan, B. 2013, ApJ, 773, 165, doi: 10.1088/0004-637X/773/2/165

Tan, B., Chen, N., Yang, Y.-H., et al. 2019, Astrphysical Journal, 885, 90, doi: 10.3847/1538-4357/ab4718

Tan, B. L., Karlický, M., Mészárosová, H., et al. 2016, Sol. Phys., 291, 2407, doi: 10.1007/s11207-016-0986-y

Tarnstrom, G. L., & Philip, K. W. 1972a, Astronomy and Astrophysics, 16, 21

—. 1972b, Astronomy and Astrophysics, 17, 267

Temmer, M., Veronig, A. M., Vršnak, B., et al. 2008, ApJ, 673, L95, doi: 10.1086/527414

Thejappa, G., & MacDowall, R. J. 2008, ApJ, 676, 1338, doi: 10.1086/528835

Thejappa, G., MacDowall, R. J., & Bergamo, M. 2012, ApJ, 745, 187, doi: 10.1088/0004-637X/745/2/187

Thome, G. D., & Wagner, L. S. 1971, J. Geophys. Res., 76, 6883, doi: 10.1029/JA076i028p06883

Thompson, A. R., Moran, J. M., & Swenson, George W., J. 2017, Interferometry and Synthesis in Radio Astronomy, 3rd Edition, doi: 10.1007/978-3-319-44431-4

Tsytovich, V. N., & ter Haar, D. 1995, Lectures on Non-linear Plasma Kinetics

van de Hulst, H. C. 1950, Bull. Astron. Inst. Netherlands, 11, 135

van Haarlem, M. P., Wise, M. W., Gunst, A. W., et al. 2013, A&A, 556, A2, doi: 10.1051/0004-6361/201220873

Vilmer, N. 1987, Sol. Phys., 111, 207, doi: 10.1007/BF00145454

Vilmer, N., Pick, M., Schwenn, R., Ballatore, P., & Villain, J. P. 2003, Annales Geophysicae, 21, 847, doi: 10.5194/angeo-21-847-2003

Vourlidas, A., Wu, S. T., Wang, A. H., Subramanian, P., & Howard, R. A. 2003, ApJ, 598, 1392, doi: 10.1086/379098

Wang, M., Fu, Q. J., Xie, R. X., & Huang, G. L. 1999, Sol. Phys., 189, 331, doi: 10.1023/A:1005213701438

Wang, S. J., Yan, Y. H., & Fu, Q. J. 2002, Sol. Phys., 209, 185, doi: 10.1023/A:1020938808381

Wang, S. J., Yan, Y. H., Liu, Y. Y., et al. 2008, Sol. Phys., 253, 133, doi: 10.1007/s11207-008-9278-5

Weber, R. R. 1978, Sol. Phys., 59, 377, doi: 10.1007/BF00951843

Weiss, L. A. A., & Stewart, R. T. 1965, Australian Journal of Physics, 18, 143, doi: 10.1071/PH650143

Wiegelmann, T., Petrie, G. J. D., & Riley, P. 2017, Space Sci. Rev., 210, 249, doi: 10.1007/s11214-015-0178-3

Wild, J. P., & McCready, L. L. 1950, Australian Journal of Scientific Research A Physical Sciences, 3, 387, doi: 10.1071/CH9500387

Wild, J. P., Sheridan, K. V., & Neylan, A. A. 1959a, Australian Journal of Physics, 12, 369, doi: 10.1071/PH590369

Wild, J. P., Sheridan, K. V., & Trent, G. H. 1959b, in URSI Symp. 1: Paris Symposium on Radio Astronomy, ed. R. N. Bracewell, Vol. 9, 176

Wohlmuth, R., Plettemeier, D., Edenhofer, P., et al. 2001, Space Sci. Rev., 97, 9, doi: 10.1023/A:1011845221808

Woo, R. 1978, ApJ, 219, 727, doi: 10.1086/155831

Woo, R., & Armstrong, J. W. 1979, J. Geophys. Res., 84, 7288, doi: 10.1029/JA084iA12p07288

Woods, T. N., Eparvier, F. G., Hock, R., et al. 2012, Sol. Phys., 275, 115, doi: 10.1007/s11207-009-9487-6

Xu, F.-Y., Xu, Z.-C., Huang, G.-I., et al. 2003, Solar Physics, 216, 273

Zaitsev, V. V. 1975, Soviet Ast., 18, 475

Zhang, P., Yu, S., Kontar, E. P., & Wang, C. 2019, ApJ, 885, 140, doi: 10.3847/1538-4357/ab458f

Zheleznyakov, V. V., & Zaitsev, V. V. 1968, Soviet Ast., 12, 14

—. 1970a, Soviet Ast., 14, 47

—. 1970b, Soviet Ast., 14, 250

Zimovets, I., Vilmer, N., Chian, A. C. L., Sharykin, I., & Struminsky, A. 2012, A&A, 547, A6, doi: 10.1051/0004-6361/201219454

Zucca, P., Morosan, D. E., Rouillard, A. P., et al. 2018, A&A, 615, A89, doi: 10.1051/0004-6361/201732308